# FY20

PROCEEDINGS OF THE U.S. ARMY COMBAT CAPABILITIES DEVELOPMENT COMMAND CHEMICAL BIOLOGICAL CENTER

# IN-HOUSE LABORATORY INDEPENDENT RESEARCH AND SURFACE SCIENCE INITIATIVE PROGRAMS

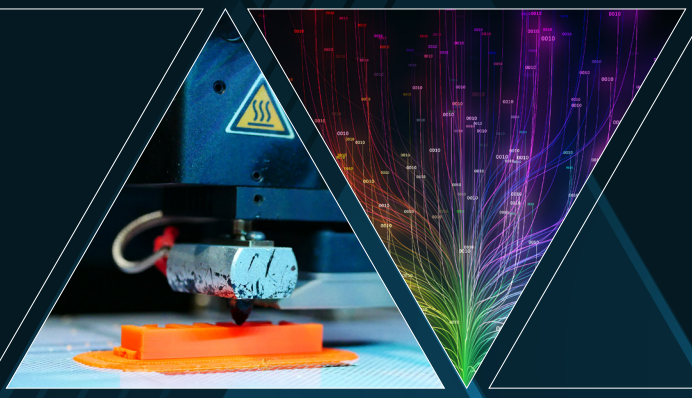

U.S. ARMY

DEVCOM CHEMICAL BIOLOGICAL CENTER

# Message from the In-house Laboratory Independent Research Program Manager

I am pleased to present the twelfth annual edition of the Proceedings of the U.S. Army Combat Capabilities Development Command Chemical Biological Center's (DEVCOM CBC) In-house Laboratory Independent Research (ILIR) and Surface Science Initiative (SSI) Programs. As the Senior Research Scientist (ST) for Chemistry and newly appointed Director of the ILIR and SSI programs, I am excited to continue the legacy of the Center's Army-funded Basic research and innovation programs. While my first few months have been spent getting to know each of our research projects and principal investigators (PIs), my ultimate goal for this portfolio is to ensure we are conducting cutting-edge research, connecting more broadly with experts and stakeholders across the Department of Defense (DoD), and transitioning our most promising projects.

This annual report includes a detailed description of the ILIR program's in-depth project selection and evaluation process. This process, when coupled with our external annual review by experts across the U.S. Government, is critical to ensuring that DEVCOM CBC not only funds projects with the greatest potential for fulfilling future Army capability needs, but that we receive an honest and unbiased assessment of our research efforts to refine our portfolio each year.

This year's report highlights the major accomplishments of our basic research portfolio despite the vast and far-reaching challenges presented due to the COVID-19 virus. In the face of the tremendous challenges and unprecedented barriers placed on the workforce for most of the operating year, our PIs demonstrated their creativity and adaptability to fulfill the research at hand and complete their objectives.

Finally, the report concludes with a technical manuscript from each of the five ILIR and six SSI projects from FY20. Together, these projects covered areas of interest across the chemical, biological, and physical sciences, including: Rational Molecular Synthesis and Novel Materials, Synthetic Biology, Nano Chemical and Biological Sensing, Panomics and Molecular Toxicology, Aerosol Sciences, Algorithm Design and Development, and Surface Science.

If you have questions regarding the ILIR Program or this report, please do not hesitate to contact the DEVCOM CBC Public Affairs Office at usarmy.apg.devcom-cbc.mbx.communications-office@mail.mil.

Sincerely,

Patricia (Trish) McDaniel, Ph.D.
Senior Research Scientist (ST) for Chemistry

# Strategic Mission and Vision

DEVCOM CBC is the Nation's principal research and development resource for non-medical chemical-biological (CB) defense. DEVCOM CBC has the unique ability to advance the mission of the Joint Warfighter and other stakeholders, while leveraging historical expertise, advanced equipment, and state-of-the-art facilities. The Center takes pride in its legacy of solutions born from more than a century of innovation.

## Mission

DEVCOM CBC's mission is to provide innovative chemical, biological, radiological, nuclear, and explosive (CBRNE) defense capabilities to enable the Joint Warfighters' dominance on the battlefield and interagency defense of the homeland. This mission recognizes that the Center's range of influence, while rooted in CB warfare defense, can be applied to all types of challenges in chemistry or biology. The Center's emerging capabilities in synthetic biology and materials science are leveraging existing innovations in biotechnology and decontamination sciences to develop next-generation solutions that ensure our Warfighters are always prepared to operate on the modern and future battlefield.

## Vision

DEVCOM CBC's vision is to be the premier provider of innovative CBRNE solutions for the Army, DoD, the Nation, and our allies. For more than 100 years, the Center has been a distinct asset—providing innovative and economical CB defense technology solutions through scientific and engineering expertise—coupled with our unique facilities and collaboration with partners.

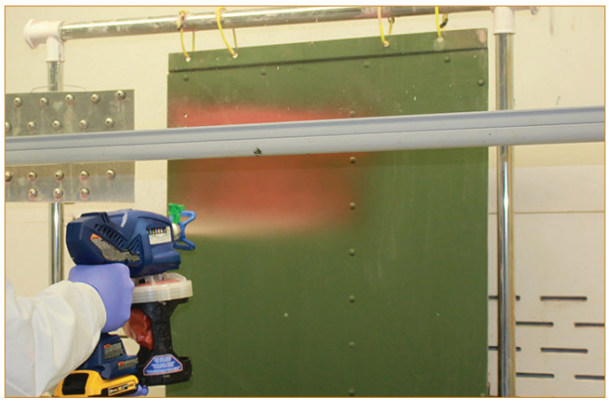

*Sprayable decontaminant slurry that Soldiers can use on vehicles exposed to chemical agent is applied to a vertical surface during testing in a research laboratory. (Photo credit: DEVCOM CBC)*

*A West Virginia National Guard 35th Civil Support Team member wears a prototype of the Center's respiration protection system as he performs a mock chemical materials investigation of a building. (Photo credit: DEVCOM CBC)*

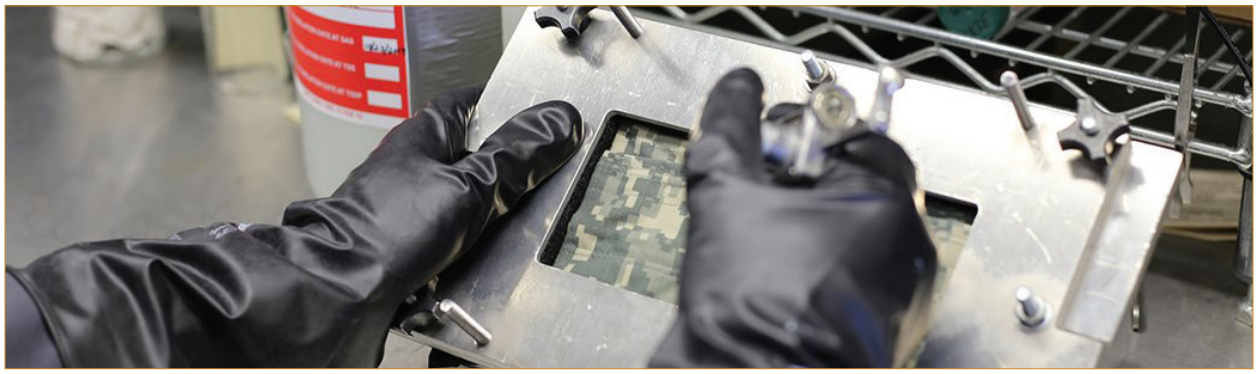

*Center researchers are developing a new device to check for possible leaks around the zippers and seams of a Soldier's protective gear. (Photo credit: DEVCOM CBC)*

# DEVCOM CBC ILIR and SSI Project Selection and Evaluation Process

The purpose of the ILIR and SSI programs is to fund innovative basic research projects that are high-risk but have high potential payoff for fulfilling future Army capability needs. The DoD defines basic research as "systematic study directed toward greater knowledge or understanding of the fundamental aspects of phenomena and of observable facts without specific applications toward processes or products in mind."[1] The ILIR and SSI programs are also specifically designed to foster increased innovation within DEVCOM CBC, where they are viewed as a critical part of the Center's efforts to ensure a high level of quality in basic science; to foster innovation in the areas of chemistry and biology; to mentor junior investigators in the art and practice of laboratory science; and to explore new technological innovations and phenomenology at the boundaries of chemistry, biology, mathematics, or physics to expand the state-of-the-possible in support of CBRNE defense missions.

The ILIR program solicits the Center's researchers for innovative proposals that correspond to topics highlighted in the DEVCOM CBC Research and Technology (R&T) Directorate's Strategic Roadmap. The FY20 ILIR topics were: Rational Molecular Synthesis and Novel Materials, Synthetic Biology, Nano Chemical and Biological Sensing, Panomics and Molecular Toxicology, Aerosol Sciences, and Algorithm Design and Development. The SSI Program solicits projects evaluating solid surfaces and material interfaces, the theory and modeling of processes at complex surfaces, and experimental work focused on the systematic understanding of surface structure and morphology. The proposals are then reviewed and critiqued by a panel comprised of resident Department of the Army Senior Research Scientists (ST), senior scientists from other DoD organizations, and civilian and military faculty members at the United States Military Academy.

The review panel evaluates and scores each ILIR and SSI proposal on its scientific objective, the scientific methods proposed, the qualifications of the investigator, and the budget; with the scientific objective and methods weighted as the most important criteria. The proposals are then ranked according to merit. Only proposals deemed by the panel as basic research are considered for funding. Quality comments from the reviewers are compiled and used, along with the numerical score, as a critical assessment of the proposal. This written feedback is essential for the Center's mentoring of researchers and for justifying the elimination of research programs that are not competitive.

Selected projects are reviewed quarterly; these reviews of project performance provide guidance to the program's participants, ensuring that projects meet significant milestones and that substantive new knowledge is being produced and transferred to

### PROPOSAL SCORING CRITERIA

**Exceptional (4)**: Comprehensive and complete in all areas; meets all significant objectives; offers a comprehensive project that exceeds the ILIR vision and is supportable by the proposed approach; has few weaknesses which are easily correctable.

**Acceptable (3)**: Meets most of the significant objectives and is responsive to the ILIR vision; offers a feasible technical solution; weaknesses are readily correctable; proposal is complete to the extent that an award could be made in present terms.

**Marginal (2)**: Minimally meets ILIR vision and objectives (i.e., offers a project vision that is marginally supported by the proposed approach, and/or claims are not documented or substantiated); significant deficiencies exist.

**Unacceptable (1)**: Fails to meet significant characteristics of the ILIR vision and/or objectives stated in the Solicitation; has weaknesses and/or deficiencies that are significant and of such magnitude that they cannot be corrected without extensive discussion/major revision of the proposal.

| | REVIEWERS | | | | | | | |
|---|---|---|---|---|---|---|---|---|
| | 1 | 2 | 3 | 4 | 5 | 6 | 7 | AVG |
| Scientific Objective | 4 | 3 | 4 | 3 | 3 | 3 | 1 | 3.0 |
| Methods and Approach | 4 | 2 | 3 | 2 | 3 | 2 | 2 | 2.6 |
| PI Qualifications | 3 | 3 | 4 | 3 | 3 | 3 | 3 | 3.1 |
| Budget | 3 | 3 | 3 | 1 | 3 | 3 | 3 | 2.7 |
| **Overall Evaluation** | 3.7 | 2.7 | 3.5 | 2.3 | 3.0 | 2.7 | 2.0 | **2.8** |

[1] *DoD Financial Management Regulation, DoD 7000.14-R, Vol. 2B, Ch. 5*

DEVCOM CBC and the broader scientific community. In FY20, 21 ILIR and SSI proposals were forwarded to the review panel for evaluation; of these, two new ILIR projects and two new SSI projects were selected for funding. Additionally, three FY19 ILIR projects and four FY19 SSI projects received continued funding in FY20.

DEVCOM CBC holds an external review in the fourth quarter—known as our Technical Advisory Board (TAB) Review—to assess year-to-date performance of the funded ILIR and SSI projects. Comments and feedback from this review were used to support continued funding, or course corrections, of each ILIR and SSI project in FY20. These comments and insights are used to improve the quality and content of the individual research projects and to guide the overall mission of the programs into the future.

Five senior scientists from diverse federal defense organizations served on the FY20 TAB panel:

- Dr. Jennifer Becker, Program Manager, Army Research Office
- Dr. Angela Ervin, Portfolio Manager, Countering Weapons of Mass Destruction, Science and Technology Directorate, Department of Homeland Security
- Dr. Ronald Hann, Director, Chemical and Biological Technologies Department, Defense Threat Reduction Agency
- Dr. Adam Rawlett, ST for Materials Science, Weapons and Materials Research Directorate, Army Research Laboratory
- Dr. Naomi Redmore, National Counter Terrorism Center

While typically a multi-day event hosted at the Center, the FY20 TAB was held virtually due to COVID-19 travel and meeting restrictions. The panel was asked to engage in an active dialogue assessing the ILIR and SSI programs and was tasked with producing an unbiased external assessment of the content, quality, innovation, accomplishments, and relevance of the R&T basic science programs. Each project was evaluated based on eight areas: (1) scientific objectives, opportunity, and significance, (2) research methodology, (3) connections to the broader community, (4) overall capabilities and metrics, (5) use of funding, (6) use of PowerPoint, (7) use of time, and (8) overall presentation, with criteria 1–4 weighted as the most important. In FY20, the panel recommended

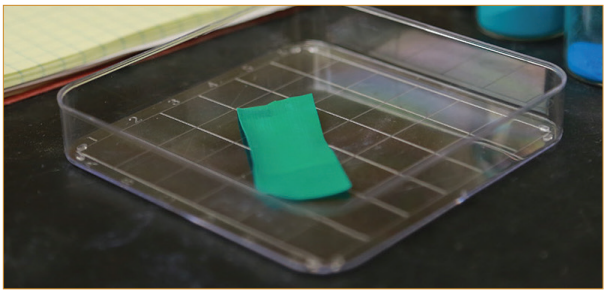

*Greg Peterson, Ph.D., Chemical Engineer, works with metal-organic frameworks and polymer films with improved dispersion to improve warfighter protection. (Photo credit: DEVCOM CBC)*

all projects for continued funding, but provided additional suggestions to enhance several projects. The comments and feedback were also used to draft a final report to the Director of the DEVCOM CBC R&T Directorate as a guide for shaping the overall mission of the ILIR and SSI programs into the future.

Overall, the TAB was pleased with the diversity and quality of projects across the portfolio, scoring both ILIR and SSI programs highly. Over the total $3M portfolio, the panel felt there was excellent productivity and that the projects spanned a diverse number of topics. The PIs were commended for adapting well and doing an excellent job at presenting virtually in response to COVID-19 restrictions. They praised DEVCOM CBC for being among the very best labs in the world and investing in its workforce—stating that the ILIR and SSI programs offer a valuable opportunity to gain experience in managing their own scientific projects, which is critical to developing future leaders. The panel thought most projects utilized state-of-the-art facilities and equipment and successfully leveraged collaborator resources. The panel identified several projects that either had broad applicability to a number of application spaces, or were high-risk with potential high payoff. They commended Mr. Riley for the presentation of his artificial intelligence and machine learning project and noted its potential for broad applicability. The panel also identified two new-start projects as high-risk but with great potential—Dr. Lux's CRISPR project and Ms. Katoski's *Coxiella burnetii* project. The *C. burnetii* project in particular is contributing to an ongoing problem faced by the warfighter. The controlled polymer erosion and chemical transport projects from Drs. Lee and Varady, respectively, were identified as some of the strongest in the SSI portfolio.

Manuscripts from each of the 11 DEVCOM CBC ILIR and SSI projects are contained within this Proceedings Report.

# FY20 Basic Research Program Highlights

## FY20 BASIC RESEARCH PROGRAM PRODUCTIVITY

**7** Presentations and posters

**7** Peer-reviewed publications

**1** Patent issued

**1** Patent filed

**1** Dissertation

*DEVCOM Chemical Biological Center research biologist Matthew Lux, Ph.D., pursues his IDEAS Program project by programming an Acoustic Liquid Handler to operate in tandem with artificial intelligence to optimize the design of sensors made from biological components. (Photo credit: DEVCOM CBC)*

## Center Researcher Obtains Ph.D. as Result of Supporting ILIR Efforts

DEVCOM CBC's Phillip G. Wilcox was recognized for obtaining his Ph.D. in FY20 from The Johns Hopkins University as a result of his work supporting Dr. Ashish Tripathi's ILIR project, *"Effect of bacterial spore deactivation methods on bacteria chemical components as determined by Raman chemical imaging."* Dr. Wilcox successfully defended his dissertation, *"Automated spore analysis using bright-field imaging and Raman microscopy"*, which focused on developing a novel analysis technique that combines bright-field microscopy images with Raman chemical microscopy to analyze spore viability of *Bacillus anthracis*.

# Peer-reviewed Publications


- Emmons, E.D.; Guicheteau, J.A.; Fountain, A.W.; Tripathi, A. Effect of Substituents on Surface Equilibria of Thiophenols and Isoquinolines on Gold Substrates Studies Using Surface-Enhanced Raman Spectroscopy. *Phys. Chem. Chem. Phys.* **2020**, *22* (28), pp 15953–15965.

- Kesavan, J.S.; Alstadt, V.J.; Laube, B.L. Aerosol Deposition in 3D Models of the Upper Airways and Trachea of Rhesus Macaques. *Aerosol Sci. Technol.* **2020**, *54* (8), pp 983–991.

- Lee, M.S.; Raig, R.M.; Gupta, M.K.; Lux, M.W. Lyophilized Cell-Free Systems Display Tolerance to Organic Solvent Exposure. *ACS Synth. Biol.* **2020**, *9* (8), pp 1951–1957.

- Ma, K.K.; Islamoglu, T.; Chen, Z.J.; Li, P.; Wasson, M.C.; Chen, Y.W.; Wang, Y.F.; Peterson, G.W.; Xin, J.H.; Farha, O.K. Scalable and Template-Free Aqueous Synthesis of Zirconium-Based Metal-Organic Framework Coating on Textile Fiber. *J. Am. Chem. Soc.* **2019**, *141* (39), pp 15626–15633.

- Peterson, G.W.; Au, K.; Tovar, T.M.; Epps, T.H. Multivariate CuBTC Metal-Organic Framework with Enhanced Selectivity, Stability, Compatibility, and Processability. *Chem. Mater.* 2019, *31* (20), pp 8459–8465.

- Peterson, G.W.; Mahle, J.J.; Tovar, T.M.; Epps, T.H., III. Bent-but-not-Broken: Reactive Metal-Organic Composites from Elastomeric Phase-Inverted Polymers. *Adv. Funct. Mater.* **2020**, *30* (51), 2005517.

- Varady, M.J.; Boyne, D.A.; Pearl, T.P.; Lambeth, R.H.; Mantooth, B.A. Composition-dependent multicomponent diffusivity of 2,5-lutidine with acetonitrile in polyurethane. *Polymer.* **2019**, 180, 121697.


# Doctoral Dissertation


- Wilcox, P.G. Automated Spore Analysis Using Bright-Field Imaging and Raman Microscopy. Ph.D. Thesis, The Johns Hopkins University, Baltimore, MD, January 2020.


*DEVCOM CBC initiated the Warfighter Innovation Leveraging (Mission) Expertise and Experimentation (WILE-E) program to empower a multifunctional CBC team using design thinking principles to understand, ideate, and propose solutions to complex challenges. In November of 2019, Capt. Matthew Grout and Master Sgt. John Binot took time to present operational information from the field to the Center's workforce in an effort to increase transparency for researchers. (Photo credit: DEVCOM CBC)*

## Issued Patent

- DeCoste, J.B.; Tovar, T.M.; Iordanov, I.O. Enhancement of Adsorption via Polarization in a Composite Material. U.S. Patent 10,427,134, issued 1 October 2019.

## Filed Patent

- Peterson, G.W.; Epps, T.H. Multivariate Carboxylate Derivatized Phenyl-Based Metal-Organic Frameworks. U.S. Patent Application 16,709,258, filed 10 December 2019.


*The DEVCOM CBC booth ready for visitors at the 2019 Defense Threat Reduction Agency (DTRA) CBD S&T Conference in Cincinnati, OH. The conference ran from 18-21 November 2019 and the Center had 12 oral presentations and 43 posters on display. (Photo credit: DTRA)*

## Presentations and Posters

- Kline, N. Probing the Connection Between Low-Frequency Vibrational Modes and Macroscopic Structural Behavior of Metal Organic Frameworks. *Presented at the 3rd International Conference on Metal Organic Frameworks and Porous Polymers*, Paris, France, **27–30 October 2019**.

- Riley, P.C.; Deshpande S.V.; Ince, B.S.; McHugh, V.M.; Hauck, B.C.; Harden, C.S.; Wade, M.M. Machine Learning Based Alarm Algorithm Frameworks for Chemical Detectors. *Presented at the 2019 Chemical and Biological Defense Science & Technology Conference*, Cincinnati, OH, **18–21 November 2019**.

- Tripathi, A.; Emmons, E.D.; Guicheteau, J.A.; Kang, J.U.; Kim, M.H.; Wilcox, P. Screening for Bacillus Spore Viability using Bright-field and Raman Chemical Imaging Microscopy. *Presented at the Pittcon Conference & Expo*, Chicago, IL, **1–5 March 2020**.

- Jabbour, R.E.; Tripathi, A.; Emmons, E.D.; Wilcox, P.G.; Guicheteau, J.A.; Balboa, A. Effect of Signal Molecules on the production of cellulose biofilm from bacterial sources. P*resented at the Material Characterization Symposium, Analytical and Material Conference*, Virtual Event, **March 2020**.

- Riley, P.C.; Deshpande S.V.; Ince, B.S.; McHugh, V.M.; Hauck, B.C.; Harden, C.S.; Wade, M.M. Machine Learning Based Alarm Algorithm Design for Ion Mobility Spectrometry Detection Devices. *Presented at the International Society of Ion Mobility Spectrometry 2020 Virtual Poster Symposium*, Virtual Event, **31 July–7 August 2020**.

- Zeigler, A.M.; Zia, R.N.; Ryu, B.K.; Varady, M.J.; Hulet, M.S.; Ruprecht, B.R. Towards Understanding the Role of Material Voids and Porosity on Transport Presentation. *Presented at the American Chemical Society Fall 2020 Virtual Meeting and Exposition*, Virtual Event, **17–20 August 2020**.

- Durke, E.M.; McEntee, M.L.; He, M.; Dhaniyala, S. Characterization of particle charge from aerosol generation process: Investigations of Material Reactivity. *Presented at the European Aerosol Conference*, Virtual Event, **31 August–4 September 2020**.

# Meet our FY20 Principal Investigators

## In-house Laboratory Independent Research (ILIR) Projects

### Matthew Lux, Ph.D.

**Research Biologist, *BioChemistry Branch, BioSciences Division***

Dr. Lux received his Ph.D. in Genetic, Bioinformatics, and Computational Biology from Virginia Polytechnic Institute and State University in 2013. Since then, he has worked as a Research Biologist in the BioSciences Division at DEVCOM CBC. He currently serves as a principal investigator on a variety of projects related to synthetic biology and DNA as an information molecule. His research has focused on cell-free systems for sensing and biomanufacturing applications, bacteriophage engineering for therapeutics, storing digital data in bacterial DNA, and DNA as a chemical taggant for item verification.

### Sarah Katoski

**Biologist, *BioDefense Branch, BioSciences Division***

Ms. Katoski received her master's degree in Biotechnology from The Johns Hopkins University in 2009. She began working at DEVCOM CBC in 2010 as a contractor, later transitioning to civilian service in 2016 where she works in the BioDefense Branch. Ms. Katoski serves as a molecular biologist and technical specialist providing support to a broad range of major biological defense systems and complex biological detection systems. She was recognized for her expertise via receipt of the 2019 CBC Excellence in Safety award and a subsequent Director of Army Safety Risk Management Safety Award in FY20 for her part in providing an integrated method for preparing, irradiating, and verifying the inactivation of anthrax spores, enabling their safe use as standard reagents for testing and evaluating detection and diagnostic devices and techniques throughout the DoD.

### Ashish Tripathi, Ph.D.

**Research Physical Scientist, *Spectroscopy Branch, Physical Sciences Division***

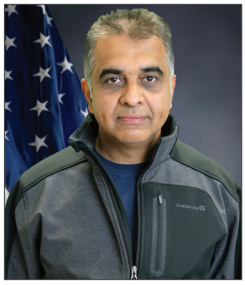

Dr. Tripathi received his Ph.D. in Chemical and Fuels Engineering from the University of Utah in 1997. He has been a researcher at DEVCOM CBC since 1997—first as a contractor until transitioning to a civilian employee in 2016. Dr. Tripathi has more than 20 years of experience in standoff and point threat detection research supporting the Spectroscopy Branch of DEVCOM CBC. His expertise focuses on the application of Raman spectroscopy and imaging and surface-enhanced Raman spectroscopy to the detection of chemical, biological, and energetic materials.

## Patrick Riley

**Research Chemist, *Detection Spectrometry Branch, Physical Sciences Division***

Mr. Riley received his bachelor's degree in Chemistry from Salisbury University in 2010. With over 10 years of experience as a Research Chemist at DEVCOM CBC, Mr. Riley's research has most recently focused utilizing machine learning to develop new alarm algorithms for chemical detection devices to include ion mobility spectrometry-based devices. Mr. Riley's experience in machine learning has extended beyond chemical detection to include participating in and leading a number of efforts to find other applications of machine learning in CBRNE defense.

## Rabih Jabbour, Ph.D.

**Chemist, *Detection Spectrometry Branch, Physical Sciences Division***

Dr. Jabbour earned his Ph.D. in Bioanalytical Chemistry from the University of Arizona in 1999. He has more than 20 years of research experience in academia and industry in the field of chemistry and biology of microorganisms that are of vital interest to the DoD. At CBC, he leads the development of the functional materials and automated biological sample preparation and detection system and has contributed to various DoD projects such as water monitoring and microbial fate using Raman imaging for Joint Service Agent Water Monitor, microbial mapping by Matrix-Assisted Laser Desorption/Ionization-Mass Spectrometry, and biodetection algorithms. Dr. Jabbour has received several government and industry awards including the U.S. Army Research and Development Achievement Award. He has published over 43 peer-reviewed articles and proceedings in the fields of chemistry, biochemistry, spectroscopy, molecular biology, bacteriology, and protein chemistry.

# Surface Science Initiative (SSI) Projects

## Marilyn Lee, Ph.D.

**Chemical Engineer, *BioChemistry Branch, BioSciences Division***

Dr. Lee earned her Ph.D. in Chemical and Biomolecular Engineering from the University of California, Berkeley in 2017. Upon graduation, she joined DEVCOM CBC as an ORISE and NRC post-doctoral researcher from 2017 to 2020 before transitioning to a civilian employee. Her area of research includes improving cell-free biocompatibility with polymers to demonstrate broad implications on the design of sensors and devices harnessing biological activity. In her short time at DEVCOM CBC, Dr. Lee has multiple publications in top peer-reviewed journals.

## Mark Varady, Ph.D.

**Research Engineer, *Decontamination Sciences Branch, CB Protection & Decontamination Division***

Dr. Varady received his Ph.D. in mechanical engineering from the Georgia Institute of Technology in 2010. He has been working with DEVCOM CBC since 2012, first as a contractor, and then transitioning to a civilian position in 2016. Dr. Varady primarily studies chemical transport mechanisms in polymer-based materials, including multicomponent diffusion, viscoelastic response upon chemical exposure, and details of the polymer-particle interface in composite systems.

## Shaun Debow

**Chemical Engineer**, ***Toxicology & Obscurants Division***

Mr. Debow received his master's degree in Chemical & Biochemical Engineering from the University of Iowa in 2004. In 2006, Mr. Debow joined the DEVCOM CBC workforce as a Chemical Engineer managing lifecycle support for weapons systems. Mr. Debow's areas of expertise include basic and applied research of novel materials, development of novel solutions in anticipation of emerging needs, high-volume production and manufacturing, demilitarization, and systems engineering. Recent research interests include additive manufacturing, 2D materials, applications in surface science, warhead design, and gas adsorbents.

## Jared DeCoste, Ph.D.

**Research Chemist,** ***CBR Filtration Branch, CB Protection & Decontamination Division***

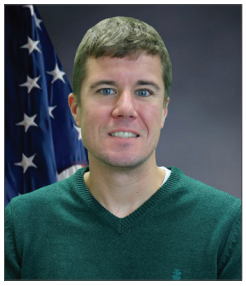

Dr. DeCoste earned his Ph.D. in Materials Chemistry in 2009 from Binghamton University. He has worked at DEVCOM CBC as a government employee, contractor, or NRC post-doctoral associate since 2010 studying the fundamental properties of metal-organic frameworks. His research interests range from basic research in the fundamentals of porous materials—especially for adsorption and catalysis—to the engineering and scaling of functional nanomaterials. He has led many projects in this area and is regarded as an expert in the field of MOFs for toxic chemical removal. His work at the Center has led to more than 60 publications in top peer-reviewed journals and has been recognized by his peers and superiors through multiple awards including the Leidos Publication Prize, Coffee with Colleagues Top Poster, DEVCOM CBC Rookie of the Year, and the 2018 Maryland American Chemical Society Chemist of the Year.

## Angela Zeigler, Ph.D.

**Research Chemist,** ***Sensors, Signatures, & Aerosol Technologies Branch, Physical Sciences Division***

Dr. Zeigler received her Ph.D. in Chemistry from the Johns Hopkins University in 2014. She began working at DEVCOM CBC as a student intern from 2004–2008, again as a contractor in 2014, and later transitioned to a civilian employee in 2017. Her primary duties at the Center have included developing concepts for design of CB aerosol spectroscopic equipment—particularly involving ultraviolet-visible and infrared wavelength regions for characterization research—and analysis of aerosol simulants and agents in the atmosphere and managing related spectroscopic detection programs. She inherited this study from Dr. Jerry Cabalo following his departure from DEVCOM CBC in 2020.

## Ivan Iordanov, Ph.D.

**Physicist,** ***Decontamination Sciences Branch, CB Protection & Decontamination Division***

Dr. Iordanov earned his Ph.D. in Physics from the Pennsylvania State University in 2012, working on theoretical modeling of the photoelectron spectra of small transition metal clusters using density functional theory and higher-level methods (Coupled-Cluster Singles and Doubles and Symmetry Adapted Cluster-Configuration-Interaction). He joined DEVCOM CBC as an NRC post-doctoral researcher in 2013 and was hired as a civilian employee in 2016. His area of expertise is the use of quantum mechanics-based computational methods to improve understanding of adsorption within porous materials or on surfaces at the atomic level.

# Table of Contents

## In-house Laboratory Independent Research (ILIR) Projects

## Surface Science Initiative (SSI) Projects

# ILIR PROJECTS

# Elucidating the prevalence of off-target effects of CRISPR-Cas editing in prokaryotes

Casey B. Bernhards[a], Pierce A. Roth[b], Alvin T. Liem[b], Matthew W. Lux[c]*
[a]Excet, Inc., 6225 Brandon Ave, Suite 360, Springfield, VA 22150
[b]DCS Corporation, 6909 Metro Park Dr, Suite 500, Alexandria, VA 22310
[c]U.S. Army Combat Capabilities Development Command Chemical Biological Center, Research & Technology Directorate, 8198 Blackhawk Rd, Aberdeen Proving Ground, MD 21010

## ABSTRACT

Genome editing using CRISPR systems has become a major dual-use biotechnology across a range of organisms. Significant work has gone into understanding off-target effects of these systems in higher organisms due to the implications of unintended mutations when used for medical applications. Here, we describe similar work to understand the off-target effects of CRISPR editing in prokaryotic organisms as a potential method to identify signatures of engineering in emerging threats. We describe a two-pronged approach based on a selection system to quantify rates *in vivo* and a parallel *in vitro* approach that assesses off-target rates using isolated molecular components. This report describes work completed in the first year of the project.

**Keywords:** gene editing, synthetic biology, bioforensics

## 1. INTRODUCTION

Named Science Magazine's 2015 Breakthrough of the Year,[1] the CRISPR-Cas (Clustered Regularly Interspaced Short Palindromic Repeats and CRISPR-associated) system has emerged as a powerful genome editing tool that has revolutionized the fields of synthetic biology and genetic engineering. Discovered in a number of bacteria, the CRISPR-Cas system naturally serves as a bacterial adaptive immune system that allows bacteria to record and destroy invading viruses.[2] When foreign DNA enters the cell, the Cas endonuclease attempts to match it to RNA transcribed from snippets of the genomes of past invaders that have been recorded in the bacterial chromosome; any matches are cleaved by double-stranded break (DSB), destroying the threat. Two factors are required for targeting: the homologous RNA (called the guide RNA or gRNA) and a short, Cas-specific recognition site (PAM sequence) nearby. Studies in 2013 demonstrated that this defense system could be repurposed as a genome editing tool through heterologous expression of the Cas9 endonuclease from *Streptococcus pyogenes* along with a gRNA specifying the DNA target region (Figure 1).[3–5]

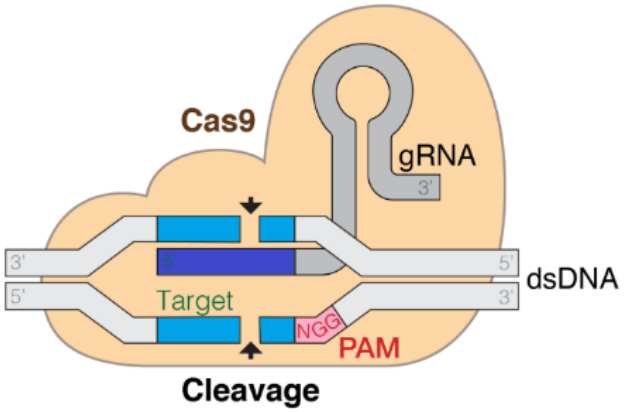


**Figure 1. CRISPR-Cas gene editing. Cas9 nuclease together with a gRNA containing approximately 20 bases of homology to the target DNA allow for site-specific genome editing. © Marius Walter / CC-BY-SA-4.0 / https://upload.wikimedia.org/wikipedia/commons/5/51/GRNA-Cas9.png.**

Since then, the use of CRISPR-Cas in genome engineering has exploded.[6] While the natural pathway for repair of CRISPR-Cas-induced DSBs in eukaryotic cells is via non-homologous end joining—an error-prone pathway resulting in small insertions or deletions (indels)—an array of precise edits (inserts, deletions, etc.) are possible through homology-directed repair by providing a DNA repair template. Importantly, this technique leaves no additional markers (antibiotic resistance cassettes, extra bases/scars) at the site of genome editing. The unprecedented simplicity, speed, specificity, and versatility of the CRISPR-Cas system has opened the possibility of facile modification of almost any sequence in any organism. Indeed, CRISPR-Cas has been successfully used in numerous organisms from bacteria to humans.[3–5]

While CRISPR-Cas is now ubiquitously used as a precise genome editing tool, CRISPR-Cas off-target effects—unintended genome modifications elsewhere in the genome as a consequence of on-target CRISPR editing—have been reported.[7] This has raised significant concern regarding the application of CRISPR-Cas to human gene therapy, as CRISPR off-target effects could have potentially disastrous consequences. As such, there have been efforts to investigate and reduce this phenomenon in eukaryotic cells. Even still, the majority of these studies have focused on the off-target effects at predicted locations based on similarity to the target sequence, which may miss off-target effects elsewhere in the genome.[8–10] Due to the cost and impracticality of sequencing enough large eukaryotic genomes with depth sufficient to identify low frequency off-target effects in cell populations edited with CRISPR-Cas, the use of whole genome sequencing (WGS) in these studies has been limited.[11,12] While progress has been made in understanding CRISPR-Cas off-target effects in eukaryotic cells, there is a significant knowledge gap in our understanding of CRISPR-Cas off-target effects in prokaryotes/bacteria. Until recently, relatively little was known about the factors determining efficiency of on-target edits in prokaryotes—another area that is well studied for eukaryotes.[13] Importantly, studies have shown distinct differences in off-target effects when human genome editing is performed in cells versus *in vitro*,[9,10] suggesting unknown mechanisms at work in human cells; no such work has been done for prokaryotes. Furthermore, since unrepaired DSBs are lethal to bacterial cells, the stress of this event during CRISPR-Cas editing may lead to an increased mutation rate due to activation of the cell's SOS response.[14] This idea is supported by the observation of off-target effects from a DNA-editing technique used in *Bacillus*[15] that also induces a DSB (C. Bernhards, unpublished). In all, off-target effects in prokaryotes remain a largely unexplored area in the literature.

The characteristics that make CRISPR-Cas a powerful genome editing tool, namely its ease of use and broad applicability, are the same qualities that increase its potential for misuse. It is now easier than ever for non-state actors to engineer biothreat organisms to increase virulence or antimicrobial resistance, or to avoid detection. This concern led the U.S. Director of National Intelligence to include gene editing/CRISPR as a weapon of mass destruction considered to be a major threat facing the United States.[16] Therefore, there is an urgent need for a working knowledge of CRISPR-Cas within the Army in order to defend against this evolving threat. There has also been intense interest in the ability to detect genetically modified organisms, especially those created using techniques like CRISPR-Cas that are "markerless." Characterization of off-target effects may facilitate detection of CRISPR-modified organisms despite a lack of markers at the point of editing.

In this work, we aim to genetically modify the model bacterium, *Escherichia coli*, using CRISPR-Cas9 and a combination of counterselection and WGS to identify off-target effects. The relatively small size of bacterial genomes and clonal populations that can be isolated following CRISPR-Cas editing make bacteria especially amenable to a WGS-based approach to identify off-target events. In parallel, we aim to apply *in vitro* editing and sequencing techniques specifically designed to identify off-target edits. We hypothesize that CRISPR editing in bacteria creates off-target effects that are detectable through these methods.

## 2. METHODOLOGIES

### 2.1 Computational methods

Software used to identify neutral genomic insertion points was developed using Perl v5.16.3 and BioPerl v1.7.5. Guide RNA sequences were designed with GuideFinder software developed by Spoto et al.[17] using the parameters listed in Table 1. Cas-OFFinder software[18] was used to screen gRNA sequences for potential off-target sites.

**Table 1. GuideFinder parameters.**

| Parameter Name | Description | Values Used |
|---|---|---|
| N | Minimum guide length | 20 |
| GC_Min | Minimum guide GC content | 0.35 |
| DistanceAsPercentageofCDS | Maximum distance of guide from the transcription start site | 1 |
| GuidesPerGene | Maximum number of guides/gene | 100 |
| DistbtGuides | Minimum distance between guides | 0 |
| Test_bad_seed | Remove sequences containing specified "bad seed" sequence | TRUE |
| Bad_seed | Specified "bad seed" sequence | "ACCCA" |
| Test_RE | Remove sequences containing specified restriction enzyme site | FALSE |
| RE_site | Specified restriction enzyme site | – |

## 3. STRAINS, PLASMIDS, AND CONSTRUCTS

NEB® 5-alpha *E. coli* from New England Biolabs (Ipswich, MA) was used for routine cloning and *E. coli* strain MG1655 from BEI Resources (Manassas, VA) was used for CRISPR editing procedures. The plasmids for Cas9 expression (pCas) and gRNA expression (pTargetF)[19] were obtained from Addgene (Watertown, MA). Strains of *E. coli* were grown in Luria-Bertani (LB) medium supplemented with kanamycin (30–50 µg/mL) or spectinomycin (50 µg/mL), as needed. Strains containing the temperature-sensitive plasmid pCas were grown at 30 °C, otherwise strains were propagated at 37 °C. New gRNA sequences were incorporated into pTargetF by inverse polymerase chain reaction (PCR) using primers containing the 20-base gRNA sequence, followed by isothermal DNA assembly (NEBuilder® HiFi DNA Assembly, New England Biolabs®). Primers sequences are listed in Table 2. Successful gRNA insertion into pTargetF was verified by DNA sequencing.

**Table 2. Primers for incorporating gRNA sequences into pTargetF.**

| gRNA Genomic Target | Primer Type | Primer Sequence (5′ to 3′) |
|---|---|---|
| All Targets | Reverse | ACTAGTATTATACCTAGGACTGAG |
| Target 1 | Forward | GTCCTAGGTATAATACTAGTTCATGGGCTAATT AGCAGTCGTTTTAGAGCTAGAAATAGCAAG |
| Target 2 | Forward | GTCCTAGGTATAATACTAGTCGGACGCTCGTT AATATTTAGTTTTAGAGCTAGAAATAGCAAG |
| Target 3 | Forward | GTCCTAGGTATAATACTAGTTGTGCGTGGGAA CAGCCTTAGTTTTAGAGCTAGAAATAGCAAG |
| Target 4 | Forward | GTCCTAGGTATAATACTAGTGAAACGCGCTGA GTCAGTCTGTTTTAGAGCTAGAAATAGCAAG |
| Target 5 | Forward | GTCCTAGGTATAATACTAGTCCTCCATGCTTAA TATAAGGGTTTTAGAGCTAGAAATAGCAAG |
| Target 6 | Forward | GTCCTAGGTATAATACTAGTCTGACAATTCATA CGATTACGTTTTAGAGCTAGAAATAGCAAG |
| Target 7 | Forward | GTCCTAGGTATAATACTAGTACTAAGTTTAGAT TTCAGGGGTTTTAGAGCTAGAAATAGCAAG |
| Non-Targeting Control NC_162[20] | Forward | GTCCTAGGTATAATACTAGTGATGTGTCACCTT CCACTGAGTTTTAGAGCTAGAAATAGCAAG |
| Non-Targeting Control NC_180[20] | Forward | GTCCTAGGTATAATACTAGTCGTGAACTTTAGC TGGCTCTGTTTTAGAGCTAGAAATAGCAAG |

### 3.1 CRISPR edits

*E. coli* MG1655 cells containing pCas were made electrocompetent by culturing in LB broth with kanamycin at 30 °C with shaking at 250 rpm until reaching an $OD_{600}$ (optical density at 600 nm) of 0.4–0.6. L-arabinose was added to a final concentration of 10 mM during growth for induction of the λ-Red genes on pCas. Cells were washed two to three times with ice-cold, sterile water, followed by one wash with ice-cold, sterile 10 % glycerol. Cells were concentrated 100–200-fold, flash frozen in liquid nitrogen, and stored at -80 °C. Derivative plasmids of pTargetF (100 ng)

containing gRNA sequences were added to 50 µL of electrocompetent cells, and electroporations were performed in 1 mm cuvettes at 1.8 kV. Cells were recovered for 90 minutes at 30 °C with shaking before being spread onto LB agar plates containing kanamycin and spectinomycin. Plates were incubated overnight at 30 °C.

## 4. RESULTS

### 4.1 Identification of neutral genomic insertion points

The first step in the project was to identify neutral insertion points in *E. coli* that we could use to create our engineered selection strain without impacting strain fitness. We used in-house custom software, called targetFinder, developed for this purpose. While appropriate neutral insertion sites can be extracted from the literature for *E. coli*, we opted to use targetFinder in order to demonstrate a methodology that would apply universally to other prokaryotic organisms rather than relying on the extensive research that has been done on a few model systems. The targetFinder software works by scanning a provided genome sequence (in this case, *E. coli* strain MG1655, RefSeq accession NC_000913.3 from the National Center for Biotechnology Information for sites that match user-adjustable parameters (Figure 2, Table 3). First, coding sequence annotations are parsed and searched for instances where two genes are convergently transcribed. Because the most critical regions of gene regulation, such as promoters and ribosome binding sites, are upstream of coding sequences, we reasoned that intergenic regions between convergently transcribed genes are least likely to contain important regulatory features. The size of such regions, called gaps, are calculated based on the stop codon of the convergently transcribed genes, then filtered based on user-defined size parameters to allow for buffering between regulatory features such as terminators. Gaps of the user-specified size are scanned for other annotations that may indicate disruption of key functions. Remaining gaps are scanned for local repetitive structures that may inhibit efficacy of editing methods, and the regions surrounding the gaps are checked for large sequences that repeat elsewhere in the genome that may indicate transposon activity. Finally, the gap sequence is compared to the entire genome sequence using the National Center for Biotechnology Information's Basic Local Alignment Search Tool (BLAST) to check for additional repetitions that may interfere with homologous recombination-based editing methods; failing this check generates a warning.

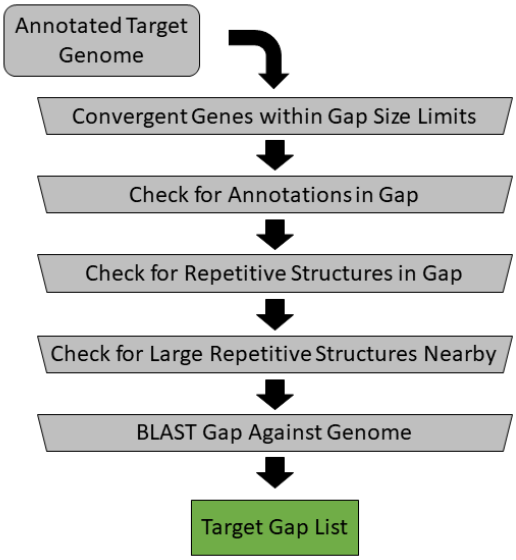


**Figure 2. Workflow of targetFinder software.**

**Table 3. targetFinder user-defined parameters.**

| Parameter Name | Description | Values Used |
|---|---|---|
| minGap | Minimum gap size (bases) | 300 |
| maxGap | Maximum gap size (bases) | 2000 |
| homRecombSize | Size of flanking sequences for homologous recombination (bases) | 750 |
| locRep_Nmer | Minimum local repeat size (bases) | 2 |
| locRep_Reps | Minimum local repeat count | 6 |
| lgRepBound | Range to search for large repetitive elements (bases) | 5000 |
| lgRepMinSize | Minimum size of large repetitive elements (bases) | 100 |
| lgRepMaxSize | Maximum size of large repetitive elements (bases) | 500 |
| min_gap_identity_warning_length | Minimum size of BLAST hit to generate a warning (bases) | 25 |
| min_identity_warning | Minimum BLAST percent identity to generate a warning (%) | 90 |

The targetFinder algorithm identifies gaps that are likely to be phenotypically neutral; however, it does not select a specific insertion point because different editing techniques have different requirements. These techniques and requirements also vary by target organism. To identify target insertion points for CRISPR editing, we used the GuideFinder software described by Spoto et al.[17] While intended for a slightly different purpose, we used GuideFinder to identify insertion points and corresponding gRNA sequences that are predicted to have high CRISPR editing efficiencies within the gaps first identified by targetFinder. Candidate gRNA sequences were further screened for potential off-target sites using Cas-OFFinder software.[18] For each gap identified by targetFinder, one gRNA sequence was selected that was near the center of the gap and had the fewest number of potential off-target sites with five or less mismatches.

Using these computational tools, we identified seven candidate sites (Figure 3) and gRNA sequences (Table 4) for neutral insertions in the *E. coli* genome. The sites are well-dispersed across the genome, offering multiple regions to probe.

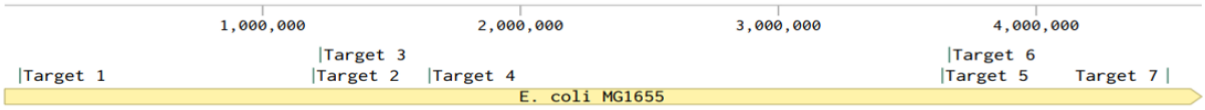


**Figure 3. Genomic map of predicted phenotypically-neutral insertion points in *E. coli*.**

**Table 4. Selected gRNA sequences.**

| Genomic Target | gRNA Sequence (5′ to 3′) |
|---|---|
| Target 1 | TCATGGGCTAATTAGCAGTC |
| Target 2 | CGGACGCTCGTTAATATTTA |
| Target 3 | TGTGCGTGGGAACAGCCTTA |
| Target 4 | GAAACGCGCTGAGTCAGTCT |
| Target 5 | CCTCCATGCTTAATATAAGG |
| Target 6 | CTGACAATTCATACGATTAC |
| Target 7 | ACTAAGTTTAGATTTCAGGG |

Prior to performing edits at these sites in *E. coli* and evaluating the neutrality of each site, the seven gRNAs were first tested for efficient Cas9 targeting/cleavage. In the absence of a DNA repair template, *E. coli* cells expressing Cas9 and an efficient gRNA should yield few colonies, as Cas9 cleavage of the *E. coli* chromosome will result in cell death for the majority of cells. The plating of *E. coli* expressing Cas9 and each of the seven gRNAs yielded no or few colonies, in contrast to the large number of colonies produced by control strains of *E. coli* expressing Cas9 and a gRNA with no matching sequence in the *E. coli* genome (non-targeting gRNA) (Figure 4). These results indicate the gRNA sequences result in efficient Cas9 cleavage of the *E. coli* chromosome.

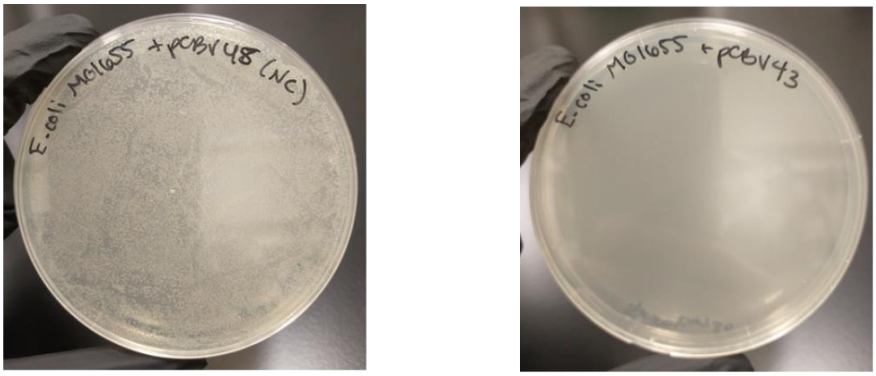


**Figure 4. Efficient Cas9 targeting by gRNA sequences. Representative results of *E. coli* colonies produced from expression of Cas9 and a non-targeting control gRNA (left) versus one of the targeting gRNA sequences (right).**

Now that successful CRISPR targeting for each of the seven gRNAs/genomic locations in *E. coli* has been demonstrated, we proceeded with validating that these sites are phenotypically neutral. A short DNA sequence, or barcode,[21] will be inserted at each site via a DNA repair template we have designed to contain the barcode and flanking DNA homologous to the insertion site. Growth assays and competition experiments will subsequently be conducted to ensure insertions at these points do not alter strain function.

### 4.2 Selection strain for off-target effects

Because CRISPR off-target effects are likely to be rare events in bacteria, we devised a counterselection system to isolate instances of off-target DSB formation in bacteria as shown in Figure 5. Two of the neutral *E. coli* insertion points identified will be used to engineer "on-target" and "off-target" sites. The on-target site consists of a promoterless chloramphenicol resistance gene, and the off-target site contains the *sacB* gene, which makes growth in the presence of sucrose toxic to cells. Both sites contain a gRNA target sequence that can be made less similar through synonymous point mutations in the gRNA region of *sacB*. Successful edits at the on-target site via homology-directed repair will result in expression of the chloramphenicol resistance gene (via incorporation of the promoter on the DNA repair template), and cells will be selected by growth on the antibiotic. Cells that survive cleavage at the off-target site through error-prone DNA repair (resulting in a frameshift mutation in *sacB*), will be selected by growth on sucrose. Colony counts from these different scenarios will be used to assess the rates of edits at the engineered sites. WGS will also be performed on resulting colonies to look for additional off-target mutations outside of the engineered site.

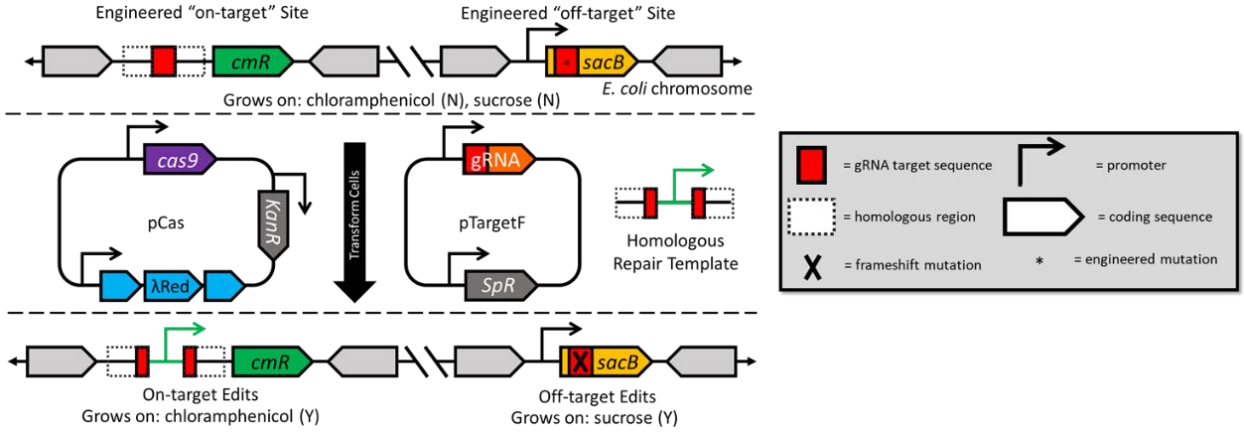


**Figure 5. Counterselection strategy to capture potentially rare CRISPR off-target effects. Two engineered sites, an "on-target" and an "off-target" site, were designed for insertion into the *E. coli* genome. Growth on plates containing chloramphenicol or sucrose will indicate if an edit has occurred at the on-target site, off-target site, or both.**

### 4.3 *In vitro* screening of off-target effects

As a complementary approach to our counterselection and WGS strategies to investigate CRISPR off-target effects, we identified an *in vitro* approach, called CIRCLE-seq (circularization for *in vitro* reporting of cleavage effects by

sequencing), which has been used successfully for off-target site discovery in eukaryotic organisms.[22] Cleavage sites determined *in vitro* using purified components (i.e., circularized genomic DNA fragments and Cas9) can additionally be utilized for targeted sequencing of *in vivo* CRISPR experiments.

## 5. CONCLUSIONS

This report describes progress toward the goal of quantifying off-target editing effects in prokaryotes. We have generated candidate neutral insertion points for a novel selection strain, performed preliminary tests of CRISPR targeting efficiencies, and designed constructs for quantifying effects. Future work will progress from this groundwork to the intended quantification of rates. Knowledge of these rates will inform tools that identify signatures of genome editing in emerging threats.

## ACKNOWLEDGMENTS

We thank Dr. Henry Gibbons from the U.S. Army Combat Capabilities Development Command Chemical Biological Center and Dr. Shengdar Tsai of St. Jude Children's Research Hospital for helpful discussions in support of this work. Funding was provided by the U.S. Army via the In-house Laboratory Independent Research Program (PE 0601101A Project 91A) at the Combat Capabilities Development Command Chemical Biological Center.

## REFERENCES

[1] Travis, J. Making the cut. *Science*. **2015**, *350* (6267), pp 1456–1457.
[2] Barrangou, R.; Fremaux, C.; Deveau, H.; Richards, M.; Boyaval, P.; Moineau, S.; Romero, D.A.; Horvath, P. CRISPR provides acquired resistance against viruses in prokaryotes. *Science*. **2007**, *315* (5819), pp 1709–1712.
[3] Jinek, M.; East, A.; Cheng, A.; Lin, S.; Ma, E.; Doudna, J. RNA-programmed genome editing in human cells. *eLife*. **2013**, *2*, e00471.
[4] Hwang, W.Y.; Fu, Y.; Reyon, D.; Maeder, M.L.; Tsai, S.Q.; Sander, J.D.; Peterson, R.T.; Yeh, J.R.; Joung, J.K. Efficient genome editing in zebrafish using a CRISPR-Cas system. *Nat. Biotechnol.* **2013**, *31* (3), pp 227–229.
[5] Jiang, W.; Bikard, D.; Cox, D.; Zhang, F.; Marraffini, L.A. RNA-guided editing of bacterial genomes using CRISPR-Cas systems. *Nat. Biotechnol.* **2013**, *31* (3), pp 233–239.
[6] Sternberg, S.H.; Doudna, J.A. Expanding the Biologist's Toolkit with CRISPR-Cas9. *Mol. Cell*. **2015**, *58* (4), pp 568–574.
[7] Fu, Y.; Foden, J.A.; Khayter, C.; Maeder, M.L.; Reyon, D.; Joung, J.K.; Sander, J.D. High-frequency off-target mutagenesis induced by CRISPR-Cas nucleases in human cells. *Nat. Biotechnol.* **2013**, *31* (9), pp 822–826.
[8] Hsu, P.D.; Scott, D.A.; Weinstein, J.A.; Ran, F.A.; Konermann, S.; Agarwala, V.; Li, Y.; Fine, E.J.; Wu, X.; Shalem, O.; Cradick, T.J.; Marraffini, L.A.; Bao, G.; Zhang, F. DNA targeting specificity of RNA-guided Cas9 nucleases. *Nat. Biotechnol.* **2013**, *31* (9), pp 827–832.
[9] Cho, S.W.; Kim, S.; Kim, Y.; Kweon, J.; Kim, H.S.; Bae, S.; Kim, J.S. Analysis of off-target effects of CRISPR/Cas-derived RNA-guided endonucleases and nickases. *Genome Res.* **2014**, *24* (1), pp 132–141.
[10] Pattanayak, V.; Lin, S.; Guilinger, J.P.; Ma, E.; Doudna, J.A.; Liu, D.R. High-throughput profiling of off-target DNA cleavage reveals RNA-programmed Cas9 nuclease specificity. *Nat. Biotechnol.* **2013**, *31* (9), pp 839–843.
[11] Kim, D.; Bae, S.; Park, J.; Kim, E.; Kim, S.; Yu, H.R.; Hwang, J.; Kim, J.I.; Kim, J.S. Digenome-seq: genome-wide profiling of CRISPR-Cas9 off-target effects in human cells. *Nat. Methods*. **2015**, *12* (3), pp 237–243.
[12] Veres, A.; Gosis, B.S.; Ding, Q.; Collins, R.; Ragavendran, A.; Brand, H.; Erdin, S.; Cowan, C.A.; Talkowski, M.E.; Musunuru, K. Low incidence of off-target mutations in individual CRISPR-Cas9 and TALEN targeted human stem cell clones detected by whole-genome sequencing. *Cell Stem Cell*. **2014**, *15* (1), pp 27–30.
[13] Choudhury, A.; Fankhauser, R.G.; Freed, E.F.; Oh, E.J.; Morgenthaler, A.B.; Bassalo, M.C.; Copley, S.D.; Kaar, J.L.; Gill, R.T. Determinants for Efficient Editing with Cas9-Mediated Recombineering in Escherichia coli. *ACS Synth. Biol*. **2020**, *9* (5), pp 1083–1099.

[14] Simmons, L.A.; Goranov, A.I.; Kobayashi, H.; Davies, B.W.; Yuan, D.S.; Grossman, A.D.; Walker, G.C. Comparison of responses to double-strand breaks between Escherichia coli and Bacillus subtilis reveals different requirements for SOS induction. *J. Bacteriol.* **2009**, *191* (4), pp 1152–1161.

[15] Plaut, R.D.; Stibitz, S. Improvements to a Markerless Allelic Exchange System for Bacillus anthracis. *PLoS One*. **2015**, *10* (12), e0142758.

[16] Regalado, A. Top U.S. Intelligence Official Calls Gene Editing a WMD Threat. https://www.technologyreview.com/2016/02/09/71575/top-us-intelligence-official-calls-gene-editing-a-wmd-threat/ (accessed 16 December 2020).

[17] Spoto, M.; Guan, C.; Fleming, E.; Oh, J. A Universal, Genomewide GuideFinder for CRISPR/Cas9 Targeting in Microbial Genomes. *mSphere*. **2020**, *5* (1), e00086–20.

[18] Bae, S.; Park, J.; Kim, J.S. Cas-OFFinder: a fast and versatile algorithm that searches for potential off-target sites of Cas9 RNA-guided endonucleases. *Bioinformatics*. **2014**, *30* (10), pp 1473–1475.

[19] Jiang, Y.; Chen, B.; Duan, C.; Sun, B.; Yang, J.; Yang, S. Multigene Editing in the Escherichia coli Genome via the CRISPR-Cas9 System. *Appl. Environ. Microbiol*. **2015**, *81* (7), pp 2506–2514.

[20] Guo, J.; Wang, T.; Guan, C.; Liu, B.; Luo, C.; Xie, Z.; Zhang, C.; Xing, X.H. Improved sgRNA design in bacteria via genome-wide activity profiling. *Nucleic Acids Res*. **2018**, *46* (14), pp 7052–7069.

[21] Bernhards, C.B.; Lux, M.W.; Katoski, S.E.; Goralski, T.D.P.; Liem, A.T.; Gibbons, H.S. barCoder: a tool to generate unique, orthogonal genetic tags for qPCR detection. *BMC Bioinf*. **2021**, *22* (98), pp 1–17.

Tsai, S.Q.; Nguyen, N.T.; Malagon-Lopez, J.; Topkar, V.V.; Aryee, M.J.; Joung, J.K. CIRCLE-seq: a highly sensitive in vitro screen for genome-wide CRISPR–Cas9 nuclease off-targets. *Nat. Methods*. 2017, *14* (6), pp 607–614.

# Characterization and production of the *Coxiella burnetii* specific O-antigen carbohydrate virenose in engineered *Escherichia coli*

Nathan D. McDonald, Sarah E. Katoski*
U.S. Army Combat Capabilities Development Command Chemical Biological Center, Research & Technology Directorate, 8198 Blackhawk Rd, Aberdeen Proving Ground, MD 21010

## ABSTRACT

*Coxiella burnetii* is a Gram-negative bacterium and the causative agent of Q fever and has been long regarded as a potential biological warfare agent. Only the phase I strains of *C. burnetii* are considered pathogenic and these strains bear a unique O-antigen in the lipopolysaccharide. This O-antigen contains the carbohydrate virenose which is only found in phase I *C. burnetii* strains making it a unique biomarker for Q fever. Despite this, the O-antigen carbohydrate virenose remains poorly understood. Virenose serves as a valuable target for detection assays as well as a potential antigen in *C. burnetii* vaccine development. While comparative proteomics analysis studies for the biosynthesis of D- or L- enantiomers of virenose *in silico* have identified a putative biosynthetic route, the complete biosynthetic pathway of virenose has yet to be experimentally determined. We hypothesize that L-virenose biosynthesis can be validated utilizing a non-native host through synthetic engineering of the predicted L-virenose pathway. Here, we leverage synthetic biology to obtain and optimize the genes associated with virenose biosynthesis.

**Keywords:** lipopolysaccharide, virenose, *Coxiella burnetii*

## 1. INTRODUCTION

The unique mechanisms of immunity and pathogenicity of *Coxiella burnetii*, the causative agent of Q fever, are not fully understood—hindering advances in early diagnosis, treatments, and the prevention of infection. Lipopolysaccharides (LPS) are a component of the outer membrane of Gram-negative bacteria and play a key role in pathogenesis. *C. burnetii*'s LPS has the ability to undergo irreversible antigenic (or phase) variations, defined as phase I and phase II strains.[1,2] These phase variations present a unique antigen/immunogen shift particularly valuable for the differentiation between the chronic, less infectious phase II strain, and the more acute infectious phase I strain.[1,2]

The outer carbohydrates of the LPS, known as O-antigens, represent the more variable section of the LPS and are implicated in *C. burnetii*'s antigenic specificity.[1] The rare O-antigen carbohydrates virenose and dihydrohydroxystreptose are major virulence determinants unique to *C. burnetii*. Virenose, an O-antigen carbohydrate found only in the virulent phase I strain of *C. burnetii*,[3] is a methylated-6-deoxyhexose and serves as a unique biomarker for the disease. Only the virulent phase I isolates of *C. burnetii* bear this O-antigen; however, despite its uniqueness, the complete biosynthetic pathway of virenose has yet to be experimentally determined (Figure 1).

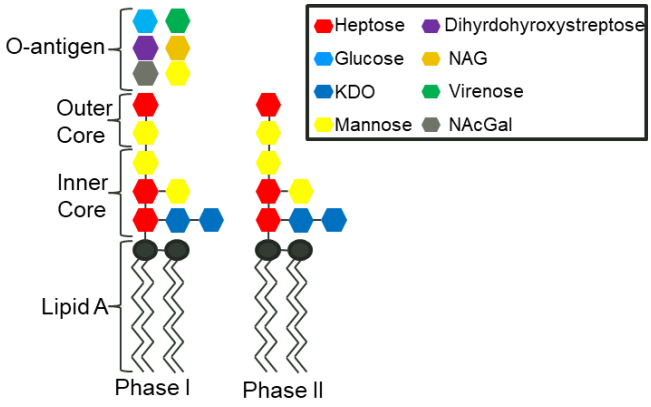


**Figure 1. LPS structure of phase I and phase II *C. burnetii*.**

Chromosomal deletion studies looking at key biosynthesis genes of phase II isolates of *C. burnetii*, have found nine genes predicted to be involved in the biosynthesis of virenose and dihydrohydroxystreptose.[3–5] Additionally, a study using comparative proteomics *in silico* analysis showed the biosynthesis of D- or L- enantiomers of virenose is likely comprised of five enzymatic steps and, based on the genes associated with the chromosomal changes in phase II strains of *C. burnetii*, the pathway elucidated was most likely that of L-virenose (Figure 2).[5] We hypothesize that the putative *C. burnetii* L-virenose pathway can be synthetically engineered into *Escherichia coli* in order to validate the biosynthetic pathway and provide a source of recombinant virenose.

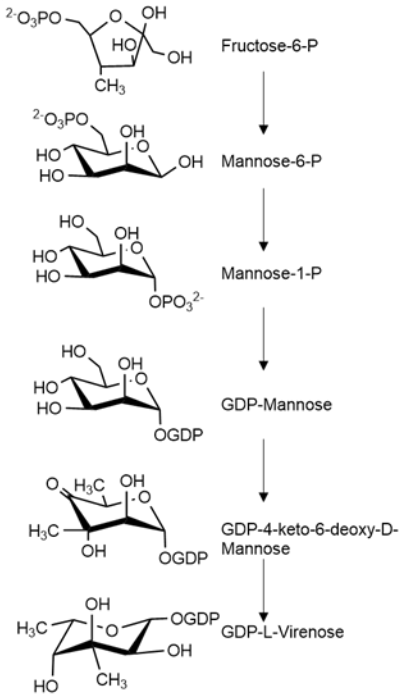


**Figure 2. Predicted biosynthetic pathway of GDP-L-virenose.**

The field of synthetic biology and genome engineering has facilitated the identification and characterization of biosynthetic pathways of countless molecules of interest. The ability to produce non-native products in engineering conducive organisms such as *E. coli* or *Saccharomyces cerevisiae* has been described in many cases.[6,7] Utilizing engineered biosynthesis pathways can be cost effective and are often more efficient than complex multi-step organic synthetic routes. Furthermore, many microbial species are engineered as biofactories for the production and characterization of rare carbohydrates which can have significant applications across many fields.[7–9] Here, we leverage synthetic biology to study the biosynthesis and recombinant production of virenose. The construction, expression, optimization, purification, and validation of recombinant L-virenose will be accomplished in the host organism, *E. coli.* Additionally, the putative virenose biosynthesis enzymes will be purified and independently verified for specific catalytic activity and involvement in virenose production.

## 2. MATERIALS AND METHODS

### 2.1 Obtaining and amplifying virenose biosynthesis genes

The sequence information for each of the five genes predicted to be involved in the biosynthesis of L-virenose were obtained from the National Center for Biotechnology Information database using the locus tags provided in Table 1. The sequences were codon optimized for expression in *E. coli* using the Codon Optimization tool available from Integrated DNA Technologies™ (Coralville, IA). The codon-optimized sequences were purchased as gBlocks™ from Integrated DNA Technologies™, and the DNA was routinely used as a template in polymerase chain reaction (PCR) amplification assays. The PCR assays were conducted utilizing Phusion® High Fidelity DNA Polymerase (New England Biolabs®; Ipswich, MA) following the manufacturer's recommended conditions. The thermocycling conditions for the PCR reactions were as follows: 98 °C for 30 seconds, 30 cycles of 98 °C for 10 seconds, 60 °C for

30 seconds, 72 °C for 90 seconds, and a final extension was held at 72 °C for 10 minutes. The amplified DNA was separated via gel electrophoresis run at 100 V on a 1 % agarose gel. DNA was visualized with Ethidium Bromide. The amplified PCR products were purified using a QIAquick® Gel extraction kit (QIAGEN; Germantown, MD) following the manufacturer's recommended protocol. The purified gene PCR products were used for downstream cloning procedures.

### 2.2 Cloning the virenose biosynthesis genes

Purified PCR gene products were used to clone into either the protein purification vector pET-21b(+) or the gene expression plasmid pMGX-HK. Both the PCR products and the plasmids were digested utilizing either XhoI/NdeI for pET-21b(+) or NdeI/BamHI for pMGX-HK. The restriction digest was carried out at 37 °C for 2 hours. The digested DNA products were purified following the QIAGEN QIAquick® Gel extraction kit manufacturer's protocol. The digested and purified DNA products were used for ligation reactions with T4 DNA ligase (New England Biolabs®; Ipswich, MA). The ligation reactions were carried out following the manufacturer's suggested protocol and incubated at 16 °C overnight. Following the ligation, the reactions were used to transform either *E. coli* Dh5α or BL21. The transformants were validated by either restriction digest or sequencing.

### 2.3 Expression test for protein purification

In order to determine the expression levels of the virenose biosynthetic enzymes for purification, an expression test was conducted. *E. coli* transformants harboring the protein expression plasmids were grown in Overnight Express™ Instant TB Medium (Sigma-Aldrich®; St. Louis, MO) at 37 °C. Following incubation, the bacterial cultures were pelleted at 13,000X g for 5 minutes. Bacterial pellets were resuspended in an equal volume of laemmli buffer and boiled at 98 °C for 5 minutes. The samples were separated on a polyacrylamide gel and the proteins were stained using the SimplyBlue™ safe stain following the manufacturer's (Invitrogen™; Carlsbad, CA) recommended protocol.

## 3. RESULTS

In order to test our hypothesis and attempt to fully characterize the biosynthesis pathway of virenose from *C. burnetii*, we first needed to optimize and obtain the genes encoding the predicted enzymes of the pathway. A previous study utilized a bioinformatics investigation of the *C. burnetii* genome to predict the enzymes involved in the biosynthesis of virenose.[5] This study identified several potential routes for virenose biosynthesis in *C. burnetii* with one route expected to be the most likely. This pathway is predicted to involve six enzymatic steps catalyzed by five unique enzymes (Table 1).

**Table 1. Genes predicted to biosynthesize virenose.**

| Gene Name | Predicted function | Locus tag | Size (base pairs) |
|---|---|---|---|
| *rfbA* | Mannose-1-P-guanylytransferase/mannose-6-P isomerase | Cbu_0671 | 1433 |
| N/A | Phosphomanomutase | Cbu_0294 | 1415 |
| *gmd* | GDP-mannose 4,6 dehydrataase | Cbu_0689 | 1046 |
| N/A | Methyltransferase | Cbu_0691 | 1238 |
| *wcaG* | GDP-L-Fucose synthase | Cbu_0688 | 998 |

In our attempt to recapitulate virenose biosynthesis in a non-native host, we chose to test the function of these five enzymes. We first obtained the DNA sequence for these five genes from the National Center for Biotechnology Information database and chose standard lab *E. coli* as the non-native host to evaluate virenose biosynthesis. Because *C. burnetii* and *E. coli* are distantly related bacteria, we needed to ensure that the genes from *C. burnetii* were optimized for expression in *E. coli*. Utilizing a bioinformatics tool available through Integrated DNA Technologies™, the coding regions for each of the five genes were optimized for the codon usages in *E. coli*. After the genes had been optimized, they were obtained as gBlocks™ and amplified via PCR for cloning into the expression vectors of interest (Figure 3).

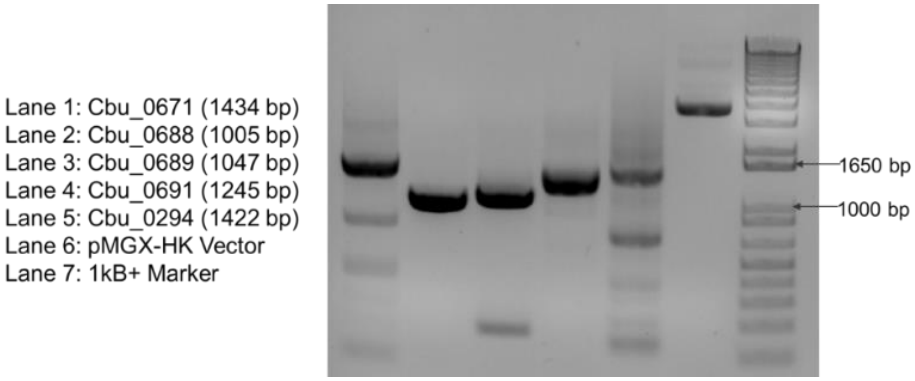


**Figure 3. Amplification of putative virenose biosynthesis genes.**

After successfully obtaining the optimized genes from *C. burnetii*, we took two approaches to characterize their potential role in virenose biosynthesis. Our first approach was to assemble each of the genes into a polycistronic operon under the control of a single inducible promoter that functions in *E. coli* (Figure 4).

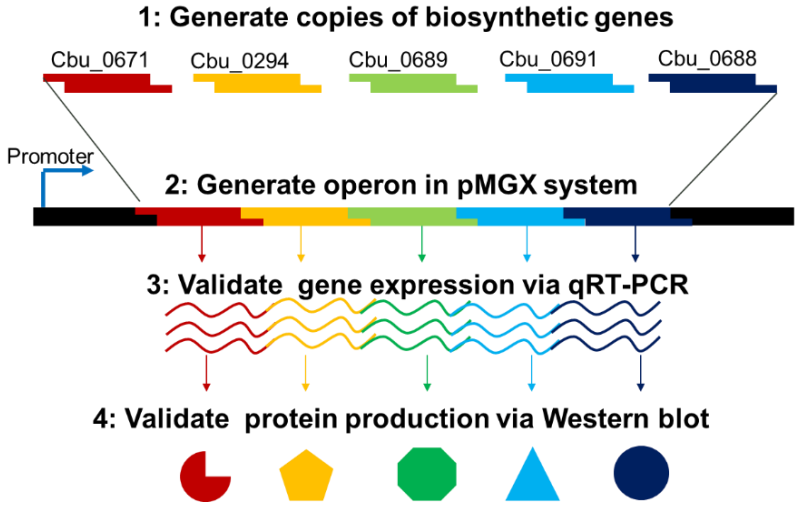


**Figure 4. Generating virenose biosynthetic pathway operon workflow.**

We utilized a previously described plasmid system which has been used to characterized biosynthetic pathways.[9] Each of the five genes were cloned individually into the pMGX-HK vector to be systemically cloned into a single operon.

Our second approach to determine if the *C. burnetii* enzymes are able to catalyze virenose biosynthesis was to evaluate the function of each enzyme *in vitro*. Purifying each of the enzymes and assessing the functions *in vitro* allows us to determine the role in virenose biosynthesis outside of the context of the non-native host background. The five genes were individually cloned into the protein expression vector pET-21b(+) which also includes a 6X-histidine tag on the proteins which were utilized for affinity chromatography. After generating the constructs, we tested the expression of the proteins prior to the purification (Figure 5).

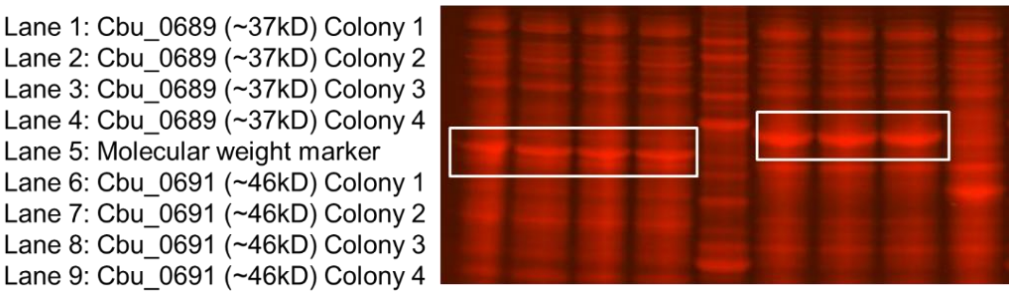


**Figure 5. Representative expression test of Cbu_0689 and Cbu_0691.**

Each of the proteins tested expressed well, and the cultures will be scaled up for immobilized metal affinity chromatography protein purification and enzyme characterization.

## 4. CONCLUSION

*C. burnetii* poses a threat to our nation and warfighters abroad. It is important to combat *C. burnetii* on two fronts—detection and prevention. Because the LPS is such a critical aspect of *C. burnetii* pathogenesis, it is important to gain a better understanding of the biology of the LPS biosynthesis. As a unique and key component of the phase I *C. burnetii* LPS, virenose has the potential to serve as a marker for detection and as an antigen for vaccine development. Here, we set out to recreate the biosynthesis pathway of virenose in *E. coli* in an effort to understand how this key carbohydrate is produced. We successfully obtained codon optimized genes for encoding the enzymes predicted to be required for virenose production in *C. burnetii*. These genes were transferred to a specialized expression vector designed for generating biosynthesis operons for characterization. Future work will focus on assembling each of the genes into a single expression vector to screen for virenose production in *E. coli*. In addition, we demonstrated that we can express the virenose biosynthesis enzymes in an effort to fully characterize the mechanism of the pathway. The ability to assess the purified enzymes *in vitro* is an essential component of understanding the biology of virenose and *C. burnetii* pathogenesis. The future of this work will include enzymatic assays to assign function to the enzymes of interest.

The use of bacterial carbohydrates and antigens for vaccines has been successfully implemented for a number of dangerous pathogens, demonstrating the utility of this approach.[10] Recent work has focused on developing carbohydrate-based vaccines for antibiotic resistant bacteria, in particular, because of the increased challenges of treating infections.[10] This is pertinent to *C. burnetii* because, in some cases, the Q fever infection can be difficult to treat by traditional antibiotics. Further demonstrating the need for *C. burnetii* vaccine development are the negative side effects associated with current products available.[11] Currently, the Q fever vaccine Q-VAX® (Seqirus™; Maidenhead, UK) is approved for use in Australia for workers at particularly high risk of *C. burnetii* exposure. Unfortunately, this vaccine comes with severe systemic side effects when vaccinated individuals had previously been exposed to *C. burnetii* and developed immunity. These side effects mean that patients must be prescreened for immunity prior to vaccination, which is costly, time consuming, and not feasible on a large scale. A carbohydrate-based vaccine for *C. burnetii* may eliminate these off-target effects resulting in an immunization which can be made widely available. An additional benefit of characterizing virenose biosynthesis is the utilization of the carbohydrate for developing handheld detection assays for the warfighter. The current detection strategies are based on phase II *C. burnetii* strains which lack the outer O-antigen and are non-pathogenic.[12] Having an antigen-based detection platform against virenose will provide a specific and sensitive readout allowing for rapid responses from warfighters and enhanced decision making abilities.

## ACKNOWLEDGMENTS

Funding was provided by the U.S. Army via the In-house Laboratory Independent Research Program (PE 0601101A Project 91A) at the Combat Capabilities Development Command Chemical Biological Center.

## REFERENCES

[1] Abnave, P.; Muracciole, X.; Ghigo, E. Coxiella burnetii lipopolysaccharide: what do we know? *Int. J. Mol. Sci*. **2017**, *18* (12), p 2509.
[2] Hackstadt, T. Antigenic variation in the phase I lipopolysaccharide of Coxiella burnetii isolates. *Infect. Immun.* **1986**, *52* (1), pp 337–340.
[3] Beare, P.A.; Jeffrey, B.M.; Long, C.M.; Martens, C.M.; Heinzen, R.A. Genetic mechanisms of Coxiella burnetii lipopolysaccharide phase variation. *PLoS Pathog.* **2018**, *14* (3), e1006922.
[4] Toman, R.; Škultéty, L.T.; Ftáček, P.; Hricovíni, M. NMR study of virenose and dihydrohydroxystreptose isolated from Coxiella burnetii phase I lipopolysaccharide. *Carbohydr. Res.* **1998**, *306* (1–2), pp 291–296.
[5] Flores-Ramirez, G.; Janecek, S.; Miernyk, J.A.; Skultety, L. In silico biosynthesis of virenose, a methylated deoxy-sugar unique to Coxiella burnetii lipopolysaccharide. *Proteome Sci.* **2012**, *10* (1), p 67.

[6] Keasling, J.D. Synthetic biology and the development of tools for metabolic engineering. *Metab. Eng.* **2012**, *14* (3), pp 189–195.
[7] Li, Z.; Gao, Y.; Nakanishi, H.; Gao, X.; Cai, L. Biosynthesis of rare hexoses using microorganisms and related enzymes. *Bielstein. J. Org. Chem.* **2013**, *9* (1), pp 2434–2445.
[8] Granström, T.B.; Takata, G.; Tokuda, M.; Izumori, K. Izumoring: A novel and complete strategy for bioproduction of rare sugars. *J. Biosci. Bioeng.* **2004**, *97* (2), pp 89–94.
[9] Hassan, M.I.; Lundgren, B.R.; Chaumun, M.; Whitfield, D.M.; Clark, B.; Schoenhofen, I.C.; Boddy, C.N. Total biosynthesis of legionaminic acid, a bacterial sialic acid analogue. *Angew. Chem.* **2016**, *55* (39), pp 12018–12021.
[10] Astronomo, R.D.; Burton, D.R. Carbohydrate vaccines: developing sweet solutions to sticky situations? *Nat. Rev. Drug Discovery.* **2010**, *9* (4), pp 308–324.
[11] Zhang, G.; Samuel, J.E. Vaccines against Coxiella infection. *Expert Rev. Vaccines.* **2004**, *3* (5), pp 577–584.
[12] Wegdam-Blans, M.C.; Wielders, C.C.; Meekelenkamp, J.; Korbeeck, J.M.; Herremans, T.; Tjhie, H.T.; Bijlmer, H.A.; Koopmans, M.P.; Schneeberger, P.M. Evaluation of commonly used serological tests for detection of Coxiella burnetii antibodies in well-defined acute and follow-up sera. *Clin. Vaccine Immunol.* **2012**, *19* (7), pp 1110–1115.

# Effect of bacterial spore deactivation methods on bacteria chemical components as determined by Raman chemical imaging

Ashish Tripathi*, Phillip G. Wilcox, Michael Kim, Erik D. Emmons, Angela M. Zeigler, Daniel R. McGrady, Waleed M. Maswadeh, Neal D. Kline, Jason A. Guicheteau, Raphael P. Moon, Kevin L. Hung, Erik S. Roese, Richard G. Vanderbeek
U.S. Army Combat Capabilities Development Command Chemical Biological Center, Research & Technology Directorate, 8198 Blackhawk Rd, Aberdeen Proving Ground, MD 21010

## ABSTRACT

Recently, distribution of unreliably deactivated *Bacillus anthracis* spore samples created disruption in the defense, health, and disease control communities. Accurate and reliable determination of viability is critical to avoiding such incidents. Multiple technologies exist to detect or identify an organism, but these do not provide any information on viability of the sample. Most often, one must rely on microbiological culture to confirm sample viability; however, this technique takes hours to days for confirmation. Recent work with *B. anthracis* Delta Sterne spores demonstrated that Raman spectroscopy could be used to discriminate between viable and gamma-deactivated spores and provided initial insight into the probable source of discrimination found in the spores. From this previous work, we believe through Raman spectral analyses of viable and deactivated spore samples, significant changes in spectral response can be resolved and ascribed to classes of biomolecules affected by the deactivation processes. We expanded upon this study to include four different *Bacillus* spores (*B. anthracis*, *B. megaterium*, *B. thuringiensis kurstaki*†, and *B. atrophaeus*) and probe multiple deactivation techniques to include gamma radiation, UV radiation, chemical, and thermal methodologies. We used sequential Raman imaging scanning electron microscopy to determine chemical (Raman spectral information) and physical (scanning electron microscopy imaging) variance between viable and deactivated spore samples.

**Keywords:** bacterial spore viability, image segmentation, Raman spectroscopy, Raman microscopy, image cytometry, bright-field, microscopy, scanning electron microscopy

## 1. INTRODUCTION

Determining a spore's viability is traditionally performed using one of a few long-standing methods. The first, and most widely used method, is to culture the sample and wait to observe growth (or lack thereof); however, this method can take days to confirm lack of growth.[1,2] Other methods include polymerase chain reaction (PCR) or quantitative PCR (qPCR) to amplify DNA fragments. Although these methods do not always discriminate the DNA from viable and non-viable cells, sample preparation methods have been demonstrated which can prevent the DNA from nonviable cells from being replicated.[3,4] To perform PCR, the DNA needs to first be extracted from the sample, with the PCR process itself taking minutes to hours to complete.[4,5] A third option involves the use of fluorescent stains or assays which can be used with flow cytometry[6] or optical microscopy.[7–11] In order to screen a large number of spores, the ideal method would require minimal sample preparation and rapid acquisition of data. Using a method based on bright-field (BF) microscopy provides an approach that can be used to quickly measure a large number of spores. Combining this method with an additional analytical technique such as Raman spectroscopy improves the confidence in the final determination of viability. Previously, Raman microscopy has demonstrated the ability to discriminate between bacterial species and strains using both normal Raman[12–14] and surface-enhanced Raman spectroscopy.[15–17] Additionally, Raman spectral differences have been documented between viable and non-viable *Bacillus* spores that were inactivated using wet-heat,[18] cold atmospheric plasma,[19] and chemical (formalin)[17] methods. In this effort, we will examine spores inactivated with gamma and ultraviolet C (UV-C) irradiation, autoclaving (thermal), and two chemical methods (bleach and aldehyde). The combination of BF and Raman imaging techniques is well suited for

† *B. thuringiensis kurstaki* is referred to as *B. thuringiensis* throughout this report.

spore screening because they are both non-contact, non-destructive, and reagent-less. In this effort, we selected attenuated strains of *B. anthracis* Sterne, *B. atrophaeus*, *B. megaterium*, and *B. thuringiensis*.

To rapidly and automatically obtain cytometric measurements that, in part, include shape and size parameters of spores from bright-field images (BFI), requires a robust and accurate segmentation method. Manual characterization of spores in images is a slow, laborious, and subjective task. In addition to counting and determining morphological information, spore segmentation plays a valuable role in selective targeting of spores for further Raman imaging analysis. This type of smart targeting has shown usefulness in forensic applications and leads to a reduction in the time required to analyze the sample by predetermining the location of the spores and interrogating only those locations.[20,21] In the case of Raman microscopy, spectral signatures are collected from the small region where the microscope objective focuses the laser and hyperspectral images are built by rastering the laser beam through the field of view (FOV). For sparse samples, such as deposited spores, a significant percentage of the overall collection time is spent on substrate regions of the image that contain no spore-like material. An additional complication can also occur when the raster scan takes equidistant steps which can result in the laser overlapping multiple spore edges on a single spectral scan. By identifying the spore regions before spectral acquisition, scans can be performed faster by ignoring regions where spore-like material is not present and spectral results can be linked back to a specific spore. These shortcomings are addressed by the approach presented in this report.

Specific software approaches to aid in the task of segmenting biological samples have been previously explored.[22,23] A variety of segmentation techniques have been applied on large cellular materials including white blood cells (which are in the 12–17 µm size range);[24–26] hematopoietic stem cells (~20–30 µm);[27] cancer cells;[28] bone marrow, blood, and cervical nuclei (~6 µm);[29,30] living *Spodoptera frugiperda* cells (~9–12 µm);[31] and fungal and bacterial spores (~2–60 µm depending on species).[32–38] These applications typically rely on a relatively small set of segmentation techniques—thresholding, edge/feature detection, morphological filtering, region growing, and deformable model fitting.[39,40] More advanced segmentation techniques, such as neural networks, require large amounts of training data to improve upon the accuracy[26] that can be achieved with traditional techniques.

In this effort, we use a combination of these traditional segmentation techniques to quickly and autonomously segment BFI of Gram-positive spores. Gram-positive spores are small (~1 µm in diameter) compared to the cells described in the previous paragraph, which can make them difficult to detect using BFI since it is close to the diffraction limit of optical microscopy. Using the microscope described later with a 100X objective, the image of a single spore is typically 11–16 pixels in length. Additionally, the spore deposition on a substrate is random, and the spores may be distributed individually or in clusters of varying sizes, which further complicates the segmentation process. To overcome these issues, a combined method incorporating watershed segmentation[38] and an unsupervised segmentation method[30] were previously proposed and demonstrated. The watershed-based methods typically showed less than 90 % success in demarcation of individual spores,[30,38] whereas the unsupervised methods showed greater than 93 % success in demarcation,[30] but used an iterative process that came at a very high computational complexity and cost. The method used in this work employs the traditional watershed based segmentation[41] in conjunction with an optimized pre-processing methodology. Since this image processing technique segments images by finding local maxima contours around "catchment basins" of lower intensity,[41] it works well for both sparse (monodispersed or well-separated clusters of spores) and dense images (poorly separated clusters or large clusters of spores).

Using the image processing method, Raman spectra of multiple viable and deactivated spores is extracted. The Raman spectra of viable and deactivated spores is examined to obtain possible spectral differences between the two populations. These differences are compared with Raman spectra of various spore biomarkers to include calcium dipicolinate acid (CaDPA), DNA, protein surrogates, phospholipids, and peptidoglycan.

## 2. EXPERIMENTAL

### 2.1 Spore formation and growth study

#### *2.1.1 Organism and growth medium*

The *Bacillus* spore strains used in this study were *B. thuringiensis* (ATCC® 33679™), *B. megaterium* (ATCC® 9885™), *B. anthracis* Sterne, and *B. atrophaeus* (ATCC® 9372™). A base of Difco™ sporulation medium (DSM) consisting of the following composition was used: 8 g/L nutrient broth (NB, Difco™), 2.15 g/L $KH_2PO_4$ (Sigma-Aldrich®) and 4.39 g/L $K_2HPO_4$ (Sigma-Aldrich®), which was sterilized at 121 °C for 30 minutes in an autoclave (Tomy ES-315).

The sterilized base DSM was further supplemented with 40 mL of a 0.2-µm filtered pre-sterilized (Corning®) sporulation salt stock solution (CCY). The CCY stock consisted of 7.35 g/L $CaCl_2 \cdot 2H_2O$, 0.99 g/L $MnCl_2 \cdot 4H_2O$, 10.17 g/L $MgCl_2 \cdot 6H_2O$, 0.0081 g/L $FeCl_3$, and 0.34 g/L $ZnCl_2$. All CCY stock components were purchased from Sigma-Aldrich® except $ZnCl_2$, which was from Thermo Fisher Scientific, Inc.

### *2.1.2 Culture conditions*

A glycerol-frozen stock of each strain was streaked onto a NB agar plate and incubated at 37 °C overnight (VWR® 3025 B). A single colony of each strain was inoculated into 1 L of DSM in a 4-L flask and incubated at 34 °C and 200 rpm. When the percentage of spores reached greater than 95 % under a phase-contrast microscope (Olympus BX51) after 2 to 3 days, the spore suspension was centrifuged (Beckman Coulter® Avanti™ J-25I) at 10,000 rpm for 10 minutes, washed 3 times with pre-sterilized deionized water, and concentrated to approximately 100 mL each.

### *2.1.3 Heat deactivation method*

A 0.5-mL aliquot of each washed and concentrated strain was placed in a 2-mL screw cap glass vial and sterilized in an autoclave (Tomy ES-315) at 121 °C for 30 minutes. After sterilization, 0.1 mL of each inactivated strain was inoculated into 250 mL of DSM in a 1-L flask and incubated at 30 °C and 225 rpm for 2 weeks. No re-germination or growth was evident in each heat-inactivated strain.

### *2.1.4 Gamma radiation deactivation*

The spore samples were irradiated utilizing a Cobalt-60 Irradiator (Model 484R) (JL Shepherd & Associates; San Fernando, CA). Four vials, each containing a 2-mL aliquot of water suspension with viable spores, were double-contained and packaged inside of a Saf-T-Pak™ (model QADOC-451) for the irradiation. The Saf-T-Pak™ was placed on a turntable and was rotated at 6 rpm for the duration of the irradiation. The samples were irradiated with a dose of 50 kGy. After deactivation, 0.1 mL of each inactivated strain was inoculated into 250 mL of DSM in a 1-L flask and incubated at 30 °C and 225 rpm for 2 weeks. No re-germination or growth was evident in each gamma radiation-deactivated strain.

### *2.1.5 UV-C radiation deactivation*

Both control and experimental slides were set up under the UV-C setup in a containment box. UV-C radiation, in the range of 249–258 nm and 60 µW/cm$^2$ power density was received at the sample location. The exposure times were 8 hours each for *B. thuringiensis* and *B. megaterium* spores, 15 hours for *B. anthracis* spores, and 23.5 hours for *B. atrophaeu*s spores. At the end of exposure, each material's conical tube was filled with 20 mL of PBS-TWEEN® solution. A sterile mesh was cut into a small piece, dipped in the PBS-TWEEN® and then swiped over the sample spot(s) to recover the exposed sample. The conical tube containing PBS-TWEEN® and mesh with the sample was vortexed with a shaker for 10 minutes. The conical tube was then vortexed right before plating for another 30 seconds with 100 µL of solution plated on up to three plates for replicates. These plated samples were incubated overnight at 37 °C. No growth was found, thus confirming sterility.

### *2.1.6 Bleach deactivation*

Spore samples were suspended in freshly prepared 10 % bleach pH adjusted to 7. The above prepared suspension incubated at room temperature for 30 minutes with intermittent vortexing. After 30 minutes, the sample was centrifuged at 10,000 rpm for 5 minutes and decanted off the 10 % bleach. Subsequently, each spore pellet was washed 3 times with 1 mL sterile deionized water. Growth confirmation experiment showed complete sterilization.

### *2.1.7 Glutaraldehyde deactivation*

One mL each of spore suspension was pipetted in 2-mL micro-centrifuge tubes and centrifuged (5417R, Eppendorf®) at 10,000 x g for 5 minutes. After the supernatant was decanted off, each spore pellet was reconstituted with 1 mL each of 2 % glutaraldehyde solution with 0.3 % w/v, vortexed, and incubated at room temperature for at least 20 hours. After the 20 hours of incubation, the deactivated samples were centrifuged at 10,000 x g for 5 minutes, decanted off the spent glutaraldehyde solution, and washed 3 times with 0.2-µm-filtered deionized water. The sterility of deactivated spore suspension was tested by inoculating 0.5 mL each of the deactivated samples into 4X 400 mL of a pre-sterilized DSM in 2-L flasks and incubated at 200 rpm and 30 °C up to 2 weeks. All growth was negative.

## 2.2 Microscopy slide preparation

For each type of spore and method of deactivation, two separate aluminum coated microscopy slides (evaporated metal film and aluminum 136 slide) were prepared. One was populated with only viable spores and the other with

deactivated spores. To wash the spores, 4-µL aliquots of water suspension carrying the spores at various concentrations (CFU/mL) were deposited on the aluminum slides at various locations. The water was allowed to dry, leaving a residue with spores on the microscopy slide surface.

### 2.3 Bright-field imaging and Raman measurements

All BFI and Raman hyperspectral cubes (RHSC) were collected utilizing an Alpha300R confocal Raman imaging microscope (WITec; Ulm, Germany) using a 100X microscope objective and a 532 nm excitation laser. A UHTS 300 VIS spectrometer (WITec; Ulm, Germany) with a 600 line/mm diffraction grating was used for Raman spectral measurements. Each spectrum was acquired with a 2-second integration time and 4 mW laser output in "continuous mode", where the sample stage was continuously moving over the length of the step size. No photo-bleaching was required as the fluorescence did not seem to deleteriously influence the Raman spectral information. The BFI option was used with the images on the 1-megapixel (1,000 pixels x 1,000 pixels) setting. The images shown in this report are cropped from these original 1-megapixel images.

### 2.4 Scanning electron microscopy

A Thermo Scientific® Phenom™ Pharos desktop scanning electron microscope (SEM) (Thermo Fisher Scientific, Inc.; Waltham, MA) was used to acquire high-resolution images of the *Bacillus* spores before and after deactivation processes. The *Bacillus* spore samples were deposited on an aluminum-coated microscopy slide (TS-AL-134) (Dynasil; Newton, MA). No additional metal coating was applied to the sample as the aluminum coating on the microscopy slide acted as a conduction device to remove SEM source electrons. The SEM images were acquired via 15 kV source and a secondary electron detector.

Additionally, aluminum-coated microscopy slides were prepared by depositing dry samples of various spore biomarkers to include CaDPA, lipoteichoic acid, and peptidoglycan from *B. subtilis* and polyhydroxybutyric acid. Raman spectroscopy is not specific in discriminating large proteins, thus ovalbumin from chicken egg whites was added to the list of biomarkers as a surrogate for large proteins. Figure 1 shows the Raman spectra of these biomarker chemicals.

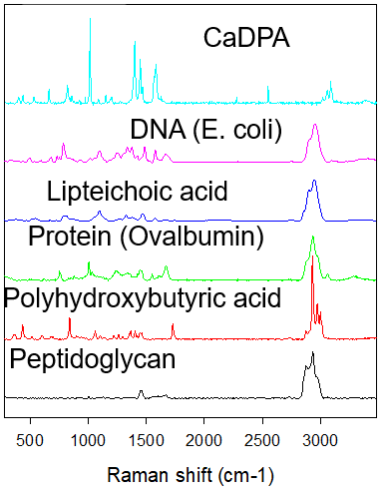


**Figure 1. Raman spectra of various spore-relevant biomarkers.**

### 2.5 Data analysis

The "cosmic-ray" and baseline correction of the Raman spectral data was performed with the built-in functions in the WITec Project 5.2 version software. The post-acquisition imaging and spectral data analysis was performed using MATLAB® R2019a software (MathWorks; Natick, MA).

## 3. STUDY LIMITATIONS AND CAVEATS

The primary goal of this effort is to determine and identify Raman spectral differences between viable and deactivated spores. The purpose is not to visit the effectiveness of Raman spectroscopy in discriminating between different

*Bacillus* spores. Additionally, it would have been ideal to repeat the study detailed in this report with multiple batches of the *Bacillus* spores, but such a study was outside the scope of the resources available.

## 4. RESULTS AND DISCUSSION

### 4.1 Spore sample characterization

A comparison study of viable and deactivated spores mandates that the sample be comprised of mostly spore material and that the amount of non-spore debris (growth media and cellular debris) be minimized. The as-received spore samples were examined with the WITec microscope both visually and chemically. The cleanest spore sample was determined to be *B. anthracis* Sterne. The *B. anthracis* spore sample was comprised of over 95 % spore material with about 2 % of polyhydroxybutyric acid. This determination was made with the help of Raman chemical imaging analysis of a FOV containing the sample, as shown in Figure 2. The BFI of the FOV is shown in the top left panel of Figure 2. An overlay of the Raman chemical imaging map with green false-colored pixels showing a greater than 0.8 Pearson's cross correlation with the average spectrum of a viable *B. anthracis* spore is shown in the bottom left panel of Figure 2. Additionally, red false-colored pixels show a greater than 0.8 Pearson's cross correlation with the spectrum of polyhydroxybutyric acid. The average spectra of *B. anthracis* spores (green), the average of all the spectra acquired at the red-pixel locations, and the polyhydroxybutyric acid spectrum (grey) is shown in the right panel of Figure 2.

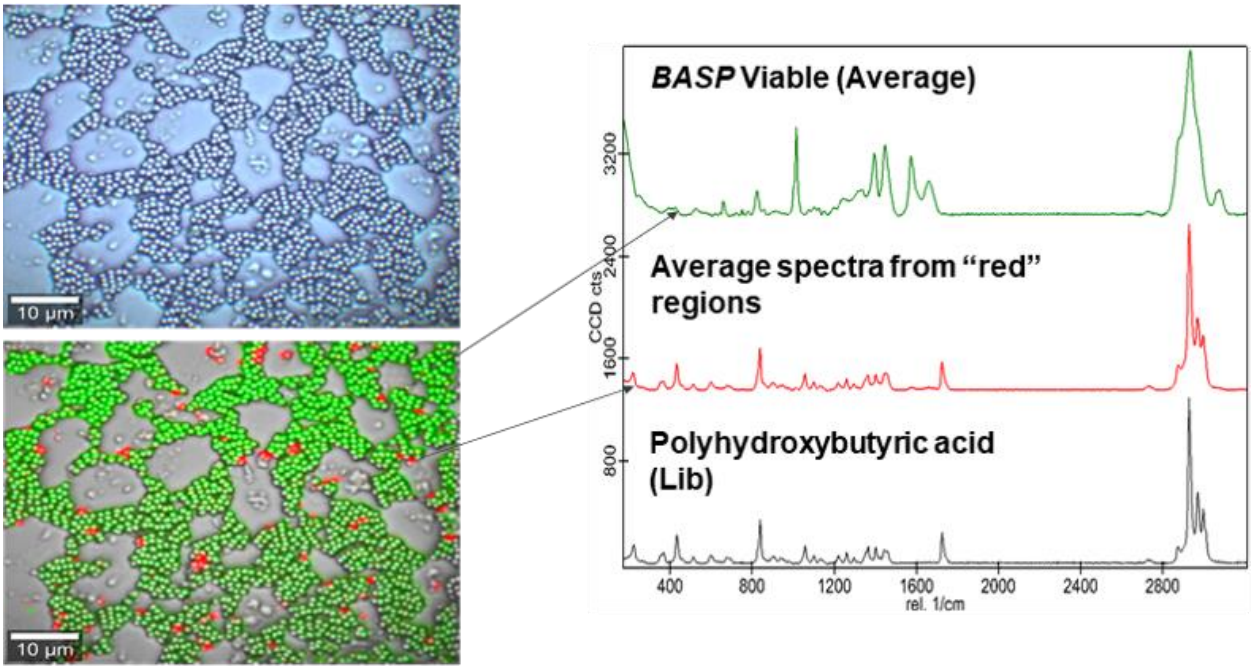


**Figure 2. As received *B. anthracis* spore sample purity determination.**

The as received *B. thuringiensis* spore sample had the least spore content by percentage. The *B. thuringiensis* spore sample was comprised of less than 40 % spore material. This determination was made with the help of Raman chemical imaging and BFI analysis of a FOV containing the sample, as shown in Figure 3. Spore-like material, characterized by about 1-micron oval shaped particles in the BFI of the FOV, were interspersed with smaller, irregularly shaped particles (shown in the top left panel of Figure 3). Raman chemical analysis showed that, indeed the 1-micron oval shaped particles presented Raman spectra that are typical of a spore (containing biomarker features from CaDPA, proteins, etc.). An overlay of the Raman chemical map with green false-colored pixels showing a greater than 0.95 Pearson's cross correlation with the average spectrum of a viable *B. thuringiensis* spore is shown in the bottom left panel of Figure 3. Additionally, false-colored red and blue pixels show a greater than 0.95 Pearson's cross correlation with extracted average spectrum as shown in the right panel of Figure 3.

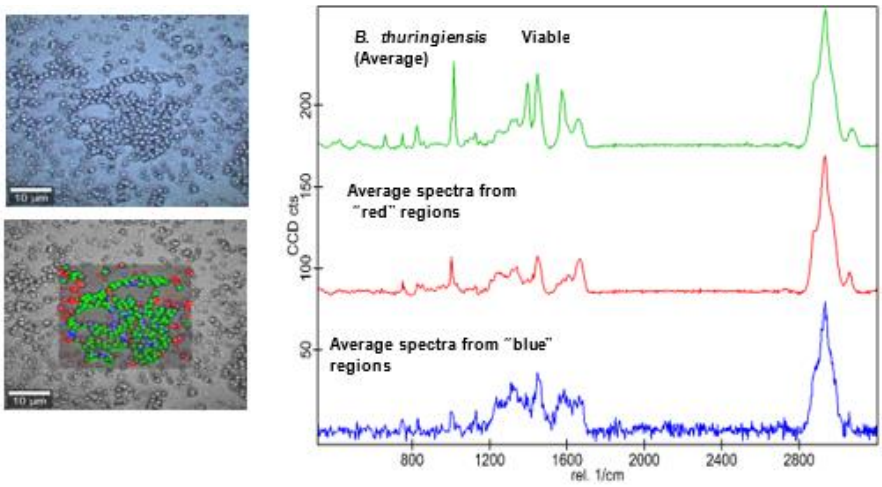


**Figure 3. As-received *B. thuringiensis* spore sample purity determination.**

The as-received sample of *B. thuringiensis* spores required purification. It was noticed that the suspension containing the spore tended to form "foam" when shaken. A small aliquot of the foam was deposited on a microscopy slide and the sample examined with the help of Raman chemical imaging and BFI analysis of a FOV containing the sample, as shown in Figure 4. Two FOVs were examined with the same methodology described in the last paragraph. The foam was comprised of 80 % spores with the rest being 20 % non-spore debris. The Raman and BFI analyses are shown in Figure 4. For the remainder of this effort, the foam of the *B. thuringiensis* spore suspension was used for analysis.

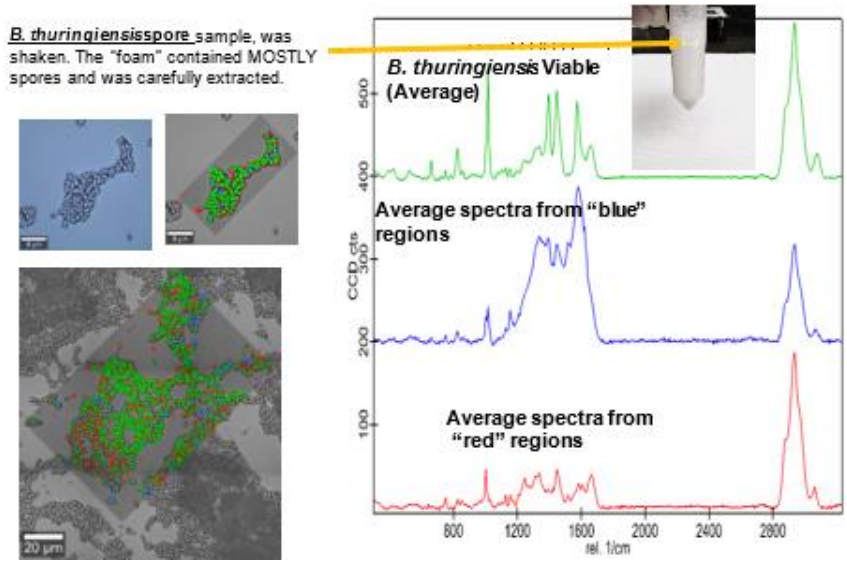


**Figure 4. Foam of the shaken *B. thuringiensis* spore suspension contains mostly spores.**

Clearly, the Raman chemical imaging microscopy reveals heterogeneity in the spore samples as received. To determine the nature of the heterogeneity, we developed sequential Raman imaging scanning electron (RISE) microscopy. We detail the RISE microscopy of viable spore samples in the following section.

### 4.2 Sequential Raman imaging scanning electron microscopy of viable spore samples

The previous section describes the presence of multiple components found in "cleaned" viable spore samples. Thus, it is imperative to determine the Raman spectra being generated by intact and visually confirmed spores from those being produced by damaged spores and cellular debris. The viable spore samples were analyzed with sequential RISE microscopy. Figure 5 shows the process used to perform the RISE microscopy on a viable *B. megaterium* sample. The spore sample, in a dry residue form deposited on an aluminum-coated microscopy slide, is placed under the 100X objective of the Raman microscope. A BFI of the FOV is acquired, as shown in Figure 5-1. Raman imaging is acquired on the entire FOV with the instrument setting described in an earlier section. The C–H band peak area (2832–3032 $cm^{-1}$) heat map is shown in Figure 5-2, as a representation of the Raman image. The acquired RHSC was

processed with the WITec PROJECT version 5.2 Raman image and spectral data processing software. A cosmic ray removal was performed with a "filter size" of 2 and "dynamic factor" of 4. The resultant RHSC was then processed with baseline removal with rolling circle filter (called "shape" correction function in the PROJECT software) of 100 spectral dimension size. This cross-correlation (CCR) and baseline-corrected RHSC were then interrogated with the "true component analysis" function of the WITec PROJECT software. The analysis was performed by truncating the spectral range into two parts: the fingerprint region 400–1850 $cm^{-1}$ range and the C–H band region in 2700–3200 $cm^{-1}$ range. The "true component analysis" determined a basis set of four unique Raman spectra that explained more than 95 % of the Raman spectral data comprising the RHSC. These four Raman spectra are shown in Figure 5-6. A Pearson's CCR heat map was constructed with each spectrum of the RHSC compared with the four Raman spectra and the CCR values determined. If the CCR value exceeded 0.75 and the CCR value was the highest against one of the four basis Raman spectra, it was assigned the color corresponding to that Raman spectra. This CCR heat map is shown in Figure 5-7.

Following the Raman analyses, the microscopy slide was analyzed with the SEM. The same FOV that was interrogated with Raman imaging was located and a SEM image was acquired with the setting described in an earlier paragraph. The SEM image is shown in Figure 5-9. Clearly and in contrast to the BFI image (Figure 5-1), the SEM image reveals a mix of intact and damaged spores. There is a dark hollow spot in the center mass of the spores that are damaged. The CCR map was overlaid on the SEM image, as shown in Figure 5-10. The green pixels (which match the green Raman spectra in Figure 5-6) correspond to intact *B. megaterium* spores. Thus, the green-colored Raman spectrum can be attributed to the viable *B. megaterium* spores. The red- and pink-colored Raman spectra correspond to damaged spores. The blue Raman spectrum is of unknown origin, perhaps resulting from remaining media.

The BFI (Figure 5-1) does not reveal the differences between damaged and intact spores—these differences are suggested by Raman image analysis (as shown in Figure 5-7) and are confirmed with the SEM image of the same FOV (Figure 5-9). Thus, sequential RISE microscopy is a powerful tool in understanding the various heterogeneities present in the viable *B. megaterium* sample.

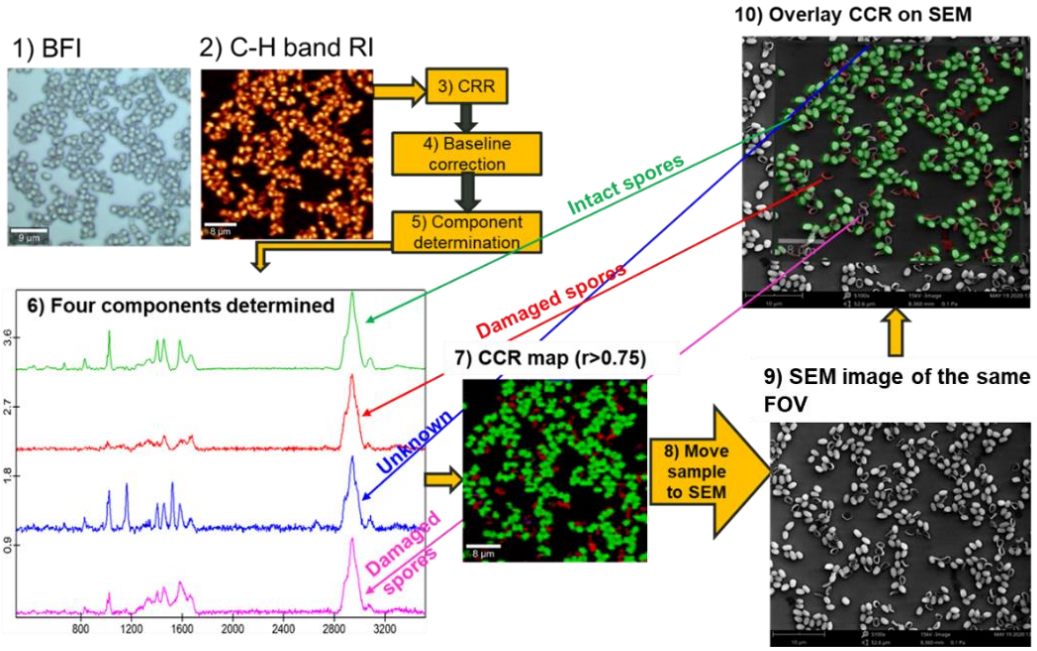


**Figure 5. Sequential RISE microscopy of *B. megaterium* spore samples.**

Sequential RISE microscopy was also performed on the viable spore samples of *B. anthracis* Sterne, *B. thuringiensis*, and *B. atrophaeus*. Figure 6 shows the results from the RISE microscopy analysis. The *B. anthracis* Sterne and *B. atrophaeus* samples were found to be comprised of over 90 % intact spores, whereas *B. thuringiensis* spore sample was populated with about equal numbers of intact (green pixels) and damaged (red pixels) spores. In the case of the *B. anthracis* Sterne sample, there was evidence of polyhydroxy butyric acid retained from the vegetative cells of *B. anthracis*. We also observed traces of two unknown hydrocarbons in *B. anthracis* Sterne samples. In the case of the *B. atrophaeus* samples, there was evidence of trace amounts of carbonaceous particles and a hydrocarbon compound.

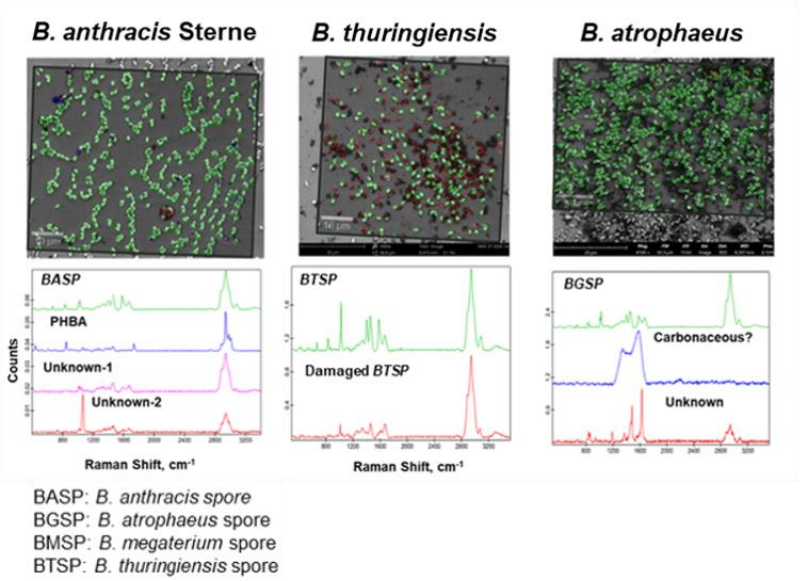


**Figure 6. RISE microscopy of viable spore samples.**

With the help of sequential RISE microscopy, a clear understanding of Raman spectral attribution was obtained. The population of viable spore Raman spectra was comprised of those attributed to intact spores in these samples (green pixels). The damaged spore spectra were excluded from the population of viable spore Raman spectra.

### 4.3 Segmentation overview

Raman chemical images are generated by raster scanning a laser over a sample to collect Raman spectra at each spatial coordinate. This generates a cube of data with spatial information stored along the *x*-axis and *y*-axis, and spectral information saved on the *z*-axis. Since the spatial resolution of BFI and Raman chemical imaging are both determined by the diffraction limit of visible light, it is technically feasible for Raman chemical imaging to reach image resolutions comparable to those obtained in BFI; however, because each pixel needs to be measured individually in an RHSC, the process of doing so is not practical, due to the time required to sample each pixel. This means that Raman chemical images typically have significantly lower spatial resolution compared to BFI.

The step size for our RHSCs was typically 0.5 µm in both spatial dimensions. Since *Bacillus* spores are ~1 µm in diameter, measuring a RHSC over a larger region means that each spore could be interrogated multiple times in several pixels. Similarly, the laser could also interrogate an area where multiple spores are present in the FOV. Additionally, the Raman spectra collected over a single spore are not uniform and the fixed step size of the raster scan can lead to the interrogation of spore edges or multiple spores at a time which may not be representative of the spore as a whole. To build an average Raman spectrum for a single and specific spore, a method was needed to map each point in the data cube to a pixel in the BFI.

Image registration is a process where two different images of the same scene are aligned to overlap one another. Because the BF microscopy image is significantly higher resolution than the RHSC, straightforward registration techniques were unable to be used. To overcome these challenges, we developed a method to combine all measured Raman spectra from a single spore to obtain an average Raman spectrum for that spore. An example BFI of *B. atrophaeus* spores is shown in Figure 7a. First, the segment of the RHSC corresponding to the C–H stretch (2938 $cm^{-1}$, C–H image), shown in Figure 7b, was extracted and resized to match the pixel size of the BFI using a nearest neighbor interpolation. Figure 7c shows an example of the misalignment present between the BF and Raman images prior to registration—a singly dispersed spore is circled on the right side of the image to highlight this misalignment. Next, a non-reflective similarity transform was applied using the MATLAB® functions 'fitgeotrans' and 'imwarp' to translate, rotate, and scale the BFI into alignment with the results shown in Figure 7d. Third, the BFI was segmented using an algorithm based on the watershed technique to demarcate the spores as shown in Figure 7e. Finally, every pixel in each demarcated spore was then mapped back to a spectrum within the RHSC. Due to its higher spatial resolution, pixels in the BFI can map back to the same pixel within the RHSC which creates a weighted average spectrum being generated for each segmented region. In order to prevent background (non-spore) data from being included in the average, spectra without the C–H stretch spectral feature at 2938 $cm^{-1}$ were excluded. If more than

40 % of the pixels identified within any segmented region mapped to exclude spectra in the RHSC, then the region was considered blank, and an average was not calculated. The section circled in Figure 7f shows spores correctly identified in the segmentation, but not included in the average due to poor Raman signal. This data was collected from top to bottom and experienced a drift in focus as the scan progressed which caused more below-threshold pixels to be located toward the bottom of the data cube. The examples shown in Figure 7 identified and generated spectra for 115 spores. The goal of this method was to generate a large number of high-quality, weighted average spectra that correspond to single spores, which will be discussed in the following sections.

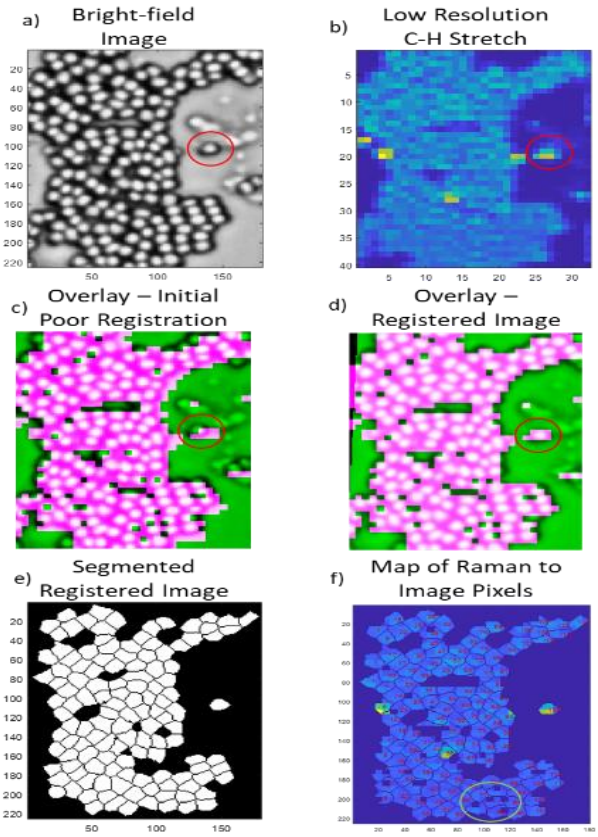


**Figure 7. Process showing the registration of a BFI (a) the C–H stretch segment of a RHSC (b) with initial poor alignment (c). After registration (d), the image is segmented (e) with each region being mapped back to a specific spectrum from the original data cube (f).**

### 4.4 Raman chemical imaging and spectroscopy

For each type of spore and method of deactivation, two separate aluminum-coated microscopy slides were prepared. The first was populated with only viable spores and the second with deactivated spores. Multiple FOVs from the two microscopy slides were interrogated with Raman chemical imaging microscopy. The Raman microscope was used in "continuous mode" where each spectra was acquired with a 0.5-µm step size over samples of all viable and deactivated spores to generate RHSCs. Preprocessing of all RHSCs was performed using WITec Project 5.2 analysis software by removal of "cosmic rays" using a filter size of 2 and dynamic factor of 5 (description of these terms is proprietary of WITec). Additionally, a baseline correction was performed using a rolling circle filter with a size of 100 spectral bins. Both viable and deactivated types of spores have strong Raman peaks associated with the C–H stretching vibrations around 2938 $cm^{-1}$, which was used as a trigger to include that spectrum in the generation of representative average spectra for each of the two classes. Average spectra were created for each population.

#### *4.4.1 Viable spores*

Spectra from at least 400 spores were extracted for each species of spore in viable and deactivated states using the method described in Section 4.3. Figure 8 shows the collection of extracted single viable spore spectra in the fingerprint region and an overlay of the average of the single-spore Raman spectra from the four species of spores.

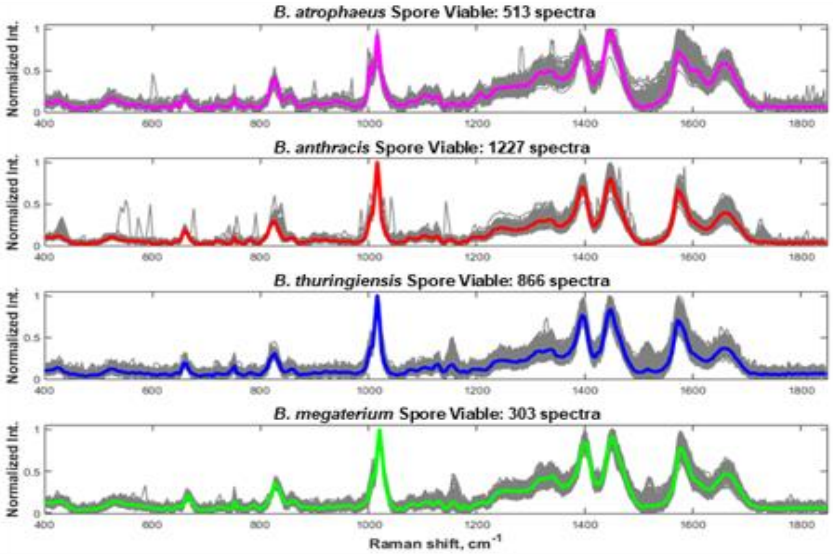


**Figure 8. Collection of extracted single viable spore spectra in the fingerprint region and an overlay of the average of the single spore Raman spectra from the four species of spores.**

A MATLAB® program was used to perform principal component analysis (PCA) on the collected viable spore spectral data in the fingerprint region. Figure 9 shows the results of the PCA. The scores of the principal components 1, 2, and 3 for the four spores are shown in the left panel of Figure 9. A good degree of separation is obtained between the four species of spores, with *B. thuringiensis* and *B. anthracis* being the nearest neighbors. From the scree plot (shown in the top right panel of Figure 9), it is evident that the first five components explain 90 % of the variance. The first five component loading vectors are shown in the bottom right panel of Figure 9.

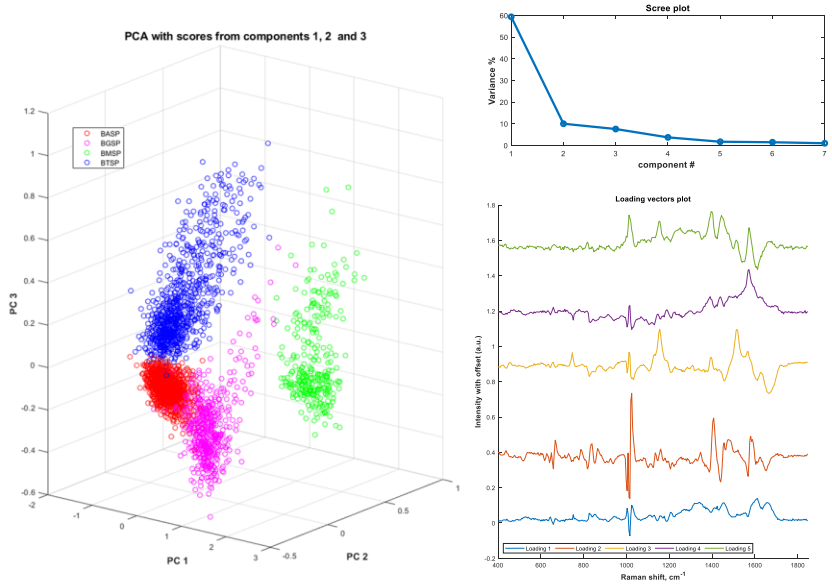


**Figure 9. The results of the PCA on the fingerprint region of Raman spectra from single viable spores of four species of the *Bacillus* genus.**

### *4.4.2 Autoclave deactivation of spores*

The four species of spores were autoclave-deactivated using the method described in Section 2.1.3. Over 400 single spore spectra from Raman images of each of the four spores' species were extracted using the method described in the Section 4.3. Figure 10 shows the individual spores' spectra in lighter green color (viable) and lighter blue color (autoclave-deactivated) along with the average spectra in darker color and thicker linewidth. SEM images of typical viable (in green border) and autoclaved spores (in blue border) are also shown. The features related to CaDPA are

absent in the autoclaved samples. Additionally, the SEM image examination reveals physical damage to the spores due to autoclave deactivation.

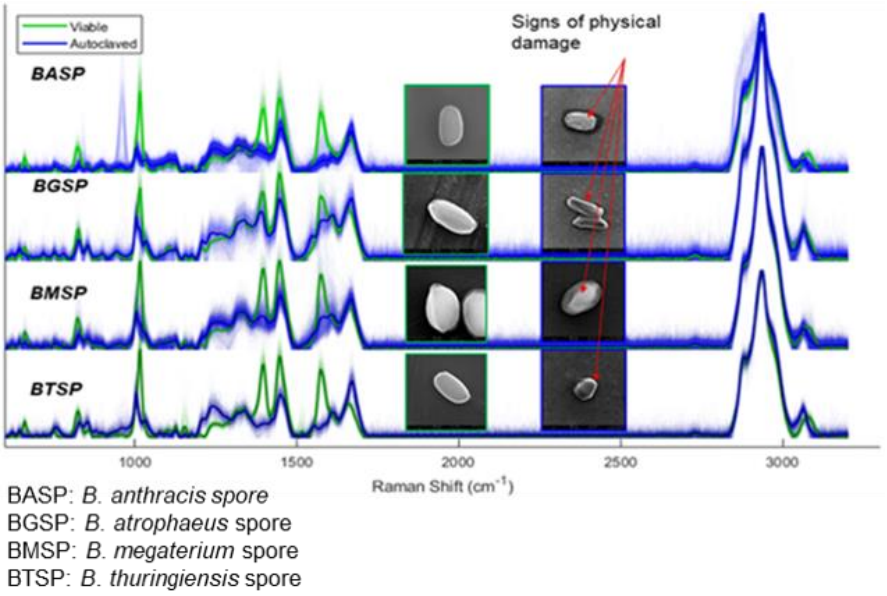


**Figure 10. Raman spectral comparison of viable and autoclave-deactivated spore samples.**

The previously mentioned MATLAB® program was used to perform PCA on the collected viable and autoclave-deactivated spore spectral data in the fingerprint (600–1800 $cm^{-1}$), C≡C band (2200–2290 $cm^{-1}$) and C–H band (2790–3120 $cm^{-1}$) regions. Figure 11 shows the results of the PCA for the four spores. The scores of the principal components 1, 2, and 3 for the viable spores (green) and autoclaved spores (blue) are shown in the top left panel of Figure 11 (for *B. anthracis* spores) and bottom three panels for *B. atrophaeus*, *B. megaterium*, and *B. thuringiensis* spores of Figure 11. The top middle panel shows the scree of *B. anthracis* spores with 90 % variance explained by the first 32 principal components. The top right panel shows the first principal component loading plot (orange) in comparison to average viable (green) and autoclave-deactivated (blue) *B. anthracis* spores' spectra. A good degree of separation is noticed between the viable and autoclave-deactivated spores.

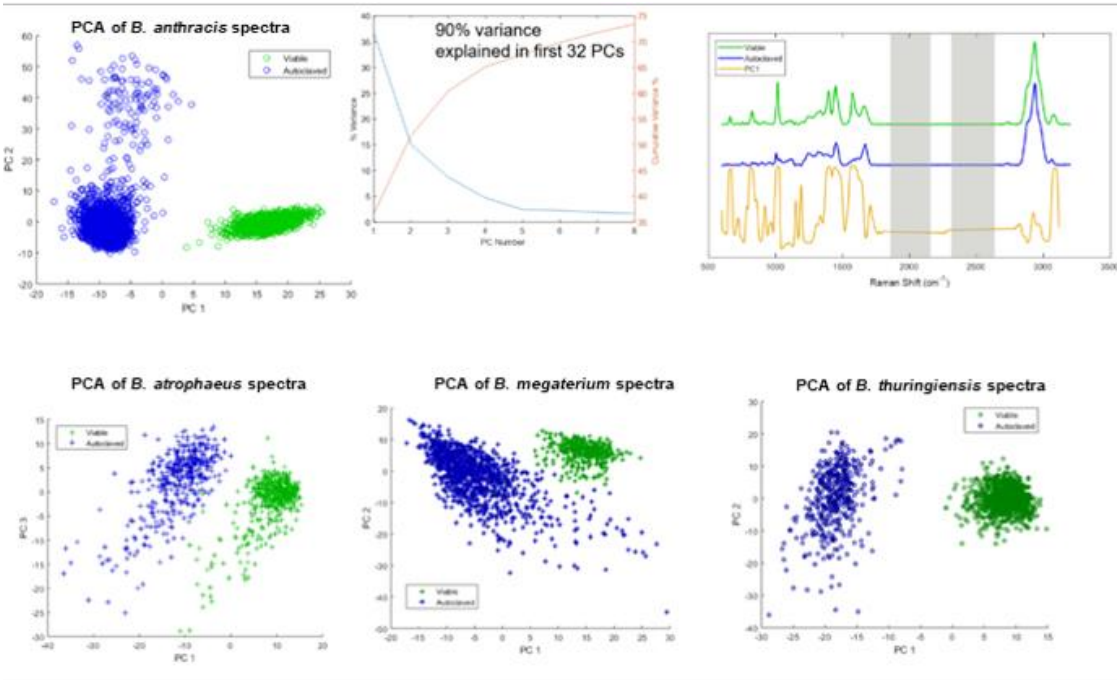


**Figure 11. PCA: viable versus autoclave-deactivated spores.**

### *4.4.3 Gamma radiation deactivation of dried spores*

The four species of spores were gamma radiation deactivated using the method described in the experimentation section in dried residue form. Over 400 single spore spectra from Raman images of each of the four spores species were extracted using the method described in section 4.3. Figure 12 shows the individual spores' spectra in lighter green color (viable) and lighter blue color (gamma-deactivated) along with the average spectra in darker color and thicker linewidth. SEM images of typical viable (in green border) and gamma-deactivated spores (in cyan border) are also shown. The features related to CaDPA are present in the gamma-deactivated samples. Additionally, the SEM image examination reveals no physical damage to the spores due to gamma-deactivation, except in the case of *B. atrophaeus* spores (second panel from the top in Figure 12).

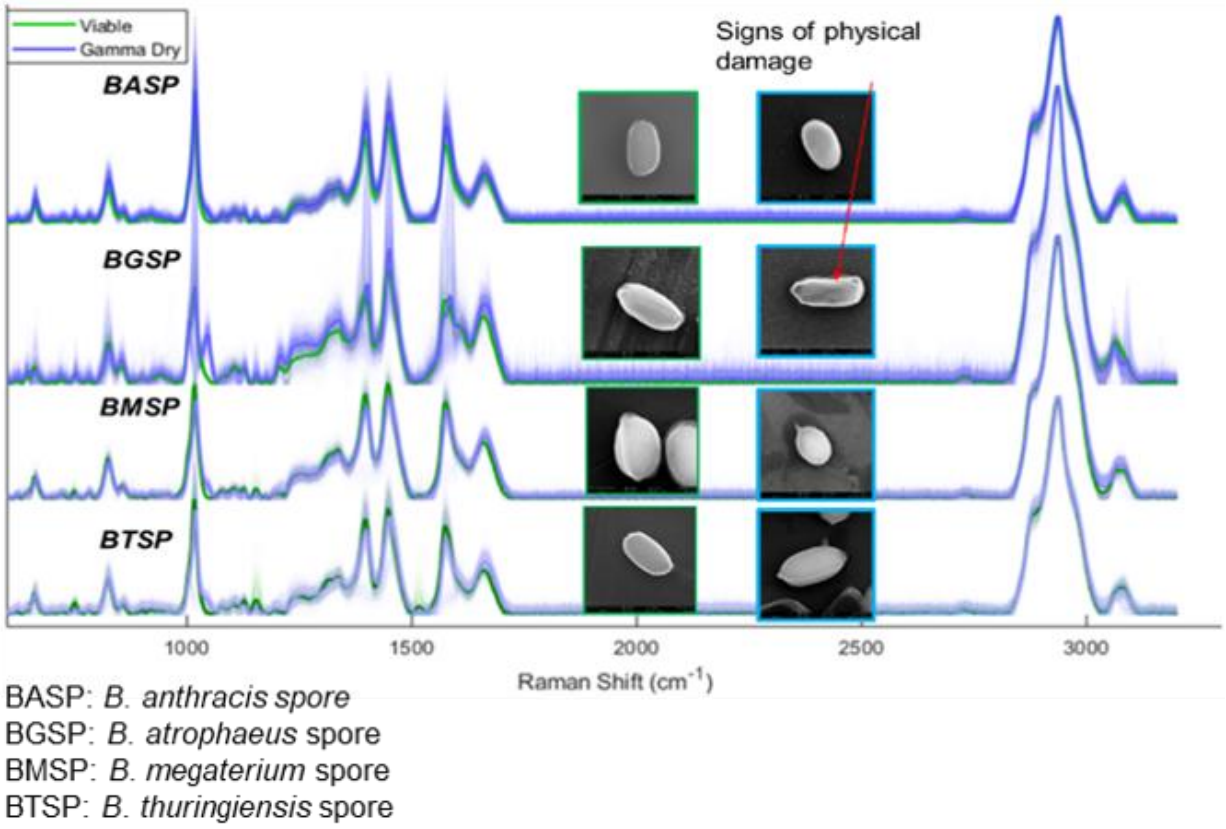


**Figure 12. Raman spectral comparison of viable and gamma-deactivated spore samples in dried residue form.**

PCA was performed on the collected viable and gamma-deactivated spore spectral data in the fingerprint (600–1800 $cm^{-1}$), C≡C band (2200–2290 $cm^{-1}$), and C–H band (2790–3120 $cm^{-1}$) regions. Figure 13 shows the results of the PCA for the four spores. The scores of the principal components 1 and 2 for the viable spores (green) and gamma-deactivated spores (blue) are shown in the top left panel of Figure 13 (for *B. anthracis* spores) and bottom three panels for *B. atrophaeus*, *B. megaterium*, and *B. thuringiensis* spores. The top middle panel shows the scree of *B. anthracis* spores with 90 % variance explained by the first 42 principal components. The top right panel shows the first principal component loading plot (orange) in comparison to average viable (green) and gamma-deactivated (blue) *B. anthracis* spores spectra. The dual clustering in the case of *B. thuringiensis* and *B. megaterium* spores were due to presence of intact and damaged spores in the original viable sample. The damaged spore show absence of CaDPA features, whereas intact spores retained the CaDPA features. Nonetheless, a good degree of separation is noticed between the viable and gamma-deactivated spores.

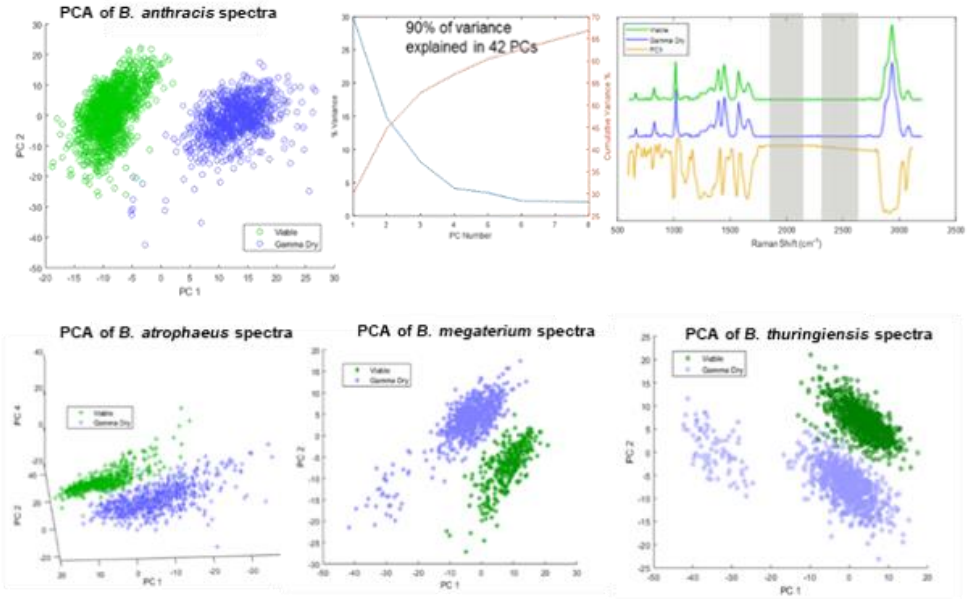


**Figure 13. PCA: viable versus gamma-deactivated dried spores.**

### *4.4.4 Gamma radiation deactivation of wet spores*

The four species of spores were gamma radiation deactivated using the method described in the experimentation section in water suspension. More than 400 single spore spectra from Raman images of each of the four spore species were extracted using the method described in Section 4.3. Figure 14 shows the individual spores' spectra in lighter green color (viable) and lighter red color (gamma-deactivated) along with the average spectra in darker color and thicker linewidth. The *B. anthracis* spore spectra were acquired from two batches of gamma-deactivated samples. The first batch was gamma-deactivated in water suspension in 2016 with 40 kGy of radiation. The extracted spectral data is shown in the top panel of Figure 14 in orange. SEM images of typical viable spores (in green border) and gamma-deactivated spores (in red border and orange border for 2016 batch of *B. anthracis* spores) are also shown. The features related to CaDPA are present in the gamma-deactivated samples of *B. anthracis* spores from the newer batch (red lines, top panel of Figure 14). The rest of the spore samples show absence of CaDPA. Additionally, the SEM image examination reveals physical damage to the spores due to gamma-deactivation, except in the case of newer batch of gamma-deactivated *B. anthracis* spores (top panel image in red border of Figure 14).

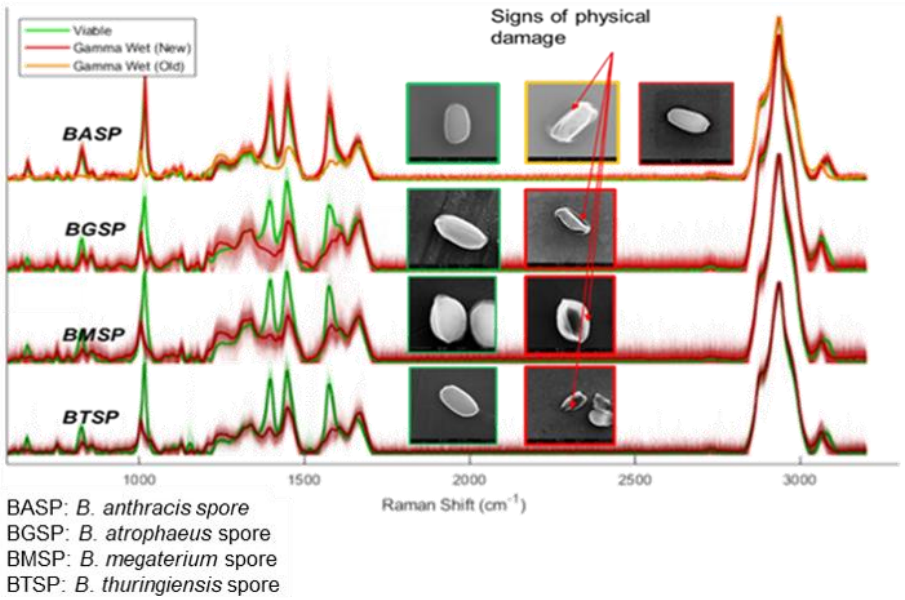


**Figure 14. Raman spectral comparison of viable and gamma-deactivated spore samples in water suspension form.**

PCA was performed on the collected viable and gamma-deactivated spore spectral data in the fingerprint (600–1800 $cm^{-1}$), C≡C band (2200–2290 $cm^{-1}$) and C–H band (2790–3120 $cm^{-1}$) region. Figure 15 shows the results of the PCA for the four spores. The scores of the principal components 1 and 2 for the viable spores (green) and gamma-deactivated spores (red for the newer batch and orange for 2016 batch) are shown in the top left panel of Figure 15 (for *B. anthracis* spores) and bottom three panels (for *B. atrophaeus*, *B. megaterium*, and *B. thuringiensis* spores). The top middle panel shows the scree of *B. anthracis* spores with 90 % variance explained by the first 33 principal components. The top right panel shows the first principal component loading plot (purple and light green) in comparison to average viable (green) and gamma-deactivated *B. anthracis* spore spectra from the newer batch (red) and the 2016 batch (orange). The dual clustering in the case of *B. anthracis* spores was due to the presence of intact and damaged spores in the 2016 and newer sample batches, respectively. The damaged spores show an absence of CaDPA features, whereas intact spores retained the CaDPA features. Nonetheless, a good degree of separation is noticed between the viable and gamma-deactivated spores.

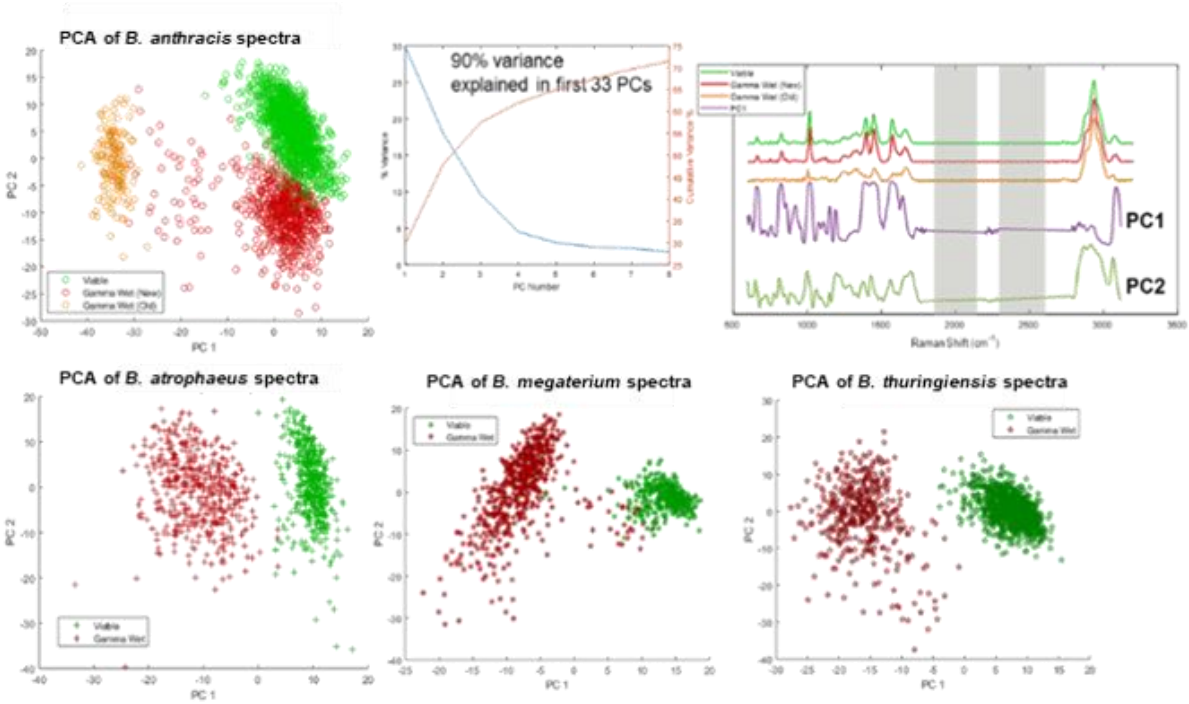


**Figure 15. PCA: viable versus gamma-deactivated spores in water suspension.**

### *4.4.5 UV-C radiation deactivation of dried spores*

The four species of spores were UV-C radiation deactivated using the method described in the experimentation section in dried residue form. Over 400 single spore spectra from Raman images of each of the four spore species were extracted using the method described in Section 4.3. Figure 16 shows the individual spores' spectra in lighter green color (viable) and lighter pink color (UV-C radiation deactivated) along with the average spectra in darker color and thicker linewidth. SEM images of typical viable (in green border) and UV-C radiation deactivated spores (in pink border) is also shown (with SEM image of *B. thuringiensis* spores yet to be acquired). The features related to CaDPA are present in the UV-C deactivated samples. Additionally, the SEM image examination reveals no physical damage to the spores due to UV-C deactivation.

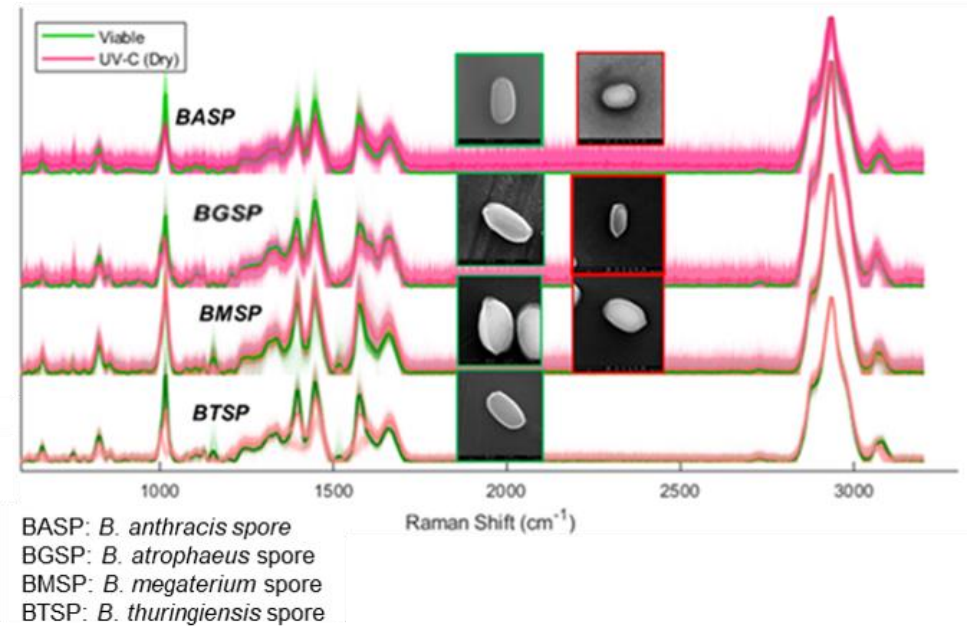


**Figure 16. Raman spectral comparison of viable and UV-C radiation deactivated spore samples in dried residue form.**

PCA was performed on the collected viable and UV-C radiation deactivated spore spectral data in the fingerprint (600–1800 $cm^{-1}$), C≡C band (2200–2290 $cm^{-1}$) and C–H band (2790–3120 $cm^{-1}$) regions. Figure 17 shows the results of the PCA for the four spores. The scores of the principal components 1 and 2 for the viable spores (green) and UV-C radiation deactivated spores (pink) are shown in the top left panel of Figure 17 (for *B. anthracis* spores) and bottom three panels (for *B. atrophaeus*, *B. megaterium*, and *B. thuringiensis* spores). The top middle panel shows the scree of *B. anthracis* spores with 90 % variance explained by the first 48 principal components. The top right panel shows the first principal component loading plot (orange) in comparison to average viable (green) and UV-C radiation deactivated (pink) *B. anthracis* spores spectra. The dual clustering in the case of *B. thuringiensis* spores was due to presence of intact and damaged spores in the original viable sample. The damaged spore show an absence of CaDPA features; whereas intact spores retained the CaDPA features. Nonetheless, a good degree of separation is noticed between the viable and UV-C radiation deactivated spores.

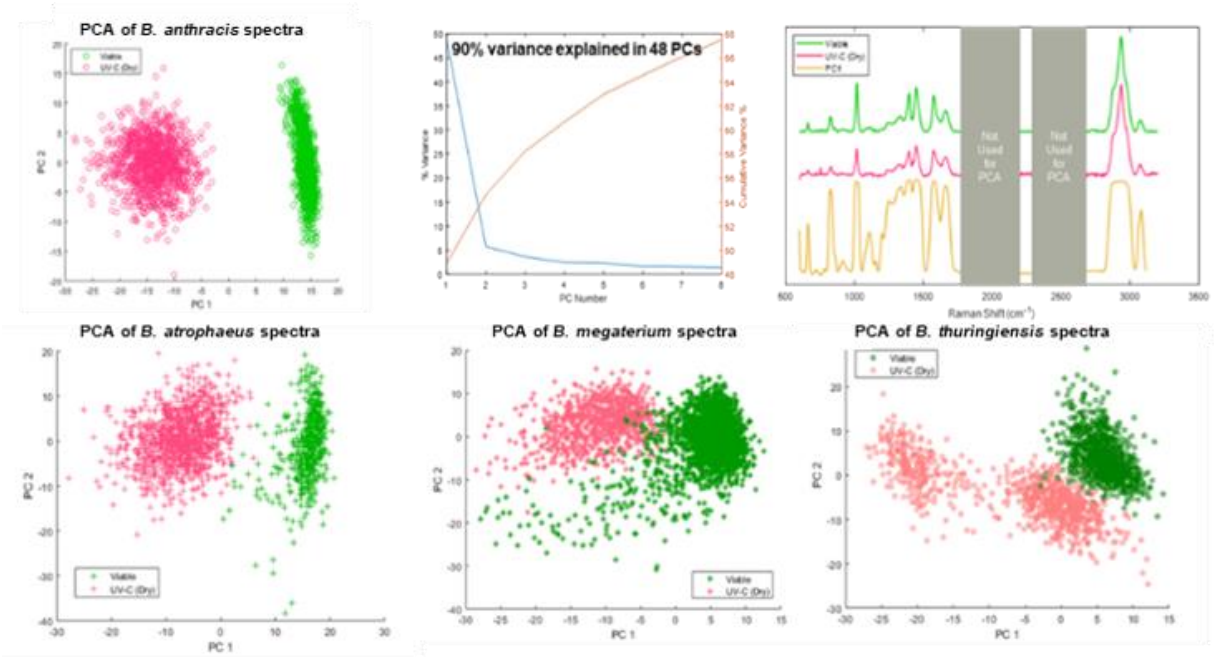


**Figure 17. PCA: viable versus UV-C radiation deactivated dried spores.**

### *4.4.6 Bleach deactivation of spores*

The four species of spores were bleach-deactivated by using the method described in the experimentation section. Over 400 single spore spectra from Raman images of each of the four spore species were extracted using the method described in Section 4.3. Figure 18 shows the individual spores' spectra in lighter green color (viable) and lighter purple color (bleach-deactivated) along with the average spectra in darker color and thicker linewidth. SEM images of typical viable (in green border) and gamma-deactivated spores (in purple border) are also shown (with SEM image of *B. thuringiensis* spores yet to be acquired). The features related to CaDPA are absent in the bleach-deactivated samples. There appears to be a remarkable chemical change noted in the bleach-deactivated spore spectra—there is a distinct feature appearing at 2247 $cm^{-1}$ which corresponds to C≡C bond stretching and is absent in viable spore spectra. Additionally, the SEM image examination reveals physical damage to the spores due to bleach deactivation.

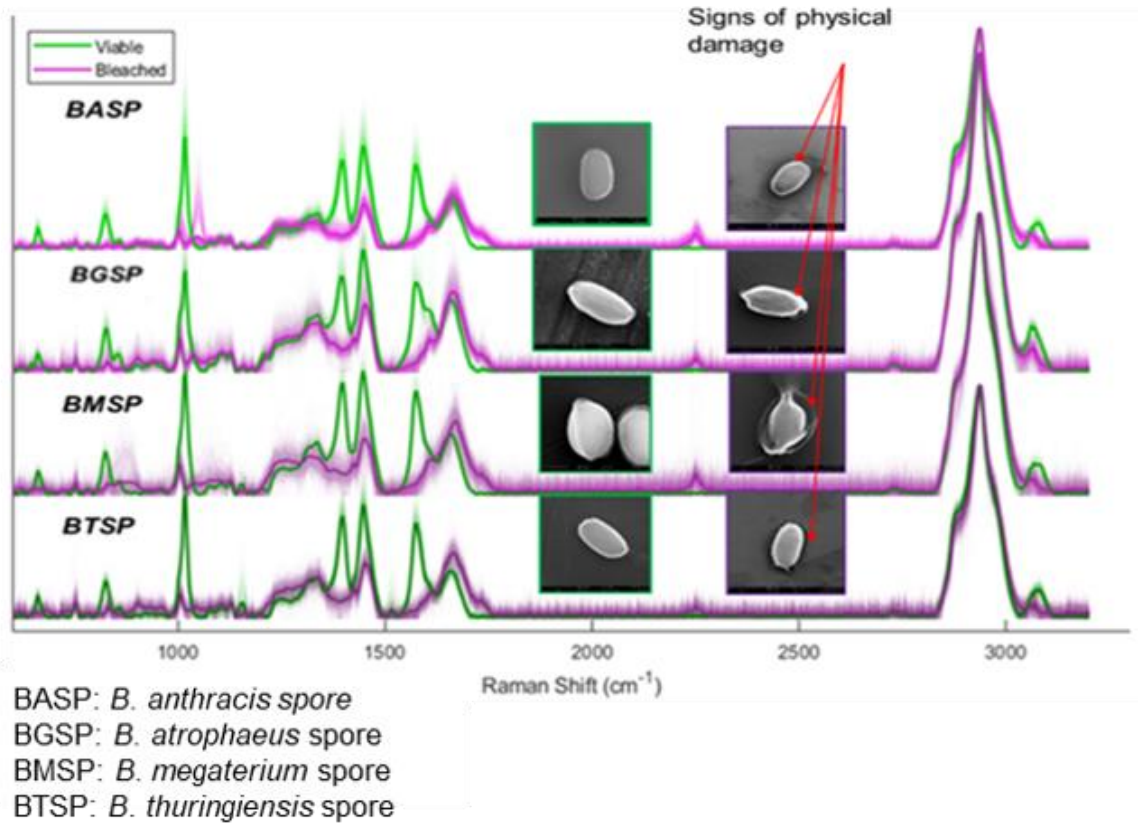


**Figure 18. Raman spectral comparison of viable and bleach-deactivated spore samples.**

PCA was performed on the collected viable and bleach-deactivated spore spectral data in the fingerprint (600–1800 $cm^{-1}$), C≡C band (2200–2290 $cm^{-1}$) and C–H band (2790–3120 $cm^{-1}$) regions. Figure 19 shows the results of the PCA for the four spores. The scores of the principal components 1 and 2 for the viable spores (green) and bleach-deactivated spores (purple) are shown in the top left panel of Figure 19 (for *B. anthracis* spores) and bottom three panels for *B. atrophaeus*, *B. megaterium*, and *B. thuringiensis* spores. The top middle panel shows the scree of *B. anthracis* spores with 90 % variance explained by the first 25 principal components. The top right panel shows the first principal component loading plot (orange) in comparison to average viable (green) and bleach-deactivated (purple) *B. anthracis* spore spectra. The deactivated spores show an absence of CaDPA features along with an appearance of C≡C features, resulting in a good degree of separation between the viable and bleach-deactivated spores.

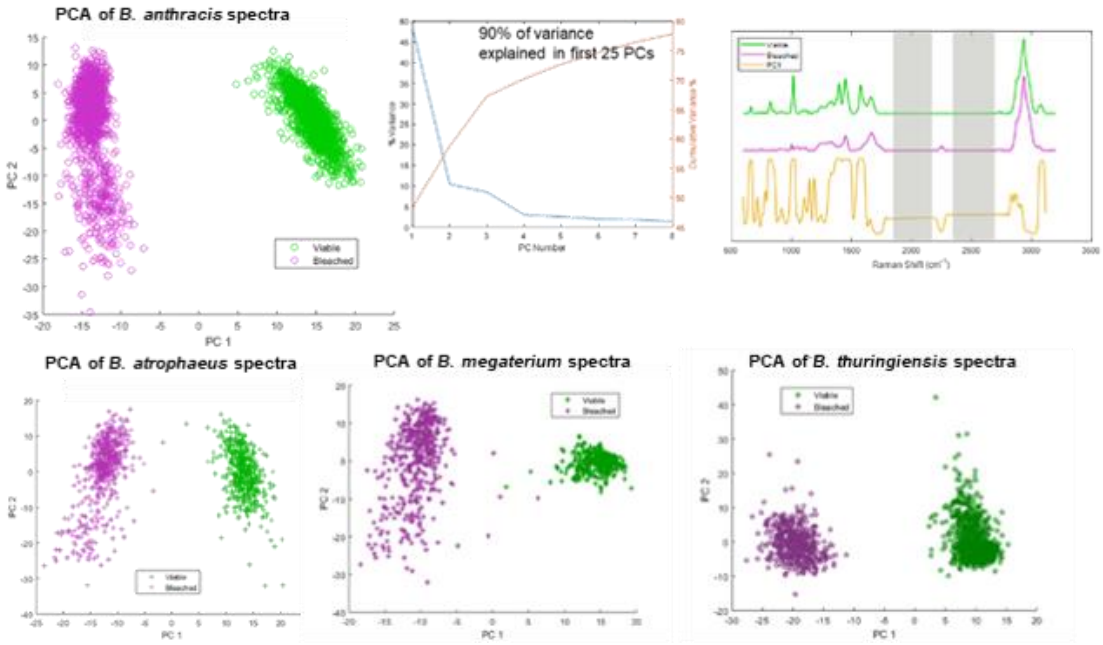


**Figure 19. PCA: viable versus bleach-deactivated spores.**

### *4.4.7 Glutaraldehyde deactivation of spores*

The four species of spores were glutaraldehyde deactivated by using the method described in the experimentation section. Over 400 single spore spectra from Raman images of each of the four spore species were extracted using the method described in Section 4.3. Figure 20 shows the individual spores' spectra in lighter green color (viable) and gray color (glutaraldehyde deactivated) along with the average spectra in darker color and thicker linewidth. SEM glutaraldehyde deactivated spores were not available at the time of writing this report, due to instrument malfunction. The features related to CaDPA are present in the glutaraldehyde deactivated samples except in the case of *B. thuringiensis* spores. The SEM imaging should determine the physical integrity of these spores when available. There appears to be a remarkable chemical change noted in the glutaraldehyde deactivated spore spectra—there is a distinct feature appearing at 1730 $cm^{-1}$—further analysis is needed to attribute this spectral change.

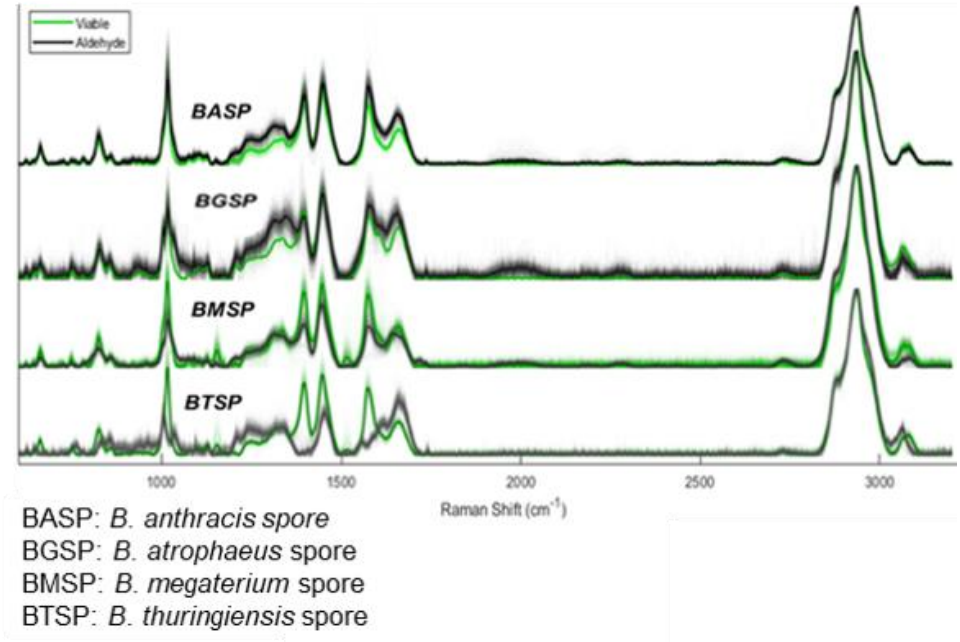


**Figure 20. Raman spectral comparison of viable and glutaraldehyde deactivated spore samples.**

PCA was performed on the collected viable and glutaraldehyde deactivated spore spectral data in the fingerprint (600–1800 $cm^{-1}$), C≡C band (2200–2290 $cm^{-1}$) and C–H band (2790–3120 $cm^{-1}$) regions. Figure 21 shows the results of the PCA for the four spores. The scores of the principal components 1 and 2 for the viable spores (green) and glutaraldehyde deactivated spores (black) are shown in the top left panel of Figure 21 (for *B. anthracis* spores) and bottom three panels for *B. atrophaeus*, *B. megaterium*, and *B. thuringiensis* spores. The top middle panel shows the scree of *B. anthracis* spores with 90 % variance explained by the first 119 principal components. The top right panel shows the first principal component loading plot (orange) in comparison to average viable (green) and glutaraldehyde deactivated (black) *B. anthracis* spore spectra. These experimental results were acquired recently. A further analysis of the data will be forthcoming.

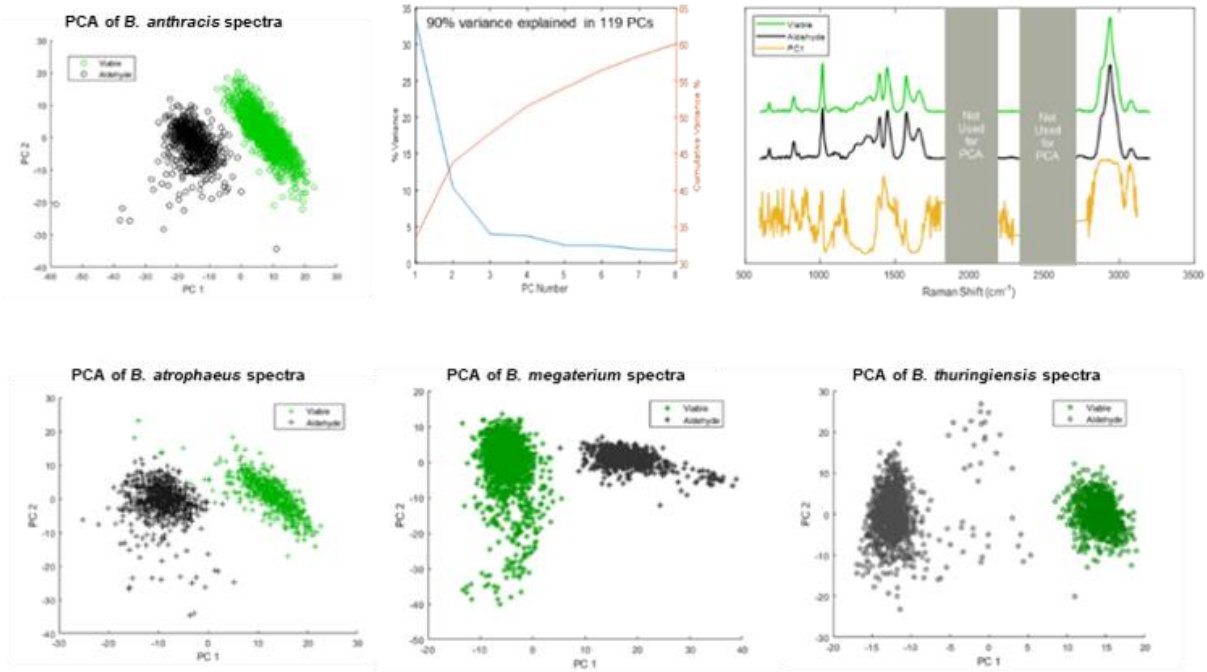


**Figure 21. PCA: viable versus glutaraldehyde deactivated spores.**

## 5. CONCLUSIONS

RISE microscopy is a useful tool in providing physiochemical understanding of the spore sample, both in viable and deactivated forms. The CaDPA related features tend to disappear in some of the deactivation methodology from spores due to physical damage caused to the spore structure. PCA of the viable and deactivated spore samples shows distinct clustering tendencies, indicating that RISE microscopy may be a good tool in discriminating between viable and deactivated spores. Multiple batches of spore samples need to be analyzed to determine the true effectiveness of this methodology as a discrimination tool between viable and deactivated spore samples.

## ACKNOWLEDGMENTS

Funding was provided by the U.S. Army via the In-house Laboratory Independent Research Program (PE 0601101A Project 91A) at the Combat Capabilities Development Command Chemical Biological Center. The authors wish to thank Ms. Rebecca Brown and Mr. Shawn Heinlein for performing the gamma radiation deactivation of spore samples, and Drs. Vipin K. Rastogi and Henry S. Gibbons for helpful discussions.

## REFERENCES


[1] ANSI/AMMI/ISO 11737-2:2009. Sterilization of medical devices – Microbiological methods, in Part 2: Tests of viability performed in the definition, validation and maintenance of a sterilization process. Association for the Advancement of Medical Instrumentation, Arlington, VA, 2014.

[2] Department of Defense. Review Committee Report: Inadvertant Shipment of Live Bacillus Anthracis Spores by DoD. Committee for Comprehensive Review of DoD Laboratory Procedures, Processes, and Protocols Associated with Inactivating Bacillus anthracis Spores. [Online], 13 July 2015, https://dod.defense.gov/Portals/1/features/2015/0615_lab-stats/Review-Committee-Report-Final.pdf.

[3] Rueckert, A.; Ronimus, R.S.; Morgan, H.W. Rapid differentiation and enumeration of the total, viable vegetative cell and spore content of thermophilic bacilli in milk powders with reference to Anoxybacillus flavithermus. *J. Appl. Microbiol*. **2005**, *99* (5), pp 1246–1255.

[4] Martinon, A.; Cronin, U.P.; Quealy, J.; Stapleton, A.; Wilkinson, M.G. Swab sample preparation and viable real-time PCR methodologies for the recovery of Escherichia coli, Staphylococcus aureus or Listeria monocytogenes from artificially contaminated food processing surfaces. *Food Control*. **2012**, *24* (1–2), pp 86–94.

[5] Murray, P.; Rosenthal, K.; Pfaller, M. *Medical Microbiology*, 8th ed; Elsevier Health Sciences: Philadelphia, PA, **2016**.

[6] Wilkinson, M.G. Flow cytometry as a potential method of measuring bacterial viability in probiotic products: A review. *Trends Food Sci. Technol*. **2018**, *78*, pp 1–10.

[7] D'Incecco, P.; Ong, L.; Gras, S.; Pellegrino, L. A fluorescence in situ staining method for investigating spores and vegetative cells of Clostridia by confocal laser scanning microscopy and structured illuminated microscopy. *Micron*. **2018**, *110*, pp 1–9.

[8] Firstencel, H.; Butt, T.M.; Carruthers, R.I. A fluorescence microscopy method for determining the viability of entomophthoralean fungal spores. *J. Invertebr. Pathol*. **1990**, *55* (2), pp 258–264.

[9] Green, L.C.; LeBlanc, P.J.; Didier, E.S. Discrimination between Viable and Dead Encephalitozoon cuniculi (Microsporidian) Spores by Dual Staining with Sytox Green and Calcofluor White M2R. *J. Clin. Microbiol*. **2000.** *38* (10), pp 3811–3814.

[10] Shafaat, H.S.; Ponce, A. Applications of a rapid endospore viability assay for monitoring UV inactivation and characterizing arctic ice cores. *Appl. Environ. Microbiol*. **2006**, *72* (10), pp 6808–6814.

[11] Yang, W.W.; Ponce, A. Rapid Endospore Viability Assay of Clostridium sporogenes spores. *Int. J. Food Microbiol*. **2009**, *133* (3), pp 213–216.

[12] Kalasinsky, K.S.; Hadfield, T.; Shea, A.A.; Kalasinsky, V.F.; Nelson, M.P.; Neiss, J.; Drauch, A.J.; Vanni, G.S.; Treado, P.J. Raman Chemical Imaging Spectroscopy Reagentless Detection and Identification of Pathogens: Signature Development and Evaluation. *Anal. Chem*. **2007**, *79* (7), pp 2658–2673.

[13] Tripathi, A.; Jabbour, R.E.; Treado, P.J.; Neiss, J.H.; Nelson, M.P.; Jensen, J.L.; Snyder, A.P. Waterborne Pathogen Detection Using Raman Spectroscopy. *Appl. Spectrosc*. **2008**, *62* (1), pp 1–9.

[14] Tripathi, A.; Jabbour, R.E.; Guicheteau, J.A.; Christesen, S.D.; Emge, D.K.; Fountain III, A.W.; Bottiger, J.R.; Emmons, E.D.; Synder, A.P. Bioaerosol Analysis with Raman Chemical Imaging Microspectroscopy. A*nal. Chem*. **2009**, *81* (16), pp 6981–6990.

[15] Cheng, H-W.; Chen, Y-Y.; Lin, X-X.; Huan, S-Y.; Wu, H-L.; Shen, G-L.; Yu, R-Q. Surface-enhanced Raman spectroscopic detection of Bacillus subtilis spores using gold nanoparticle based substrates. *Anal. Chim. Acta*. **2011,** *707* (1), pp 155–163.

[16] Jarvis, R.M.; Brooker, A.; Goodacre, R. Surface-enhanced Raman scattering for the rapid discrimination of bacteria. *Faraday Discuss*. **2006**, *132*, pp 281–292.

[17] Guicheteau, J.; Argue, L.; Emge, D.; Hyre, A.; Jacobson, M; Christesen, S. Bacillus Spore Classification via Surface-Enhanced Raman Spectroscopy and Principal Component Analysis. *Appl. Spectrosc*. **2008**, *62* (3), pp 267–272.

[18] Zhang, P.; Kong, L.; Setlow, P.; Li, Y.Q. Characterization of Wet-Heat Inactivation of Single Spores of Bacillus Species by Dual-Trap Raman Spectroscopy and Elastic Light Scattering. *Appl. Environ. Microbiol*. **2010**, *76* (6), pp 1796–1805.

[19] Wang, S.; Doona, C.J.; Setlow, P.; Li, Y.Q. Use of Raman Spectroscopy and Phase-Contrast Microscopy To Characterize Cold Atmospheric Plasma Inactivation of Individual Bacterial Spores. *Appl. Environ. Microbiol*. **2016**, *82* (19), pp 5775–5784.

[20] Kammrath, B.W.; Koutrakos, A.; Castillo, J.; Langley, C.; Huck-Jones, D. Morphologically-directed Raman spectroscopy for forensic soil analysis. *Forensic Sci. Int.* **2018**, 285, pp e25–e33.

[21] Tripathi, A.; Emmons, E.D.; Wilcox, P.G.; Guicheteau, J.A.; Emge, D.K.; Christesen, S.D.; Fountain III, A.W. Semi-Automated Detection of Trace Explosives in Fingerprints on Strongly Interfering Surfaces with Raman Chemical Imaging. *Appl. Spectrosc*. **2011**, *65* (6), pp 611–619.
[22] Carpenter, A.E.; Jones, T.R.; Lamprecht, M.R.; Clarke, C.; Kang, I.H.; Friman, O.; Guertin, D.A.; Chang, J.H.; Lindquist, R.A.; Moffat, J.; Golland, P.; Sabatini, D.M. CellProfiler: image analysis software for identifying and quantifying cell phenotypes. *Genome Biol.* **2006**, *7* (10), pp R100.1–R100.11.
[23] Schindelin, J.; Ignacio, A.C.; Frise, E.; Kaynig, V.; Longair, M.; Pietzsch, T.; Preibisch, S.; Rueden,S.; Saalfeld, S.; Schmid, B.; Tinevez, J.Y.; White, D.J.; Hartenstein, V.; Eliceiri, K.; Tomancak, P.; Cardona, A. Fiji: an open-source platform for biological-image analysis. *Nat. Methods*. **2012**, *9*, pp 676–682.
[24] Fatichah, C.; Purwitasari, D.; Hariadi, V.; Effendy, F. Overlapping white blood cell segmentation and counting on microscopic blood cell images. *Int. J. Smart Sens. Intell. Syst*. **2014**, *7* (3), pp 1271–1286.
[25] Jiang, K.; Liao, Q.-M.; Dai, S-Y. A novel white blood cell segmentation scheme using scale-space filtering and watershed clustering. In *Proceedings of the 2003 International Conference on Machine Learning and Cybernetics*. 2–5 November 2003; Institute of Electrical and Electronics Engineers, Inc.: Danvers, M.A., 2003; *5*, pp 2820–2825.
[26] Fang, Y.; Chongxun, Z.; Chen, P.; Li, L. White blood cell image segmentation using on-line trained neural network. *Presented at the 27th Annual International Conference of the IEEE Engineering in Medicine and Biology*, Shanghai, China, 3 Jan 2005.
[27] Buggenthin, F.; Marr, C.; Schwarzfischer, M.; Hoppe, P.; Hilsenbeck, O.; Schroeder, T.; Theis, F.J. An automatic method for robust and fast cell detection in bright field images from high-throughput microscopy. *BMC Bioinf.* **2013**, *14*, pp 1–12.
[28] Simon, I.; Pound, C.R.; Partin, A.W.; Clemens, J.Q.; Christens-Barry, W.A. Automated image analysis system for detecting boundaries of live prostate cancer cells. *Cytometry*, **1998**, *31* (4), pp 287–294.
[29] Malpica, N.; de Solórzano, C.O.; Vaquero, J.J.; Santos, A.; Vallcorba, I.; García-Sagredo, J.M.; del Pozo, F. Applying watershed algorithms to the segmentation of clustered nuclei. *Cytometry*. **1997**, *28* (4), pp 289–297.
[30] Jung, C.; Kim, C.; Chae, S.; Oh, S. Unsupervised segmentation of overlapped nuclei using bayesian classification. *IEEE Transactions on Biomedical Engineering*. **2010**, *57* (12), pp 2825–2832.
[31] Tscherepanow, M.; Zöllner, F.; Hillebrand, M.; Kummert, F. Automatic segmentation of unstained living cells in bright-field microscope images. In *Advances in Mass Data Analysis of Images and Signals in Medicine, Biotechnology, Chemistry, and Food Industry*: Third International Conference, MDA 2008, Leipzig, Germany, 14 July 2008; Perner, P., Salvetti, O. Eds.; Springer: Berlin, 2008; pp 158–172.
[32] Jones, C.L.; Lonergan, G.T.; Mainwaring, D.E. The use of image analysis for spore counts of white-rot fungi. *Biotechnol. Tech*. **1992**, *6* (5), pp 417–422.
[33] Korsnes, R.; Westrum, K.; Fløistad, E.; Klingen, I. Computer-assisted image processing to detect spores from the fungus pandora neoaphidis. *MethodsX*. **2016**, *3*, pp 231–241.
[34] Oh, K.; Chen, Y.; Matsuoka, H.; Yamamoto, A.; Kurata, H. Morphological recognition of fungal spore germination by a computer-aided image analysis and its application to antifungal activity evaluation. *J. Biotechnol*. **1996**, *45* (1), pp 71–79.
[35] Perner, P.; Jänichen, S.; Perner, H. Case-based object recognition for airborne fungi recognition. *Artificial Intelligence in Medicine*. **2006**, *36* (2), pp 137–157.
[36] Xu, P.; Li, J. Computer assistance image processing spores counting. Presented at the 2009 International Asia Conference on Informatics in Control, Automation and Robotics, Bangkok, Thailand, 1–2 February 2009.
[37] Wagner, J.; Macher, J. Automated spore measurements using microscopy, image analysis, and peak recognition of near-monodisperse aerosols. *Aerosol Sci. Technol*. **2012**, *46* (8), pp 862–873.
[38] Nasr-Isfahani, S.; Mirsafian, A.; Masoudi-Nejad, A. A new approach for touching cells segmentation. In *Proceedings of the First International Conference on BioMedical Engineering and Informatics (BMEI 2008), Volume I*, Sanya, China, 27–30 May 2008; Peng, Y., Zhang, Y., Eds.; the IEEE Computer Society: Los Alamitos, CA, 2008; pp 816–820.
[39] Bengtsson, E.; Wählby, C.; Lindblad, J. Robust cell image segmentation methods. *Pattern Recognition and Image Analysis*. **2004**, *14* (2), pp 157–167.
[40] Meijering, E. Cell segmentation: 50 years down the road. *IEEE Signal Processing Magazine*. **2012**, *29* (5), pp 140–145.
[41] Beucher, S.; Meyer, F. The morphological approach of segmentation: the watershed transformation. In *Mathematical Morphology in Image Processing, 1st Edition*; Dougherty, E.R., Ed.; Optical Engineering Series; Marcel Dekker, Inc.:New York, 1993; 34, pp 433–4.81.

# Deep learning for the prediction of experimental spectra

Patrick C. Riley[a]*, Samir V. Deshpande[b], Brian S. Ince[a], Brian C. Hauck[b]
[a]U.S. Army Combat Capabilities Development Command Chemical Biological Center, Research & Technology Directorate, 8198 Blackhawk Rd, Aberdeen Proving Ground, MD 21010
[b]Science & Technology Corporation, 21 Enterprise Pkwy, Suite 150, Hampton, VA 23666

## ABSTRACT

A supervised deep neural network model's training data set directly impacts its generalization to other similar devices. Often, a large sum of data must be collected at great expense and time to achieve a deep neural network to classify or approximate a given training data set. A mature chemical detection technology—such as the ion-mobility spectrometry-based Joint Chemical Agent Detector—has an existing large data set from the development of alarm algorithms intended to alert soldiers to the presence of hazardous chemicals. Alarm algorithms require that instruments and environmental impacts to peak behavior are captured such that the detectors alarm as intended when used in complex operating environments. Here, the design of a theoretical long short-term memory framework is presented that considers both instrument parameters and molecular properties to simulate the chemistry of an ion mobility spectrometry technology for which it was trained and to predict experimental spectra. This network, by accounting for these sources of variance traditionally measured in laboratories, can simulate additional data—reducing the cost and time needed to develop alarm algorithms for ion-mobility spectrometry-based detectors or provide a method for reducing cost in the development of future chemical detection technologies.

**Keywords:** deep neural network, machine learning, ion-mobility spectrometry, false alarm reduction

## 1. INTRODUCTION

Ion-mobility spectrometry (IMS)-based chemical detectors are frequently used for the detection of explosives, toxic industrial compounds, narcotics, and chemical warfare agents. These detectors utilize hard-coded alarm windows to provide presumptive identification of chemical vapors. These windows require the collection of large quantities of data across multiple chemical detectors at multiple conditions. By capturing the variance in peak position that occurs due to instrument properties or environmental conditions, a boundary space can be empirically determined, as shown in Figure 1. When a peak appears in the boundary space the detector will alarm to a preset chemical compound. Increasingly, the design of these alarm windows grows more complex and expensive as new threats emerge. These algorithms need to be robust enough to prevent false alarms to interferents, yet sensitive enough to alarm to the incredibly small doses that prove lethal.

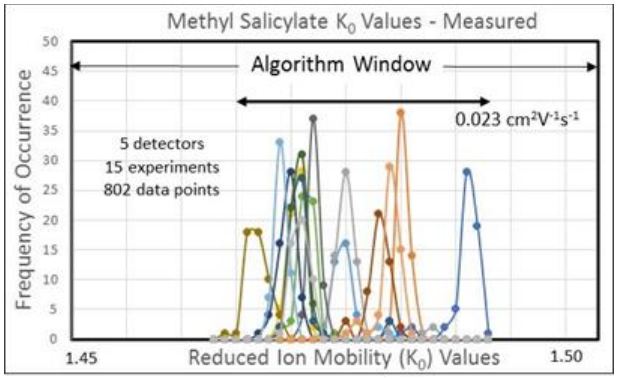


**Figure 1. Variance in peak position of methyl salicylate across multiple detectors and conditions.**

Deep neural networks (DNN) present a unique opportunity to improve upon the current hard-coded alarm windows method, by classifying spectra without the need for alarm windows. DNNs are a technique in machine learning (ML) that transform inputs through a series of nodes, called hidden layers, by applying a weight and an activation function.

The performance of a DNN is directly impacted by the total available data, and the development of IMS alarm windows has left a great deal of data to design DNNs. While DNNs can certainly decrease false alarm rates, expensive and lengthy laboratory testing must still be performed to add additional chemicals to train a DNN model.

One chemical detection technology often deployed for use in handheld design is IMS—a technology easily shrunk to handheld size, has a rapid response, and is highly sensitive.[1] While IMS is highly sensitive, it lacks selectivity and will often false alarm to interferent chemicals.[2] IMS alarm algorithms function by calculating the reduced mobility ($K_0$) value of ions in the detector and comparing this to "detection windows"—a range of $K_0$ values where the ion of a chemical has previously been measured to appear.

To calculate the $K_0$, IMS detectors function by measuring the time it takes for ions to travel a discreet path within an electric field and a carrier gas. This discreet path in the instrument is referred to as the drift region and the time it takes for ions to travel in the drift region is referred to as the drift time ($t_d$). The $K_0$ value of the ions is calculated from the $t_d$ of the ion, the path length of the drift region ($L$), and the applied voltage ($V$), temperature ($T$), and pressure ($P$) of the drift gas, as shown in

$$K_0 = \frac{L^2}{V t_d}\left(\frac{273.15}{T}\right)\left(\frac{P}{760}\right). \quad (1)$$

To improve the false alarm rate of IMS-based chemical detectors, a variety of techniques are employed such as calibration or modeling. In calibration, highly accurate measurements of $K_0$ values are used to shrink and move detection windows when it is provided with a chemical compound with a well-documented and accurate $K_0$.[3,4] Modeling attempts to account for environmental conditions, instrument parameters, and molecular properties to improve the predictive nature of the alarm algorithms. One challenge of utilizing these techniques is the inherent non-linear behavior between the various instrument parameters being measured. Selecting or measuring key values over others may introduce a bias into the model or reduce predictive capability when a key value is left out of the model.

One technique to minimize bias in a model is to utilize DNNs—a sub-technique of ML. ML is a field of computational science that uses several techniques for modeling a data set to allow computers to "learn" and make predictions or classify inputs. DNNs are a type of ML algorithm that uses a series of computations structured as interconnected nodes or "neurons" to model non-linear data. The network is formed by using data transform functions, called the activation function, in multiple hidden layers to determine the neurons that are passed from the input to the output layer. Research has shown that, when utilizing multiple hidden layers during backpropagation, the network is impeccable at removing this feature bias.[5] Backpropagation is where a DNN iteratively reweights features while attempting to reach a point where it is able to accurately predict from a training data set. Therefore, designing a DNN for predicting or classifying IMS spectra could improve false alarm rates.

The use of ML for the prediction or classification of analytical spectra is common.[6–11] In one study split across two publications, a neural network (NN) was trained to predict the functional groups of analytes based on IMS spectra alone.[12,13] Another NN was trained with tandem ion-mobility spectrometry–mass spectrometry measurements to predict the IMS drift times of peptides and assist in protein identification.[6] More recent work has seen the development of a convolutional neural network (CNN) for classifying the collision cross section (CCS) of IMS ions, utilizing long short-term memory (LSTM) for making mass spectral substance detections.[8,9,11,15,16] CNN and LSTM are types of DNNs with differing approaches. CNN is often used in the classification of images and LSTM in natural language prediction. While each of these studies present a novel method for accurately predicting or classifying chemical information from spectra, none have demonstrated a network that is generalizable to multiple detection technologies utilizing the same analytical technique.

The manufacturing techniques and rugged use of handheld chemical detectors ensures that variance exists from instrument to instrument. This partly contributes to the wide detection windows seen across these devices. To accurately predict spectra or classify spectra of these instruments, a data set that appropriately captures all this variance would be required. The exact source of variance from detector to detector has not been well documented. Therefore, if an ML model was designed to account for all potential instrument parameters and molecular properties that are the source of this variance, it could be hypothesized that the network is capable of simulating the chemistry of a detection technology, for which it is trained, to predict the experimental result. This work describes the design of a data input stream and resulting network performance for an LSTM based DNN for predicting experimental spectra for an IMS detector by accounting for instrument parameters and molecular properties. The findings of this work would direct the design of features for modeling spectral variance in highly variable handheld chemical or biological detection devices.

# 2. METHODS

## 2.1 Dataset

Two IMS training data sets were acquired. One from the accurate ion mobility instrument (AIMI) which is an IMS in a stacked-ring design capable of measuring the variables affecting $K_0$ values to ± 0.1 % accuracy.[3,4] AIMI was selected because it is considered the "gold standard" of IMS data and recent work by DeepMind Technologies (London, UK) used high quality "gold standard" optical coherence tomography image input data before the DNN model was applied to a second platform. Training the model using this "gold standard" data set is theorized to generalize the model to more accurately analyze lower quality and ambiguous optical coherence tomography scans during the testing phase.[14] Therefore, it is believed training the LSTM network on the "gold standard" in laboratory grade IMS would translate better prediction to lower grade handheld IMS detectors, such as the Joint Chemical Agent Detector (JCAD).

The second dataset was obtained from JCAD, which is an ambient air drift tube IMS used for the detection of chemical warfare agent vapors. The full JCAD dataset is large with many different chemicals collected at various conditions, across multiple detectors. However, the JCAD dataset provides less accurately measured environmental datapoints, and cannot be used to determine the CCS of a molecule that it detects. The JCAD data being collected using traditional means provides examples against which to test the performance of an LSTM based spectra prediction model.

All chemicals used for the training data set were obtained from Sigma-Aldrich®. Dimethyl methylphosphonate (DMMP), di-*tert*-butylpyridine (D*t*BP), and triethyl phosphate (TEPO) were obtained as 97 %, 97 %, and 99.8 % pure standards, respectively. Di(propylene glycol) monomethyl ether (DPM), was obtained as a 99 % pure standard consisting of a mixture of isomers. All training data was collected in the positive ion detection mode and a time-of-flight mass spectrometer (Ionwerks™, Inc.; Houston, TX) was used to mass identify all mobility peaks. Two different ionization sources were used for data collection—a $^{63}$Ni ionization source for DMMP and a corona ionization source for all other chemicals.

Table 1 provides the total spectra counts for both AIMI and the JCAD across the four chemicals and none. Data are labeled none when there is only reactant ion peak (RIP) and no other relevant peaks. From AIMI, a total of 111, 87, 83, 89, and 0 data points were collected for DMMP, DtBP, TEPO, DPM, and none respectively. The total data collected for the JCAD was 103,177, 54,568, 216,885, 26,199, and 230,258 for DMMP, DtBP, TEPO, DPM, and none, respectively. While background spectra are collected for AIMI, they are traditionally not collected in quantities useable for ML-related modeling. The low-throughput of highly accurate AIMI data means that fewer datapoints can be collected in comparison to the JCAD dataset.

**Table 1. Total spectra count for both AIMI and the JCAD across the four chemicals and none.**

| Chemical | Spectra Counts per IMS | |
|---|---|---|
| | AIMI | JCAD |
| DMMP | 117 | 103,177 |
| DtBP | 83 | 54,568 |
| TEPO | 89 | 216,885 |
| DPM | 87 | 26,199 |
| None | N/A | 230,258 |

## 2.2 Algorithm selection

Ions in an IMS separate based on the CCS, as larger molecules have an increased chance of collision with the drift gas and lower $K_0$ values. CCS is defined in

$$\Omega = \frac{3e}{16N}\left(\frac{2\pi}{\mu kT}\right)^{1/2}\left(\frac{1}{K}\right), \quad (2)$$

where $e$ is the elementary charge, $N$ is the drift gas number density, $\mu$ is the reduced mass of the ion-neutral pair, $k$ is Boltzmann's constant, $T$ is the neutral drift gas temperature, and $K$ is the mobility of the ion (not normalized against standard pressure and temperature).Considering equations (1) and (2), the resulting spectrum generated contains reduced mobility as the time-series component on the $x$-axis and total response reported as amplitude on the $y$-axis. To properly predict peak behavior this time, series behavior and gaussian distribution of the peak amplitudes must be considered. LSTM is a DNN algorithm that contains a memory component and is excellent at accounting for the time series behavior of datasets. In addition, IMS spectra are often reported once every five seconds. Figure 2 shows a basic LSTM cell composed of three hidden layers—called the forget gate, input gate, and output gate—where the forget gate

determines what components of the cell memory to keep, the input gate updates the cell memory, and finally, the output gate determines what information is passed to the subsequent layer. As opposed to traditional recurrent NNs, LSTM minimizes the issues associated with the vanishing gradient problem.

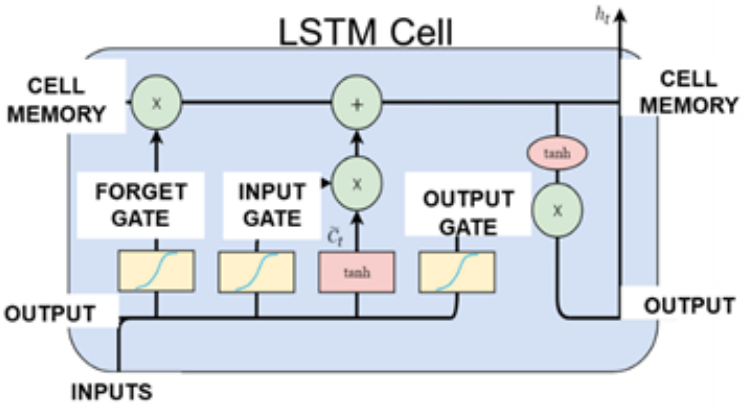


**Figure 2. Single LSTM cell.**

### 2.3 Modeling and data processing

All modeling and data processing were performed on a Lambda Labs Quad desktop equipped with Ubuntu 18.04 LTS operating system, Intel®Core™ i-9-9820X CPU, and two NVIDIA® GeForce® RTX 2080 Ti GPUs. The code was written in Python version 3.6, running in Jupyter Notebook 6.1.0. The software used for key data processing was NumPy 1.18.1 and pandas 1.0.5. Data modeling was performed using scikit-learn 0.23.1, TensorFlow 2.3.0, and Keras 2.4.3. Lastly, figure generation performed in the above software packages was done with Matplotlib 3.2.2 and seaborn 0.10.1.

### 2.4 Feature selection

A total of 32 features considered instrument parameters and molecular properties (IP/MP) (shown in Table 2) were initially selected for each chemical compound from the AIMI dataset. Features ending in _1, _2, or _3 represent a feature specific to the reactant ion peak, monomer peak, or dimer peak, respectively.

**Table 2. Feature set and corresponding correlation values. Blue highlighting represents features added to the model.**

| Feature (Feature#) | Positive Correlation Value | Feature (Feature#) | Negative Correlation Value |
|---|---|---|---|
| Molecular mass (amu)_3 | 9.96E-01 | $K_0$ ($cm^2v^{-1}s^{-1}$)_3 (10) | -9.74E-01 |
| Reduced mass w/air (g)_3 | 9.90E-01 | $K_0$ ($cm^2v^{-1}s^{-1}$)_2 (9) | -9.66E-01 |
| CCS_3 ($cm^2$) (11) | 9.70E-01 | Ion source | -8.00E-01 |
| Reduced mass w/air (g)_2 | 9.69E-01 | Ion mass protonated (amu)_3 | -7.81E-01 |
| Molecular mass (amu)_2 | 9.16E-01 | Dipole Moment (cm)_2 | -5.10E-01 |
| CCS_2 ($cm^2$) (8) | 8.71E-01 | Electric Field (V/cm) | -3.96E-01 |
| *P* (torr) | 8.12E-01 | Radius gas (cm) | -3.39E-01 |
| $t_d$ (G1-G2)_3 (s) | 8.01E-01 | CCS_1 ($cm^2$) (7) | -2.61E-01 |
| $t_d$ (G1-G2)_2 (s) | 7.64E-01 | Radius ion (cm)_1 | -2.41E-01 |
| Drift gas Number Density ($cm^{-3}$) | 6.56E-01 | [$H_2O$] (ppmv) | -1.54E-01 |
| $t_d$ (G1-G2)_1 (s) | 5.13E-01 | Dipole Moment (cm)_1 | -1.11E-16 |
| Ion mass protonated (amu)_2 | 5.05E-01 | Reduced mass w/air (g)_1 | -1.05E-16 |
| $K_0$ ($cm^2v^{-1}s^{-1}$)_1 (6) | 2.71E-01 | Molecular mass (amu)_1 | -4.18E-17 |
| Proton Affinity (kJ/mol)_2 | 2.20E-01 | | |
| Length (G1-G2) (cm) | 1.64E-01 | | |
| Drift gas *T* (K) | 1.14E-01 | | |
| Proton Affinity (kJ/mol)_1 | 1.11E-16 | | |
| Ion mass ammoniated (amu) | 1.05E-16 | | |
| Ion mass protonated (amu)_1 | 4.18E-17 | | |

These features can be separated into categories of molecular properties, instrument parameters, or a combination of both, as shown in Figure 3.

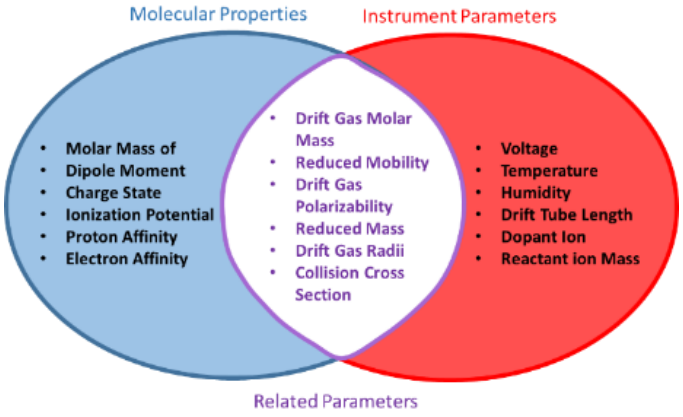


**Figure 3. Venn diagram depicting features assigned to molecular properties, instrument parameters, or both.**

Most data points were numerical in nature, and no feature engineering was performed before passing to any training models. Several features are considered "uncollected data points", or features that were not physically collected during testing or calculated from parameters determined during testing with the AIMI. One such data point—simplified molecular input line entry specification (SMILES), which uses the American Standard Code for Information Interchange characters to describe molecular structure—was added to the TensorFlow pipeline by converting it into a one-hot vector. To convert SMILES into a one-hot vector, each American Standard Code for Information Interchange character was assigned a numerical value, which was then represented by an array of vectors made of 0s and 1s. By designating a molecule in this manner, as opposed to a traditional one-hot vector, the structure represented by the SMILES is passed into the feature set.

Features of this dataset were downselected to prevent overfitting of the data and increase model run time. Features were assigned a binary predictor and a correlation matrix was generated to inform feature down-selection, as shown in Table 2. Several highly correlated features were determined to be sources of bias due to their discreet nature. For example, pressure *P* (torr) was considered an instrument parameter; but, as a feature, had two discreet values across the four chemicals collected. This occurred during data collection when DMMP was collected at high altitude and the other three compounds at sea level. Table 2 highlights key selected features in blue but adds the addition of SMILES, which is not listed in the table. A final correlation matrix of the selected features is shown in Figure 4.

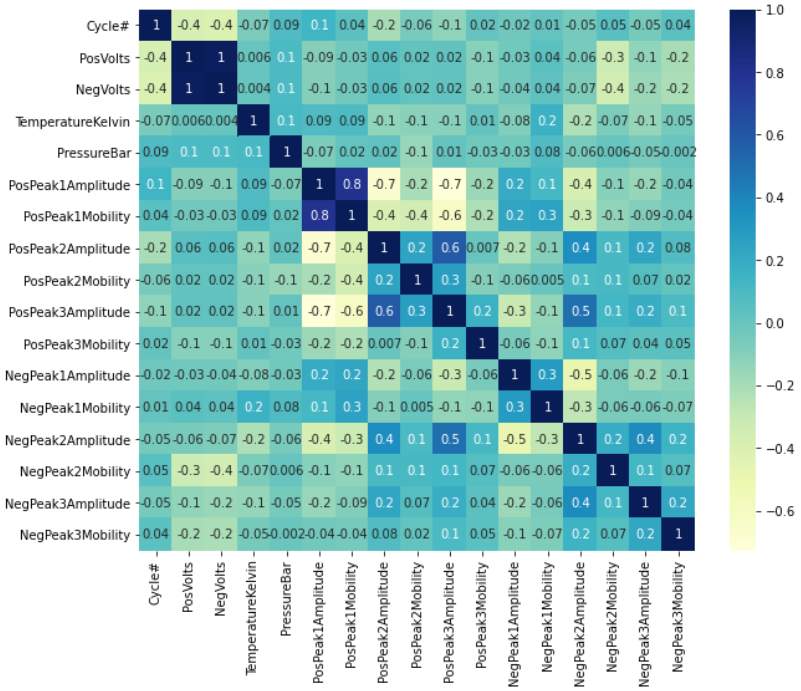


**Figure 4. Final correlation matrix of the selected features.**

As shown, many features were downselected and mobility and CCS were primarily kept. $K_0$ and CCS equations contain many of the variables expressly written as discreet values in Table 2. Therefore, by modeling initially on CCS and $K_0$, instrument parameters and molecular properties will be passed into the model, and training time will be reduced. The features for $K_0$, CCS, and SMILES were put into an LSTM network as described in Figure 5.

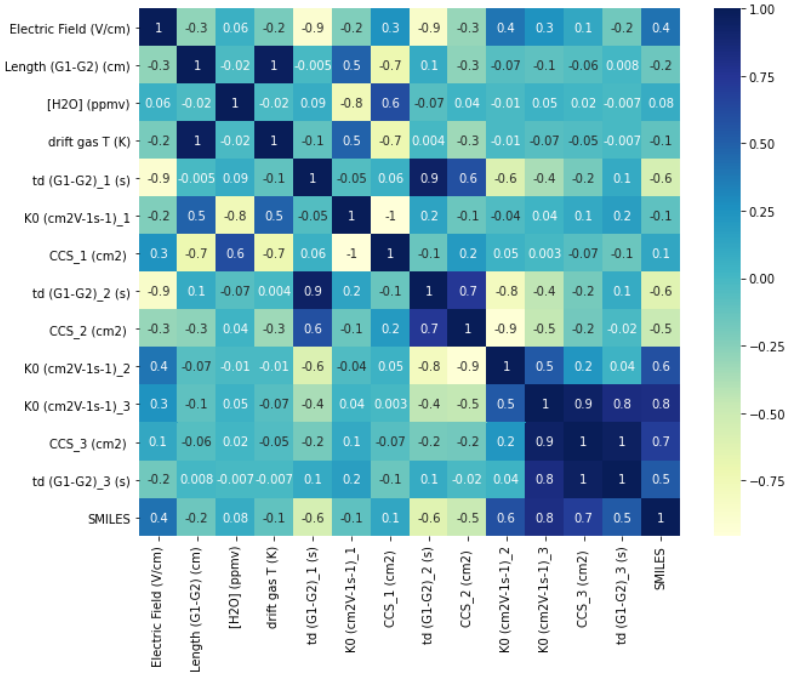


**Figure 5. Correlation matrix of selected AIMI features.**

Utilizing the features from the AIMI dataset, a number of similar IP/MP were selected as features from the JCAD dataset. The JCAD dataset does not contain as many features and are measured internally on each device. This means variance in the accuracy of the measurement could impact the predictive power of the model. In addition, latent heat from the operation of the instrument causes temperature to slowly rise during instrument operation. Figure 6 shows the impact of instrument operation on temperature, pressure, and both detection mode voltages.

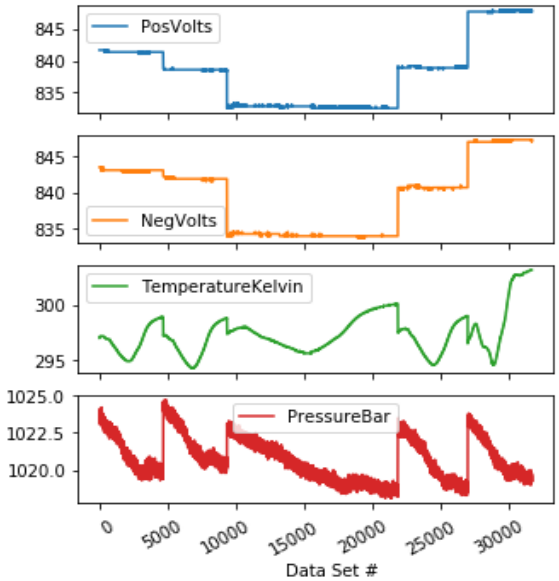


**Figure 6. Temperature, pressure, and voltage plotted as a time series. Showing drift in values over the course of several separate experiments. All training data was plotted at once, and separate experiments cause a sudden change in reported value.**

Large swings in the temperature, pressure, or voltage measurement are due to an instrument being shut down and powered on for a new test day. The final selected JCAD features are shown as part of a correlation matrix in Figure 4, where a feature containing the label Peak 1, Peak 2, or Peak 3 represents the top three largest peaks by amplitude in the detector.

Peak 1, Peak 2, and Peak 3 can be said to generally represent the RIP, monomer, and dimer, respectively. This is not always the case in JCAD data and is dependent upon the concentration of a chemical analyte. This introduces a sensitivity dependence on how a model may attribute these features to a particular chemical. For instance, high vapor pressure chemicals may more readily reduce the RIP amplitude below being labeled Peak 1. While this is useful in obtaining unique features for classification, this presents a challenge in drawing spectra where temperature impacts the vapor pressure of chemicals.

However, the AIMI dataset only contains 376 datapoints, while the JCAD dataset contains greater than 500,000 datapoints. This makes tuning hyperparameters to classify from IP/MP simple because of the larger number of datapoints. Due to the potential issues associated with lack of data, or poor features, a second feature set for each instrument was selected by extracting a whole spectra as a single datapoint consisting of 838 features, where each feature represented a drift-time bin taken from the IMS. Each bin reports a unitless measure of amplitude correlated to the concentration of ions at a particular time contacting the detector. This would expand the number of potential features to approximately 1,000 datapoints, where each spectrum was trimmed to only contain amplitudes reported from a $K_0$ 3.0 to a $K_0$ 0.5.

## 3. RESULTS

Initially the AIMI dataset was used to analyze the feature selection and tune hyperparameters for predicting spectra from the IP/MP feature set. Several classification methods were selected to assess the performance of the data. The three methods were random forest (RF), a dense feed-forward network (FFN), or multilayer perceptron (MLP), and a classification LSTM network. RF is excellent at assessing the strength of features, by analyzing feature importance. The MLP can be utilized to assess the classification strength of the dataset, and the impact of LSTM on potentially improving this. Table 3 shows an analysis of many types of decision trees and AdaBoost by predicting based on two features—this would demonstrate any underlying issues with the selected features. Decision trees categorize well and function more efficiently on less data than a FFN or LSTM model. Therefore, low score values would indicate an issue with the feature selection.

**Table 3. Decision tree and AdaBoost analysis displaying scores when classifying on two features.**

| Algorithm | # of Estimators | Feature 1 | Feature 2 | Scores |
|---|---|---|---|---|
| *DecisionTree* | N/A | 9 | 11 | 0.5844595 |
| *RandomForest* | 17 | 9 | 11 | 0.5810811 |
| *ExtraTrees* | 17 | 9 | 11 | 0.5844595 |
| *AdaBoost* | 17 | 9 | 11 | 0.4864865 |
| *DecisionTree* | N/A | 9 | 10 | 0.6486486 |
| *RandomForest* | 17 | 9 | 10 | 0.6520270 |
| *ExtraTrees* | 17 | 9 | 10 | 0.7195946 |
| *AdaBoost* | 17 | 9 | 10 | 0.4966216 |
| *DecisionTree* | N/A | 9 | 8 | 0.7972973 |
| *RandomForest* | 17 | 9 | 8 | 0.7972973 |
| *ExtraTrees* | 17 | 9 | 8 | 0.7972973 |
| *AdaBoost* | 17 | 9 | 8 | 0.5168919 |
| *DecisionTree* | N/A | 9 | 6 | 0.9898649 |
| *RandomForest* | 17 | 9 | 6 | 0.9864865 |
| *ExtraTrees* | 17 | 9 | 6 | 0.9898649 |
| *AdaBoost* | 17 | 9 | 6 | 0.6216216 |
| *DecisionTree* | N/A | 9 | 7 | 0.9797297 |
| *RandomForest* | 17 | 9 | 7 | 0.9628378 |
| *ExtraTrees* | 17 | 9 | 7 | 0.9831081 |
| *AdaBoost* | 17 | 9 | 7 | 0.5912162 |

The resulting analysis of decision trees demonstrates high scores for classification, indicating that features selected were appropriate for making predictions. An MLP was then trained utilizing all features simultaneously in a classification network. Table 4 shows the results from the MLP analysis, where the hyperparameters of epochs or backpropagations, batch size, type of output activation function, and number of hidden layers were tuned to increase accuracy. Changes in accuracy due to a difference in these variables would indicate how to tune the hyperparameters for the LSTM model. Lower accuracy, even with parameter modification, would indicate a lack of data.

**Table 4. TensorFlow FFN analysis depicting accuracy determined when classifying based on all features and manipulating network parameters, number of hidden layers, output activation function, batch size, and number of epochs.**

| # of Hidden Layers | Activation Function | Batch Size | #Epochs | Accuracy |
|---|---|---|---|---|
| *3, 1 output* | RELU, Output RELU | 5 | 5 | 0.2167 |
| | | 5 | 10 | 0.2167 |
| | | 5 | 50 | 0.2830 |
| | | 15 | 5 | 0.4667 |
| | | 15 | 10 | 0.4333 |
| | | 15 | 50 | 0.2833 |
| | | 30 | 5 | 0.1833 |
| | | 30 | 10 | 0.4167 |
| | | 30 | 50 | 0.1833 |
| *2, 1 output* | RELU, Output RELU | 5 | 5 | 0.4000 |
| | | 5 | 10 | 0.4000 |
| | | 5 | 50 | 0.1333 |
| | | 15 | 5 | 0.3167 |
| | | 15 | 10 | 0.5000 |
| | | 15 | 50 | 0.4333 |
| | | 30 | 5 | 0.3500 |
| | | 30 | 10 | 0.3167 |
| | | 30 | 50 | 0.1833 |
| *2, 1 output* | RELU, Output Sigmoid | 5 | 5 | 0.4833 |
| | | 5 | 10 | 0.4833 |
| | | 5 | 50 | 0.4833 |
| | | 15 | 5 | 0.5000 |
| | | 15 | 10 | 0.5000 |
| | | 15 | 50 | 0.5000 |
| | | 30 | 5 | 0.2667 |
| | | 30 | 10 | 0.5000 |
| | | 30 | 50 | 0.5000 |

Table 4 also shows that all reported accuracy was less than or equal to 0.5, indicating a lack of data. This is further demonstrated by the accuracy changes across batch size and outliers within the given data set. Since the final data set was split between training, testing, and validation at random, a small data set would show higher variance and lower accuracy when predicting. For instance, if a random selection of data took more data points for DMMP, this would decrease accuracy because there are fewer DMMP rows to predict correctly and less training data for the other chemicals to accurately predict.

Due to the lack of data in the AIMI dataset, the JCAD dataset was used to tune hyperparameters when classifying with the IP/MP feature set. The final hyperparameters did not differ per instrument, in addition, classification models were trained and hyperparameters optimized for classification from both the AIMI and JCAD datasets using spectra as the feature set. Table 5 shows the current hyperparameters determined for each model separated by instrument dataset for both IP/MP feature and spectra features. Table 5 shows the final scores for the RF, accuracy for the MLP, and the loss and accuracy for the LSTM classification models after hyperparameter tuning.

**Table 5. Classification accuracy of RF, MLP, and LSTM for each detector across two feature sets.**

| Classification Accuracy for DPM, DMMP, TEPO, DtBP, and None | | | | | |
|---|---|---|---|---|---|
| **Data Type** | **Instrument** | **Number of Data points (total, train/test)** | **RndForest (score)** | **MLP (train/val/test accuracy)** | **LSTM (loss,acc)** |
| Ins/Mol | AIMI | (370, 296/74) | 1.0000 | (0.3136,0.2500,0.3378) | (1.3321,0.4223) |
| Spectra | AIMI | (370, 296/74) | 0.99331 | (1.0000,1.0000,1.0000) | (0.0129,0.9967) |
| Ins/Mol | JCAD | (631087, 503903/127184) | 0.94352 | (0.6844,0.6824,0.6844) | (0.8160,0.6762) |
| Spectra | JCAD | (631087, 315543/315544) | 0.91054 | (0.8672,0.8561,0.8580) | (0.1589,0.9427) |

## 4. CONCLUSIONS

Several classification models were developed and tuned for high accuracy classification of two feature datasets. The results demonstrate that classifying from spectra, where the feature count is highest, provides the most accurate results for a LSTM based model. This shows that predicting spectra based upon IP/MP features alone does not provide enough predictive power for an LSTM model. Next steps will extract features from spectra to combine with IP/MP features to predict spectra given a SMILES.

## ACKNOWLEDGMENTS

Funding was provided by the U.S. Army via the In-house Laboratory Independent Research Program (PE0601101A Project 91A) at the Combat Capabilities Development Command Chemical Biological Center. The authors acknowledge Dr. Augustus W. Fountain, III and Dr. Patricia McDaniel for their technical guidance and mentorship as well as Dr. Mary M. Wade for her general supervision, editing, and support.

## REFERENCES

[1] Forbes, T.P.; Najarro, M. Ion mobility spectrometry nuisance alarm threshold analysis for illicit narcotics based on environmental background and a ROC-curve approach. *Analyst*. **2016**, *141* (14), pp 4438–4446.

[2] Eiceman, G.A.; Yuan-Feng, W.; Garcia-Gonzalez, L.; Harden, C.S.; Shoff, D.B. Enhanced selectivity in ion mobility spectrometry analysis of complex mixtures by alternate reagent gas chemistry. *Anal. Chim. Acta*. **1995**, *306* (1), pp 21–33.

[3] Hauck, B.C.; Siems, W.F.; Harden, C.S.; McHugh, V.M.; Hill, H.H., Jr., Construction and evaluation of a hermetically sealed accurate ion mobility instrument. *Int. J. Ion Mobility Spectrom.* **2017**, *20* (3–4), pp 57–66.

[4] Hauck, B.C.; Siems, W.F.; Harden, C.S.; McHugh, V.M.; Hill, H.H., Jr. High Accuracy Ion Mobility Spectrometry for Instrument Calibration. *Anal. Chem.* **2018**, *90* (7), pp 4578–4584.

[5] Hinton, G.E.; Salakhutdinov, R.R. Reducing the Dimensionality of Data with Neural Networks. *Science*. **2006**, *313* (5786), pp 504–507.

[6] Wang, B.; Valentine, S.; Plasencia, M.; Raghuraman, S.; Zhang, X. Artificial neural networks for the prediction of peptide drift time in ion mobility mass spectrometry. *BMC Bioinf.* **2010**, *11*, pp 1–11.

[7] Gastegger, M.; Behler, J.; Marquetand, P. Machine learning molecular dynamics for the simulation of infrared spectra. *Chem. Sci*. **2017**, *8* (10), pp 6924–6935.

[8] Liu, J.; Zhang, J.; Luo, Y.; Yang, S.; Wang, J.; Fu, Q. Mass Spectral Substance Detections Using Long Short-Term Memory Networks. *IEEE Access.* **2019**, *7*, pp 10734–10744.

[9] Plante, P.-L.; Francovic-Fontaine, É.; May, J.C.; McLean, J.A.; Baker, E.S.; Laviolette, F.; Marchand, M.; Corbeil, J. Predicting Ion Mobility Collision Cross-Sections Using a Deep Neural Network: DeepCCS. *Anal. Chem.* **2019**, *91* (8), pp 5191–5199.

[10] Riley, P.C.; Deshpande, S.V. Machine learning based spectral interpretation in chemical detection. *In Proceedings Volume 1106: Artificial Intelligence and Machine Learning for Multi-Domain Operations Applications*. SPIE Defense + Commercial Sensing. Baltimore, MD, 14–18 April 2019; Pham, T., Ed.; SPIE: Bellingham, WA, 2019; CID 11006-68.

[11] Kantz, E.D.; Tiwari, S.; Watrous, J.D.; Cheng, S.; Jain, M. Deep Neural Networks for Classification of LC-MS Spectral Peaks. *Anal. Chem.* **2019**, *91* (19), pp 12407–12413.

[12] Bell, S.; Nazarov, E.; Wang, Y.F.; Eiceman, G.A. Classification of ion mobility spectra by functional groups using neural networks. *Anal. Chim. Acta.* **1999**, *394* (2–3), pp 121–133.
[13] Bell, S.; Nazarov, E.; Wang, Y.F.; Rodriguez, J.E.; Eiceman, G.A. Neural Network Recognition of Chemical Class Information in Mobility Spectra Obtained at High Temperatures. *Anal. Chem.* **2000**, *72* (6), pp 1192–1198.
[14] De Fauw, J.; Ledsam, J.R.; Romera-Paredes, B.; Nikolov, S.; Tomasev, N.; Blackwell, S.; Askham, H.; Glorot, X.; O'Donoghue, B.; Visentin, D.; van den Driessche, G.; Lakshminarayanan, B.; Meyer, C.; Mackinder, F.; Bouton, S.; Ayoub, K.; Chopra, R.; King, D.; Karthikesalingam, A.; Hughes, C.O.; Raine, R.; Hughes, J.; Sim, D.A.; Egan, C.; Tufail, A.; Montogmery, H.; Hassabis, D.; Rees, G.; Back, T.; Khaw, P.T.; Suleyman, M.; Cornebise, J.; Keane, P.A.; Ronneberger, O. Clinically applicable deep learning for diagnosis and referral in retinal disease. *Nat. Med.* **2018**, *24* (9), pp 1342–1350.
[15] Rivera, E.S.; Jones, M.A.; Guiberson, E.R.; Norris, J.L. Fundamentals of Mass Spectrometry-Based Metabolomics. In Toxic Chemical and Biological Agents [Online]; Sindona G., Banoub J.H., Di Gioia M.L., Eds.; NATO Science for Peace and Security Series A: Chemistry and Biology; Springer: Dordrecht, 2020; pp 61–81. https://link.springer.com/chapter/10.1007/978-94-024-2041-8_4#citeas (accessed December 18 2020).
[16] Meier, F.; Köhler, N. D.; Brunner, A.-D.; Wanka, J.-M. H.; Voytik, E.; Strauss, M. T.; Theis, F. J.; Mann, M., Deep learning the collisional cross sections of the peptide universe from a million experimental values. *Nat. Commun.* **2021,** *12* (1), p 1185.

# Effect of quorum sensing molecules on the production of bacterial nanocellulose materials

Rabih E. Jabbour[a]*, Alex Balboa[a], Hany F. Sobhi[b], Erik D. Emmons[a], Ashish Tripathi[a]
[a]U.S. Army Combat Capabilities Development Command Chemical Biological Center, Research & Technology Directorate, 8198 Blackhawk Rd, Aberdeen Proving Ground, MD 21010
[b]Department of Chemistry and Biochemistry, Coppin State University, 2500 W North Ave, Baltimore, MD 21216

## ABSTRACT

Bacterial nanocellulose is produced by several bacterial species such as *Gluconacetobacter xylinus* and are promising multifunctional materials with unique physiochemical properties. The bacterial nanocellulose has been shown as a remarkably versatile nano-biomaterial with wide applications in medicine, defense, electronics, optics, and food. While advantageous in many ways, bacterial nanocellulose materials can be difficult to manufacture and process into useable forms, because bacterial nanocellulose pellicles are not uniform in their composition. This is often due to a heterogeneity of cell density which often leads to large clusters of dense cellular growth. The aim of this project is to study the mechanism of quorum sensing molecules—specifically, homoserine lactones—and their effect on the production of bacterial nanocellulose by utilizing a synthetic biology approach. We believe that the bacterial nanocellulose morphology can be controlled through manipulation of the quorum sensing pathways of the bacterium. We investigated the morphological parameters that are affected by the homoserine lactone molecules using different surface characterization techniques. The data showed that there is a direct correlation with the type of the quorum sensing molecules introduced during growth phase and the surface of the produced bacterial nanocellulose films. Morphological studies showed a direct impact of the homoserine lactone molecules and the thickness of the fiber, structure, and uniformity based on diffuse reflectance infrared Fourier transform spectroscopy, scanning electron microscope and atomic force microscopy data. These data will enhance our understanding and optimization of the quorum sensing molecules signals and expression levels to improve bacterial nanocellulose production and customization.

**Keywords:** bacterial nanocellulose, biofilm, mass spectrometry, diffuse reflectance infrared Fourier transform spectroscopy, scanning electron microscope, atomic force microscopy, quorum sensing, homoserine lactones

## 1. INTRODUCTION

Bacterial nanocellulose (BNC) is a unique biofilm with promising multifunctional properties, due to its desired chemical and physical properties which make it very useful in various applications including tissue engineering, medicine, defense, food, fabrics, and electronics. Nanocellulose can be obtained from two main sources—plant, in which the nanocellulose fibrils can be isolated, or bacteria, mainly from the *Gluconacetobacter xylinus* bacterial genus. However, the plant-based nanocellulose material is energetically costly and laborious to manufacture. Additionally, while the small rod-like structures can be used in the production of thin films and other materials, the physical properties of the materials are often reduced compared to that of the bacterial-based ones that have superior chemo-physical properties over the plant nanocellulose.

BNC is formed at the air-media interface of active *G. xylinus* cultures. BNC nanofibers are synthesized from glucose units by *Acetobacter* cellulose synthase operon proteins and secreted by forming an interconnected cellulose "pellicle" around cells.[1–3] BNC pellicles are comprised of long cellulose fibrils that intertwine with one another and are highly free from other chemical compounds (i.e., lignin and pectin). BNC films often demonstrate a higher strength and flexibility than plant-based ones.[4] BNC can also be easily modified and functionalized through genetic engineering and/or synthetic biology approaches.[5–11] However, BNC materials can be difficult to manufacture and process into useable forms due to bacterial growth conditions and changes in bacterial behavior during the production stage of the biofilm. In many instances, bacterial cellulose pellicles are not uniform in composition. This is often due to a

heterogeneity of cell density which often leads to large clusters of dense cellular growth. While methods have been developed to circumvent some of these BNC production challenges, abnormalities and irregularities in the pellicles are still encountered with no success in controlling fibril density, mechanical properties of the film, or rate of production.

Homoserine lactones (HSL) are vital quorum sensing (QS) molecules that enable bacterial cells to regulate growth and behavior of their community. HSLs consists of various acyl side chain of 4–14 carbon atoms and may also contain double bonds. The carbon chain of HSLs can be hydroxylated or oxidized to a carbonyl-carbon; thus, resulting in quite different physicochemical properties. HSLs are the most common QS signals in Gram-negative bacteria and coordinate important temporal events—more specifically, the formation of biofilms in nature and in humans.[12,13] Little is known about the correlation between the bacterial cellulose production, fibril density, pellicle thickness, and the expression of different HSL QS molecules. As such, we will address vital questions related to the proposed hypothesis, such as the kinetic impact of the QS signals of the HSL on the synthesis of the bacterial cellulose. The rate of the cellulose production is affected at specific time points in the presence or absence of QS molecules. The contribution of each QS molecule to the production of cellulose and its impact on its fibril density and pellicle thickness is being characterized.

Understanding the effect of HSL, as a signaling molecule, on the production mechanism of BNC is vital to aid in producing desired biofilms that can be utilized in various applications. To understand the effect of the signal molecules on the production of the BNC, we need to determine the surface characterization of the produced BNC after alteration of the type and amount of the HSL molecules. The surface characterization will provide the needed information to develop customized methods to produce specific BNC with specific desired properties. This research project will investigate the effect of adding different HSL signaling molecules to the bacterial growth media. Various concentrations of the HSL molecules were utilized and samples were collected at each experimental condition. Morphological analyses showed that different signaling molecules affected the structural uniformity of the BNC film. The cellulose fibril's thickness, structure, and distribution were also correlated to the type of the signaling molecules used during the growth phase. The results showed that there is a direct correlation between the utilized HSLs—acting as QS molecules—and the morphological properties of the produced BNC biofilms.

## 2. MATERIALS AND METHODS

### 2.1 Bacterial strains

The bacterial strain used to produce the nanocellulose was *G. xylinus*. The bacterial strain was obtained from ATCC® as *G. xylinus* strain 10245™ (Manassas, VA). The *G. xylinus* strain was cultured in Hestrin and Schramm medium (HS medium) with 2 % glucose (w/v). The stock bacterial culture was added to 10 mL of HS media in 50-mL conical tubes and was grown at 27 °C for 3–7 days, depending on the amount of biofilm formation. The growth was done under static culture in which no agitation of the culture broth was performed. Once the bacterial cellulose biofilm was formed, it was removed for further processing and characterization.

### 2.2 Cellulose production and purification

The bacterial cellulose was formed on average after 72 hours of growth time. The formation of bacterial cellulose occurred in static culture, in which cells were grown in 50-mL conical tubes containing 10 mL of HS medium at 27 °C for 3–7 days. The cellulose pellicles were then isolated and purified by treating them with 0.5 % NaOH at 100 °C for 1 hour, followed by extensive washing with Milli-Q® ultrapure water to remove the excess NaOH solution and reduce the pH. The pH of the pellicle was checked periodically during the water washing step and was maintained at 4–5. Following the water wash, the pellicles were dried out at 30 °C for 24 hours and then weighed on an analytical balance. The mass obtained was normalized to include the culture volume used to compare the pellicle's yield from the addition of different HSLs. Pellicles which were cleaned but not processed were kept in 0.1 M sodium azide solution.

### 2.3 Scanning electron microscopy measurement of BNC biofilm

The measurements were performed with a Thermo Scientific® Phenom™ Pharos desktop scanning electron microscope (SEM). Beam energies ranging from 5–15 keV were used to obtain the images shown. The samples were coated with ~30 nm of gold using a vacuum thermal evaporator system prior to the measurements to reduce charging and beam damage effects from the electron beam. The SEM is also equipped with energy dispersive spectroscopy (EDS) capability to allow for determination of the elemental content of the analyzed materials.

### 2.4 *In situ* diffuse reflectance infrared Fourier transform spectroscopy of BNC biofilm

Individual bio-synthesized cellulose samples were cut using stainless steel "fly-tying" scissors from a larger film to fit snuggly into ceramic cups (6.0 mm outer diameter, 4.0 mm height, 4.7 mm inner diameter, 2.0 mm depth). The cut samples were gently pressed into the ceramic cup with a sample loading tool. The cellulose film-containing ceramic cups were placed onto a macro diffuse reflectance infrared Fourier transform spectroscopy (DRIFTS) cell holder. The macro DRIFTS cell holder was then inserted in a Praying Mantis™ Diffuse Reflection Accessory (Harrick Scientific Products Inc.; Pleasantville, NY) located within the chamber compartment of a Thermo Scientific™ Nicolet™ Avatar 380 FTIR (Waltham, MA) outfitted with a mercury cadmium telluride Type A detector and potassium bromide beam splitter. The optics bench and accessory were purged using a Fourier-transform infrared (FTIR) Purge Gas Generator. Diamond dust (4,000 grit, annealed to 350 °C for 90 minutes) was used as baseline spectra for the Kubelka-Munk single beam spectral scans.

Background spectra were collected with 1,024 scans per spectrum. Sample data spectra were collected in the following manner: 128 scans were collected with a collection length of 346.40 seconds. Instrumental resolution was kept at 2000 $cm^{-1}$ with levels of zero filling kept at zero. For each scan, there were 33,056 points with 32,768 FFT points. HeNe laser frequency was 15798.25 $cm^{-1}$ (632.97 nm), and the interferogram peak position at 16384 $cm^{-1}$. Happ-Genzel anodization function and the Mertz phase correction were used for the FTIR signal processing. The data represents 3,475 points between 649.3 to 3999.84 $cm^{-1}$ with a spectral data spacing of 0.96 $cm^{-1}$. Optical velocity was held at 0.47 cm/s with an aperture of 100 %, sample gain of 2.0. The high-pass filter and low-pass filter were set to 20 Hz and 11,000 Hz, respectively.

### 2.5 Atomic force microscopy of BNC biofilm

A Nanotec Electronica scanning probe microscope (Madrid, Spain) was used to produce the atomic force microscopy (AFM) imaging for this project. The AFM instrument was kept at ambient conditions with relative humidity of 30 % using $N_2$ gas from liquid nitrogen boil-off into the chamber. The WSxM software (version 12.4) was used to process the AFM images. Aluminum-coated silicon cantilevers (AC240TS, Asylum Research; Santa Barbara, CA) with a nominal tip radius of 10 nm or less were used. A nominal spring constant of 2 N/m and nominal resonance frequency of 70 KHz were used.

The amplitude-modulated AFM was used to acquire topography imaging of various BNC samples. The amplitude set point of 90 % of $A_o$ was used at a free cantilever amplitude of 99 nm. Each BNC sample was put on an AFM holder by using carbon tape and was taken in semi-contact mode using a silicon cantilever. The BNC sample height can be determined unambiguously from the height of the crystal surface above the mica surface. The height can be used to determine the cellulose diameter and estimate its width.

## 3. RESULTS AND DISCUSSION

### 3.1 Effect of HSL molecules on the morphology of the BNC biofilm

Three different HSL molecules were added to the growth media of *G. xylinus* and the produced BNC biofilms from each growth condition were collected and processed for morphological analysis using SEM technique. SEM provides useful morphological information about the potential 2D-spatial variation due to the presence of different HSLs in the growth media of *G. xylinus*. The SEM analysis was focused on determining any potential changes of the BNC fiber in terms of its diameter and distribution after the addition of the HSL signaling molecules. The diameter of the nanofibers was measured by the software program, Fibermetric®, interfaced to a bench-top SEM. We acquired the SEM images for pellicles from different growth conditions. The SEM data were collected between 5–15 keV and 50–200 nm resolution. Six different pellicle samples were analyzed in which three of them had HSL signaling molecules and three were control samples with no HSL signaling molecule. Figure 1 shows a comparison between the control-BNC and the N-dodecanoyl-L-homoserine lactone (DDHL)-BNC fibers. There is variability in the structure and diameter size for the pellicles when comparing the control to the HSLs modified fibers. In Figure 1a. the cellulose from the control samples were more uniformly distributed as compared to that of the DDHL-BNC fibers, shown in Figure 1b. Moreover, in the DDHL-BNC sample, the resulting fibrils were not well formed and showed structural deformity in the fibrils that could be the result of the DDHL molecules disrupting the formation mechanism of the cellulose fibrils. Overall, the DDHL-BNC fibrils showed high non-uniformity cellulose fibers and high porosity as compared to that of the control-BNC samples. Investigating the in-depth projections of these BNC fibrils showed that

the DDHL-BNC fibrils had more layers than that of the control-BNC samples, and within the same layer, the width of the fiber diameter has more variation in the DDHL-BNC sample. These SEM data are important in terms of utilizing such BNC fibrils in applications that require high porosity such as filtration and sample extraction. It is noteworthy that the DDHL-fibrils have less water capacity than the control-BNC ones. This observation was noticed during sample processing, in which each sample was weighed wet and dry to determine its respective water-holding capacity. Measurements of the average diameter of the BNC fibers for the control-BNC and DDHL-BNC samples were determined using the SEM analysis software. These measurements showed that the average diameter of the DDHL-BNC (143 nm) sample was greater than that of the control-BNC (129 nm) sample.

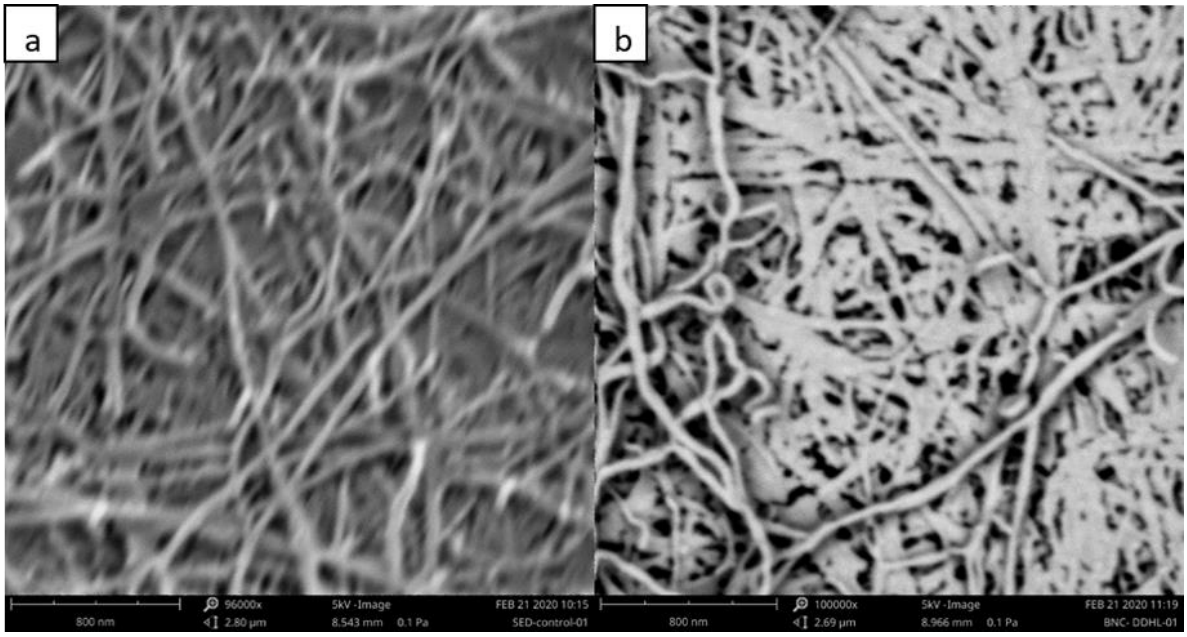


**Figure 1. SEM images of the control-BNC sample (a) and of the DDHL-BNC sample (b). The SEM images were acquired at 5 keV and resolutions of 100 kX magnification in secondary electron dispersion mode.**

The comparison between the control-BNC and the N-(3-Oxododecanoyl)-L-homoserine lactone (ODDHL)-BNC fibers are shown in Figure 2. There is variability in the structure and diameter size for the pellicles when comparing the control to the ODDHL-BNC fibers. In Figure 2a, the cellulose fibrils from the control samples were less uniformly distributed as compared to those of the ODDHL-BNC fibers, shown in Figure 2b. The ODDHL-BNC SEM image in Figure 2b shows that the fibrils are well formed and tightly packed with high density of BNC fibers in the field of view as compared to that of the control-BNC SEM image. The ODDHL-BNC image shows well-formed cellulose fibrils with less structural deformity when compared with the DDHL-BNC shown in Figure 2b. The ODDHL-BNC fibrils showed less porosity and higher fiber density as compared to those of the control-BNC or the DDHL samples. Investigating the in-depth projections of these BNC fibrils layers showed that the ODDHL-BNC fibrils are distributed in close-packed layers when compared to the control-BNC fibrils, which have more spatial separation on the *y*-axis projection and with significant difference in density of fibrils as shown in Figure 2a. The SEM data are important in terms of utilizing such ODDHL-BNC fibrils in applications that require high fibril density, more uniformity, and less porosity—such as electronic display circuitry and sensing applications. The water capacity of the ODDHL-fibrils was greater than of the control-BNC, and this was observed during the sample processing step. The ODDHL-BNC fibrils held up to 1.8 times more water than those of the control-BNC. Measuring the average diameter of the BNC fibers for the control-BNC and DDHL-BNC samples was also performed using the SEM analysis software. These measurements showed that the average diameter of the ODDHL-BNC (155 nm) sample was greater than that of the control-BNC (129 nm) sample.

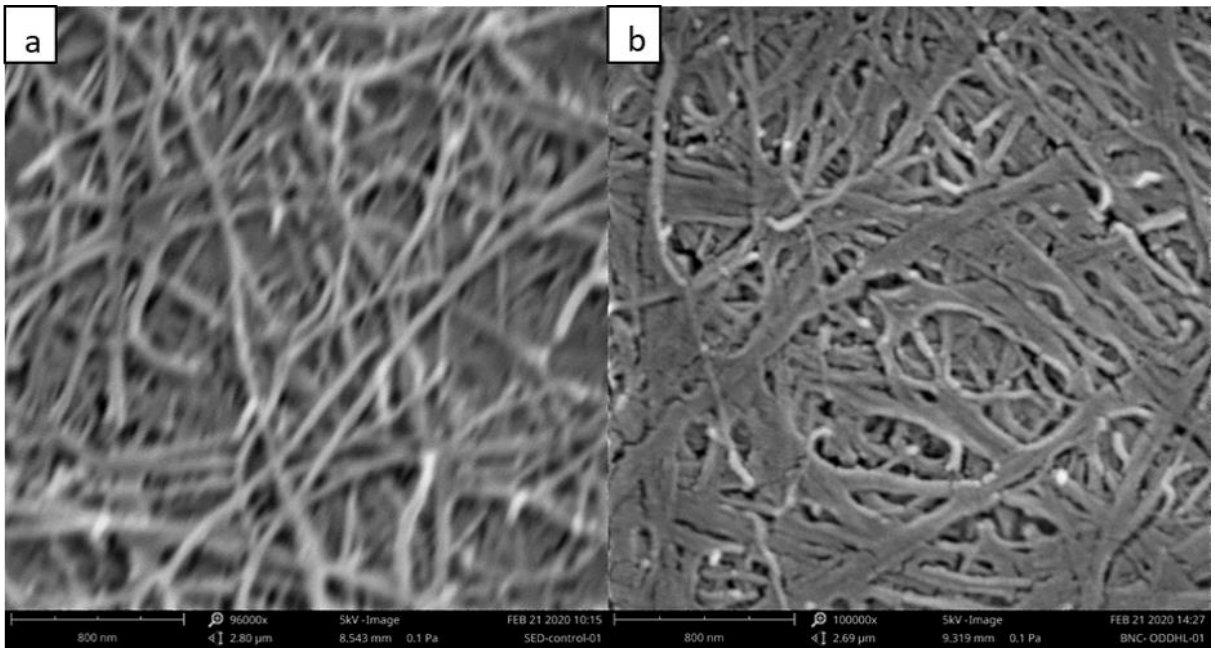


**Figure 2. SEM images of the control-BNC sample (a) and of the ODDHL-BNC sample (b). The SEM images were acquired at 5 keV and resolutions of 100 kX magnification in secondary electron dispersion mode.**

Figure 3 shows a comparison between the control-BNC and the N-Decanoyl-DL-homoserine lactone (DHL)-BNC fibers. There is variability in the structure and diameter size for the pellicles when comparing the control to the DHL-BNC fibers. In Figure 3a, the cellulose from the control samples is less uniformly distributed as compared to that of the DHL-BNC fibers, shown in Figure 3b. The DHL-BNC SEM image in Figure 3b shows that the fibrils are well-formed and tightly-packed with a high density of BNC fibers in the field of view as compared to that of the control-BNC SEM image. The DHL-BNC fibrils have similar morphology to the ODDHL-BNC fibers, except the former is more uniform with less variability in the fiber morphological properties—such as width, thickness, and distribution. The DHL-BNC image shows well-formed cellulose fibrils and more structural uniformity as observed with the ODDHL-BNC shown in Figure 2b. The DHL-BNC fibrils show uniform porosity and greater fiber density as compared to that of the control-BNC samples. Investigating the in-depth projections of these BNC fibrils showed that the DHL-BNC fibrils are distributed in close-packed layers as compared to the control-BNC fibrils that have more spatial separation on the *y*-axis projection and with significant difference in the density of fibrils in various layers as shown in Figure 3a. The SEM data are important in terms of utilizing such DHL-BNC fibrils in applications that require high fibril density, more uniformity, and less porosity—such as electronic display circuitry, wearable sensors, and detection technologies. The water capacity of the DHL-BNC fibrils was similar to that of the ODDHL-BNC fibrils (greater than that of the control-BNC); this was observed during the sample processing procedures. The DHL-BNC fibrils held as much as 1.6 times more water than that of the control-BNC samples. Measuring the average diameter of the BNC fibers for the control-BNC and DDHL-BNC samples was performed using the SEM analysis software. These measurements showed that the average diameter of the ODDHL-BNC (162 nm) sample was greater than that of the control-BNC (129 nm) sample. It should be noted that the DHL-BNC fibrils have the most uniformity in terms of fiber diameter, and unlike the other HSL molecules, the DHL-BNC showed better fiber integrity and formation.

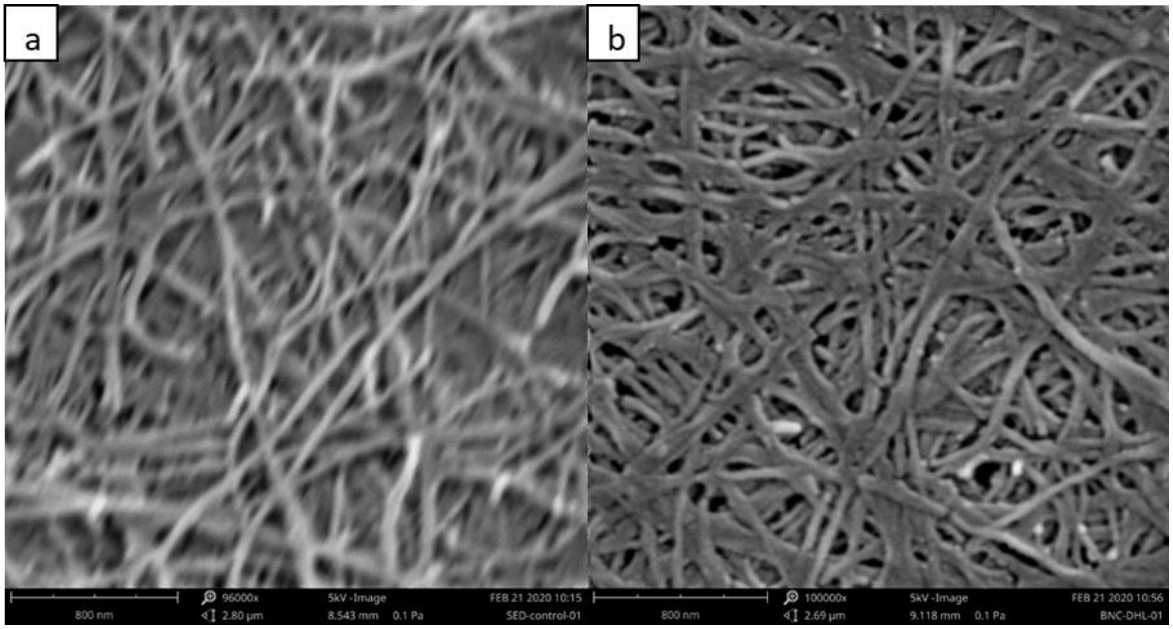


**Figure 3. SEM images of the control-BNC sample (a) and of the DHL-BNC sample (b). The SEM images were acquired at 5 keV and resolutions of 100 kX magnification in secondary electron dispersion mode.**

Comparing the SEM data for all HSLs used in the production of the BNC fibrils in these experiments showed that their presence affected the formation and the morphological properties of the BNC pellicles. The effect of the HSLs on the morphological properties of the BNC pellicles varied based on the molecule used. The DHL-BNC fibrils had the best morphological properties as compared to other HSLs—namely, the ODDHL-BNC and DDHL-BNC fibrils. One common effect among all used HSLs was the enlargement of the fiber average diameter as compared to that of the control-BNC samples. While this explanation is based on experimental morphological data, further genomic and mechanistic investigations of the factors affecting the enlargement of the pellicle in the presence of HSLs are needed. These experiments will address, on a molecular level, the impact of genetic materials responsible for the secretion of HSLs and how such factors, when manipulated, can impact the formation of BNC pellicles. Also, AFM experiments have been initiated to provide specific information on the 3D-spatial variation of the pellicle morphology. Such experiments are valuable in terms of providing 3D images of the morphological changes and determining if these changes are a direct result of the presence of HSLs in the growth media of *G. xylinus*.

Overall, SEM data showed that HSLs play a critical role in affecting the morphology of the BNC pellicles and using different HSL molecules showed that the signal molecules affected the mechanism of formation of the pellicles to various degrees and resulted in unique BNC pellicles that can be utilized for various applications. Comprehensive surface characterization of the BNC pellicles from different HSL growth conditions is a vital step to produce tailored biofilms that can have multifunctional properties. For example, DHL-BNC fibrils showed uniform layers of BNC fibers with the most uniform distribution in diameter sizes as compared to other HSLs. Hence, DHL-BNC fibrils can be utilized with applications that require uniformity and ruggedness of the biofilm—such as electronic, food, drug delivery, and sensing technologies. Meanwhile, other HSL-produced BNC fibrils with different morphology and properties can be utilized with most suitable applications other than the one mentioned in the DHL-BNC example.

### 3.2 Effect of the type of HSL on the uniformity of BNC biofilm

The DRIFTS technique was used to determine structural differences of the BNC fibrils. DRIFTS can provide useful information on the changes in the crystalline and amorphous structures of the cellulose and on the uniformity of the BNC film. Samples were collected from different HSL-BNC fibrils and from control-BNC samples. The first sample was ODDHL-BNC fibrils which were formed in a disc shape. Samples collected from ODDH-BNC disc/film were ground to form a homogenous powder to be analyzed by the DRIFTS technique. These HSL samples were selected from the peripheral and center regions of the disc. The DRIFTS results for these ODDHL-BNC samples are shown in Figure 4. In the DRIFTS spectra, there are two important regions that are considered to determine structural properties—the hydroxyl (–OH) region between 4000–2500 $cm^{-1}$ and the fingerprint region ranging from 1600–600 $cm^{-1}$. The relevant variation in the –OH region is in its bandwidth range. The variation in the –OH region band width represents structural variation of the film. For example, the wider the –OH region the more amorphous

structure the film is, and the narrower the –OH band region the more crystalline structure and uniform the film.[14–16] Figure 4 (top) shows the DRIFTS spectra of the control-BNC fibrils and Figure 4 (bottom) shows the DRIFTS spectra of the ODDHL-BNC fibrils. The difference between the two samples lies in the –OH stretching bands, which show that the control-BNC fibril is not uniform in the three analyzed samples as compared to the ODDHL-BNC sample. The latter fibrils had a narrower –OH stretching band than the control-BNC as shown in Figure 4. Moreover, the ODDHL-BNC fibrils were more uniform because of smaller variation in the –OH stretching band as seen in Figure 4 (bottom). These spectra were reproducible from the three samples of ODDHL-BNC, indicating that there is a uniformity in the structure of the BNC fibril across the whole film area more than that of the control-BNC film. The band width in ODDHL-BNC is narrower than the control-BNC, which suggests that the predominant intermolecular hydrogen bonds in ODDHL-BNC film exhibit an isotropic behavior more than that of control-BNC film. Moreover, the narrower –OH absorption band in ODDHL-BNC is indicative of more crystalline structure as compared to the more amorphous structure exhibited by the control-BNC sample.

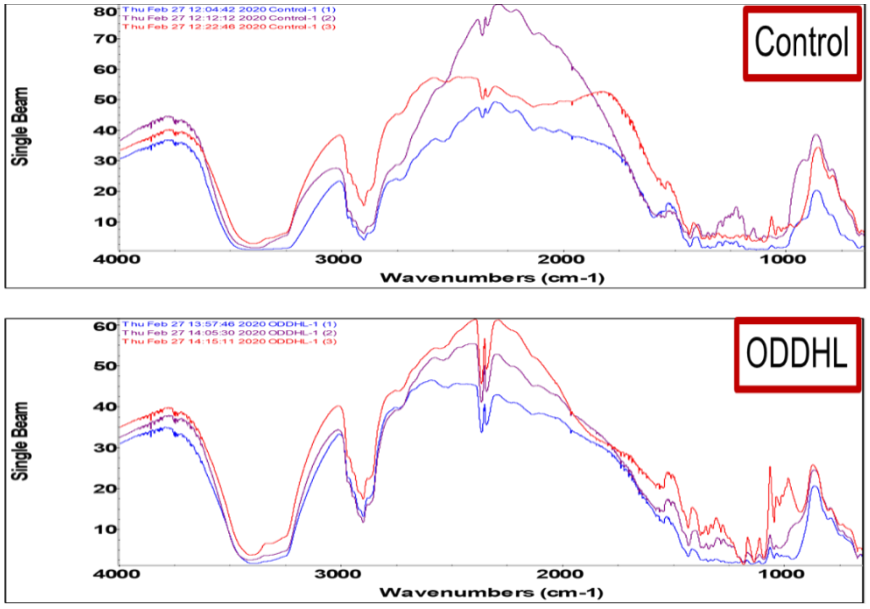


**Figure 4. DRIFTS data of three control-BNC samples collected from different regions of a disc shape BNC film (top). DRIFTS data of three ODDHL-BNC samples collected from different regions of a disc shape BNC film. (bottom).**

In the fingerprint region, the ODDHL-BNC showed significant inter- and intra-structural differences when compared to the control-BNC fibrils. The ODDHL-BNC had less variabilities in this fingerprint region than that of the control-BNC fibrils. The C–O–C stretching band absorption at 1050 $cm^{-1}$ is more predominant in the ODDHL-BNC than that of control-BNC fibrils, which indicates more crystalline structure properties as the absorption increases. Also, in the fingerprint region there is a clear difference in the spectral reproducibility observed with the control-BNC fibrils, Figure 4 (top). This is another indication of the clear difference in the uniformity of the BNC film in the control-BNC sample. This variation in the fingerprint region is not observed with the ODDHL-BNC where the differences in the spectral signature across the three analyzed samples is in the absorption intensity rather than the number of peak signatures. As such, we can conclude that the ODDHL-BNC film is more uniform than that of the control-BNC. This is in agreement with the SEM data that showed the ODDHL-BNC fibrils to be more uniform with less variation in thickness, fiber size, and layer distribution (see Figure 2). Also, the shape of the peak at 750 $cm^{-1}$ along with the shoulder grooves at 710 $cm^{-1}$ in both spectra enabled us to characterize the crystalline structure of the two BNC films. In this case, the control-BNC has more shoulders and roughness in the region between 750–700 $cm^{-1}$, which is indicative of an amorphous structure in a monoclinic arrangement.[17]

Figure 5 shows the DRIFTS results for the samples that were collected from three different regions of DHL-BNC film and three different regions of a control-BNC film. Figure 5 (top) shows the DRIFTS spectra for the control-BNC samples and Figure 5 (bottom) shows the DRIFTS spectra for the DHL-BNC samples. These three samples were selected from different regions of the same disc—specifically, the peripheral and center areas. The DRIFTS results for the DHL-BNC samples showed a highly reproducible –OH region between 4000–2500 $cm^{-1}$ and fingerprint region between 1600–600 $cm^{-1}$ (Figure 5 (bottom)). This was not the case for the three samples of the control-BNC sample,

where the variation in the –OH region is clear in terms of the stretching band width variation and band formation (Figure 5 (top)). The variation in the –OH region band width represents structural variation of the film; for example, the wider the –OH region, the more amorphous structure the film has and the narrower the –OH band region, the more crystalline structure and uniform the film.[14–16] In Figure 5, the difference between the two samples lies in the —OH stretching bands, which show that the control-BNC fibril is not uniform in the three analyzed samples as compared to the DHL-BNC samples. The latter had a narrower –OH stretching band as shown in Figure 5 (bottom). Moreover, the DHL-BNC fibrils were more uniform because of smaller variation in the –OH stretching band region. This reproducible –OH stretching band region observed with the DHL-BNC samples indicates that there is a uniformity in the DHL-BNC film more than that of the control-BNC film. The –OH region band width in DHL-BNC is narrower than the control-BNC, which suggests that the predominant intermolecular hydrogen bonds in the DHL-BNC film exhibit an isotropic behavior more than that of control-BNC film. Moreover, the narrower absorption band in DHL-BNC is indicative of a more crystalline structure as compared to the more amorphous structure exhibited by the control-BNC sample.

In the fingerprint region, comparing the DHL-BNC to the control-BNC fibrils showed that there are similar fingerprint peaks expressed in the DHL-BNC samples as compared to those observed with the control-BNC film (Figure 5). The C–O–C stretching band absorption at 1050 $cm^{-1}$ is slightly higher in intensity in the DHL-BNC than in that of control-BNC spectra, which indicates more crystalline structure property attributes in the DHL-BNC sample due to an increase in absorption intensity. There is also a clear difference in the spectral reproducibility observed with the control-BNC fibrils in the fingerprint region (Figure 5 (top)), and less variation in the shoulder peaks which indicate smoothness of molecular distribution or more uniform molecular density in this DHL-BNC film (Figure 5 (top)). This spectral signature in the 750 $cm^{-1}$ for the control-BNC samples with more shoulder peaks is indicative of differences in the uniformity of the BNC film produced in the control growth conditions. This variation in the fingerprint region is not observed with the DHL-BNC. As such, we can conclude that the DHL-BNC film is more uniform than that of the control-BNC. This is in agreement with the SEM data that showed the DHL-BNC fibrils to be more uniform with less variation in thickness, fiber size, and layer distribution (see Figure 3). In this case, the control-BNC has more shoulders and roughness in the region between 750–700 $cm^{-1}$, which is indicative of a crystalline structure in a monoclinic arrangement.[17] Comparing the HSL BNC films' uniformity using the DRIFTS data showed that DHL is more uniform than that of the ODDHL and this is supported by the SEM data. These DRIFTS results are important because they indicate that HSLs can improve the morphological properties and structures of the BNC fibrils, resulting in more reproducible biofilm synthesis and different morphological properties than native BNC films.

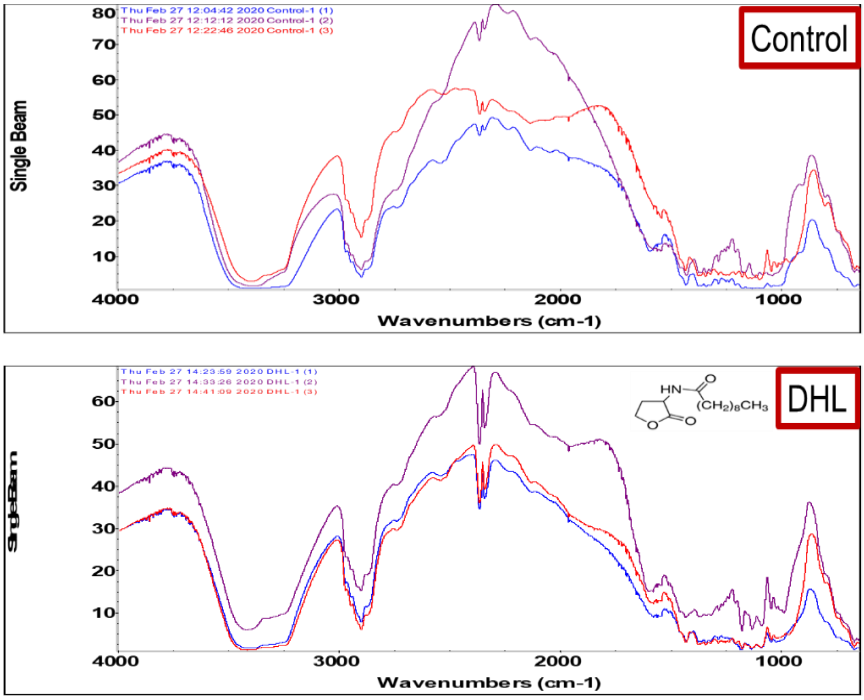


**Figure 5. DRIFTS data of three control-BNC samples collected from different regions of a disc shape BNC film (top). DRIFTS data of three DHL-BNC samples collected from different regions of a disc shape BNC film (bottom).**

### 3.3 Effect of metal ions on the BNC morphological properties

Metal ions represent a significant factor in determining how the signal molecules communicate within their QS environment to ensure the proper signals are transduced to produce appropriate biofilm formation triggers in the presence of metal ions in the growth media. Metal ions are well known to transport through the ion-channel proteins of a given biological system and thus their type and transportation mechanism could affect the signal molecules of QS signaling. On the other hand, there is a practical aspect of investigating metal ions as to determine their impact on the morphological properties of the BNC fibrils and if there is a potential in incorporating them with the BNC fibrils. The metal ions effect was studied primarily using AFM because we wanted to understand their respective morphological impact on the BNC fibrils. In these AFM experiments, we utilized five different chlorinated salts of magnesium (Mg), manganese (Mn), lithium (Li), calcium (Ca), and cesium (Cs) ions. All *G. xylinus* samples were inoculated with equal amounts of each of the metal salts and followed previously discussed growth conditions.

The morphological structure of various cellulose samples which were produced in the presence of Mg, Mn, Li, Ca, or Cs ions were analyzed with AFM. To obtain the AFM images, each BNC fibril sample was put on an AFM holder by using carbon tape and images were taken in semi-contact mode using a silicon cantilever. Figure 6 shows the topography and Mag mode—amplitude of oscillation of the cantilever—images of each metal ion cellulose sample. The Mag images clearly show the structure of the cellulose sample and these AFM images allow us to measure various morphological properties such as the surface roughness and the width of the cellulose fibers. The images in Figure 6 were obtained in 4 µm x 4 µm areas from the 256 x 256 scan points and the field of view was 99 nm x 99 nm. The AFM data showed the surface structure of BNC fibers at the nanometer scale were observed in the Mag mode images projected at an angle of 21.3° from the *x*-axis.

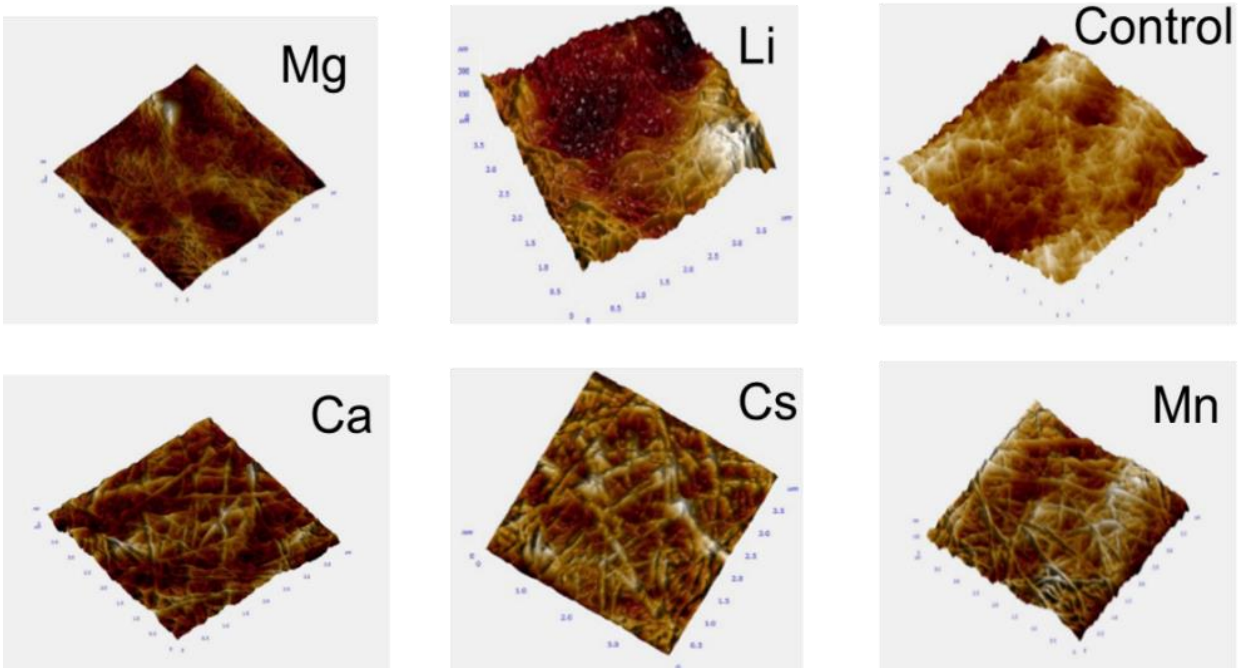


**Figure 6. The AFM images of BNC fibrils produced post-exposure to five different metal ions. The AFM images were captured in the Mag mode and the field of view was 99 nm x 99 nm with 256 x 256 scan points.**

Figure 7 shows the AFM measurements that reflect the effect of the metal ion on the roughness property of the BNC film. The AFM data in Figure 7 shows that the BNC film grown in the presence of Cs ions at 50 nM resulted in the smoothest film surface, roughness of 18 nm; while the BNC film grown in the presence of Li ions at 50 nM produced the roughest surface with roughness around 118 nm. This is interesting data when comparing the mentioned metal ions, namely Cs and Li ions. These two ions belong to the same group within the periodic table—the alkali metal group—and their difference primarily lies in their atomic/ionic size, with Li being much smaller than Cs. Such a physical difference affects the surface of the BNC film, which could be due to the ease of the ion-transportation mechanism of Li as compared to that of Cs, or the potential of the Li ion size allowing it to easily penetrate the gaps in the 3D structure of the BNC film, which effectively disrupts the cellulose structure more than that of the larger Cs ion, thus increasing the surface roughness.

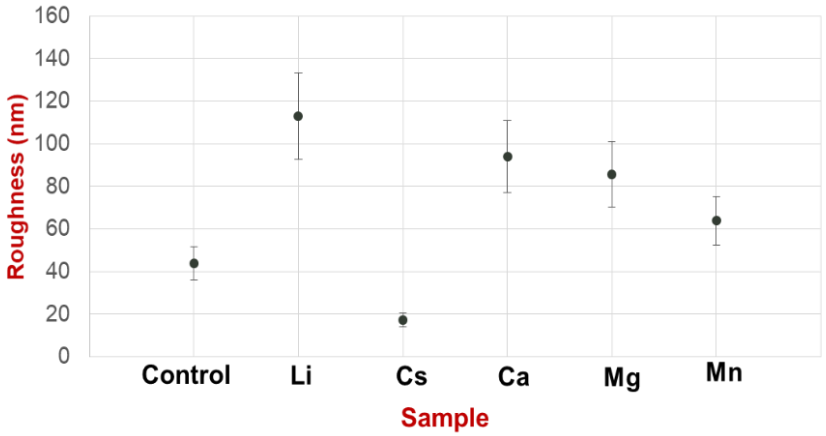


**Figure 7. AFM results representing the effect of metal ions on the surface roughness of BNC films.**

On the other hand, the AFM was used to measure the effect of the metal ion on the diameter of the BNC fiber diameters as shown in Figure 8. These AFM results showed that the presence of Mg salt in the bacterial growth media produced BNC fibers with the smallest average diameter—56 nm—and the presence of Cs ions in bacterial growth produced BNC fibers with the largest diameter—126 nm. The overall order in terms of increasing BNC fiber diameter was as follows: Mg, Ca, Li, Mn, and Cs. The ionic size of the metal ions did not have direct correlation with their effect on the diameter of the BNC fiber, and while alkaline metal ions produced the smallest diameter BNC fibers, the alkali metals produced bigger diameter BNC fibers. The Mn ion, which is a transition metal ion, produced the second largest diameter of the BNC fibers. It is interesting that using Cs ions can enlarge the fiber diameter by a factor of 2X as compared to using Mg ions. The potential difference in Lewis acidity strength between these metal ions could be a factor in this effect. However, such factors need more metal ions within a given series of metal groups to validate such a hypothesis. Choosing these metal ions was based on providing comprehensive coverage of the variety of metal ions and the relevance of these metal ions in their various applications. For example, the ability to bind Li ions to the BNC fiber will produce BNC fibrils with unique electrochemical properties that have various applications in electronic and communication technologies. Overall, the metal ions helped in providing more useful information about how to control the morphological properties of the BNC fibrils and produce custom made fibers with specific morphological properties for desired applications.

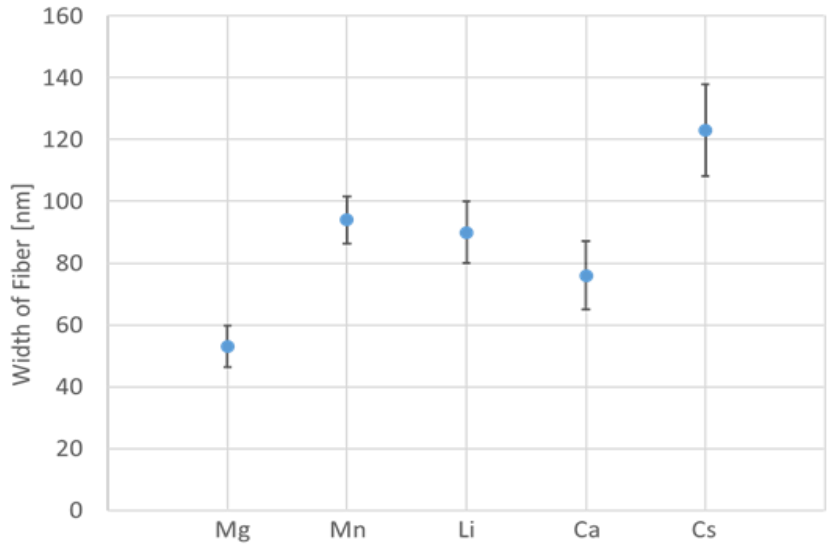


**Figure 8. AFM results representing the effect of metal ions on the diameter of the BNC fibers.**

## 4. CONCLUSION

The surface characterization data in this research project showed that BNC pellicles can be manipulated using different HSL signaling molecules and metal ions. The addition of HSL molecules to the bacterial growth media showed that the HSLs directly affected the morphological properties of the BNC fibrils and produced different films with different structural properties. Moreover, metal ions have drastic differences in the effect on the roughness and fiber diameter. This information will have useful impact when designing specific BNC films for multifunctional utilizations. While more work is needed to confirm the present findings, they are useful to understand the BNC biofilm formation and how its physical and morphological properties are affected by HSL QS molecules. More in-depth research into the genetic materials that control the formation and secretion of the HSL signaling molecules is needed to gain insight on the characteristics of BNC biofilm formation. Modulation of the HSL production by regulatory circuits may influence the BNC biofilm formation and provide a natural way to produce tailored BNC for certain applications. Identifying and characterizing such regulatory processes may be useful in developing efficient synthetic biology approaches to produce desired BNC biofilms.

Molecular-level experimentation including genomic-based and genetic engineering experiments are planned to determine the genetic molecules that affect the morphological properties of the BNC fibrils. The genetic engineering/synthetic biology study of the BNC pellicle physical properties will provide a better understanding of the BNC biofilm formation mechanism during the secretion of HSL signaling molecules. This genetic engineering approach will include utilizing a specific enzyme—such as acyl-HSL synthase—that can be altered by functionality to produce different types of HSLs. Obtaining such information will lead to correlating these genetic-based molecules with the signaling molecules network and the developem genetic engineering tools that can efficiently produce desired and optimal BNC pellicles.

## ACKNOWLEDGMENTS

Funding was provided by the U.S. Army via the In-house Laboratory Independent Research Program (PE 0601101A Project 91A) at the Combat Capabilities Development Command Chemical Biological Center.

## REFERENCES

[1] Lee K.-Y.; Buldum G.; Mantalaris, A.; Bismarck, A. More than meets the eye in bacterial cellulose: Biosynthesis, bioprocessing, and applications in advanced fiber composites. *Macromo. Biosci*. **2014**, *14* (1), pp 10–32.
[2] Rognoli, V.; Bianchini, M.; Maffei, S.; Karana, E. DIY Materials. *Mater. Des.* **2015**, *86*, pp 692–702
[3] Wong, H.C.; Fear, A.L.; Calhoon, R.D.; Eichinger, G.H.; Mayer, R.; Amikam, D.; Benziman, M.; Gelfand, D.H.; Meade, J.H.; Emerick, A.W. Genetic organization of the cellulose synthase operon in Acetobacter xylinum. *Proc. Natl. Acad. Sci. U. S. A.* **1995**, *87* (20), pp 8130–8134.
[4] Williams, W.S.; Cannon, R.E. Alternative environmental roles for cellulose produced by Acetobacter xylinum. *Appl. Environ. Microbiol.* **1989**, *55* (10), pp 2448–2452.
[5] Zhong, C.; Gurry, T.; Cheng, A.A.; Downey, J.; Deng, Z.; Stultz, C.M.; Lu, T.K. Strong underwater adhesives made by self-assembling multiprotein nanofibres. *Nat. Nanotechnol.* **2014**, *9* (10), pp 858–866.
[6] Chen, A.Y.; Billings, N.; Seker, U.; Lu, M.; Citorik, R.; Zakeri, B.; Lu, T. Synthesis and patterning of tunable multiscale materials with engineered cells. *Nat. Mater.* **2014**, *13* (5), pp 515–523.
[7] Yadav, V.; Paniliatis, B.J.; Shi, H.; Lee, K.; Cebe, P.; Kaplan, D. Novel in vivo-degradable cellulose-chitin copolymer from metabolically engineered Gluconacetobacter xylinus. *Appl. Environ. Microbiol.* **2014**, *76* (18), pp 6257–6265.
[8] Mohite, B.V.; Patil, S.V. Physical, structural, mechanical and thermal characterization of bacterial cellulose by G. hansenii NCIM 2529. *Carbohydr. Polym.* **2014**, *106*, pp 132–141.
[9] Hsieh, Y.C.; Yano, H.; Nogi, M.; Eichhorn, S.J. An estimation of the Young's modulus of bacterial cellulose filaments. *Cellulose*. **2008**, *15* (4) pp 507–513.
[10] Rusli, R.; Eichhorn, S.J. Determination of the stiffness of cellulose nanowhiskers and the fiber-matrix interface in a nanocomposite using Raman spectroscopy. *Appl. Phys. Lett.* **2008**, *93* (3) pp 033111–0331113.
[11] Gelin, K.; Bodin, A.; Gatenholm, P.; Mihranyan, A.; Edwards, K.; Stromme, M. Characterization of water in bacterial cellulose using dielectric spectroscopy and electron microscopy. *Polymer*. **2007**, *48* (26) pp 7623–7631.

[12] Yuen, J.D.; Walper, S.A.; Melde, B.J.; Daniele, M.A.; Stenger, D.A. Electrolyte-Sensing Transistor Decals Enabled by Ultrathin Microbial Nanocellulose. *Sci. Rep.* **2017**, *7*, 40867.
[13] Rudrappa, T.; Biedrzycki, M.L.; Bais, H.P. Causes and consequences of plant-associated biofilms. *FEMS Microbiol. Ecol.* **2008**, *64 (2)*, pp 153–166.
[14] Silverstein, R.M.; Bassler, G.C.; Morrill, T.C. *Spectrometric Identification of Organic Compounds*, 4th ed; Wiley; New York, 1981, pp 241–253.
[15] Soares, S.; Camino, G.; Levchik, S. Comparative study of the thermal decomposition of pure cellulose and pulp paper. *Polym. Degrad. Stab*. **1995**, *49* (2), pp 275–283.
[16] Pastorova, I.; Botto, R.E.; Arisz, P.W.; Boon, J.J. Cellulose char structure: a combined analytical Py-GC-MS, FTIR, and NMR study. *Carbohydr. Res.* **1994**, *262* (1), pp 27–47.
[17] Hardy, B.J.; Sarko, A. Molecular dynamics simulations and diffraction-based analysis of the native cellulose fibre: structural modelling of the I-α and I-β phases and their interconversion. *Polymer*. **1996**, *37* (10), pp 1833–1839.

# SSI PROJECTS

# Extending bio-functionality in materials via controlled polymer erosion

Marilyn S. Lee[a]*, Rebecca M. Raig[b,c], Danielle L. Kuhn[a], Steven M. Blum[a], Maneesh K. Gupta[b], Matthew W. Lux[a]

[a]U.S. Army Combat Capabilities Development Command Chemical Biological Center, Research & Technology Directorate, 8198 Blackhawk Rd, Aberdeen Proving Ground, MD 21010

[b]U.S. Air Force Research Laboratory, 2179 12th St, B652/R122 Wright-Patterson Air Force Base, OH 45433

[c]UES, Inc., 4401 Dayton-Xenia Rd, Dayton, OH 45432

## ABSTRACT

Cell-free systems have growing importance as a way to use synthetic biology tools in resource-poor environments. Lysates may be dried for storage, delivering biochemical activity for sensing or producing molecules on-demand upon rehydration at the point of need. Up to now, cell-free protein synthesis reactions have been studied as aqueous solutions in test tubes or absorbed onto paper or cloth. Embedding biological functionality into broadly used materials, such as plastic polymers, has long been an attractive goal. This goal has, for the most part, remained out of reach, often due to the fragility of biological systems outside of aqueous environments. In this work, we describe and utilize a surprising and useful feature of lyophilized cell-free lysate systems—tolerance to polymer casting methods involving exposure to organic solvents or heat up to 90 °C. To explore this newly discovered feature, a variety of casting conditions were tested, and cell-free protein synthesis reaction components were screened for protective properties. Cell-free protein synthesis is compatible with several polymer types. Tolerance to polymer casting enables the delivery of dry cell-free reactions in the form of coatings or fibers, among other processing possibilities.

**Keywords:** cell-free protein synthesis, polymers, synthetic biology, protein stability, sensing

## 1. INTRODUCTION

Cell-free systems are a collection of techniques for activating cellular machinery outside of living cells. Key cell-like functionalities in these systems include cell-free protein synthesis (CFPS)[1–4] and complex metabolism that can both provide energy to the system and produce small molecules of interest.[5–9] In these reactions, there is no need to maintain cell growth or viability, and removal of the cell membrane facilitates direct addition or measurement of molecules like DNA. These systems have been used for wide range of applications, including sensing, manufacturing, genetic prototyping, and education.[10] There are two main approaches to reconstitute cellular activity *in vitro* (Figure 1A). One approach is the use of crude cell lysates, where cells are simply broken open and additional building blocks and buffers are added to allow the proteins and nucleic acids in the mixture to retain most of their native function.[3,11] Since many undefined components from the cell are still present, there is limited control over biochemical activity. Another approach is the PURE system, where the protein components essential for transcription, translation, and energy cycling are purified before the mixture is reconstituted with energy and substrate solutions.[12] This system is much better defined, though it is more expensive to implement and lacks any metabolic enzymes present in lysate that are not individually identified and purified to be included in the reaction.

A major emerging application of CFPS reactions is rapid field-deployed sensing[13–17] or molecule production at the point of need[17,18] with minimal required equipment. Though many biological reagents are normally stored frozen or refrigerated, CFPS reactions may be lyophilized for room temperature storage and retain high levels of protein synthesis activity upon rehydration.[19–21] CFPS may be used to quickly prototype and implement gene circuit designs that can sense analytes via a variety of mechanisms and produce human readable outputs such as a colorimetric, fluorescent, or even electrochemical reporters.[22] Drying CFPS reactions onto paper tickets or cloth has greatly broadened the scope of applications for cell-free techniques.[13,14,16,23,24] Paper-based reactions retain activity, enabling formats similar to pH paper that are less cumbersome for field use. A draw-back to CFPS reactions is that the short reaction lifetimes of a few hours make these systems single-use only. It is also necessary to manually add water to

activate the reaction and carefully account for matrix contaminants in the material to be analyzed. Some of these issues could be addressed by using material science to once again redesign the reaction environment.

There is great potential to leverage materials to modulate hydration, and therefore activation, of cell-free systems (Figure 1B). Polymers have been widely used to control release timing for cargos that include anything from pharmaceuticals to fertilizers.[25,26] The same principle may be used to extend the lifetime of activity of a detection device. For instance, continual activation of fresh bio-active cargo, such as enzymes, embedded in a material may be achieved by polymer erosion.[27,28] However, this type of formulation requires the biological molecule to be cast into polymers that have low solubility in water, likely necessitating the application of heat or organic solvents. These treatments have a deleterious effect on the activity of most enzymes, unless their structure can be protected in some way.[29] For a complex mixture like CFPS reactions, such effects on any of the numerous enzymes and other constituent components could result in reduction or elimination of overall protein production.

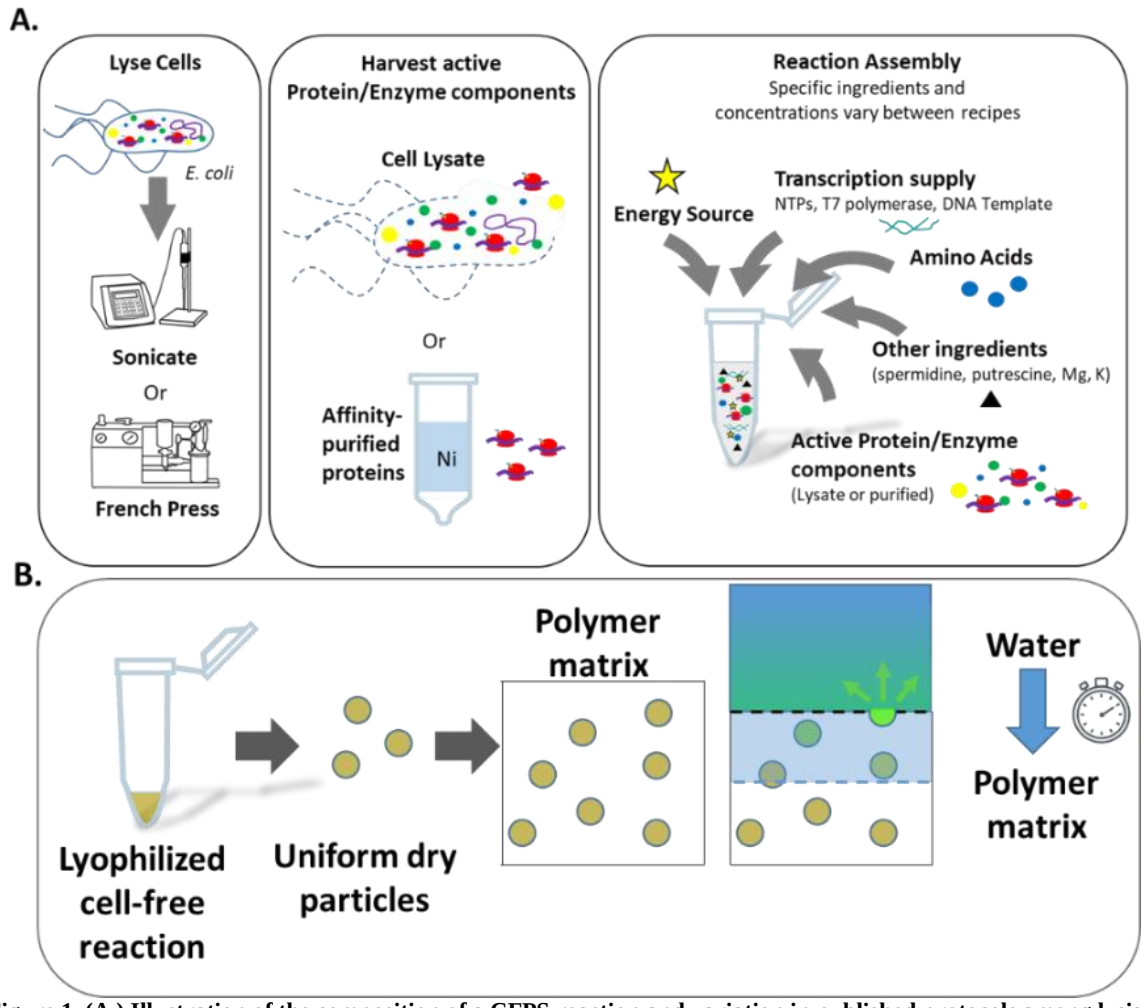


**Figure 1. (A.) Illustration of the composition of a CFPS reaction and variation in published protocols among lysis methods, purity of active enzyme components, and buffer ingredients. (B.) Illustrated example of a delayed activation concept design where lyophilized CFPS reaction material is embedded with a polymer matrix that delays rehydration.**

Over the past few decades, researchers in this field have shown that a subset of purified proteins can, under certain circumstances, maintain their fold and activity when suspended in organic solvents.[30,31] An important factor influencing protein behavior in organic solvents is the amount of water present in the mixture. Too much water will allow the protein to change conformations, leading to irreversible folding and inactivation. This has been seen in studies titrating organic solvents into aqueous bio-mixtures such as a CFPS reaction.[32,33] Therefore, freeze-drying or spray-drying is necessary to carefully remove water from an enzyme sample before solvent addition to better maintain enzyme activity. Tolerance to non-aqueous solvents has been studied for a small subset of purified proteins but has

never before been explored for a complex bio-mixture—like a CFPS reaction—in which many proteins, nucleic acids, and metabolites must be preserved to maintain transcription and translation activity.

Heat is another challenge to the stability of a biological mixture, which causes proteins to unfold and degradation reactions to proceed at a faster rate. Removal of water could also improve stability to this challenge, by removing molecular interactions influencing protein aggregation, preventing hydrolysis-mediated degradation, and reducing the motility of molecules in general by placing them in the solid state. The heat stability of lyophilized cell-free formulations has already been demonstrated with room temperature shelf storage for weeks to months. It is possible that much higher temperatures could be tolerated for the short period of time necessary for polymer casting.

In this work, we describe the effects of exposing lyophilized CFPS reactions to organic solvents. We find that CFPS activity is recovered upon rehydration after exposure of the dried reaction to a variety of organic solvents, though some polar solvents, such as ethanol, reduce activity. Screens of CFPS reaction recipes, reagent mix components, and solvent removal methods indicate that tolerance to certain solvents is dependent on the presence of additives. Further, lyophilized CFPS reactions tolerate high temperatures up to 90 °C for short periods of time (0.5–1 hour), exhibiting normal protein synthesis post-treatment. Both solvent tolerance and heat tolerance enable the casting of these biological active ingredients into polymer materials. We show that dry CFPS is compatible with solvent-cast poly (lactic-co-glycolic acid) (PLGA). CFPS reagents were also cast into polycaprolactone (PCL) by thermal compression. The rehydration and activation of these CFPS-polymer composites are described.

## 2. RESULTS AND DISCUSSION

### 2.1 Lyophilized CFPS powder tolerates organic solvent exposure

Initial experiments exposing CFPS reactions to organic solvents utilized an *Escherichia coli* lysate system closely mimicking the recipe constructed by Jewett et al.[11] and referred to as PANOx-SP. A panel of solvents including acetone, acetonitrile, chloroform, dichloromethane (DCM), dimethylformamide (DMF), dimethylsulfoxide (DMSO), ethanol, ethyl acetate, methanol, and tetrahydrofuran (THF) were used to challenge both the *E. coli* lysate component lyophilized alone, and the complete lyophilized CFPS reaction mixture. The treatment sequence is summarized in Figure 2A. Each solvent was mixed with the dry cake in microplate wells to form a suspension, then incubated for 1 hour at room temperature. The dried CFPS cake material is largely insoluble in all the organic solvents tested, with insoluble particulates settling quickly after mixing. The solvents were removed by aspiration after brief centrifugation to settle the CFPS material into a pellet. Residual solvent was removed by evaporation with a vacuum. Then, the reactions were rehydrated with water to reach the desired reaction volume. For samples in which only the lysate is dried and exposed to solvent, the other components of the CFPS reaction were added in the form of aqueous solutions at the rehydration step to initiate protein synthesis activity.

CFPS activity was assessed by tracking green fluorescent protein (GFP) production from a plasmid DNA template with a T7 promoter (Figure 2B). GFP productivity after organic solvent exposure clearly has some dependence on both the properties of the solvent and the components included during drying and solvent exposure. When the complete reaction is exposed to organic solvents, acetonitrile and ethyl acetate exposure did not result in any loss of activity. Acetone, THF, chloroform, and DCM caused partial loss in activity. Ethanol, DMF, DMSO, and methanol caused total or near total loss of activity. When lysate alone is exposed to solvents, a different pattern emerges. Acetonitrile and ethyl acetate are again the most compatible, but acetone, ethanol, chloroform, DMF, methanol, and DCM all yield varying levels of activity. DMSO and THF completely deactivate the un-supplemented lysate. It is notable that, depending on the solvent type, activity may only be lost for the complete reaction (DMF, methanol, ethanol) or only for the lysate THF, suggesting multiple mechanisms for CFPS inactivation are present.

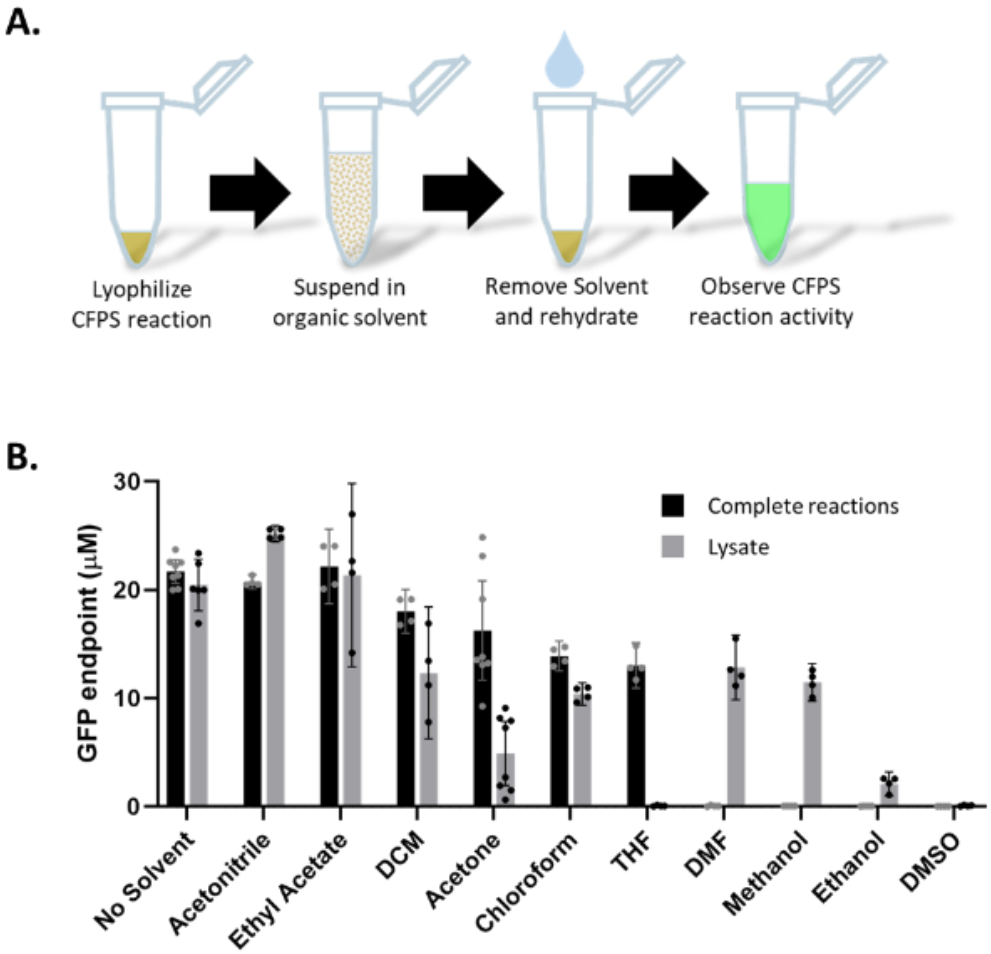


**Figure 2. (A) Treatment sequence for CFPS reactions includes lyophilization, suspension in an organic solvent, removal of the organic solvent, rehydration, and assessment of CFPS activity via monitoring the appearance of GFP. (B.) Endpoint concentration of GFP in reaction mixtures after lyophilized lysate (grey bars) or complete CFPS reactions (black bars) were exposed to an organic solvent and rehydrated. In the "no solvent" control the dried reactions were rehydrated without solvent exposure. Error bars represent the 95 % confidence interval.**

There are several possible ways treatment with an organic solvent might impact the productivity of a CFPS reaction. First, the solvent could cause protein unfolding in the lysate or supplemented polymerase and RNase inhibitor protein components in the dry state. Second, the solvent could extract critical resource molecules from the dried cake into solution and cause them to be removed from the system when the solvent is aspirated away. Third, residual solvent not sufficiently removed by evaporation could cause protein unfolding or other inhibition when water is reintroduced.[32] Depending on the properties of each solvent, a different combination of these effects may have an impact.

### 2.2 CFPS reaction component screen for improvement of acetone tolerance

The observation that the complete-dried CFPS reaction performed better than the lysate alone after exposure to acetone, chloroform, or THF suggested that some component of the resource mix might act as a protective additive. To test this hypothesis, components of the resource mix were combined with lysate individually and screened for protective effects upon exposure to acetone and removal of the solvent without a vacuum (Figure 3). In this experiment, three "components" are themselves aqueous mixtures. 10xSS contains magnesium, potassium, and ammonium glutamate. 15xMM contains ATP, GTP, UTP, CTP, folinic acid, and tRNA. 20AA is a mixture of all 20 canonical amino acids. CFPS ingredients each have varying effects on GFP productivity after acetone treatment. Plasmid DNA and HEPES buffer both significantly stabilize the lysate. Remarkably, the 10xSS component alone is sufficient to stabilize the lysate to acetone exposure as well as the complete reaction mixture. This experiment is the first confirmation that altering the composition of the lyophilized CFPS reaction mixture greatly impacts tolerance to organic solvent exposure.

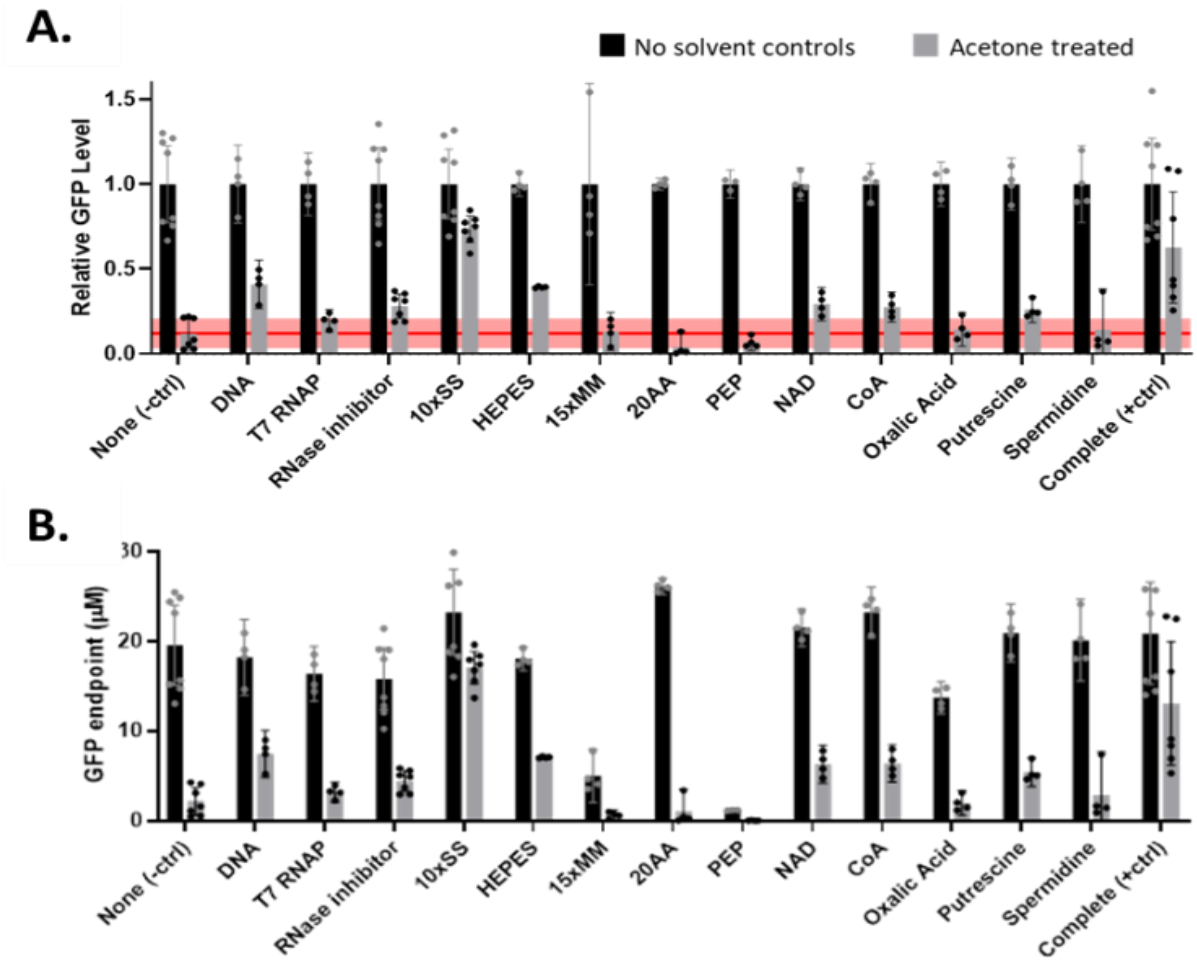


**Figure 3. (A.) Results of screening CFPS components for protective effect during acetone exposure. Black bars are results from controls without solvent exposure. Grey bars refer to a one-hour acetone exposure. Acetone is evaporated under ambient conditions in this experiment. Each set of bars is labeled with the CFPS ingredient used to supplement the lysate sample during drying. The negative control, labeled "None", is lysate without any supplemented additive. The positive control, labeled "Complete", includes all CFPS ingredients. The red reference line coincides with the mean relative GFP productivity of an un-supplemented lysate control exposed to acetone, with lighter red shading representing the 95 % confidence interval. GFP levels are normalized to the no solvent control treatment for each component. (B.) Depicts the same data without normalization.**

### 2.3 Comparing the solvent tolerance of different published CFPS styles

The clear dependence of solvent tolerance on the composition of the reaction led us to investigate solvent tolerance across different published CFPS systems. We tested the performance of three systems: the commercial PURExpress® system based on the PURE system approach described above,[12] the PANOx-SP system used in all experiments above,[11] and the 3-PGA system which uses a different strain of *E. coli*, lysis method, and recipe for reaction additives.[3,34] Table 1 (see methodology) is a side-by-side comparison of the composition of the CFPS reaction for each recipe. We note that the PURE system CFPS recipe from the literature may differ from commercial PURExpress®, the exact contents of which are not published. In each case, the reactions are lyophilized and exposed to solvent as described above, with four solvent conditions tested: acetone, acetonitrile, chloroform, or no solvent.

The GFP productivity results confirm that alternate CFPS recipes respond to solvents in different ways (Figure 4). Compared to the lysate-based CFPS reactions, the PURExpress® formulation has less starting productivity but also minimal sensitivity to treatments with the three solvents tested. Chloroform was the only solvent that significantly reduced GFP productivity in the PURExpress® system. On the other hand, the two lysate-based CFPS recipes have very different susceptibility to the organic solvents. 3-PGA is much more susceptible to inactivation by solvent exposure across all three solvent types compared to PANOx-SP.

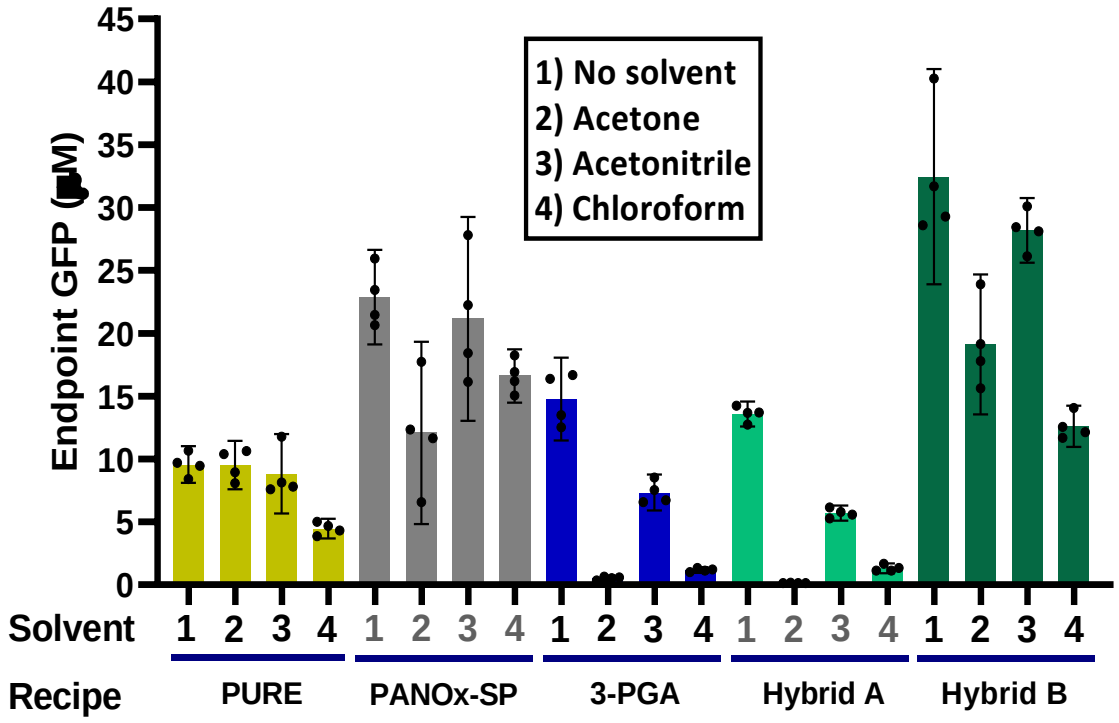


**Figure 4. Comparison of different CFPS recipes challenged with organic solvents. Endpoint GFP concentrations are compared for five CFPS recipes after exposure to organic solvents. Error bars represent the 95 % confidence interval. Recipe labeled "Hybrid A" is a CFPS reaction mixing PANOx-SP *E. coli* extract and 3-PGA reagent mix. "Hybrid B" is a mixture of 3-PGA extract and PANOx-SP reagent mix.**

To learn what components of the CFPS reaction are responsible for increased solvent sensitivity, the *E. coli* extract and reagent mix components of PANOx-SP and 3-PGA CFPS recipes were swapped so that PANOx-SP extract and 3-PGA reagent mix were combined in the "Hybrid A" mixture, and 3-PGA extract and PANOx-SP reagent mix were combined in the "Hybrid B" mixture. These hybrid CFPS recipes were then lyophilized, treated with solvent, and rehydrated as before. The results of this test clearly show that samples containing 3-PGA reagents are more susceptible to solvent inactivation than samples containing PANOx-SP reagents. When combined with PANOx-SP reagent mix, 3-PGA extract performed very similarly to PANOx-SP, indicating that differences in the cell extract were not the primary factor contributing to solvent sensitivity. Among many differences in the supplemented reagents, a major difference is the type of energy source. PANOx-SP makes used of phosphoenolpyruvate to regenerate ATP in the reaction, while 3-PGA utilizes maltodextrin to energize the reaction through substrate phosphorylation and glycolysis. Further experimentation is needed to elucidate specific components leading to solvent sensitivity.

### 2.4 Solvent cast CFPS-polymer composites

Next, we sought to test whether CFPS reaction components can be embedded in a solvent cast polymer. The polymer chosen to test first was PLGA. PLGA is a biocompatible polymer that degrades in water via hydrolysis of ester linkages. It is possible to adjust the rate of degradation by changing the relative levels of lactic (L) and glycolic (G) acid groups. PLGA is soluble in several solvents. For this test, PLGA was solvent cast in the form of a film or coating. Two casting methods were tested. In one method, the CFPS reaction mixture was dried in the form of a semi-spherical bead and coated with PLGA dissolved in ethyl acetate (Figure 5A). In a second method, dried CFPS components were ground to a powder form and suspended in a PLGA acetone solution to be cast as a film on a glass slide (Figure 5B–D). The formation of GFP upon rehydration of the CFPS-polymer composites clearly indicates that CFPS activity is compatible with both solvent casting methods.

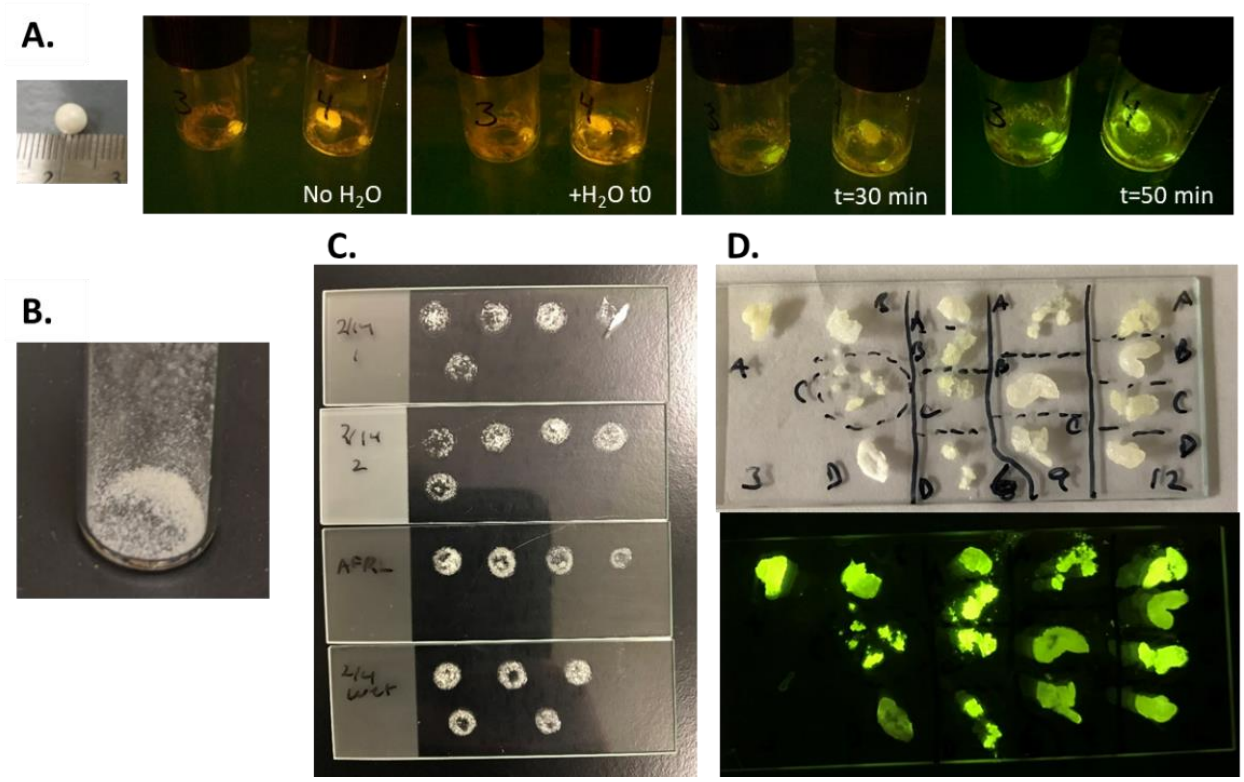


**Figure 5. From left to right: (A) CFPS reaction mixture is lyophilized in the form of mm-scale beads. These beads are coated with PLGA dissolved in ethyl acetate. The coated beads are then activated upon exposure to water to form GFP over 1 hour. Three time points during the rehydration step (0 min, 30 min, and 50 min) are shown. (B) CFPS reaction mixture is lyophilized and ground into a powder form (C). CFPS powder is solvent cast into films with acetone and PLGA solution. (D) Images of CFPS-PLGA films after removal from the slide and rehydration for 24 hours. Upper image is white light exposure, lower image shows GFP fluorescence with blue light and orange lens filter. Films display clouding and degradation due to hydrolysis of PLGA.**

GFP productivity was measured in CFPS-PLGA films by transferring the films to a microplate to be rehydrated and monitored for fluorescence in a microplate reader (Figure 6). GFP productivity in the PLGA films is much more variable than productivity of un-treated or acetone-treated CFPS powder. This is most likely due to variability in the loading of CFPS powder into each film. Poor suspension of the powder is the subject of ongoing optimization, with testing of additives like surfactants and bulking agents taking the primary focus. Encapsulation in a PLGA film does not appear to delay the rehydration of the CFPS reaction material, because the dynamics of GFP formation in the films are similar to the untreated case. Polymer types that absorb water more slowly, or casts with increased polymer thickness may lead to the desired control or delay of activation. In Figure 6B, several different batches of CFPS powder with different degrees of dryness or water content were tested as untreated, acetone-treated, or PLGA-embedded samples. CFPS powder with increased water content had improved activity when immediately rehydrated, but dried cake had poor powder quality and poor dispersion in the acetone compared to drier samples.

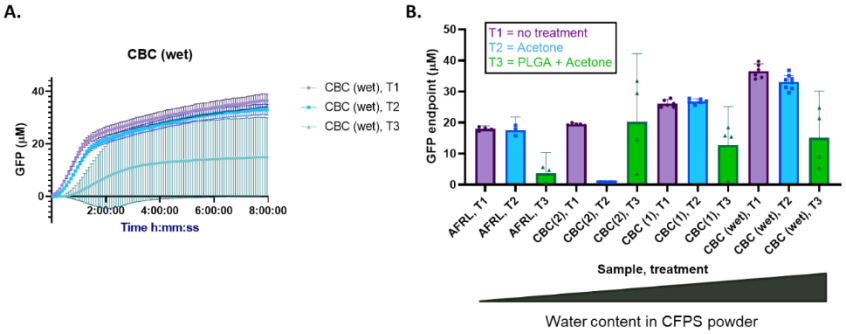


**Figure 6. (A) The production of GFP fluorescence from CFPS overtime from samples treated one of three ways: T1 is untreated, T2 is exposed to acetone, and T3 is solvent cast CFPS-PLGA film. (B) Several batches of lyophilized CFPS powder with different water contents are compared by endpoint GFP productivity after three treatments.**

GFP productivity was measured in CFPS-PLGA films by transferring the films to a microplate to be rehydrated and monitored for fluorescence in a microplate reader (Figure 6). GFP productivity in the PLGA films is much more variable than productivity of un-treated or acetone-treated CFPS powder. This is most likely due to variability in the loading of CFPS powder into each film. Poor suspension of the powder is the subject of ongoing optimization, with testing of additives like surfactants and bulking agents taking the primary focus. Encapsulation in a PLGA film does not appear to delay the rehydration of the CFPS reaction material, because the dynamics of GFP formation in the films are similar to the untreated case. Polymer types that absorb water more slowly, or casts with increased polymer thickness may lead to the desired control or delay of activation. In Figure 6B, several different batches of CFPS powder with different degrees of dryness or water content were tested as untreated, acetone-treated, or PLGA-embedded samples. CFPS powder with increased water content had improved activity when immediately rehydrated, but dried cake had poor powder quality and poor dispersion in the acetone compared to drier samples.

### 2.5 Heat tolerance

An alternative way to introduce powdered CFPS reactions into a polymer is to use a thermoset polymer that can be heated to soften or melt, combined with CFPS powder, pressed into form, then cooled to form a solid. In order to use this method, the lyophilized CFPS reagents must tolerate exposures to temperatures approaching 100 °C, but only for a short period of time during the casting process. Lyophilized CFPS reactions were exposed to high temperatures in a thermocycler, then rehydrated and monitored for GFP productivity (Figure 7). GFP productivity results indicate that CFPS activity is maintained when the dried reactions are exposed up to 80 °C for at least three hours, and up to 90 °C for at least 0.5 hours. These results indicated that lyophilized CFPS powder can likely survive a high-temperature casting process, so long as the treatment is not prolonged.

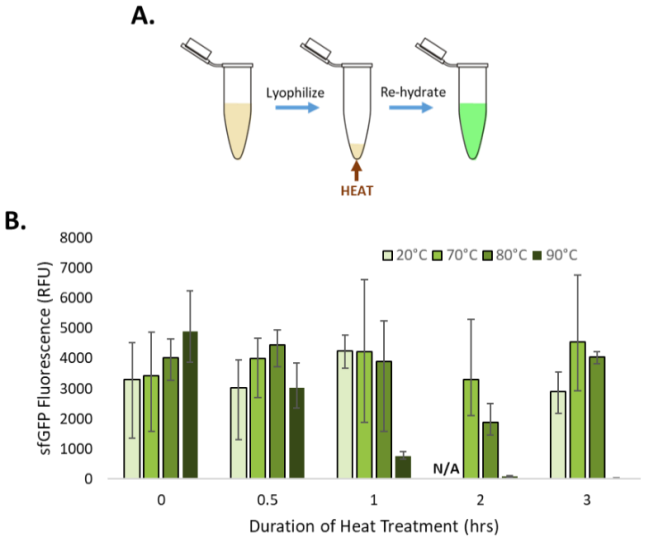


**Figure 7. (A.) Treatment sequence for CFPS reactions includes lyophilization, heating to desired temperature via thermocycler, then rehydration and assessment of CFPS activity via monitoring the appearance of GFP. (B.) Endpoint GFP fluorescence produced by CFPS reactions exposed to 20 °C, 70 °C, 80 °C, or 90 °C for 0, 0.5, 1, 2, or 3 hours.**

### 2.6 Thermal compression molded CFPS-PLGA composites

As a proof-of-concept, lyophilized CFPS powder was incorporated into PCL. PCL is a biocompatible polyester and also has the potential for biodegradation in water, albeit much more slowly than PLGA. PCL has a relatively low melting temperature of 60 °C, making it a good starting point to test stability to this casting method. Thermal compression via a heat press set to 80 °C was used to press PCL pellets into disks (Figure 8A). To incorporate CFPS, the powder was spread between two disks and re-pressed at 80 °C to completely seal the powder between laminated PCL layers (Figure 8B). Small CFPS-PCL disks were rehydrated intact or cut to expose the embedded CFPS powder and were monitored for the formation of GFP fluorescence compared to a blank PCL disk negative control and untreated CFPS powder positive control. The cut disks produced GFP fluorescence and the intact disks did not, indicating that the PCL polymer blocks the intrusion of water into the matrix and that the CFPS powder maintains activity after the thermal compression casting process. Endpoint GFP productivity appears to be variable due to the non-uniformity of CFPS powder distribution in the disks.

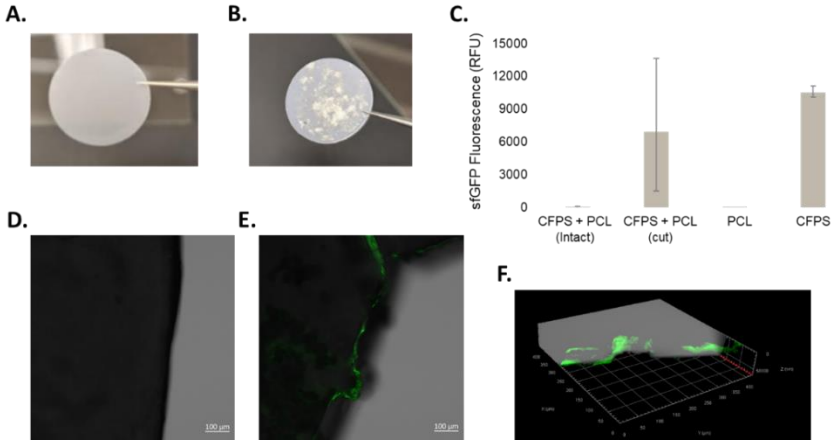


**Figure 8. (A.) PCL disk. (B.) PCL disk with embedded CFPS powder. (C.) Endpoint GFP fluorescence in intact CFPS-PCL disk, cut CFPS-PCL disk, PCL disk without CFPS, and CFPS powder without PCL. (D.) Green fluorescence and differential interference contrast (DIC) dual channel microscopy image of intact CFPS-PCL composite exposed to water. (E.) Green fluorescence and DIC dual channel microscopy image of cut CFPS-PCL composite exposed to water and exhibiting GFP formation at the cut site. (F.) 3D microscopy rendering of the same cut edge of the CFPS-PCL composite shown in (E.).**

## 3. METHODOLOGY

### 3.1 Reagents

Unless otherwise noted, all other reagents were purchased from MilliporeSigma® (St. Louis, MO). Commercial PURExpress® kits were purchased from New England BioLabs, Inc.® (Ipswich, MA). The plasmid template for expression of GFP via CFPS is PY71sfGFP with GenBank® accession number MT346027.[35] Plasmid DNA was purified from transformed *E. coli* using a PureYield™ plasmid miniprep kit (Promega Corporation; Madison, WI), followed by ethanol precipitation to further concentrate and purify the DNA. DNA is stored in RNase- and DNase-free water at -20 °C until reaction assembly.

### 3.2 CFPS reaction preparation

PANOx-SP cell extract is prepared from shake flask cultures of *E. coli* BL21 Star (DE3) according to the growth and sonication protocol detailed previously by Kwon and Jewett.[11] 3-PGA cell extract is prepared from shake flask cultures of *E. coli* BL21 Rosetta2 and lysed by pressure with a Microfluidizer cell homogenizer. The growth and lysis methods were based closely on protocols published previously by Noireaux et al.[3,34]

Lysates were aliquoted, flash frozen in liquid nitrogen, and stored at -80 °C until use in CFPS reaction assembly. To assemble reactions, CFPS components including PURExpress® kit solutions, cell lysates, and reagent stock solutions were thawed on ice, then combined with DNase-free water to reach the final concentrations listed in Table 1. Reaction mixtures were well mixed and distributed 15 µL per well into 96-well, V-bottom, polypropylene plates (Corning® Costar® 3357).

**Table 1. Final concentrations of components in three different CFPS buffers.**

| Component | PANOx-SP | 3-PGA | PURE |
|---|---|---|---|
| Magnesium glutamate | 12 mM | 10 mM + 4.62 mM† | - |
| Potassium glutamate | 130 mM | 30 mM + 49.5 mM† | 100 mM |
| Ammonium glutamate | 10 mM | - | - |
| Magnesium acetate | 3.7 mM* | - | 13 mM |
| Potassium acetate | 16.02 mM* | - | - |
| Tris acetate | 2.67 mM (pH 8.2)* | 1.65 mM (pH 8.2)† | - |
| HEPES | 57 mM (pH 7.4) | 50 mM (pH 8) | 50 mM (pH 7.6) |
| ATP | 1.2 mM | 1.5 mM | 2 mM |
| GTP | 0.85 mM | 1.5 mM | 2 mM |
| CTP | 0.85 mM | 0.9 mM | 1 mM |
| UTP | 0.85 mM | 0.9 mM | 1 mM |
| Folinic acid | 0.072 mM | 0.068 mM | 0.02 mM |
| tRNA | 170.6 µg/mL | 200 µg/mL | 2.8 $A_{260}$ units in 50 µL = 3.5 mg/mL |
| Alanine | 2 mM | 3 mM | 0.3 mM |
| Arginine | 2 mM | 3 mM | 0.3 mM |
| Histidine | 2 mM | 3 mM | 0.3 mM |
| Lysine (monoHCl) | 2 mM | 3 mM | 0.3 mM |
| Aspartic acid | 2 mM | 3 mM | 0.3 mM |
| Glutamic acid | 2 mM | 3 mM | 0.3 mM |
| Isoleucine | 2 mM | 3 mM | 0.3 mM |
| Leucine | 2 mM | 3 mM | 0.3 mM |
| Methionine | 2 mM | 3 mM | 0.3 mM |
| Phenylalanine | 2 mM | 3 mM | 0.3 mM |
| Tryptophan | 2 mM | 3 mM | 0.3 mM |
| Tyrosine | 2 mM | 3 mM | 0.3 mM |
| Valine | 2 mM | 3 mM | 0.3 mM |
| Serine | 2 mM | 3 mM | 0.3 mM |
| Threonine | 2 mM | 3 mM | 0.3 mM |
| Asparagine | 2 mM | 3 mM | 0.3 mM |
| Glutamine | 2 mM | 3 mM | 0.3 mM |
| Cysteine | 2 mM | 3 mM | 0.3 mM |
| Glycine | 2 mM | 3 mM | 0.3 mM |
| Proline | 2 mM | 3 mM | 0.3 mM |
| Phosphoenolpyruvate | 33 mM | - | - |
| NAD | 0.33 mM | 0.33 mM | - |
| CoA | 0.27 mM | 0.26 mM | - |
| Spermidine | 1.5 mM | 1 mM | 2 mM |
| Putrescine | 1 mM | - | - |
| Oxalic acid | 4 mM | - | - |
| T7 RNA polymerase | 100 µg/mL | 100 µg/mL | 10 µg/mL |
| Plasmid DNA | 6.4 nM | 6.4 nM | 6.4 nM |
| RNase Inhibitor | 0.8 U/µL | - | - |
| Cell extract | 26.7% v/v* | 33% v/v† | - |
| Maltodextrin | - | 30 mM | - |
| PEG | - | 1.5 % w/v | - |
| cAMP | - | 0.75 mM | - |
| 3-PGA | - | 30 mM | - |
| DTT | 0.8 mM* | 1 mM+0.33mM† | 1 mM |
| Creatine Phosphate | - | - | 20 mM |

* Items in Style I recipe added as part of the cell extract solution
† Items in Style II recipe added as part of the cell extract solution

### 3.3 Lyophilization of CFPS reactions

To lyophilize CFPS reactions in a microplate, the 96-well plate is dipped in liquid nitrogen and transferred to a shelf-type lyophilizer (SP Scientific, VirTis Wizard 2.0) with initial temperature set to -40 °C. When the lyophilizer chamber is sealed, the vacuum is initiated to reach approximately 200–300 mTorr. Then, primary drying is initiated with a shelf temperature of -20 °C and maintained for four hours. The secondary drying step changes the shelf temperature to 15 °C and is maintained overnight or approximately 17 hours. Microplate samples removed from the lyophilizer were immediately treated with solvent as indicated and rehydrated to monitor protein synthesis activity. Larger volumes of CFPS reaction may be lyophilized in vials. A longer secondary drying step of at least 48 hours is necessary to achieve good powder formation with less than 3 wt% water content. The dry weight of the PANOx-SP CFPS reaction is approximately 76 mg per 1 mL aqueous mixture. The water content was measured with thermogravimetric analysis (TGA).

### 3.4 Solvent treatment and rehydration of CFPS reactions

All solvent treatments were performed in a chemical fume hood. 100 µL of each solvent was added to the lyophilized CFPS reaction mixture in designated wells. No solvent was added to lyophilized control reactions. Wells were sealed with a flexible polypropylene mat (Costar® 3080) to prevent evaporation. Reactions were incubated with solvent for one hour at room temperature. Following solvent incubation, plates were briefly spun at low speed in a centrifuge to settle the insoluble CFPS reaction components, then solvents were removed by aspiration with a pipette without disturbing the pellet. The residual solvent was removed by evaporation. This was achieved either by allowing the plate to sit uncovered in the fume hood for ambient evaporation or applying a vacuum at room temperature using a vacuum oven with the heating element turned off for 20 minutes. After solvent removal, all reactions were rehydrated with 15 µL of DNase free water to return CFPS reaction components to their original aqueous concentration.

### 3.5 Monitoring GFP formation via microplate reader

Immediately after rehydration, plates were sealed with a polypropylene mat, transferred to a BioTek® Synergy™ H1 microplate reader, and incubated at 30 °C for eight hours. Formation of GFP fluorescence was monitored with ex/em: 485/528 nm with a gain of 100. GFP readings in RFU were converted to µM GFP using fluorescence measurements of purified GFP standards.

### 3.6 Solvent casting PLGA composites

There are many possible solvent casting conditions, utilizing different solvents, polymers, concentrations, and casting formats. Two proof-of-concept examples are described in this report.

For the coated "bead" format, droplets of freshly prepared CFPS solution were dropped into a vial containing liquid nitrogen to make frozen spheroid beads. The frozen CFPS beads were lyophilized to form dry, air-filled, 2–5 mm beads as depicted in Figure 5. PLGA 50:50 powder (Sigma-Aldrich® 719870) was dissolved at 14 % w/v in ethyl acetate. One or two beads were placed in glass vials, then 0.2 mL of the PLGA solution was deposited over each bead, the beads were dipped in and out of the PLGA solution several times to build up layers, then submerged to allow the evaporation of the ethyl acetate. The resulting polymer-coated beads were rehydrated and monitored for fluorescence under a blue light with an orange filter to track the formation of GFP.

PLGA-CFPS composites were also cast as films. Lyophilized CFPS reaction mixture was crushed into powder. Several batches with different measured water content were tested (Table 2). PLGA 75:25 (Sigma-Aldrich® 719919) was dissolved 30 % w/v in acetone. CFPS powder was combined with PLGA solution at a 1X concentration, where the weight of powder corresponding to 0.1 mL liquid CFPS reaction was suspended in 0.1 mL PLGA solution. CFPS-PLGA-acetone suspensions (15 µL) were cast as films on glass slides. The acetone was allowed to evaporate, then a razor blade was used to remove films from the glass and place each film in a well of a 96-well microplate. To rehydrate and initiate the reaction, 15 µL of water was added. The plate was incubated and GFP fluorescence measured in a microplate reader as described above.

**Table 2. CFPS powder samples.**

| Sample | %water |
|---|---|
| 20200213 Sample (1) - O.N. dry | 9.45 |
| 20200213 Sample (2) - 3 day dry | 1.30 |
| 20200221 AFRL sample (3 day dry) | 1.36 |
| 20200203 Sample - low vac O.N. dry | 15.3 |

### 3.7 Thermal compression molding of PCL composites

CFPS powder dried using a 48-hour lyophilization protocol was placed between two 20 mg PCL disks and pressed using a manual heat press set to 80 °C, sealing the powder between PCL layers. The thicknesses of the resulting CFPS-PCL disks were approximately 0.2 mm. Cut or intact disks were rehydrated in microplate wells. A Zeiss LSM800 Axio Observer confocal microscope was used to image GFP fluorescence in cut and intact PCL films.

## 4. CONCLUSIONS

The study of the stability of lyophilized cell-free reaction components to challenges posed by polymer casting, including exposure to heat and organic solvents, revealed several new findings. Lyophilized CFPS reactions tolerate exposure to a variety of organic solvents without loss or with only partial loss of transcription and translation activity. The degree to which activity is lost by solvent exposure depends on the type of solvent and the ingredients in the lyophilized mixture. Experiments comparing different CFPS recipes indicate that differences in the cell extract preparation are less important for solvent tolerance than the composition of the other ingredients in a CFPS reaction. For acetone exposure, 10xSS alone was sufficient to provide solvent tolerance to the *E. coli* lysate, and DNA and HEPES buffer components provided partial protection. The advanced heat stability of lyophilized CFPS reactions up to 90 °C for short periods of time reveals another processing step useful for incorporation of these biological systems into materials.

These newly-discovered characteristics of cell-free systems open the door to many previously elusive applications and directions of study. CFPS systems were cast into PLGA and PCL polymers, demonstrating that stability to solvent and heat treatments enables polymer casting. Initial measurements of activity in these formats confirm our hypothesis that the properties of the polymer greatly impact the hydration rate, and therefore activation of the cell-free reaction. We predict that detailed understanding of water intrusion into the composite material and its effect on CFPS activation will fuel the design of coatings and fibers that continuously release CFPS components for an extended activity lifetime. This understanding will include optimization of parameters such as polymer and CFPS formulation and improved casting methodology. Other potential benefits include exploiting new device form factors and controlling localization in cell-free reactions to improve function.

## ACKNOWLEDGMENTS

We thank Stephanie Cole for providing materials for the 3-PGA experiments. We also thank Michael Jewett's laboratory at Northwestern University and Vincent Noireaux's laboratory at the University of Minnesota for sharing advice and detailed protocols. This work was made possible by initial funding from the Office of the Secretary of Defense's Applied Research for the Advancement of Science and Technology Priorities program, as well as partial support from the U.S. Army through the Combat Capabilities Development Command Chemical Biological Center's Biological Engineering for Applied Materials Solutions program. Follow-on funding was provided by the U.S. Army via the Surface Science Initiative Program (PE 0601102A Project VR9) at the Combat Capabilities Development Command Chemical Biological Center.

## REFERENCES

[1] Jewett, M.C.; Swartz, J.R. Mimicking the Escherichia coli cytoplasmic environment activates long-lived and efficient cell-free protein synthesis. *Biotechnol. Bioeng.* **2004**, *86* (1), pp 19–26.

[2] Jewett, M.C.; Calhoun, K.A.; Voloshin, A.; Wuu, J.J.; Swartz, J.R. An integrated cell-free metabolic platform for protein production and synthetic biology. *Mol. Syst. Biol*. **2008**, *4* (1), pp 1–10.

[3] Sun, Z.Z.; Hayes, C.A.; Shin, J.; Caschera, F.; Murray, R.M.; Noireaux, V. Protocols for Implementing an Escherichia coli Based TX-TL Cell-Free Expression System for Synthetic Biology. *J. Visualized Exp.* **2013**, (79), e50762.

[4] Caschera, F.; Noireaux, V. Synthesis of 2.3 mg/ml of protein with an all Escherichia coli cell-free transcription–translation system. *Biochimie.* **2014**, *99*, pp 162–168.

[5] Wu, Y.Y.; Sato, H.; Huang, H.; Culler, S.J.; Khandurina, J.; Nagarajan, H.; Yang, T.H.; Van Dien, S.; Murray, R.M. System-level studies of a cell-free transcription-translation platform for metabolic engineering. 2017, 172007. *bioRxiv*. https://www.biorxiv.org/content/10.1101/172007v1.full (accessed Dec 13, 2020).
[6] Kim, D.-M.; Swartz, J.R. Regeneration of adenosine triphosphate from glycolytic intermediates for cell-free protein synthesis. *Biotechnol. Bioeng.* **2001**, *74* (4), pp 309–316.
[7] Dudley, Q.M.; Karim, A.S.; Jewett, M.C. Cell-free metabolic engineering: Biomanufacturing beyond the cell. *Biotechnol. J.* **2015**, *10* (1), pp 69–82.
[8] Karim, A.S.; Jewett, M.C. A cell-free framework for rapid biosynthetic pathway prototyping and enzyme discovery. *Metab. Eng.* **2016**, *36*, pp 116–126.
[9] Karim, A.S.; Heggestad, J.T.; Crowe, S.A.; Jewett, M.C. Controlling cell-free metabolism through physiochemical perturbations. *Metab. Eng.* **2018**, *45*, pp 86–94.
[10] Silverman, A.D.; Karim, A.S.; Jewett, M.C. Cell-free gene expression: an expanded repertoire of applications. *Nat. Rev. Genet.* **2020**, *21* (3), pp 151–170.
[11] Kwon, Y.-C.; Jewett, M.C. High-throughput preparation methods of crude extract for robust cell-free protein synthesis. *Scientific Reports.* **2015**, *5*, 8663.
[12] Shimizu, Y.; Inoue, A.; Tomari, Y.; Suzuki, T.; Yokogawa, T.; Nishikawa, K.; Ueda, T. Cell-free translation reconstituted with purified components. *Nat. Biotechnol.* **2001**, *19* (8), pp 751–755.
[13] Gräwe, A.; Dreyer, A.; Vornholt, T.; Barteczko, U.; Buchholz, L.; Drews, G.; Ho, U.L.; Jackowski, M.E.; Kracht, M.; Lüders, J.; Bleckwehl, T.; Rositzka, L.; Ruwe, M.; Wittchen, M.; Lutter, P.; Müller, K.; Kalinowski, J. A paper-based, cell-free biosensor system for the detection of heavy metals and date rape drugs. *PLoS One.* **2019**, *14* (3), e0210940.
[14] Takahashi, M.K.; Tan, X.; Dy, A.J.; Braff, D.; Akana, R.T.; Furuta, Y.; Donghia, N.; Ananthakrishnan, A.; Collins, J.J. A low-cost paper-based synthetic biology platform for analyzing gut microbiota and host biomarkers. *Nat. Commun.* **2018**, *9* (1), p 3347.
[15] McNerney, M.P.; Zhang, Y.; Steppe, P.; Silverman, A.D.; Jewett, M.C.; Styczynski, M.P. Point-of-care biomarker quantification enabled by sample-specific calibration. *Sci. Adv.* **2019**, *5* (9), eaax4473.
[16] Meyer, A.; Saaem, I.; Silverman, A.; Varaljay, V.A.; Mickol, R.; Blum, S.; Tobias, A.V.; Schwalm III, N.D.; Mojadedi, W.; Onderko, E.; Bristol, C.; Liu, S.; Pratt, K.; Casini, A.; Eluere, R.; Moser, F.; Drake, C.; Gupta, M.; Kelley-Loughnane, N.; Lucks, J.P.; Akingbade, K.L.; Lux, M.P.; Glaven, S.; Crookes-Goodson, W.; Jewett, M.C.; Gordon, D.B.; Voigt, C.A. Organism Engineering for the Bioproduction of the Triaminotrinitrobenzene (TATB) Precursor Phloroglucinol (PG). *ACS Synth. Biol.* **2019**, *8* (12), pp 2746–2755.
[17] Pardee, K. Perspective: Solidifying the impact of cell-free synthetic biology through lyophilization. *Biochem. Eng. J.* **2018**, *138*, pp 91–97.
[18] Bundy, B.C.; Hunt, J.P.; Jewett, M.C.; Swartz, J.R.; Wood, D.W.; Frey, D.D.; Rao, G. Cell-free biomanufacturing. *Curr. Opin. Chem. Eng.* **2018**, *22*, pp 177–183.
[19] Karig, D.K.; Bessling, S.; Thielen, P.; Zhang, S.; Wolfe, J. Preservation of protein expression systems at elevated temperatures for portable therapeutic production. *J. R. Soc., Interface.* **2017**, *14* (129), 20161039, pp 1–8.
[20] Gregorio, N.E.; Kao, W.Y.; Williams, L.C.; Hight, C.M.; Patel, P.; Watts, K.R.; Oza, J.P. Unlocking Applications of Cell-Free Biotechnology through Enhanced Shelf Life and Productivity of E. coli Extracts. *ACS Synth. Biol.* **2020**, *9* (4), pp 766–778.
[21] Smith, M.T.; Berkheimer, S.D.; Werner, C.J.; Bundy, B.C. Lyophilized Escherichia coli -based cell-free systems for robust, high-density, long-term storage. *BioTechniques.* **2014**, *56* (4), pp 186–193.
[22] Sadat Mousavi, P.; Smith, S.J.; Chen, J.B.; Karlikow, M.; Tinafar, A.; Robinson, C.; Liu, W.; Ma, D.; Green, A.A.; Kelley, S.O.; Pardee, K. A multiplexed, electrochemical interface for gene-circuit-based sensors. *Nat. Chem.* **2020**, *12* (1), pp 48–55.
[23] Pardee, K.; Green, A.A.; Ferrante, T.; Cameron, D.E.; DaleyKeyser, A.; Yin, P.; Collins, J.J. Paper-Based Synthetic Gene Networks. *Cell.* **2014**, *159* (4), pp 940–954.
[24] Duyen, T.T.M.; Matsuura, H.; Ujiie, K.; Muraoka, M.; Harada, K.; Hirata, K. Paper-based colorimetric biosensor for antibiotics inhibiting bacterial protein synthesis. *J. Biosci. Bioeng.* **2017**, *123* (1), pp 96–100.
[25] Tibbitt, M.W.; Dahlman, J.E.; Langer, R. Emerging Frontiers in Drug Delivery. *J. Am. Chem. Soc.* **2016**, *138* (3), pp 704–717.
[26] Tian, H.; Liu, Z.; Zhang, M.; Guo, Y.; Zheng, L.; Li, Y.C. Biobased Polyurethane, Epoxy Resin, and Polyolefin Wax Composite Coating for Controlled-Release Fertilizer. *ACS Appl. Mater. Interfaces*. **2019**, *11* (5), pp 5380–5392.
[27] Ding, D.; Zhu, Q. Recent advances of PLGA micro/nanoparticles for the delivery of biomacromolecular therapeutics. *Mater. Sci. Eng., C.* **2018**, *92*, pp 1041–1060.

[28] Kamaly, N.; Yameen, B.; Wu, J.; Farokhzad, O.C. Degradable Controlled-Release Polymers and Polymeric Nanoparticles: Mechanisms of Controlling Drug Release. *Chem. Rev.* **2016**, *116* (4), pp 2602–2663.
[29] Dennis, P.B.; Walker, A.Y.; Dickerson, M.B.; Kaplan, D.L.; Naik, R.R. Stabilization of Organophosphorus Hydrolase by Entrapment in Silk Fibroin: Formation of a Robust Enzymatic Material Suitable for Surface Coatings. *Biomacromolecules.* **2012**, *13* (7), pp 2037–2045.
[30] Klibanov, A.M. Improving enzymes by using them in organic solvents. *Nature.* **2001**, *409* (6817), pp 241–246.
[31] Schmitke, J.L.; Stern, L.J.; Klibanov, A.M. Comparison of x-ray crystal structures of an acyl-enzyme intermediate of subtilisin Carlsberg formed in anhydrous acetonitrile and in water. *Proc. Natl. Acad. Sci. U. S. A.* **1998**, *95* (22), pp 12918–12923.
[32] Kay, J.E.; Jewett, M.C. A cell-free system for production of 2,3-butanediol is robust to growth-toxic compounds. *Metab. Eng. Commun.* **2020**, *10*, p e00114.
[33] Doukyu, N.; Ogino, H. Organic solvent-tolerant enzymes. *Biochem. Eng. J.* **2010**, *48* (3), pp 270–282.
[34] Garamella, J.; Marshall, R.; Rustad, M.; Noireaux, V. The All E. coli TX-TL Toolbox 2.0: A Platform for Cell-Free Synthetic Biology. *ACS Syn. Biol.* **2016**, *5* (4), pp 344–355.
[35] Bundy, B.C.; Swartz, J.R. Site-Specific Incorporation of p-Propargyloxyphenylalanine in a Cell-Free Environment for Direct Protein−Protein Click Conjugation. *Bioconjugate Chem.* **2010**, *21* (2), pp 255–263.

# Cooperative interactions between functionalized particles and binders in polymer composites and their effect on chemical transport

Mark J. Varady[a]*, Melissa S. Hulet[b], Adam R. Hinkle[c], Thomas P. Pearl[c], Melissa L. Sweat[a], Kenneth E. Strawhecker[d], Alice M. Savage[d], Jonathan P. Ligda[d], Yossef A. Elabd[e]
[a]U.S. Army Combat Capabilities Development Command Chemical Biological Center, Research & Technology Directorate, 8198 Blackhawk Rd, Aberdeen Proving Ground, MD 21010
[b]Leidos, 1750 Presidents St, Reston, VA 20190
[c]DCS Corporation, 6909 Metro Park Dr, Suite 500, Alexandria, VA 22310
[d]U.S. Army Research Laboratory, 2800 Powder Mill Rd, Adelphi, MD 20783
[e]Department of Chemical Engineering, Texas A&M University, 3122 TAMU Room 200, College Station, TX 77843

## ABSTRACT

Protective coatings on military assets are complex polymer composites consisting of a high loading of several different particle types to achieve the desired coating functionality. The transport properties at the particle-polymer interface can differ significantly from those in the polymer bulk, and when the interfacial regions overlap, undesirable fast chemical transport pathways can open up. Improving the chemical resistance of protective coatings while maintaining the desired properties requires a detailed understanding of how the interface can be tuned to improve the interfacial transport properties. In this work, atomic force microscopy-based colloidal force spectroscopy and imaging techniques are used to elucidate the nature of the particle-polymer interface in silica-polyurethane composites and how this interface changes with modification of the silica surface. Corresponding measurements of the chemical transport dynamics in these composites are measured using a well-established attenuated total reflectance Fourier transform infrared spectroscopy technique. Parallel molecular dynamics studies are also performed on a polyurethane-silica interface to determine how the polymer structure is influenced by modification of the silica surface and exposure to a chemical. Comparing how specific modifications to the particle surface influence the nature of the interface versus how they influence chemical transport is an important step in developing structure-property relationships for chemical transport in polymer composites and developing more rational approaches to controlling transport properties.

**Keywords:** Transport phenomena, diffusion, polymer composites, atomic force microscopy, colloidal force spectroscopy, interface adhesion, chemical resistance

## 1. INTRODUCTION

Protective coatings on military assets are complex polymer composites consisting of different solid particle types and sizes bound together by a polymer binder matrix. The particles provide rheology modification for processing and application, required optical and signature management properties of the coating, and camouflage. To achieve all of these functions, the particle (or solids) loading in the polymer binder must be relatively high, up to 60 wt%. In these high-loading composite coatings, it has been observed that the breakthrough of a chemical is significantly faster than for the corresponding pure polymer. Since the particles used in these systems are impermeable, this suggests that the transport properties of the polymer are modified by the presence of the particles. At the polymer-particle interface, the arrangement of polymer chains can be different than in the bulk, and the nature of the interface is mediated by interactions between the polymer and particle. Thus, to understand and control chemical transport in polymer composites, it is necessary to determine how changes in the polymer-particle interface manifest as changes in the overall transport properties of the system to identify effective strategies for modifying the particle surface to improve chemical resistance.

The major application areas for polymer composites in the context of chemical transport is for chemical separations and ion exchange membranes for fuel cells. In mixed matrix membranes, functional porous materials such as zeolites

and metal-organic frameworks (MOFs) are incorporated into a polymer membrane to improve the membrane permeability and selectivity for a given separations process. The importance of tuning the polymer-solid interface to prevent undesirable transport pathways has been noted; for example, by Bachman et al.,[1] who showed that ethane/ethylene separation using composites of 6FDA-DAM polymer with M2(dobdc) MOFs was non-selective in cases where there was poor integration of the MOF in the polymer. Su et al.[2] showed a broadening of the glass transition in PEG-silica membranes with increasing particle loading using differential scanning calorimetry and related this to the permeability through the membrane. A whole review article has been dedicated to tuning the interface in mixed matrix membranes.[3] Although most studies focus solely on the macroscopic transport properties of the membrane, some work has been done to elucidate chemical transport near the solid polymer interface using neutron reflectivity[4,5] and positron annihilation lifetime spectroscopy.[6,7] Molecular dynamics calculations have also been employed to investigate details of the interface during chemical transport: for example $CO_2$ and $CH_4$ diffusion near a polyimide-zeolite interface.[8]

The influence of the local particle-polymer interface on macroscale mechanical properties of polymer composites have also been recognized and led to several studies on this topic. For example, atomic force microscopy (AFM),[9] nanoindentation,[10,11] and nanoscratch[12] techniques have been used to show that the polymer exhibits different mechanical properties near a solid interface compared to the bulk. AFM phase contrast imaging can distinguish different regions of a material by variations of viscoelastic response or tip-sample interaction.[13,14] Details of the interactions between particles and polymer surfaces have also been studied using so-called colloidal force spectroscopy using AFM.[15,16] In colloidal force spectroscopy, a small particle (~1–50 µm diameter) is attached to the end of an AFM cantilever as shown in Figure 1. This particle is brought in contact with the surface, pressed in, then pulled off. During this process, the deflection, $\delta$, of the cantilever is recorded and converted to a force, $F$, with knowledge of the cantilever spring constant, $k$ ($F = k\delta$). The adhesion between the particle and the surface is captured during the retraction, or pull-off, of the cantilever. Pham et al.[17] examined deformation and adhesion of rubbery polydimethylsiloxane with a silica colloidal probe, and illustrated the need to account for capillary forces due to the liquid-like behavior of the soft polydimethylsiloxane. Feldman et al.[18] measured the adhesion of both polar and non-polar colloidal probes on an array of polymers, providing general suggestions to achieve quantitative data.

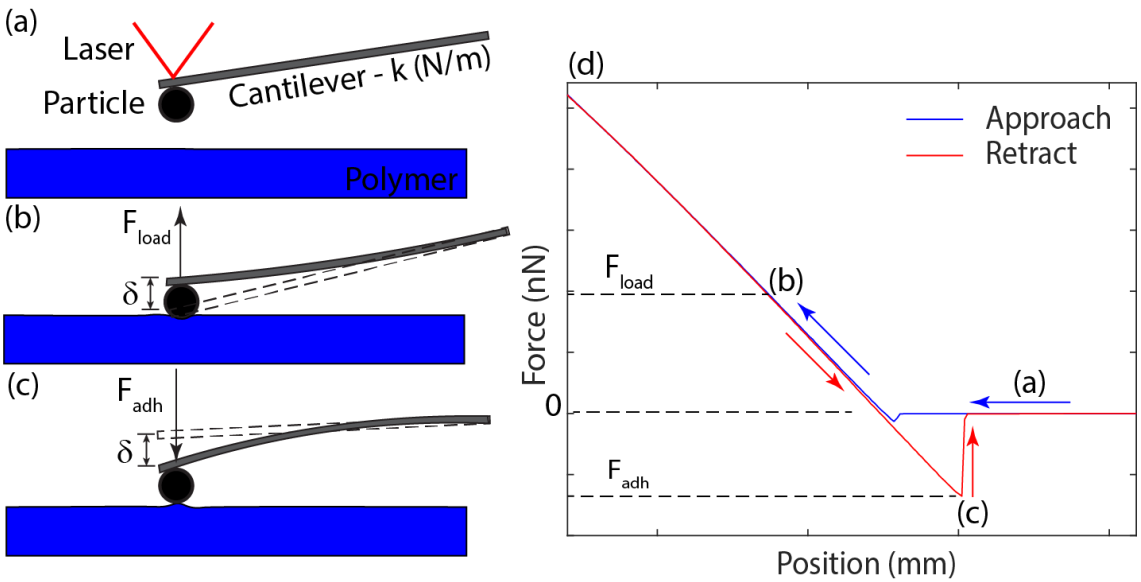


**Figure 1. Schematic of colloidal force spectroscopy using AFM: (a) The cantilever with attached particle in a retracted (from the surface) position. (b) The particle pressed into the surface resulting in a positive cantilever deflection. (c) The particle adhering to the surface during pull-off resulting in a negative cantilever deflection. (d) Plot of the force on the particle versus vertical cantilever position.**

This work focuses on utilizing the AFM imaging of composite cross-sections and colloidal force spectroscopy to characterize the polymer-particle interface and how it changes with different particle surface modifications and chemical exposure. Corresponding measurements of chemical transport through the composite materials are used to correlate changes in the interface to corresponding changes in transport properties. Additionally, molecular dynamics simulations of the particle-polymer interface are used to assess changes in local structure and transport properties with surface modification.

## 2. MATERIALS AND METHODS

### 2.1 Materials

Polyurethane (PU) and polyhydroxyurethane polymers were synthesized by the U.S. Army Combat Capabilities Development Command (DEVCOM) Army Research Laboratory (ARL), and described in a previous publication.[19]

Silica and functionalized silica particles were obtained from Sigma-Aldrich® (9–13 µm glass spheres) or Polysciences, Inc. (0.5 µm and 5 µm silica, carboxyl functionalized silica, and amine functionalized silica).

Solutions of 100 mg/mL PU or polyhydroxyurethane in cyclopentanone (Sigma-Aldrich®, > 99 % purity) were prepared and spin cast onto attenuated total reflectance (ATR) crystals (Pike Technologies, Germanium 45 deg, 80 mm x 10 mm x 4 mm) or glass slides (Fisher Scientific™, 1-inch diameter). For the ATR crystals, 200 µL of solution was spread onto the ATR crystal and rotated at 300 rpm for 5 minutes in a spin coater (WS-650 Series Spin Processer, Laurell Technologies®). For the glass slides, 200 µL of solution was spread onto the glass slide and rotated at 1,500 rpm for 5 minutes in a spin coater.

Silica-polymer composites were created by dispersing varying masses of 0.5 µm particles in 1 mL of cyclopentanone using a homogenizer (Scilogex D160) operating at ~9,000 rpm for 10 minutes before mixing with the 100 mg/mL polymer solutions as described above.

Colloidal AFM probes with bare particles were acquired from Applied NanoStructures, Inc. (5-µm silica particle on $k$ ~20 N/m cantilever, ACTA-$SiO_2$-A). Colloidal probes with functionalized particles were obtained from Novascan (~5 µm amine or carboxyl functionalized polystyrene or silica particle on end of $k$ ~16 N/m cantilever).

### 2.2 Methods

Composites were cross-sectioned using either a Leica EM UC7 ultramicrotome or a Leica EM TIC020 triple beam ion miller. For both techniques, a ~500 µm thick PU-silica composite was rough-cut to expose the cross-section. For microtoming, the samples were cooled to -80 °C and cut with a glass knife. For ion beam milling, the samples were polished by aligning the ion beam parallel to the surface.

Imaging and colloidal force spectroscopy were performed with a Nanosurf™ Flex Axiom AFM. Phase contrast and force modulation imaging were used to image the composite cross-sections to resolve the particles and probe near the particle surface. Each colloidal AFM probe was calibrated prior to use by using the thermal tuning capability of the instrument to obtain the resonant frequency and spring constant of the cantilever. Additionally, the deflection sensitivity (relating photodetector voltage to cantilever deflection) of each colloidal probe was obtained by measuring the photodetector voltage as a function of $z$-position as the colloidal probe is pressed into a rigid silicon wafer. Both the cantilever spring constant and deflection sensitivity are required for obtaining quantitatively accurate measurements of the particle-polymer interaction force. Standard force spectroscopy was performed by approaching the colloidal probe to the polymer surface using default settings, performing a 2 µm indentation over 1 second followed by a pull-off over 1 second. Modifications to the standard force spectroscopy procedure were also investigated and are described in the Results and Analysis section.

Details of the chemical breakthrough experiments have been described in previous publications.[19] Briefly, a controlled vapor concentration was created by flowing dry $N_2$ gas through a custom blown, glass saturator cell (Glassblowers, Inc.) that was saturated with the desired liquid chemical. The vapor concentration delivered (i.e., effective partial pressure or activity) was modulated by combining the saturated vapor flow with dry $N_2$ and setting the corresponding mass flow controllers in the desired ratio with a total flow rate of 50 SCCM in all cases. This flow was passed over the top of the polymer-coated ATR crystal and infrared light was shone through the backside of the crystal, creating an evanescent wave at the polymer-crystal interface. Monitoring the intensity of the reflected infrared light as a function of wavelength allows the presence of species with corresponding absorption bands to be detected. Because the evanescent wave penetrates less than 600 nm into the polymer, this measurement only detects species near the polymer-crystal interface. Integration over the absorption band(s) corresponding to a particular species of interest allows quantification of the amount of species absorbed as a function of time.

## 3. RESULTS AND ANALYSIS

### 3.1 Particle-polymer adhesion

One challenge in using colloidal force spectroscopy to quantify the interaction strength between a single particle and the surface of a polymer is if the operating temperature of the composite is below the glass transition temperature ($T_g$) of the polymer, as is the case for the PU used in this work ($T_g$ ~60 °C). In this situation, the polymer-particle interface is unable to achieve its equilibrium configuration due to the slow relaxation dynamics of the polymer chains. In contrast, when the composite is prepared by solution casting, the $T_g$ of the solution is much lower than the processing temperature and the polymer chains are free to reach their equilibrium configuration as the solvent evaporates. To ensure the interface achieves equilibrium in the colloidal probe experiments, a thermal annealing procedure is used in which the silica particle is brought into contact with the PU surface at operating temperature (below $T_g$). The system is then heated to above $T_g$ for a short time then cooled back to operating temperature while maintaining the same contact force, then retracted to obtain the force curve as illustrated in Figure 2.

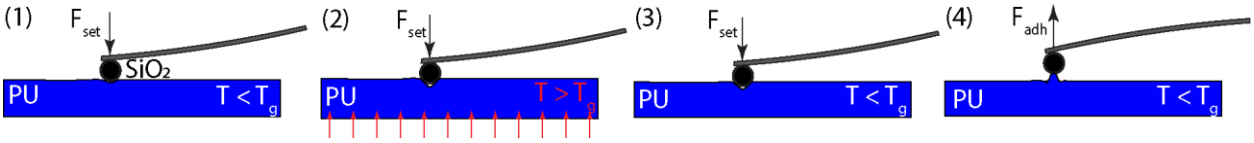


**Figure 2. Schematic of thermal annealing procedure employed for adhesion force experiments: (1) the colloidal probe is brought into contact with polymer surface at a set force at the operating temperature, (2) the system is heated above $T_g$ to allow the particle-polymer interface to come to equilibrium maintaining the set force, (3) the system is cooled back to operating temperature, and (4) the probe is pulled off the surface to acquire the force curve.**

This procedure was followed using a set force of 80 nN, an operating temperature of 40 °C for 30 seconds, then heated to a temperature of 85 °C for 90 seconds, and then the system was allowed to cool back to 40 °C over a period of 480 seconds before retracting the colloidal probe from the surface. The resulting force curves for 5 µm diameter bare silica and carboxyl-functionalized silica spheres on PU are shown in Figure 3 along with the actual set force during the 600 second hold period.

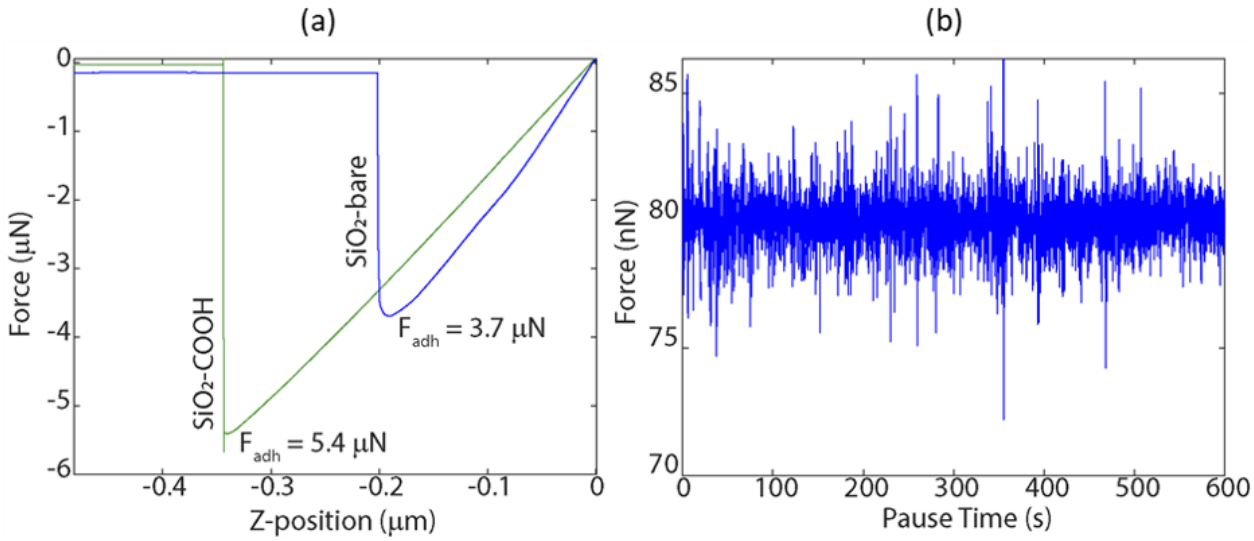


**Figure 3. (a) Adhesion force curves for 5 µm bare (blue) and carboxyl-functionalized (green) silica particles on PU with thermal annealing procedure. (b) Contact force of the bare silica particle on PU during thermal annealing process.**

Comparing the adhesion force data for different surface treatments requires knowledge of the contact area to normalize the adhesion force to a pressure. This was obtained in separate colloidal probe experiments and using the Johnson-Kendall-Roberts contact mechanics model to compute the contact radius, $a$ equation (1), from the measured indentation, $\delta$ equation (2), and adhesion force, $F_{adh}$ equation (3), on PU for each silica surface treatment.

$$a = \left[\frac{3(1-\nu^2)R}{4E}\left(F + 3\pi RW + \sqrt{6\pi RWF + (3\pi RW)^2}\right)\right]^{1/3}, \quad (1)$$

$$\delta = \frac{a^2}{R} - \frac{2}{3}\sqrt{\frac{9(1-\nu^2)\pi Wa}{2E}}, \quad (2)$$

and,

$$F_{adh} = \frac{3\pi RW}{2}. \quad (3)$$

Figure 4 shows the contact radius and the PU modulus as a function of temperature computed from the Johnson-Kendall-Roberts model for each type of silica particle. From both plots, there is clearly a transition between 60–70 °C, which corresponds to the known $T_g$ of the PU used in these experiments. Using the contact radius $a$ ~850 nm for bare silica and $a$ ~900 nm for carboxyl functionalized silica, $p_{adh}$ = 6.5 pN/nm$^2$ for bare silica and $p_{adh}$ = 8.5 pN/nm$^2$ for carboxyl functionalized silica on PU.

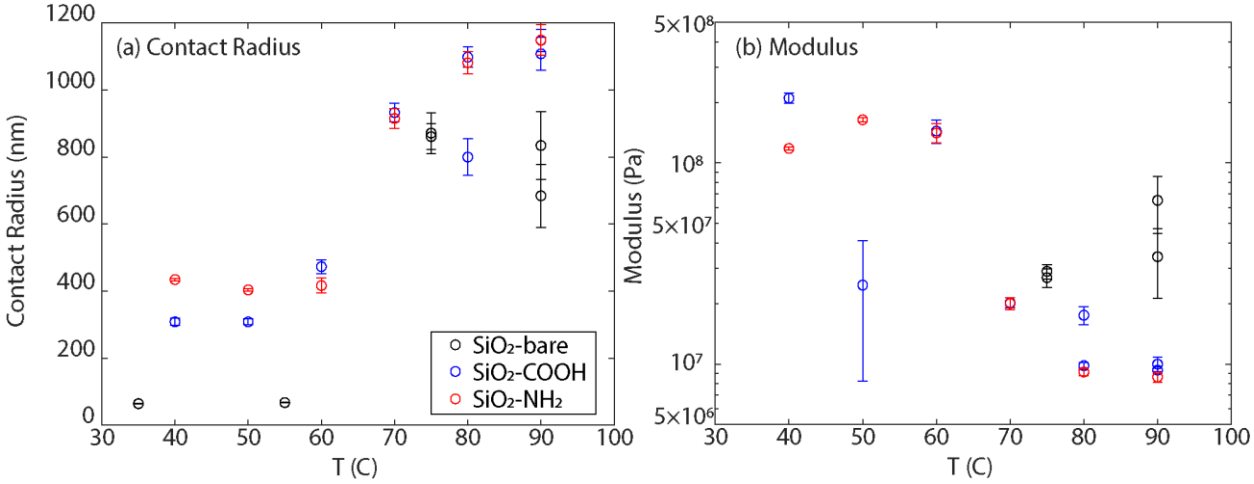


**Figure 4. Results of colloidal probe experiments for bare (black), carboxyl-functionalized (blue), and amine-functionalized (red) 5 µm silica particles on PU: (a) contact radius and (b) PU modulus as a function of temperature.**

### 3.2 Cross-section imaging

Cross-sections of a 20 wt% of 500 nm diameter silica particles in PU were formed using the cryotoming method and imaged using AFM force modulation imaging and scanning electron microscopy which revealed that the particles were pushed out of the polymer by the cryotome blade rather than cut. Further work on cross-sectioning using the cryotoming method is planned in collaboration with DEVCOM ARL using a diamond knife instead.

The same 20 wt% silica-PU composites were also cross-sectioned using the ion polishing method. These cross-sections were imaged using both force modulation and phase contrast imaging using the AFM. Figure 5 shows representative images using the phase contrast imaging. The lower magnification phase contrast image shows different phases in the PU as expected due to the hard and soft segments typical in polyurethanes. Additionally, there are striations on the surface, which seem to be a result of the ion bombardment during the polishing process and makes it difficult to resolve a clear interfacial region around the particle. However, the particles themselves are very clearly resolved using phase contrast imaging and the particles do seem to be sectioned as desired.

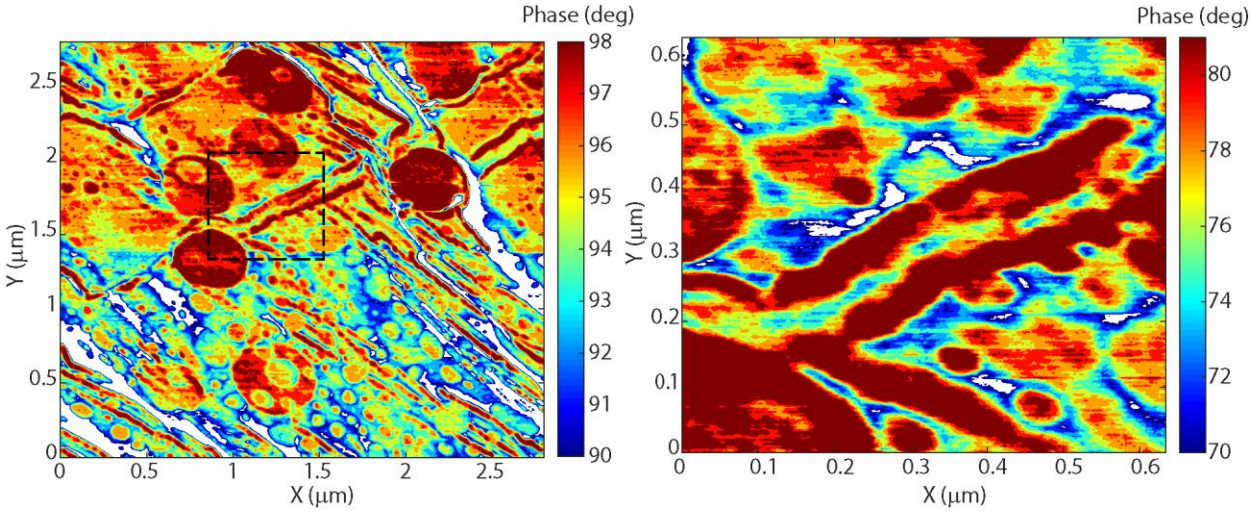


**Figure 5. Cross-section images of PU-silica composite obtained using AFM phase contrast imaging. The composite consists of 20 wt% of 500 nm silica particles in polyurethane and was cross-sectioned using ion polishing. The image on the right corresponds to the region enclosed in the dashed black line of the image on the left.**

Force modulation images are shown in Figure 6, and the particles are also clearly resolved in this case. Again, the striations on the surface indicate the damage to the surface caused by the ion polishing process. A single particle was isolated and imaged using force modulation as shown on the right side of Figure 6, and it is difficult to resolve an interfacial region around this particle at the image magnification.

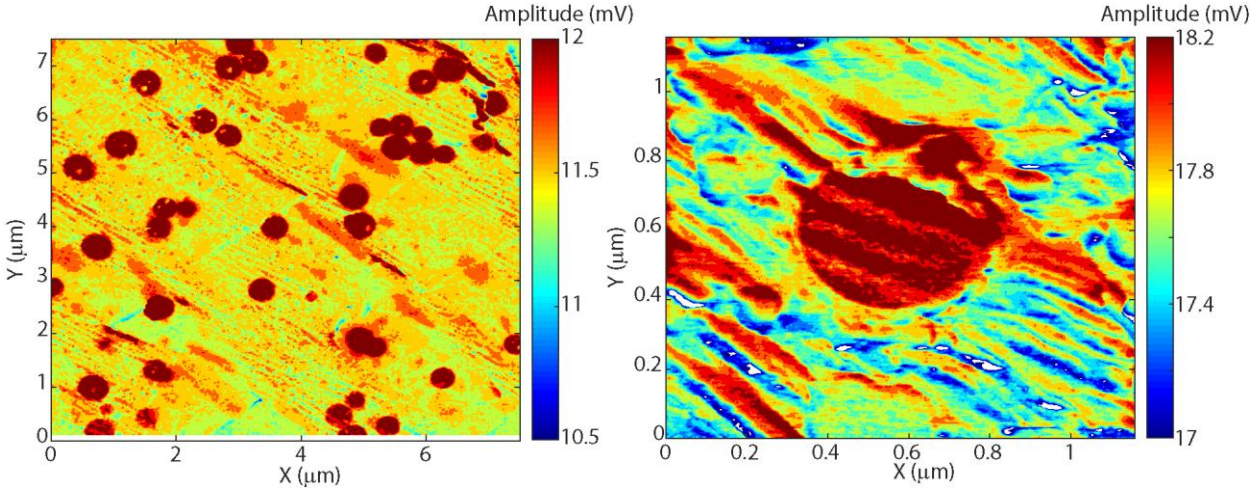


**Figure 6. Cross-section images of PU-silica composite obtained using AFM force modulation imaging. The composite consists of 20 wt% of 500 nm silica particles in polyurethane and was cross-sectioned using ion polishing.**

Another way to image the surface is through adhesion force mapping. Adhesion force line and area scans are shown in Figure 7, which show an interfacial region around the particle surface on the order of 10 nm thickness. In the 2D scan, it is apparent that the interfacial regions of two particles overlap and display a lower adhesion force compared to the bulk polymer.

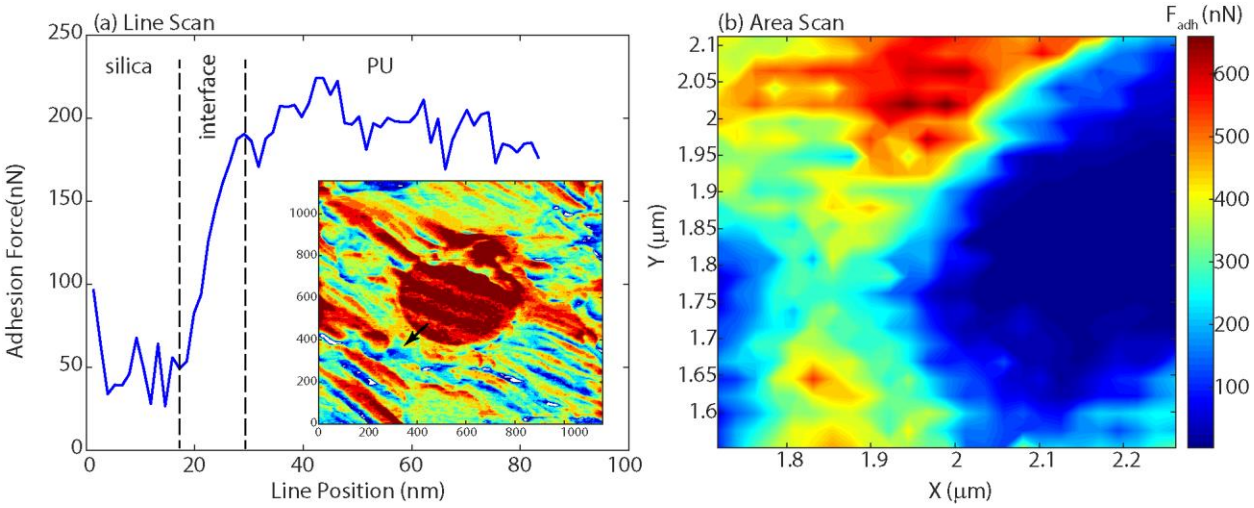


**Figure 7. Adhesion force maps on silica-PU cross-section in (a) one-dimension and (b) two-dimensions. The inset in (a) shows the corresponding force modulation image around a single particle and the line along which the scan was done with the arrow pointing in the scan direction.**

Further work is needed on attempting to resolve interfacial properties around the particles in PU-silica composites. Improved quality cross-sections will be attempted by tuning the ion energy and sample temperature in the ion polishing process and by using a diamond knife for the cryotomed samples. Samples will also be scanned using a higher resolution AFM in collaboration with DEVCOM ARL.

### 3.3 Chemical breakthrough in polymer composites

Chemical breakthrough experiments were performed on pure PU and silica-PU composite films with different particle loadings (10 wt%, 20 wt%, 30 wt%, and 40 wt% particles) and surface functionalization's (bare or no functionalization, carboxyl and amine). In all cases, the films were exposed to 0.1 activity methanol vapor in $N_2$ at 25 °C for 24 hours. Figure 8 shows the normalized MeOH peak area (1010–1039 $cm^{-1}$) as a function of time for each composite film along with the corresponding curve for pure PU. For all three particle types, the breakthrough dynamics become slower with increasing particle loading up to 30 wt%, indicating that the particles act as a barrier to diffusion. The deviation comes at 40 wt% where the bare silica particles show an increase in breakthrough rate while the breakthrough rate continues to slow for the functionalized particles, indicating the possibility of a less dense/thicker interfacial region around the bare silica particles compared to that of the functionalized particles. This aligns with the preliminary adhesion force measurements, which showed a 25 % lower interaction strength of bare silica with PU compared to carboxyl functionalized silica.

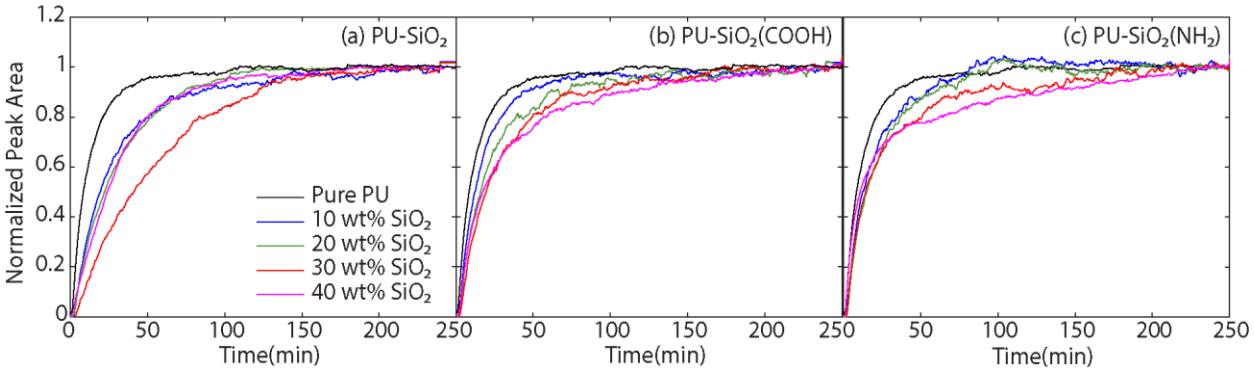


**Figure 8. Breakthrough of MeOH in PU-silica composites, (a) bare silica, (b) carboxyl-functionalized silica, and (c) amine-functionalized silica with particle loadings of 10 (blue), 20 (green), 30 (red), and 40 (magenta) wt%. Curves for pure PU are in black. Each curve is an average of 2–3 experimental runs.**

### 3.4 Molecular dynamics simulations

Molecular dynamics (MD) calculations have been performed to characterize the interfacial region between a silica particle and the surrounding PU which is believed to experience local transport properties that differ in a significant

way from the bulk (non-interfacial) PU. These computational studies have been undertaken to complement concurrent transport experiments and to help provide a more revealing description of the underlying physics at the atomistic and molecular scales that affect macroscopic transport. To that end, we have begun studying structural features of the polymer (e.g., local density near the particle interface) and have begun simulations that address surface modification of the particles. An important goal of the MD is to assess the effect that modified particle surfaces (e.g., the addition of a functional group) have upon the interfacial region, and therefore upon the diffusive transport of a chemical penetrant.

The MD systems have been prepared with 10–25 PU chains of 10–15 monomer units and are randomly packed into a large simulation cell that is compressed to a density of approximately 1.2 g/cm$^3$. The systems are heated using the canonical constant volume and temperature (NVT) ensemble to 400 K and then cooled below $T_g$ and equilibrated for 10 ns under constant temperature and pressure (NPT) ensemble conditions. A slab of amorphous silica is located in the center of the simulation cell and is held rigid throughout all simulations with the PU. As shown in Figure 9a, the systems are approximately 12 nm in the longest dimension which is allowed to relax, and they have a fixed cross-sectional area of 30.25 nm$^2$. The MD setup describes a flat interface between the silica and the PU and therefore considers the large-particle limit (microns) found in actual PU coatings. Periodic boundaries are used in all directions.

In the majority of the simulations the polymer consistent force field (PCFF) provided by the commercially available software BIOVA Materials Studio has been used to parameterize the systems, while the calculations have been carried out using the open-source LAMMPS MD code. Additional MD calculations using a version of the chemically reactive force field, ReaxFF, were carried out to help validate the accuracy of the PCFF and determine to what extent it can describe chemistry and structure formation within the important interfacial region. Initial results suggest that the PCFF is in good agreement with predictions using ReaxFF insofar as coordination analysis, indicating very similar PU systems after the protocol described above.

Figure 9b, shows the average local density of the PU along the relaxed dimension of the simulation cell. A distinct, interfacial region extending about 1.0 nm in size is present where the PU density fluctuates significantly before tending to its bulk average. This behavior is seen using both the PCFF and ReaxFF potentials. Interestingly, when the system is heated beyond melting using ReaxFF, and the PU chain structure is destroyed, the cooled system exhibits no signature of the interfacial region in the density profiles. This result and the fluctuations described earlier indicate that layering of the polymer chains may play an important role in the interfacial region.

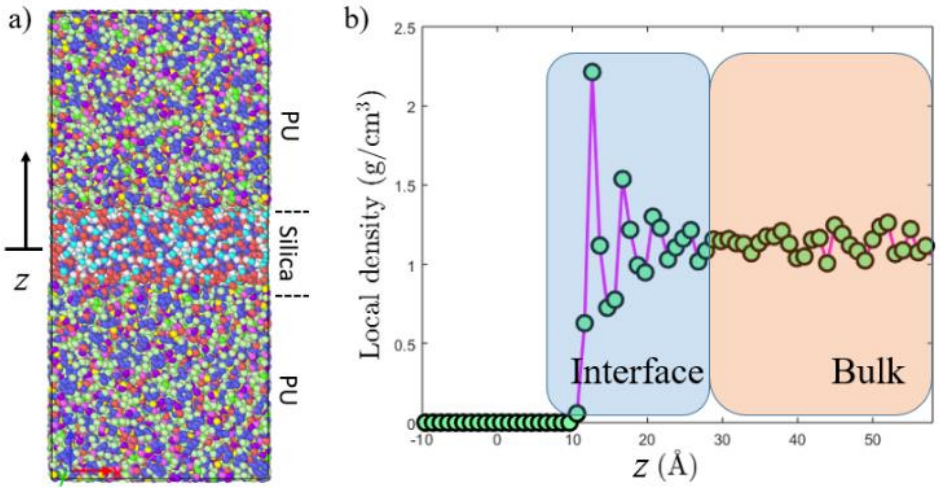


**Figure 9. (a) The polymer-silica composite system is approximately 12 nm in the *z*-direction after equilibration and has a fixed square cross-sectional area of 30.25 nm$^2$. The slab of amorphous silica in the center is held rigid, while the PU is cooled below $T_g$. (b) The average local density of the PU along the *z*-dimension using bins of approximately 0.1 nm wide. A distinctive interfacial region is seen and is characterized by fluctuations in the PU density.**

Additional simulations are being carried out to calculate diffusivities for a range of chemical penetrants in the PU systems that vary in their molecular size (e.g., methanol, butanol, and hexanol), as well as hydrogen-bond strength (e.g., hexane, pentylamine, and hexanol). At the same time, permutations of the system have been created to address the ability of a modified particle surface to affect diffusion of these penetrants and will closely align with complementary experiments.

## 4. CONCLUSIONS AND NEXT STEPS

A method for measuring *ex situ* particle-polymer adhesion using colloidal probe spectroscopy was developed using a thermal annealing procedure to ensure that the interface reaches an equilibrium state before pull-off. Preliminary results suggest the possibility of resolving differences in the particle-polymer interaction for different surface treatments of the silica particle, although additional runs are needed to achieve statistically significant results. Cross-sections of the PU-silica composites were also imaged using AFM phase contrast, force modulation, and adhesion force mapping, and interfacial regions were resolved using adhesion force mapping. Damage to the surface introduced by the ion polishing cross-sectioning method prevented high-resolution imaging of the interface in phase contrast and force modulation modes. Further work on improving the quality of the composite cross-sections is planned by modifying the ion energy in the ion polishing and attempting to cryotome the composite with a diamond knife. Additionally, both the colloidal force and cross-section imaging will be performed with the sample exposed to chemical vapor to assess how the interfacial region changes as a chemical penetrant is introduced to the composite.

Breakthrough curves generally showed slower transport for higher particle loadings for all silica surface modifications except for bare silica, which showed an increase in breakthrough rate between 30–40 wt% particle loading. This aligns with the preliminary adhesion force results showing that bare silica has about a 25 % lower adhesion to PU than carboxyl functionalized silica.

MD simulations were able to resolve a clear interfacial region at near the silica interface in which the structure and density of the PU differed from the bulk. Further simulations are being run that examine the effects of functionalization of the silica surface and introduction of a chemical species for direct comparison with experimental results.

## ACKNOWLEDGMENTS

The authors would like to thank Dr. Brent Mantooth for his insights on transport in polymer composites. Funding was provided by the U.S. Army via the Surface Science Initiative Program (PE 0601102A Project VR9) at the Combat Capabilities Development Command Chemical Biological Center.

## REFERENCES

[1] Bachman, J.E.; Smith, Z.P.; Li, T.; Xu, T.; Long, J.R. Enhanced ethylene separation and plasticization resistance in polymer membranes incorporating metal-organic framework nanocrystals. *Nat. Mater.* **2016**, *15* (8), pp 845–849.

[2] Su, N.C.; Smith, Z.P.; Freeman, B.D.; Urban, J.J. Size-Dependent Permeability Deviations from Maxwell's Model in Hybrid Cross-Linked Poly(ethylene glycol)/Silica Nanoparticle Membranes. *Chem. Mat.* **2015**, *27* (7), pp 2421–2429.

[3] Lin, R.; Hernandez, B.V.; Ge, L.; Zhu, Z. Metal organic framework based mixed matrix membranes: an overview on filler/polymer interfaces. *J. Mater. Chem. A.* **2018**, *6* (2), pp 293–312.

[4] Kim, S.; Dura, J.A.; Page, K.A.; Rowe, B.W.; Yager, K.G.; Lee, H.-J.; Soles, C.L. Surface-Induced Nanostructure and Water Transport of Thin Proton-Conducting Polymer Films. *Macromolecules.* **2013**, *46* (14), pp 5630–5637.

[5] Lin, E.K.; Kolb, R.; Satija, S.K.; Wu, W.-L. Reduced polymer mobility near the polymer solid interface as measured by neutron reflectivity. *Macromolecules.* **1999**, *32* (11), pp 3753–3757.

[6] Butt, H.-J.; Duran, H.; Egger, W.; Faupel, F.; Harmandaris, V.; Harms, S.; Johnston, K.; Kremer, K.; Lin, F.Y.; Lue, L.; Ohrt, C.; Raetzke, K.; Ravelli, L.; Steffen, W.; Vianna, S.D.B. Interphase of a Polymer at a Solid Interface. *Macromolecules.* **2014**, *47* (23), pp 8459–8465.

[7] Ohrt, C.; Ratzke, K.; Oshima, N.; Kobayashi, Y.; O'Rourke, B.E.; Suzuki, R.; Uedono, A.; Faupel, F. Free Volume Profiles at Polymer-Solid Interfaces Probed by Focused Slow Positron Beam. *Macromolecules.* **2015**, *48* (5), pp 1493–1498.

[8] Dutta, R.C.; Bhatia, S.K. Structure and Gas Transport at the Polymer-Zeolite Interface: Insights from Molecular Dynamics Simulations. *ACS Appl. Mater. Interfaces.* **2018**, *10* (6), pp 5992–6005.

[9] Zhang, M.; Askar, S.; Torkelson, J.M.; Brinson, L.C. Stiffness Gradients in Glassy Polymer Model Nanocomposites: Comparisons of Quantitative Characterization by Fluorescence Spectroscopy and Atomic Force Microscopy. *Macromolecules.* **2017**, *50* (14), pp 5447–5458.

[10] Gibson, R.F. A review of recent research on nanoindentation of polymer composites and their constituents. *Compos. Sci. Technol.* **2014**, *105*, pp 51–65.
[11] Kalidindi, S.R.; Mohan, S.; Rossi, A. Mechanical Characterization of Mesoscale Interfaces Using Indentation Techniques. *JOM*. **2017**, *69*, pp 22–29.
[12] Schöneich, M.; Zamanzade, M.; Stommel, M. Fiber-matrix interphase in applied short glass fiber composites determined by a nano-scratch method. *Compos. Sci. Technol.* **2015**, *119*, pp 100–107.
[13] Forchheimer, D.; Forchheimer, R.; Haviland, D.B. Improving image contrast and material discrimination with nonlinear response in bimodal atomic force microscopy. *Nat. Commun.* **2015**, *6* (1), 6270.
[14] Olmos, D.; Rodriguez-Gutierrez, E.; Gonzalez-Benito, J. Polymer structure and morphology of low density polyethylene filled with silica nanoparticles. *Polym. Compos.* **2012**, *33* (11), pp 2009–2021.
[15] Kappl, M.; Butt, H.-J. The colloidal probe technique and its application to adhesion force measurements. *Part. Part. Syst. Charact.* **2002**, *19* (3), pp 129–143.
[16] Leite, F.L.; Herrmann, P.S.P. Application of atomic force spectroscopy (AFS) to studies of adhesion phenomena: a review. *J. Adhes. Sci. Technol.* **2005**, *19* (3-5), pp 365–405.
[17] Pham, J.T.; Schellenberger, F.; Kappl, M.; Butt, H.J. From elasticity to capillarity in soft materials indentation. *Phys. Rev. Mater.* **2017**, *1* (1), p 8.
[18] Feldman, K.; Tervoort, T.; Smith, P.; Spencer, N.D. Toward a force spectroscopy of polymer surfaces. *Langmuir.* **1998**, *14* (2), pp 372–378.
[19] Boyne, D.A.; Varady, M.J.; Lambeth, R.H.; Eikenberg, J.H.; Bringuier, S.A.; Pearl, T.P.; Mantooth, B.A. Solvent-Assisted Desorption of 2,5-Lutidine from Polyurethane Films. *J. Phys. Chem. B.* **2018**, *122* (7), pp 2155–2164.

# Novel MXene/titania nanocomposite fibers for enhanced charge injection

Shaun M. Debow[a]*, Brendan G. DeLacy[a], Yury G. Gogotsi[b], Yi Rao[c], William R. Creasy[d]
[a]U.S. Army Combat Capabilities Development Command Chemical Biological Center, Research & Technology Directorate, 8198 Blackhawk Rd, Aberdeen Proving Ground, MD 21010
[b]Department of Engineering, Drexel University, 3100 Market St, Philadelphia, PA 19104
[c]Department of Chemistry and Biochemistry, Utah State University, 0300 Old Main Hill, Logan, UT 8432
[d]Leidos, 1750 Presidents St, Reston, VA 20190

## ABSTRACT

MXenes are a recently discovered class of materials with exceptional electrical, thermal, mechanical, and electromagnetic properties, first discovered by Gogotsi et al. in 2011 at Drexel University. This class of materials is produced by selective etching and delaminating early transition metal compounds to form nanoparticles with two-dimensional structures. MXenes have the ability to: 1) efficiently absorb light of varying wavelengths (visible through infrared) and 2) efficiently store and transfer energy. We hypothesized that MXenes efficiently grown or attached to a semiconductor substrate (with suitable band gap) will efficiently absorb light, generate excited electrons, and inject that charge into the semiconductor. In order to test this hypothesis, we fabricated novel $Ti_3C_2$-MXene-$TiO_2$ fiber nanocomposites and subsequently measured their charge injection properties using transient absorption measurements. The charge transfer properties are being correlated to chemical reactivity using test reactions involving photoreaction of methyl orange at 600–800 nm, for comparison to previous studies at of methylene blue at 400 nm. This project provides the U.S. Army Combat Capabilities Development Command Chemical Biological Center with a new and exciting material to be explored in a range of applications including decontamination and obscuration.

**Keywords:** MXene, photoexcitation, photoreactivity, nanofibers, nanoparticles, electrocatalysis, electrolyzer

## 1. INTRODUCTION

MXenes are a recently discovered novel class of materials. They are two-dimensional in structure and made of transition metal carbides, carbonitrides, and nitrides.[1] They form flat, conductive sheets a few atoms in thickness, and they exhibit exceptional electrical, thermal, mechanical, and electromagnetic properties. The first class of two-dimensional transition metal carbides were discovered and characterized by Gogotsi et al. in 2011 at Drexel University called MXenes.[2] These materials have since expanded to include carbonitride and nitride materials, all produced by selective etching and delaminating layers using a range of early transition metal compounds.[3,4]

At the inception of this program, we hypothesized this exciting class of materials should also exhibit superior charge injection characteristics. These characteristics can be studied in semiconductors by exciting electrons using laser light to generate free electrons as charge carriers. This method was used to study the MXene's ability to efficiently absorb incident radiation and the ability to store and transfer charge. MXenes have the ability to store energy as pseudo-capacitors, which can enhance their ability to promote chemical reactivity for potential applications such as photoreactions.

Assuming an efficient electron acceptor is near or adjacent to the MXene, it was hypothesized that the excited electron should hop, or inject, into an acceptor substrate (e.g., a semiconductor material). A MXene nanostructure efficiently grown or attached to a semiconductor substrate—with a suitable band gap—will efficiently absorb light, store that charge in a controllable fashion, and inject that charge into the adjacent semiconductor substrate. Furthermore, we hypothesized that the way in which the 2D sheets of MXene are prepared or attached to the semiconductor substrate will greatly impact the charge injection process.

To test this hypothesis, we identified $TiO_2$ as a suitable semiconductor substrate that could be used to study the charge carrier transfer dynamics between the $Ti_3C_2$ MXene and the $TiO_2$ substrate. $TiO_2$ is an ideally-suited material for this

study, due to its inherent band gap, its ease of fabrication, and its ability to grow or attach to other nanostructures, such as MXenes. Hence, a primary goal during year one of this study was to fabricate and characterize MXene-$TiO_2$ composites. The primary method that was used was electrospinning. A Chinese patent was recently filed on a related method for electrospinning MXene-containing fibers.[5] A large number of fiber samples were generated and characterized for this project using the technique of electrospinning.

Several aspects of this study may have transition application to the U.S. Army and the warfighter. First, they could potentially serve as attenuating aerosols for use in a complex electromagnetic environment.[1,2] The conductivity of MXenes provides potential as next-generation aerosol materials with radiation shielding properties across broad radiation range (visible, infrared (IR), or microwave bands). A second application could be their utilization as novel catalysts that are inexpensive to fabricate, have high efficiency, and are an environmentally friendly means to decontaminating chemicals. $TiO_2$ is a well-studied photocatalyst—it is known to react with and degrade chemical warfare agents (CWA) such as sulfur mustard[6] and soman (GD).[7] A third application could lead to the development of MXene as efficient, low-cost, non-precious metal electrocatalysts that are easily commercialized for affordable alkaline hydrogen fuel cells and water electrolysis systems. Before these applications can be further developed, it is important to understand the energy transfer and absorption properties of the composite. This understanding will enable refinement of the best methods to produce the nanocomposite production process and to optimize their properties for specific applications. These questions of material characterization were addressed in year two and three of this project.

An important property of MXenes is that they are hydrophilic after processing, with the degree of hydrophilicity depending on the surface terminations (–F, –HO, or =O) that are formed during synthesis.[1,8] This inherent hydrophilicity enables many more applications when compared with hydrophobic materials, such as graphene. The hydrophilic surface also affects the chemical reactivity in aqueous media and their physical handling. If colloidal suspensions with good stability in aqueous solutions are easily achieved, these could facilitate their processing from aqueous media or dispersal as an aerosol fog. As a result, some of the studies in this project involved developing aqueous suspensions of MXenes and fibers for possible evaluation of their attenuation properties in complex electromagnetic environments.

The hydrophilic properties could provide important new options for novel approaches to attenuate various wavelengths of radiation. Aerosol dispersion of a MXene or MXene-containing composite as fog could replace the use of incendiary or energetic dispersal methods. The best performance should be obtained by properly matching the flake size with intended wavelengths of electromagnetic radiation to be attenuated. Previous research published in the scientific literature described a method to achieve specific lateral size distributions through the use of gradient centrifugation.[9] Alternatively, the flakes could be used in a broad, lateral-size distribution—this may produce a broadband attenuating material covering a wider range of wavelengths (e.g., from microwave through the IR radiation bands). Full characterization of the attenuating properties of MXenes and MXene-containing composites as attenuating aerosols was not possible in this study due to a limited amount of the materials available. However, the Gogotsi group has made progress in efficient methods to produce large quantities of MXenes that will be necessary for such studies.[10] This project may be an important step for efficient utilization of MXenes by allowing them to be coated as monolayers on less expensive substrates.

MXenes may enable or enhance photoreactions that have potential applications for decontaminating CWA or degrading hazardous chemical waste. $TiO_2$ is a well-known material for promoting photoreactions due to its ability to form electron-hole pairs; however, it has a large bandgap that drives photoabsorption to the near UV (<400 nm) radiation range.[11–13] The addition of MXene to $TiO_2$ significantly increases the absorbance of radiation from visible to IR bands, which attributed to the broadband absorbance of radiation by MXene. Alternatively, the MXene may provide a capability for energy storage as a capacitor, so reactions may occur faster than with $TiO_2$ alone, or reactions may occur that were otherwise energetically unfavorable. It is likely that the mechanism of energy transfer in the composite material could be significantly different at <400 nm compared to the visible radiation range.

## 2. METHODS

$TiO_2$ fibers and $Ti_3C_2$-MXene-$TiO_2$ nanocomposites were fabricated and analyzed using methods described below. Photoreaction studies and surface modification studies was performed as described below.

### 2.1 $TiO_2$ fiber substrates

Our laboratory has both the expertise and equipment to electrospin titania fibers with controllable dimensions. These fibers were used as the substrate for embedding and attaching MXene nanostructures. The fibers were characterized in terms of composition and size via transmission electron microscopy (TEM) and scanning electron microscopy (SEM).

### 2.2 MXene fabrication

MXene fabrication involved collaboration with Dr. Yury Gogotsi and his laboratory group at Drexel University; Dr. Gogotsi is the preeminent leader in the field of MXene synthesis and preparation. This expertise reduced the time and labor needed to produce usable MXenes, specifics are provided in Section 3.1. We focused on $Ti_3C_2$ MXene in this study, but a wide range of other compounds, made by varying the transition metal, are options for future studies.

### 2.3 Charge injection

Charge injection studies were performed in collaboration with Dr. Yi Rao and his research group at Utah State University. Dr. Rao's expertise in pump-probe transient absorption spectroscopy allowed us to evaluate the movement of excited charge carriers in ways we could not have otherwise. Further details are described below in Section 3.3. Dr. Rao was funded to assist with the characterization of the MXene-$TiO_2$ nanocomposite fibers. Transient absorption spectroscopy is a pump/probe technique when the injection of charge into a substrate is monitored by pumping the composite with a femtosecond laser of a given wavelength and power, and subsequently probing/monitoring the absorption properties of the substrate (at a different wavelength) to determine whether excited charge carrier transfer occurs.

### 2.4 $TiO_2/Ti_3C_2$ nanocomposite fabrication

An approach to quickly fabricate $Ti_3C_2$-MXene-$TiO_2$ nanocomposites is by electrospinning $TiO_2$ fibers containing the MXene using a sol-gel process. This approach is based upon a prior study in which electrospun polymer-only fibers and thin films were loaded with MXenes. These composites were shown to have greater electrical conductivity, when compared with the corresponding neat polymer.[14,15] The electrical conductivity of polymers loaded with MXene increased by three-orders of magnitude when compared with the neat polymer.[16]

### 2.5 Photoreaction studies

Photoreactions in aqueous suspensions were performed in U.S. Army Combat Capabilities Development Command Chemical Biological Center (DEVCOM CBC) laboratories. Degradation reactions of indicator dyes were used to characterize the relative reactivity of composite fibers that were made under varying conditions relative to pristine $TiO_2$ fibers. Results from these reactions guided the examination of selected fibers to determine the morphology of the most reactive fibers. Initial studies were performed using 400 nm radiation or artificial sunlight. The results from charge injection studies indicated that photoreaction using 600–800 nm radiation might be effective, so the studies were expanded to lower wavelengths.

### 2.6 Surface modification studies

The $Ti_3C_2$ MXene surface was modified by growing NiMo nanoparticles using a solvothermal method to produce NiMo-$Ti_3C_2$ MXene composites. The resulting composites were evaluated for their use as hydrogen evolution reaction (HER) and hydrogen oxidation reaction (HOR) electrocatalysts.

## 3. EXPERIMENTAL

### 3.1 Synthesis of $TiO_2$-$Ti_3C_2$ and $TiO_2$ composite nanofibers

A laboratory quantity of $Ti_3C_2$ MXene was fabricated by Gogotsi's group following procedures previously reported.[15] Briefly, this method involves etching a $Ti_3AlC_2$ MAX phase with an acid, followed by sonication or vigorous shaking to delaminate into monolayers.

The resulting $Ti_3C_2$ monolayers from Gogotsi were incorporated into electrospun $TiO_2$ fibers at DEVCOM CBC following electrospinning procedures reported by Liu et al.[16] with modifications to incorporate $Ti_3C_2$ MXene, and applying concepts similar to those implemented by Mayerberger et al.[15] and Kiennork et al.[18] Mayerberger discovered that the polymer jet ejection characteristics vary depending upon $Ti_3C_2$ concentration, due to changes in viscosity and

electrical conductivity. [15] They determined the ideal concentration for electrospun $Ti_3C_2$ in a polymer solution is 1 % w/w. This concentration was the starting point for $TiO_2$ electrospinning; however, these parameters—in addition to electrospinning voltage potentials, needle size, and pump rate—required tuning to be optimized.

As a control, pristine $TiO_2$ fibers (without MXene) were also fabricated using a simple sol-gel synthesis process. This sol-gel process disperses MXene and titanium isopropoxide (TTiP) into a uniform suspension containing polymethyl methacrylate (PMMA) that is ideal for electrospinning. Fibers were electrospun using the sol-gel suspension, then thermally treated in a controlled environment to evaporate PMMA and convert the TTiP to $TiO_2$.

A brief description of the procedure follows: 320 mg of PMMA was slowly added to 2 mL of chloroform while stirring; the solution was stirred until the PMMA was completely dissolved, for approximately 30 minutes. TTiP was added dropwise to the stirring solution, the volume varied from 0.29 mL to 0.67 mL, depending upon the desired MXene-to-TTiP concentration. The solution was allowed to stir for an additional 30 minutes. Following the addition of TTiP, a variable volume of MXene/N,N–dimethylformamide (DMF) suspension (0.9 mg/mL MXene/DMF) was added and allowed to stir for two hours. Fibers were electrospun using an MTI KJ Group electrospinning cabinet, model MSK-NFES-3LDV. The solution was drawn into a syringe with an 18-gauge needle attached. The syringe was clamped into a syringe pump, with the needle positioned 8 cm away from a horizontally rotating drum mandrel. The following process parameters were used: the mandrel operated at 400 rpm, the syringe pump flow was set to a nominal 0.12 mL/min, and a 10 kV potential was applied to the syringe tip. Pristine $TiO_2$ nanofibers were electrospun by applying the sol-gel synthesis process previously described for MXene-$TiO_2$ fibers, but without the addition of any MXene—they were produced using 0.67 mL of TTiP and 320 mg of PMMA.

The resulting MXene-TTiP-PMMA and TTiP-PMMA nanofibers mats were allowed to stand for 24 hours under ambient conditions. This allowed the TTiP in the electrospun fibers to hydrolyze into $Ti(OH)_4$ and then further condensate to amorphous $TiO_2$ prior to thermal treatment.[19]

Fibers were thermally treated by calcining in a Thermo Scientific™ Lindberg/Blue™ M TF55035A-1 tube furnace for 4 hours at 400 °C under an Ar–$H_2$ (10 % $H_2$) atmosphere or under air. A weight difference was noted between the pre-calcined and post-calcined fibers, this difference was consistent with the evaporation of PMMA and water.

### 3.2 Synthesis of $TiO_2$-$Ti_3C_2$ composite nanofibers with self-assembled surface $Ti_3C_2$ MXene

MXene flake was self-assembled to the surface of some electrospun TTiP-PMMA and MXene-TTiP-PMMA fibers. The self-assembly process started with as-spun fiber mats, these mats were electrospun following procedures outlined in Section 3.1, prior to the calcination step. Briefly, a colloidal suspension of MXene in water was produced by adding 0.0330 g of MXene to 40 mL of deionized water. This solution was sonicated at 24 W for 70 minutes using a Misonix Sonciator 3000 with a horn having a one-inch diameter tip operating at 20 kHz. Following sonication, 0.129 g of electrospun fibers were added to the colloidal suspension and stirred for 15 minutes. During this time, MXene self-assembled onto the fiber surface. The resulting fibers were centrifuged at 4,100 rpm for 15 minutes, then filtered. Coated fibers were thermally treated using the previously described procedures.

### 3.3 Visible pump-transient IR absorption spectroscopy

The experimental setup includes an integrated Ti:sapphire regenerative amplifier laser system (UpteK Solutions Corp.) operating at 1 kHz and 800 nm, producing 100 fs pulses of 4.0 mJ. Twenty percent of the 800 nm output was attenuated to a pulse energy of 10 µJ and used as the pump beam. The remaining 80 % of the output laser pulse was used to pump an optical parametric generator and amplifier with a difference frequency generator (TOPAS, DFG, Light Conversion) to produce an IR pulse of 5,000 nm (1900 $cm^{-1}$) having a pulse energy of 18 µJ. The IR beam was attenuated by more than 1,000 times before the samples were pumped. The IR probe was detected by a liquid nitrogen cooled HgCdTe detector (Infrared Associates, Inc., Model MCT-13-4.0), followed by an amplifier. The pump pulse was modulated by a chopper (New Focus™, Model 3501) operating at 500 Hz. The amplified signal from the detector was sent to a lock-in amplifier (Stanford Research, Model SR830). The digitized outputs were processed and recorded by a home-made Labview program. The instrumentation response function for the transient IR pulse was 300 fs. As mid-IR is sensitive to intraband transitions of free carriers in the conduction band or valance band of semiconductors, the change in the IR absorption is used for probing electron injection.

### 3.4 Photoreactivity studies

$Ti_3C_2$-MXene-$TiO_2$ fibers were studied to determine their catalytic or reactive capabilities, particularly with a goal toward CWA decontamination. After survey studies were completed, reactions were selected for in-depth study and for use to compare different formulations.

#### *3.4.1 Methylene blue bleaching*

The first photoreactivity study evaluated the degradation performance of composite fibers against methylene blue (MB) [3,7-bis(dimethylamino) phenazathionium chloride, purchased as a solid from Sigma-Aldrich®, M9140-25G]. This study began in FY19 and concluded during FY20. Briefly, a solution of $2.5 \times 10^{-5}$ M dye was made with 2.62 M acetic acid and 0.03 % $H_2O_2$ in aqueous solution. This reaction was used to compare the reactivity of several MXene fiber preparations in solution. Hydrogen peroxide was added to the solution to allow catalytic conversion of $H_2O_2$ into OH radicals, which then reacted with the MB. Reactions were carried out in 40 mL glass vials using 10 mL of solution (to give a 1 cm path length). A typical reaction solution was composed of 1–3 mg of a fiber sample. Aliquots of 0.1–0.5 mL of solution were periodically pulled from the vial, filtered, and analyzed. Reagent concentrations were selected to allow the reactions to nearly reach completion in 60–90 minutes. Residual MB was detected using a UV-vis spectrometer (JASCO, Inc.). Control samples were made without fibers, this enabled MB to be independently monitored in the presence of only light and $H_2O_2$.

Solutions having suspended MXene-containing composites were shown to cause faster MB photoreaction rates, while using simulated sunlight over the entire visible wavelength range, compared to fibers with only $TiO_2$. But significant degradation of MB alone in solution was observed due to light absorption in the visible range by MB. As a result, the study was changed from using simulated sunlight to using a 400 nm light source with a 50 W LED array. At this wavelength, there is little absorption by MB and the background reaction of the dye was significantly less. There were differences between $TiO_2$ with and without MXene using different fiber preparation methods over the range of 5–10 times.

#### *3.4.2 Methyl orange bleaching*

The transient absorption studies of charge carriers described in Sections 3.3 and 4.2 indicated that comparable activity was observed at 800 nm (near IR) relative to 400 nm, even though pristine $TiO_2$ has no activity at 800 nm wavelength. As a result, a second reaction studied degradation of methyl orange (MO) (4-[4-(dimethylamino)phenylazo] benzenesulfonic acid sodium salt, purchased as a solid from Sigma-Aldrich®, 114510-25G). Similar to the MB study, a solution of $3 \times 10^{-5}$ M dye was made with 2.62 M acetic acid and 0.03 % $H_2O_2$ in an aqueous solution. The pH of the solution is more important for MO than MB, since MO is a pH indicator and undergoes a significant absorption peak shift with pH. This dye was chosen since it had little absorption of 800 nm radiation, while MB dye absorbs strongly at 800 nm, causing background reactions. Both dyes undergo bleaching by reactions with OH radicals.

Two types of LED lamps were used. One LED lamp had a combination of 600 and 800 nm diodes, 600 nm being visible radiation. The second lamp had only 800 nm diodes, which is in the near-IR radiation band.

In order to simplify sample preparation, reaction mixtures were prepared and run in 4-mL (1 cm x 1 cm) cuvettes that were periodically analyzed *in situ* using a UV-vis spectrometer (Agilent Cary 60). This approach allowed the samples to be rerun multiple times without consuming the sample, which is valuable for slow reactions. This method was adequate for semiquantitative determination of bleaching of the dye solution. Reducing the cuvette size also made it possible to run more samples at the same time with one lamp. However, one complication arose from cuvettes containing suspended solids: these solids introduced background scattering that varied from spectrum to spectrum. In order to obtain the MO peak absorbance, the signal for the MO peak was subtracted from the background signal at 800 nm.

#### *3.4.3 MXene surface modification with NiMo nanoparticles*

All commercial chemicals were used as received without any further purification. Nickel chloride ($NiCl_2 \cdot 6H_2O$), potassium hydroxide (KOH), and sodium molybdate ($Na_2MoO_4$) were purchased from Fisher Chemical™. Hydrochloric acid (HCl) was purchased from Pharmco. Sodium borohydride ($NaBH_4$) was purchased from Sigma-Aldrich®. Lithium fluoride (LiF) was purchased from Alfa Aesar. $Ti_3AlC_2$ MAX phase was produced by Carbon Ukraine and received from the Gogotsi group at Drexel University. Deionized (DI) water (18 MΩ cm) was obtained using a Barnstead™ E-Pure™ system.

Typically, 10 mg of MXene was ultrasonically dispersed in 10 mL of water for two hours and subsequently mixed with aqueous solutions of NiMo, each having different molar ratios. The resulting aqueous suspension was further dispersed for half an hour after the addition of NiMo. $NaBH_4$ (37 mg, 1 mmol) was then added to the suspension, and stirred for another hour to fully deposit the metallic nanoparticles onto the support. Finally, the desired catalyst NiMo-MXene was collected by centrifuging and washed with deionized water five times and then dried in a vacuum at room temperature. The obtained sample was calcined at 500 °C for one hour under 95 % Ar and 5 % $H_2$.

## 4. RESULTS AND DISCUSSION

### 4.1 Electrospun $TiO_2$-$Ti_3C_2$ MXene fibers

The primary goal for the first year of this multi-year project was to develop methods and procedures to attach MXene to a semiconductor substrate so the composite would efficiently absorb light and enable charge carrier excitation below the bandgap of $TiO_2$. During the second year, at least 14 MXene composites were fabricated for testing using the general method developed during the first year. It was unknown at the inception of this project if MXene could form an intermediate or composite that would allow for easily handling and processing (e.g., electrospinning) to produce a MXene-semiconductor composite. At that time, no literature references were found to indicate this had previously been done. Results showing our electrospun fibers, including morphology the SEM and TEM micrographs of the composites are detailed in the FY18 Proceedings of the Edgewood Chemical Biological Center In-house Laboratory Independent Research and Surface Science Initiative Programs.

The amount of MXene in the best-performing fibers was determined to be 0.5–0.7 wt% MXene-$TiO_2$. This was calculated using the concentration of MXene in a DMF suspension made in the Gogotsi laboratory at Drexel University. The concentration was determined from the known mass extinction coefficient and the absorbance of the solution.[20] There is some uncertainty in the calculation since the stacking and agglomeration to larger particles in the suspension is variable and not well characterized. Sample 190726-01 contained 0.54 wt% MXene-$TiO_2$, while sample 190729-01 contained a slightly higher weight of MXene, 0.7 wt% MXene-$TiO_2$; however, it exhibited a slightly lower photoreaction rate. The results indicate that MXene can be used in an efficient way by forming $TiO_2$-MXene composite fibers.

### 4.2 Transient absorption measurements (pump-probe)

In collaboration with the group of Professor Yi Rao at Utah State University, studies of two-laser pump-probe optical properties were studied on several films. Electron injection studies were performed for the samples using transient absorption spectroscopy. Personnel in the Rao group who were involved with this effort include Tong Zhang, Xusheng Liu, Ganghua Deng, Yuqin Qian, and Yi Rao.

#### *4.2.1 Carrier relaxation of photoexcited MXene*

The MXene alone exhibits broad spectral absorption from 300 nm to > 1,000 nm. The IR absorbance at the probe wavelength of 5,000 nm is transparent to any chemical groups, but sensitive to the change in the absorption of free carriers created by the laser pump pulse. Therefore, the transient IR absorption measures the intra-band transition of free carriers by varying the time between pump and probe pulses.

In a semiconductor, photoexcitation normally generates free carriers and increases conductivity, that is, it produces a positive photoconductivity. Photoexcitation suppresses conductivity of the MXene film, indicating that the MXene has metallic characteristics. This phenomenon has been observed in graphene.[21] Photoexcitation of metallic MXene does not result in an increase in carrier density. Instead, carrier scattering rate increases as hot carriers are strongly coupled with phonons, resulting in a transient decrease in $\Delta T/T$. The scattering time was found to be from 3–10 ps. The increased THz transparency of a sample after photoexcitation corresponds to a photoinduced decrease in the THz conductivity. This result is expected in the context of photoexcitation of a metal.

#### *4.2.2 Charge flow in MXene-$TiO_2$ composites*

We previously measured the fluence-dependent kinetics for MXene-$TiO_2$ under the photoexcitation of 800 nm from 279–13,021 μJ/cm$^2$, these results were described in the FY19 Proceedings of the U.S. Army Combat Capabilities Development Command Chemical Biological Center In-house Laboratory Independent Research and Surface Science Initiative Programs. Briefly, we identified an approximately linear dependence on fluence, indicating that multiphoton effects are not important in carrier generation. Both the fast and slow time constants for the carrier relaxation remain

almost constant across the fluence. These intensity independent results suggest that the cooling of excited carriers by phonon emission is not screened efficiently, leading to high density-independent carrier-phonon scattering rates in MXene-$TiO_2$.

With the knowledge of carrier dynamics in the MXene pellet, we then switched our attention to carrier flow in MXene-$TiO_2$ composites. Figure 1 shows the kinetic traces of photo-induced changes in transmission detected at 5,000 nm under the photoexcitation of 400 nm and 800 nm for MXene-$TiO_2$ and pristine $TiO_2$ on a long time scale of 100 ps (Figure 1 a and c), and on a short time scale of 2 ps (Figure 1 b and d), respectively. The kinetic traces show a decrease in the transient IR transmission for the MXene-$TiO_2$ and $TiO_2$, corresponding to the increase in charge carriers that absorb at the detection wavelength.

In the early time scale of Figure 1, we examined charge transfer in MXene-$TiO_2$. The photoexcitation of MXene-$TiO_2$ exhibits a much slower formation under 400 nm than that under 800 nm. Carriers are generated only from MXene under the photoexcitation of 800 nm since the excitation is below the onset of $TiO_2$ transition. This is the clear example that MXene is responsible for generating carriers at IR wavelengths that do not exist for $TiO_2$ alone. For 400 nm excitation, photogenerated carriers are more abundant from both MXene and $TiO_2$ but are generated by $TiO_2$ alone.

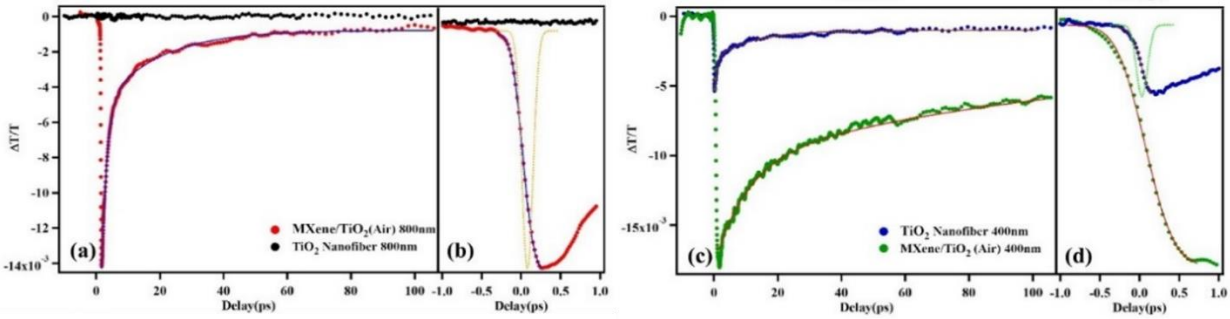


**Figure 1. Kinetic traces of photoinduced IR transmission (5,000 nm) change $\Delta T/T$ under 800 nm (left) and 400 nm (right), at a long-time scale of 100 ps [(a) and (c)], and at a short time scale of 2 ps [(b) and (d)].**

As expected, no photoinduced IR transmission was observed for $TiO_2$ alone at 800 nm since the pump energy was below the band gap of $TiO_2$ (Figure 1, top panel black trace). Carriers in $TiO_2$ are generated instantaneously under the photoexcitation of 400 nm, with a formation time constant as fast as 120–150 fs. These results indicate that photogenerated carriers transfer from MXene to $TiO_2$ in a more efficient way than from $TiO_2$ to MXene.

Fitting the data to a biexponential function yielded a biexponential relaxation process of 1.66 ps and 17.73 ps for MXene-$TiO_2$ under 800 nm, shown in the longer time scale in Figure 1. The fast process was attributed to back carrier transfer from the accepting $TiO_2$ to MXene and the slow process to trap-assisted recombination in the $TiO_2$. The slow recombination in $TiO_2$ was also evidenced by that under 400 nm in Figure 1.

### 4.3 Photoreactivity studies

#### *4.3.1 Methylene blue reactions at 400 nm*

The first photoreactivity studies investigated using MB in aqueous acidic solution. MB was chosen as an indicator because it is well studied in the scientific literature, and reaction conditions can be compared to prior work.[22] Hydrogen peroxide ($H_2O_2$) was added to the solution, so the reaction mechanism likely involved converting $H_2O_2$ into $^{\bullet}OH$ radicals, which then reacted with the MB. This conversion to $^{\bullet}OH$ radicals indicates the reactive contribution from the MXene.

The MB photoreaction results at 400 nm are summarized in the FY19 Annual Report; the fastest reaction rate was found with Sample 190726-01.

To further explore the contribution of $Ti_3C_2$ MXene toward reactivity, a secondary preparation method was used to add more MXene to the fibers after they were calcined. For photoreactions at 400 nm radiation, the reaction rate for sample 190722-01-01 was increased in comparison to 190722-01, which did not have additional MXene added, although the improvement was not large. More dramatic improvements were observed for 600–800 nm photoreactions. When a small amount of MXene suspension was added to fiber suspensions without drying in dilute amounts, a significant improvement in rate was observed. Calculated from the concentration of the suspension, the

amount of MXene that was added was about 1 % by weight of the fiber, and it caused a change of 10X in the rate of reaction, so this could be an efficient method to improve the rate of photoreactions.

#### *4.3.2 Methyl orange reactions at 600–800 nm*

Studies were performed using MO dye using 600–800 nm radiation, but otherwise similar to the MB studies. The reactions were slower, but it is not known whether the difference was due to light intensity differences between light sources, photon energy, or the inherent nature of MXene reactions. The illuminance of the sources at the distance that the samples were positioned was measured using a silicon-diode-based light meter (BTMETER, BT-881E, available from Amazon.com), and it was 60,000–80,000 lux. However, it is not clear whether the light meter has a flat response across the frequency range, and it did not respond to 800 nm radiation.

UV-vis spectra were taken of the reaction suspensions without filtering out the catalyst particles, due to the experimental approach of measuring reaction kinetics in cuvettes. This direct-measurement method introduced a variable amount of background scattering, causing an increase in the background spectra. Figure 2 shows a comparison of the blank solution (green line) which the MO dye absorption centered at 503 nm and a low baseline from 600–800 nm, with a sample with suspended solids (blue trace). The suspended solids caused an elevated background signal, which was subtracted. The red line shows the same sample after MO was completely bleached showing a lower background signal due to more settling of the particles.

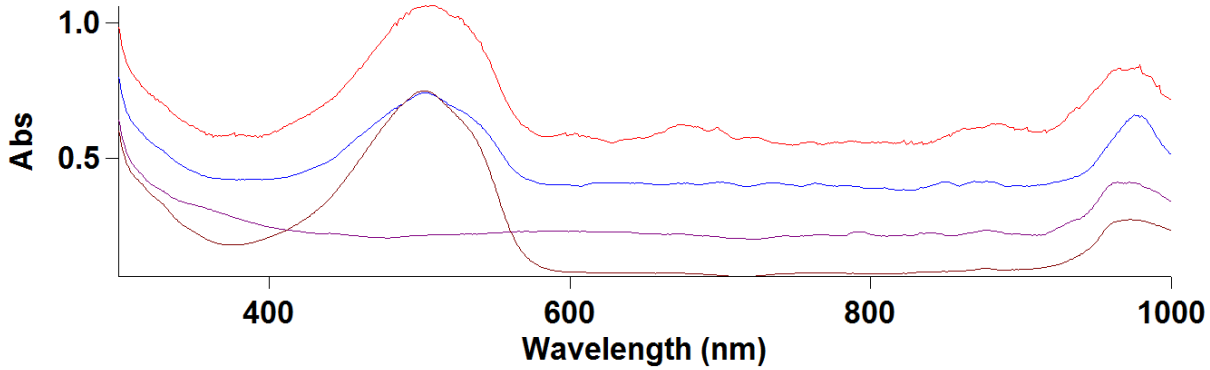


**Figure 2. UV-vis spectra of MXene photoreaction runs of MO under 600–800 nm radiation: brown, blank solution; red and blue, sample 3 on 9/29 at 1.25- and 2.5-hour reaction time; purple, sample 3 on 9/30 (no MO remains). Intensities are relative due to variations in suspended particles, of importance is the disappearance of MO dye absorbance (~500 nm).**

Results of kinetic runs are shown in Figure 3. For illumination with either the 600–800 nm or the 800 nm LED lamps, the reaction rates of the blank dye solution with $H_2O_2$ were very slow, and the dye lasted for many days under the lamps. Reactions of suspensions with fibers were about the same rate, or they could be slightly faster. Figure 3 shows the rate plots for fiber preparation numbers 190726-01 ($TiO_2$ with added MXene) and 190715-02 ($TiO_2$ with no additional MXene in the electrospinning solution), which had the slowest and fastest rates for the MB photoreaction, but both had the same photoreaction rate as the blank solution, within the measurement errors. Some samples with fibers had rates that were slightly faster, and it was not clear what caused the differences. The rate of photoreaction significantly increased by adding additional MXene to the fiber suspension of 1 wt% of MXene solid relative to the fiber suspension. The kinetic plot in Figure 3 is 10X faster than the fiber samples without extra MXene. A sample with a similar amount of MXene, but without fiber, does not show a faster rate. It appears that the accelerated rate involves an interaction between the MXene and the $TiO_2$ fibers. It is reasonable to expect that the hydrophilic MXene would attach to the outside of the fibers, but there is not any definitive evidence of complete binding between the fiber and the added MXene, or that the bound species are responsible for the rate increase. The mechanism of the rate acceleration is currently unclear. Unlike the 400 nm photoreaction, the longer illumination wavelengths are below the bandgap of the $TiO_2$ fibers, indicating the photoreaction likely involves the absorption of radiation by MXene. The mechanism of energy transfer from MXene to the reagent $H_2O_2$ requires further study. In general, there did not appear to be a strong dependence of the reaction rate to the amount of fiber present. However, some of the fibers seemed to form a more stable suspension in water, likely due to variations in the lateral dimensions, while other samples settled out faster. More study is needed to identify the sources of variation and find ways to optimize the rates.

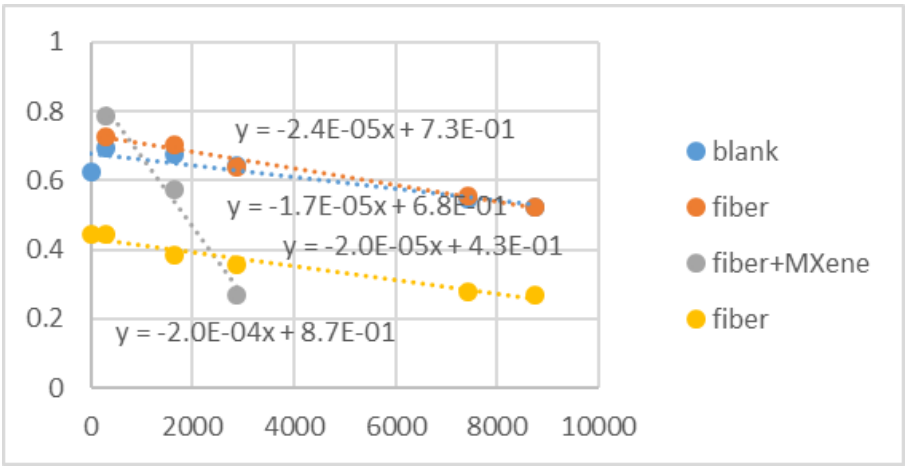


**Figure 3. Kinetic rate data from photoreaction of MXene fibers with methyl orange +$H_2O_2$ in acidic solution using an 800 nm LED lamp.**

### *4.3.3 Micro-infrared determination*

In order to obtain more information about the fiber morphology and MXene distribution, fibers were inspected using micro-IR spectroscopy. Samples of dry fibers were pressed onto grids, and specific spots of the fiber samples were probed to obtain IR spectra of small areas. Study of the secondary preparation method that was used to self-assemble additional MXene to the fibers provides evidence that the MXene is present on the surface of the fibers. Sample spectra are shown in Figure 4. The red trace is taken from sample 190722-01-01; these results were obtained using the surface-self-assembly method of MXene to the fiber surface and has a surface layer of MXene that was added after the electrospinning and calcification process was complete. The micro-IR results show a response from surface carbon groups in the spectrum. By comparison, the black trace shows pristine $TiO_2$ fibers without added MXene—these do not exhibit features from carbon groups. The most intriguing features of the micro-IR spectra are the blue and green traces. Both of these spectra represent electrospun fiber samples containing MXene in the suspension. Unlike the red spectrum, the features from carbon groups are not observed, but instead there are features from $H_2O$ and $CO_3$ groups. The band at 500–800 $cm^{-1}$ is much stronger and shifted to higher wavenumbers. It is possible that these features are strong IR bands caused by surface groups on the MXene. When MXene is etched from the MAX phase and then becomes functionalized with –OH, =O, or –F terminations, some of these may hydrogen bond with water, resulting in hydrophilic properties. The relationship between the surface atoms and reactivity is a topic that requires further study, since the method of preparation may further optimize the reaction characteristics.

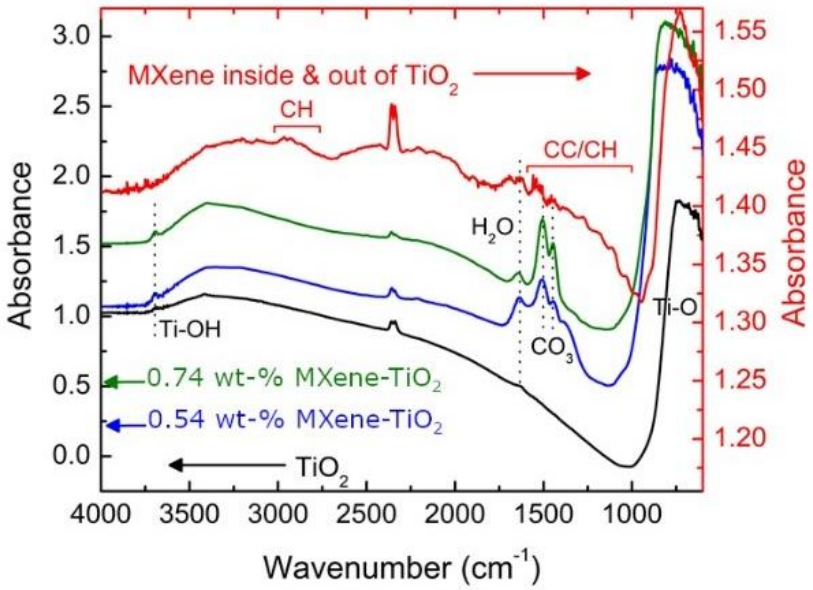


**Figure 4. Micro-IR measurement of four $TiO_2$/MXene fiber samples.**

### 4.4 MXene surface modification with NiMo nanoparticles

Monodisperse NiMo nanoparticles were grown directly on the MXene surface to form the NiMo/$Ti_3C_2$ composites. As controls in the experiments, the catalytic properties of NiMo nanoparticles and NiMo/reduced graphene oxide (RGO), were also evaluated. Our results demonstrate that the NiMo/$Ti_3C_2$ composite produced superior catalytic results, when compared to $Ti_3C_2$, NiMo, and NiMo/RGO. The NiMo NPs/MXene in 1.0 M KOH yielded an HER current of -10 mA $cm^{-2}$ at -0.044 V versus reversible hydrogen electrode—nearly 232 mV less than that of the parent NiMo NPs. The NiMo/MXene composite produced a HOR current density of 1.5 mA $cm^{-2}$ at 0.1 V (versus reversible hydrogen electrode).

Most electrochemical catalysts use precious metals like platinum, but they are limited in their wide-spread adaptation due to high cost. Alternative non-precious metal catalysts are attractive, but typically suffer from sluggish kinetics and performance. To investigate the potential application space of MXene for water electrolysis, we grew i-functional non-precious metal nanoparticles on the MXene surfaces. The NiMo-MXene electrocatalyst we developed, demonstrated much lower required potential compared to a NiMo-reduced Graphene Oxide (rGO) composite, shown in the left panel of Figure 5. NiMo-MXene electrocatalyst demonstrated an excellent low current density relative to the best catalysts that are in use, shown in the right panel of Figure 5.

The observed synergy between NiMo and $Ti_3C_2$ provides a framework for future work involving the use of other metal NP-MXene composites as electrocatalysts for fuel cell and electrolysis applications. This is a preliminary demonstration of improvements for an energy storage or production application that is potentially of great interest to the U.S. Army. A publication has been submitted.[23]

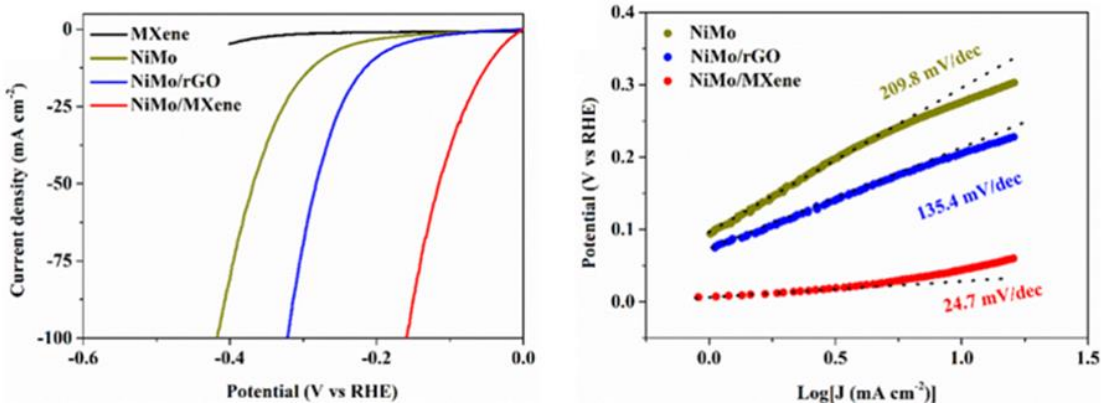


**Figure 5. Linear sweep voltammetry curves of NiMo/MXene, NiMo/rGO, NiMo, and MXene in $H_2$-saturated 1.0 M KOH (Left); Tafel plots of NiMo/MXene, NiMo/rGO, and NiMo in $H_2$-saturated 1.0 M KOH (Right).**

## 5. CONCLUSIONS

At the conclusion of this three-year effort, we fabricated several novel composites, gained an understanding of charge carrier excitation and transfer between MXene and semiconductor substrates, established new collaborations, and explored the potential application spaces for these materials. These advances include methods to fabricate electrospun composite materials that enhanced the contact area between $TiO_2$ fibers and MXene sheets and attempts to enhance photocatalytic activity were successful; characterizing the materials by using transient absorption measurements to gain a better understanding of the charge separation process. We demonstrated that for the MXene/$TiO_2$ materials, absorption at 800 nm was nearly as efficient as at 400 nm. These two wavelengths are at the red and blue ends of the visible spectrum, implying that the composite materials will have activity for visible absorption. Surface functionalization through use of NiMo nanoparticles demonstrates good catalytic properties and could replace the use of expensive noble metal catalysts. Photoreactivity of the $TiO_2$-$Ti_3C_2$ composites occurred at both 400 nm and 800 nm, implying that the composite will be active over the entire visible spectrum. The composites demonstrated the ability to photoreact and degrade two commercial dyes; it is hypothesized that these reactions may be extended to generate excited singlet $O_2$, which may provide a method for CWA decontamination.

## ACKNOWLEDGMENTS

Funding was provided by the U.S. Army via the Surface Science Initiative Program (PE 0601102A Project VR9) at DEVCOM CBC. The authors further extend their gratitude to the Dr. Way Fountain, Dr. Patricia McDaniel, and other Senior Research Scientists, internal and external senior scientists, and professionals who invested their time to evaluate the initial proposal and participate during the year-end Technical Advisory Board review. The authors acknowledge and thank the professionals at the W. M. Keck Center for Advanced Microscopy and Microanalysis at the University of Delaware for use of their instrumentation and support of this project. The authors also extend their sincere gratitude to Dr. Monica McEntee (DEVCOM CBC's Chemical, Biological, and Radiological Filtration Branch) for providing her expertise and assistance with micro-IR analysis.

## REFERENCES

[1] Naguib, M.; Mochalin, V.N.; Barsoum, M.W.; Gogotsi, Y. 25th Anniversary article: MXenes: A new family of two-dimensional Materials. *Adv. Mater.* **2014**, *26*, pp 992–1005.

[2] Naguib, M; Kurtoglu, M.; Presser, V.; Lu, J.; Niu, J.; Heon, M.; Hultman, L.; Gogotsi, Y.; Barsoum, M.W. Two-dimensional nanocrystals produced by exfoliation of $Ti_3AlC_2$. *Adv. Mater.* **2011**, *23* (37), pp 4248–4253.

[3] Naguib, M.; Mashtalir, O.; Carle, J.; Presser, V.; Lu, J.; Hultman, L.; Gogotsi, Y.; Barsoum, M. Two-Dimensional Transition Metal Carbides. *ACS Nano*. **2012**, *6* (2), pp 1322–1331.

[4] Urbankowski, P.; Anasori, B.; Makaryan, T.; Er, D.; Kota, S.; Walsh, P.L.; Zhao, M.; Shenoy, V.B.; Barsoum, M.W; Gogotsi, Y. Synthesis of two-dimensional titanium nitride $Ti_4N_3$ (MXene). *Nanoscale*. **2016**, *8* (22), pp 11385–11391.

[5] Dai, Y; Guo, X. MXene Nanowire Composite Electrospun Fiber Membrane for Photothermal Desalination. People's Republic of China Utility Patent Appl. CN107537323A, 2018.

[6] Ramacharyulu, P.V.R.K.; Nimbalkar, D.B.; Kumar, J.P.; Prasad, G.K.; Ke, S-C. N-doped, S-doped $TiO_2$ nanocatalysts: synthesis, characterization and photocatalytic activity in the presence of sunlight. *RSC Adv*. **2015**, *5* (47), pp 37096–37101.

[7] Wagner, G.W.; Procell, L.R.; Munavalli, S. $^{27}Al$, $^{47,49}Ti$, $^{31}P$, and $^{13}C$ MAS NMR Study of VX, GD, and HD Reactions with Nanosize $Al_2O_3$, Conventional $Al_2O_3$ and $TiO_2$, and Aluminum and Titanium Metal. *J. Phys. Chem. C.* **2007**, *111* (47), pp 17564–17569.

[8] Hart, J.L.; Hantanasirisakul, K.; Lang, A.C.; Anasori, B.; Pinto, D.; Pivak, Y.; van Omme, J.T.; May, S.J.; Gogotsi, Y.; Taheri, M. L. Control of MXenes' electronic properties through termination and intercalation. *Nat. Comm.* **2019**, *10*, 522.

[9] Maleski, K.; Ren, C.E.; Zhao, M-Q.; Anasori, B.; Gogotsi, Y. Size-Dependent Physical and Electrochemical Properties of Two-Dimensional MXene Flakes. *ACS Appl. Mater. Interfaces.* **2018**, *10* (29), pp 24491–24498.

[10] Shuck, C.E.; Sarycheva, A.; Anayee, M.; Levitt, A.; Zhu, Y.; Uzun, S.; Balitskiy, V.; Zahorodna, V.; Gogotsi, O.; Gogotsi, Y. Scalable Synthesis of $Ti_3C_2T_x$ MXene. *Adv. Eng. Mater.* **2020**, *22* (3), p 1901241.

[11] Guo, Q.; Ma, Z.; Zhou, C.; Ren, Z.; Yang, X. Single molecule photocatalysis on $TiO_2$ surfaces. *Chem. Rev.* **2019**, *119* (20), pp 11020–11041.

[12] Schneider, J.; Matsuoka, M.; Takeuchi, M.; Zhang, J.; Horiuchi, Y.; Anpo, M.; Bahnemann, D.W. Understanding $TiO_2$ photocatalysis: mechanisms and materials. *Chem. Rev.* **2014**, *114* (19), pp 9919–9986.

[13] Linsebigler, A.L.; Lu, G.; Yates, J.T., Jr. Photocatalysis on $TiO_2$ surfaces: Principles, Mechanisms, and Selected Results. *Chem. Rev*. **1995**, *95* (3), pp 735–738.

[14] Liu, J.; McCarthy, D.L.; Cowan, M.J.; Obuya, E.A.; DeCoste, J.B.; Skorenko, K.H.; Tong, L.; Boyer, S.M.; Bernier, W.E.; Jones, W.E., Jr. Photocatalytic activity of $TiO_2$ polycrystalline sub-micron fibers with variable rutile fraction. *Appl. Catal., B.* **2016**, *187*, pp 154–162.

[15] Ghidiu, M.; Lukatskaya, M.R.; Zhao, M-Q.; Gogotsi, Y.; Barsoum, M. Conductive two-dimensional titanium carbide 'clay' with high volumetric capacitance. *Nature*. **2014**, *516*, pp 78–81.

[16] Mayerberger, E.A.; Urbanek, O.; McDaniel, R.M.; Street, R.M.; Barsoum, M.W.; Schauer, C.L. Preparation and characterization of polymer-$Ti_3C_2T_x$ (MXene) composite nanofibers produced via electrospinning. *J. Appl. Polym. Sci.* **2017**, *134* (37), pp 1–7.

[17] Alhabeb, M.; Maleski, K.; Anasori, B.; Lelyukh, P.; Clark, L.; Sin, S.; Gogotsi, Y. Guidelines for Synthesis and Processing of TwoDimensional Titanium Carbide ($Ti_3C_3T_x$ MXene). *Chem. Mater*. **2017**, *29* (18), pp 7633–7644.

[18] Kiennork, S; Nakhowong, R; Chueachot, R; Tipparach, U. Preparation and Characterization of Electrospun $TiO_2$ Nanofibers via Electrospinning. *Integr. Ferroelectr.* **2015**, *165* (1), pp 131–137.
[19] Mahshid, S.; Askari, M.; Ghamsari, M.S. Synthesis of $TiO_2$ nanoparticles by hydrolysis and peptization of titanium isopropoxide solution. *J. Mater. Process. Technol.* **2007**, *189* (1–3), pp 296–300.
[20] Hantanasirisakul, K.; Alhabeb, M.; Lipatov, A.; Maleski, K.; Anasori, B.; Salles, P.; Ieosakulrat, C; Pakawatpanurut, P.; Sinitskii, A.; May, S.J.; Gogotsi, Y. Effects of Synthesis and Processing on Optoelectronic Properties of Titanium Carbonitride MXene. *Chem. Mater.* **2019**, *31* (8), pp 2941–2951.
[21] Jnawali, G.; Rao, Y.; Yan, H.; Heinz, T.F. Observation of a transient decrease in terahertz conductivity of single-layer graphene induced by ultrafast optical excitation. *Nano Lett.* **2013**, *13* (2), pp 524–530.
[22] Salem, I.A.; El-Maazawi, M.S. Kinetics and mechanism of color removal of methylene blue with hydrogen peroxide catalyzed by some supported alumina surfaces. *Chemosphere.* **2000**, *41* (8), pp 1173–1180.
[23] Zhang, T.; Debow, S.; Tang, L.; Qian, Y.; Creasy, W.R.; DeLacy, B.G.; Rao, Y. Novel NiMo/MXene Catalysts for Superior Hydrogen Electrochemistry. *ACS Nano*., submitted for publication 2021.

# Toward understanding the generation and lifetime of singlet oxygen species in photosensitized rigid crystalline structures

Ann M. Kulisiewicz[a], Sergio J. Garibay[b], Ivan O. Iordanov[a], Matthew A. Browe[a], Gabrielle Pozza[c], Lisa A. Kelly[c], Jared B. DeCoste[a]*
[a]U.S. Army Combat Capabilities Development Command Chemical Biological Center, Research & Technology Directorate, 8198 Blackhawk Rd, Aberdeen Proving Ground, MD 21010
[b]Leidos, 1750 Presidents St, Reston, VA 20190
[c]Department of Chemistry and Biochemistry, University of Maryland Baltimore County, 1000 Hilltop Cir, Baltimore, MD 21250

## ABSTRACT

Oxygen is generally considered a non-reactive gas in its ground triplet state; however, upon excitation to its singlet state it becomes a mild oxidant that can be utilized in fine chemical synthesis, waste water treatment, cancer therapy, as insecticides or herbicides, and in the destruction of toxic chemicals, including sulfur mustard. The generation of singlet oxygen and its subsequent lifetime is of utmost importance to these applications. One way to generate singlet oxygen is through the irradiation of a photosensitizer with the appropriate wavelength of light. Various photosensitizers have been incorporated into porous metal-organic frameworks to date, but fundamental studies on photosensitizer proximity, charge transfer, and photosensitizer composition have been largely unexplored. We hypothesize that the quantum yield of metal-organic framework photosensitizers toward singlet oxygen generation and subsequent lifetime of these species in metal-organic frameworks is maximized by the high density of the photosensitizer in positions that discourage quenching. This can be controlled by the topology of the metal-organic framework and the nature of the photoactive species. Several NU-1000 derivatives—NU-1000, NU-1000-*o*-$Cl_4$, NU-1000-*m*-$Cl_4$, NU-1000-*m*-$(NO_2)_4$, NU-1000-*o*-$(NO_2)_4$, NU-1000-*o*-$(NH_2)_4$, NU-1000-*o*-$(CH_3)_4$—have been synthesized and analyzed for their reactivity with 2-chloroethyl ethyl sulfide. In addition, several of the metal-organic framework linkers were analyzed for singlet oxygen generation through transient absorption spectroscopy and computational modeling was utilized to predict the band gap of the linkers to guide experimental design as well as corroborate experimental data.

**Keywords**: metal-organic framework, photocatalysis, singlet oxygen, sulfur mustard, 2-chloroethyl ethyl sulfide

## 1. INTRODUCTION

In recent years, many groups have been examining ways to incorporate photosensitizers in systematic ways into porous structures such as metal-organic frameworks (MOFs).[1–4] These photosensitizers have included organic linkers based on pyrene or porphyrins, metal complexes (including $Ru(bpy)_3$), and metals (including lanthanides) within the framework. While all of these approaches have been successful in generating singlet oxygen, fundamental studies in how different metals and organic linkers interact with one another based on their proximity are lacking. Singlet oxygen generation is of particular interest as it can be of great use in fine chemical synthesis, waste water treatment, cancer therapy, as insecticides or herbicides, and in the destruction of sulfur mustard.[5] The mild nature of singlet oxygen makes it ideal as it is non-hazardous and prevents the over oxidation to less desired products—as in the case of sulfur mustard to the sulfone, which is a vesicant.

MOFs are interesting materials for studying these fundamental interactions. They consist of metal/metal oxide secondary building units (SBUs) linked together in a regular pattern by organic linkers, forming crystalline structures. Most of these structures are very porous in nature and have large internal surface areas.[6] The porous nature and ability to understand the location of each functional moiety within its structure, make MOFs ideal for fundamentally studying the effect photosensitizer proximity, charge transfer, and photosensitizer composition has on the quantum efficiency and lifetime of singlet oxygen.

The generation of singlet oxygen by a photosensitizer requires a process where an electron is excited, typically by UV or visible light, followed by an intersystem crossing to a MOF triplet state, which transfers the energy to create the excited singlet oxygen species, as shown in Figure 1. While the inherent activity of these MOFs toward species such as the mustard simulant 2-chloroethyl ethyl sulfide (2-CEES) have been examined, understanding the fundamental underpinnings of the photophysics and how that can affect the production of singlet oxygen has been relatively unexplored in the literature.[2–4]

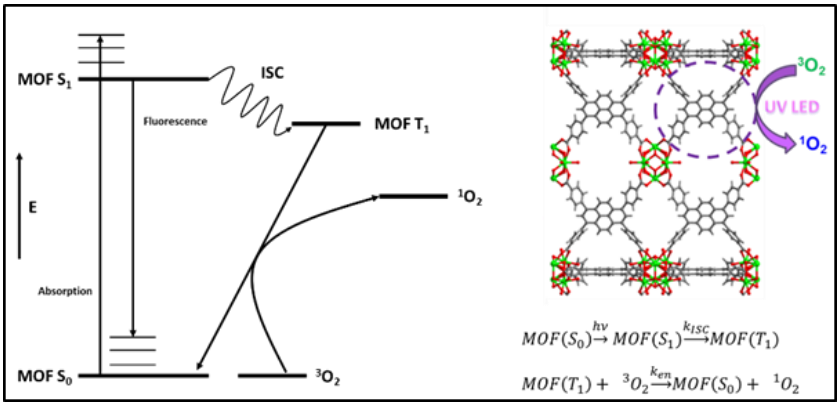


**Figure 1. The photosensitized production of singlet oxygen by a MOF linker occurs via irradiation of light to excite an electron into an excited state for the MOF linker. This is followed by an intersystem crossing to the MOF linker triplet state. Returning of the electron to the ground state releases a photon of appropriate energy to excite the oxygen from its triplet state to singlet state.**

In the literature, pyrene (NU-1000),[2,3] porphyrins (PCN-222),[4] and Ru complexes(UiO-67-Ru(bpy)$_3$[1] have been examined in MOF organic linkers as species that can produce singlet oxygen. However, there has been very limited work done with respect to synthesis of pyrene linker derivatives of NU-1000, and there have been no systematic studies detailing its effects on photocatalysis and singlet oxygen generation. To date, the only reported functionalization of H4TBAPy within a MOF was in the form of an amine functionalization on the benzoic acid portion of the linker.[7] Derivatives of the H4TBAPy linker can be readily synthesized via the conventional palladium cross-coupling reaction between 1,3,6,8-tetrabromopyrene and functionalized 4-methylcarbonylphenylboronic acid derivatives, followed by deprotection of the ester (Figure 2). By modifying the C and D positions on the H4TBAPy linker, we can determine the effect of substituents that vary in electronegativity on the lifetime of the excited triplet state of the MOF and subsequent generation of singlet oxygen. These effects were determined directly by transient absorption spectroscopy (TAS) and confirmed by computational measurements of band gap energies and the rate of photocatalytic oxidation of 2-CEES (Figure 3). We show here that the carboxylic acid form of the linker has an enhanced triplet state lifetime relative to the ester precursor indicating that the linker bound within the MOF structure should have inherent enhanced photocatalytic activity. We also show that heavy halogen groups incorporated onto the *meta* and *ortho* positions of benzene ring in the linker will extend the lifetime of the triplet state of the MOF and that heavy halogen groups *ortho* to the pyrene will have the largest enhancement on the reactivity as previously observed with tetraphenylporphyrins.[8] However, it is also indicated from our results that the topology of the MOF plays a large role in the activity and could cause potential self-quenching effects.

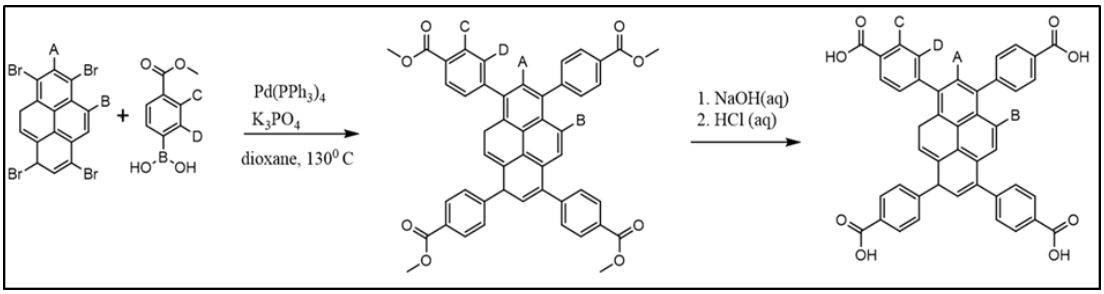


**Figure 2. Synthesis of the tetratopic H4TBAPy linker found in NU-1000 and NU-901 occurs through a palladium cross-coupling reaction followed by a deprotection workup. Positions A and B on the pyrene ring and C and D on the benzoic acid ring are hydrogen atoms in H4TBAPy; however, these locations can be functionalized prior to the cross-coupling reaction leading to a variety of functionality that may alter the photophysics of the pyrene system.**

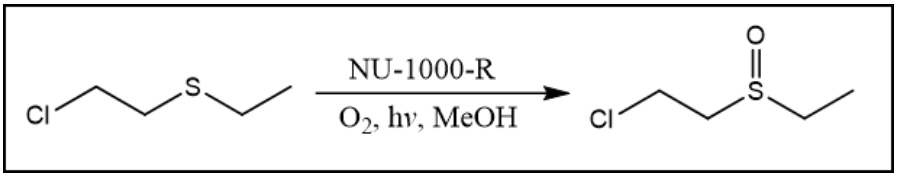


**Figure 3. Reaction scheme of 2-CEES with a functionalized NU-1000 photosensitizer to form its sulfoxide oxidation product.**

## 2. EXPERIMENTAL METHODS

### 2.1 Synthesis

#### *2.1.1 Linker synthesis*

All reagents were purchased from commercial sources and used without further purification. H4TBAPy and functionalized derivatives were synthesized following published procedures.[7]

#### *2.1.2 Synthesis of NU-1000*

$ZrOCl_2 \cdot 8H_2O$ (98 mg, 0.3 mmol) and benzoic acid (2 g, 16.4 mmol) were mixed in 8 mL of dimethylformamide (DMF) in an 8-dram vial and ultrasonically dissolved. The clear solution was incubated in an oven at 100 °C for 1 hour. After cooling down to room temperature, H4TBAPy (40 mg, 0.06 mmol) and trifluoro acetic acid (50 µL, 0.65 mmol) were added and ultrasonically mixed. The yellow solution was incubated in an oven at 100 °C for 18 hours. The yellow material was isolated by centrifuge (5 minutes, 7,500 rpm) and solvent exchanged with fresh DMF three times (10 mL each) followed by acetone three times (10 mL). The material was dried in a vacuum oven at 80 °C for 1 hour, and then activated at 120 °C for 18 hours.

#### *2.1.3 Synthesis of NU-1000-o-$Cl_4$*

$ZrOCl_2 \cdot 8H_2O$ (65 mg, 0.2 mmol) and benzoic acid (2.68 g, 22 mmol) were mixed in 8 mL of DMF in an 8-dram vial and ultrasonically dissolved. The clear solution was incubated in an oven at 80 °C for 1 hour. After cooling down to room temperature, H4TBAPy-*o*-$(Cl)_4$ (49 mg, 0.06 mmol) and trifluoro acetic acid (50 µL, 0.65 mmol) were added and ultrasonically mixed. The yellow solution was incubated in an oven at 100 °C for 18 hours. The yellow material was isolated by centrifuge (5 minutes, 7,500 rpm) and solvent exchanged with fresh DMF three times (10 mL each) followed by methanol three times (10 mL). The material was dried in a vacuum oven at 80 °C for 1 hour, and then activated at 120 °C for 18 hours.

#### *2.1.4 Synthesis of NU-1000-m-$Cl_4$*

$ZrOCl_2 \cdot 8H_2O$ and benzoic acid (2.68 g, 22 mmol) were mixed in 8 mL of DMF in an 8-dram vial and ultrasonically dissolved. The clear solution was incubated in an oven at 80 °C for 1 hour. After cooling down to room temperature, H4TBAPy-*m*-$(Cl)_4$ (49 mg, 0.06 mmol) and trifluoro acetic acid (50 µL, 0.65 mmol) were added and ultrasonically mixed. The yellow solution was incubated in an oven at 100 °C for 18 hours. The yellow material was isolated by centrifuge (5 minutes, 7,500 rpm) and solvent exchanged with fresh DMF three times (10 mL each) followed by methanol three times (10 mL). The material was dried in a vacuum oven at 80 °C for 1 hour, and then activated at 120 °C for 18 hours.

#### *2.1.5 Attempted synthesis of NU-1000-o-$(NO_2)_4$ (PCN-224-o-$(NO_2)_4$)*

$ZrOCl_2 \cdot 8H_2O$ (48 mg, 0.15 mmol) and benzoic acid (1 g, 8.2 mmol) were mixed in 4 mL of DMF in an 8-dram vial and ultrasonically dissolved. The clear solution was incubated in an oven at 80 °C for 1 hour. After cooling down to room temperature, H4TBAPy-*o*-$(NO_2)_4$ (26 mg, 0.03 mmol) and trifluoro acetic acid (25 µL, 0.33 mmol) were added and ultrasonically mixed. The solution was incubated in an oven at 100 °C for 18 hours. The yellow material was isolated by centrifuge (5 minutes, 7,500 rpm) and solvent exchanged with fresh DMF three times (10 mL each) followed by methanol three times (10 mL). The material was dried in a vacuum oven at 80 °C for 1 hour, and then activated at 120 °C for 18 hours.

#### *2.1.6 Attempted synthesis of NU-1000-m-$(NO_2)_4$ (NU-901-m-$(NO_2)_4$)*

$ZrOCl_2 \cdot 8H_2O$ (48 mg, 0.15 mmol) and benzoic acid (1 g, 8.2 mmol) were mixed in 4 mL of DMF in an 8-dram vial and ultrasonically dissolved. The clear solution was incubated in an oven at 80 °C for 1 hour. After cooling down to room temperature, H4TBAPy-*m*-$(NO_2)_4$ (26 mg, 0.03 mmol) and trifluoro acetic acid (25 µL, 0.33 mmol) were added and ultrasonically mixed. The solution was incubated in an oven at 100 °C for 18 hours. The yellow material was isolated by centrifuge (5 minutes, 7,500 rpm) and solvent exchanged with fresh DMF three times (10 mL each) followed by methanol three times (10 mL). The material was dried in a vacuum oven at 80 °C for 1 hour, and then activated at 120 °C for 18 hours.

#### *2.1.7 Synthesis of NU-1000-o-$(NH_2)_4$*

$ZrOCl_2 \cdot 8H_2O$ (48 mg, 0.15 mmol) and benzoic acid (1 g, 8.2 mmol) were mixed in 4 mL of DMF in an 8-dram vial and ultrasonically dissolved. The clear solution was incubated in an oven at 80 °C for 1 hour. After cooling down to room temperature, H4TBAPy-*o*-$(NH_2)_4$ (22 mg, 0.03 mmol) and trifluoro acetic acid (25 µL, 0.33 mmol) were added and ultrasonically mixed. The yellow solution was incubated in an oven at 100 °C for 18 hours. The material was isolated by centrifuge (5 minutes, 7,500 rpm) and solvent exchanged with fresh DMF three times (10 mL each) followed by methanol three times (10 mL). The material was dried in a vacuum oven at 80 °C for 1 hour, and then activated at 120 °C for 18 hours.

#### *2.1.8 Synthesis of NU-1000-o-$(CH_3)_4$*

$ZrOCl_2 \cdot 8H_2O$ (98 mg, 0.3 mmol) and benzoic acid (2 g, 16.4 mmol) were mixed in 8 mL of DMF in an 8-dram vial and ultrasonically dissolved. The clear solution was incubated in an oven at 80 °C for 1 hour. After cooling down to room temperature, H4TBAPy-*o*-$(CH_3)_4$ (44 mg, 0.06 mmol) and trifluoro acetic acid (50 µL, 0.65 mmol) were added and ultrasonically mixed. The yellow solution was incubated in an oven at 100 °C for 18 hours. The material was isolated by centrifuge (5 minutes, 7,500 rpm) and solvent exchanged with fresh DMF three times (10 mL each) followed by methanol three times (10 mL). The material was dried in a vacuum oven at 80 °C for 1 hour, and then activated at 120 °C for 18 hours.

### 2.2 Characterization

#### *2.2.1 Powder X-ray diffraction*

Powder X-ray diffraction (PXRD) patterns were measured on a Rigaku® MiniFlex 600 diffractometer equipped with a D/teX Ultra detector with Cu-Kα radiation (λ = 1.5418 Å) over a range of 2θ = 3–50° at a scan rate of 5° $min^{-1}$.

#### *2.2.2 Attenuated total reflectance-Fourier transform infrared*

Attenuated total reflectance-Fourier transform infrared (ATR-FTIR) spectra were measured on a Bruker Tensor 27 spectrometer from 4000–400 $cm^{-1}$ at a resolution of 2 $cm^{-1}$.

#### *2.2.3 $N_2$ physisorption*

$N_2$ isotherms were measured using a Micromeritics® ASAP® 2420 analyzer at 77 K. Samples were off-gassed at 120 °C under vacuum for ~16 hours. The Brunauer-Emmett-Teller (BET) method was used to calculate specific surface area in $m^2/g$.

#### *2.2.4 UV-vis spectroscopy*

Solid state UV-vis measurements of MOF samples from 200–800 nm were collected on a JASCO® V-650 UV-vis spectrophotometer equipped with a 150 mm integrating sphere.

### 2.3 Photocatalysis experiments

For 2-CEES oxidation experiments, 2.2 mg of the MOF was dispersed in 1 mL anhydrous methanol and sealed in a 17 x 83 mm glass microwave vial. After purging with $O_2$ for 20 minutes, 23 µL (0.2 mmol) 2-CEES and 5 µL (0.04 mmol) internal standard (1-bromo-3,5-difluorobenzene) were added to the microwave vial with a 25 µL glass syringe. The vial was then exposed to either UV (396 nm) or blue (465 nm) LED irradiation using an LED setup constructed from solderless LEDs purchased from RapidLED that were then mounted onto a U-shaped aluminum sheet (Figure 4). Twenty-five µL aliquots from the reaction vial were withdrawn using a syringe at 5-minute intervals, filtered, and diluted with 1 mL of methanol into a gas chromatography vial. The samples were then subjected to a gas chromatography with flame ionization detector to monitor the reaction progress.

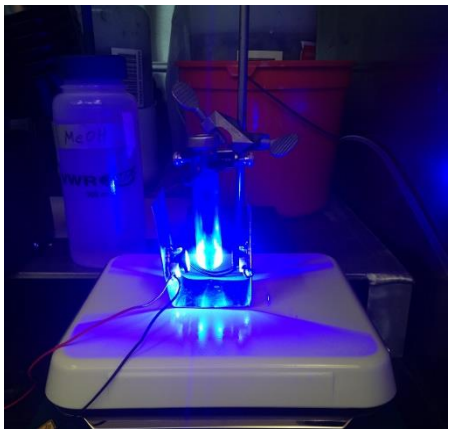

**Figure 4. Homemade LED setup for photocatalysis experiments.**

### 2.4 TAS via nanosecond laser flash photolysis

Production, decay and oxygen-reactivity of the triplet excited states (T1) of the TBAPy compounds (–$H_4$, –OEt–, *o*-Me, and *m*-$NO_2$) were studied using laser flash photolysis (LFP). The third harmonic (355 nm) of a Q-switched Nd:YAG laser (Continuum® Surelite™ II, pulse width ca. 8 ns) was used for laser flash excitation. Pulse energies of up to 50 mJ $cm^{-2}$ $pulse^{-1}$ were typically employed. The sample was excited through a 1 cm x 2 mm aperture. Laser-induced transmittance changes were monitored using white light from a 75 W Xenon source (Oriel® Instruments) focused through the sample, then re-imaged on the entrance slit of a Teledyne Princeton Instruments SP-2150 monochromator equipped with a 500 nm blazed grating. The monochromated light was detected with a Hamanatsu R-928 PMT, and the current was routed through a back-off circuit which stored and compensated for Io. The real-time current was recorded across 50 Ω on a Teledyne T3DSO2304 digital oscilloscope. The timing pulses to trigger the laser flashlamps, Q-switch, Uniblitz® (Vincent Associates) probe shutter, back-off circuit and oscilloscope were generated using a National Instruments PCIe Counter/Timer card. Data collection and analyses were controlled and performed using LabView 18 for Windows 10.

Powdered TBAPy samples were obtained from U.S. Army Combat Capabilities Command (DEVCOM) and dissolved in spectroscopy grade DMF to achieve an absorbance of ca. 0.20 at the 355 nm excitation wavelength. Samples were deoxygenated or fully oxygenated by bubbling (for ca. 20 minutes) with either argon or oxygen, respectively. The T1-Tn absorption of the TBAPy samples was monitored at the maximum of their absorption spectrum (between 500 nm and 550 nm, depending on the sample). Concomitant recovery of the ground-state bleach was also monitored at 380 nm.

### 2.5 Computational band gap measurements

The HOMO-LUMO gap calculations for H4TBAPy and TCPP derivatives were performed using the Gaussian 16 electronic structure package.[9] Calculations were performed at the B3LYP/3-21G level of theory using default optimization criteria. Initial molecular specifications were constructed by building the molecules in the Avogadro molecular editor and performing a preliminary single-point energy minimization procedure using the Universal force field and steepest descent algorithm. The value for the HOMO-LUMO gap was calculated by simply subtracting the reported HOMO and LUMO energies.

## 3. RESULTS

Under similar reaction conditions the majority of functionalized H4TBAPy linkers generated MOFs with **csq** topology that were analogous to NU-1000. However, both *meta* and *ortho* nitro functionalized H4TBAPy linkers generated MOFs with **scu** and **she** topologies characteristically similar to NU-901 and PCN-224 respectively (Figure 5). While PXRD can clearly distinguish the **she** MOF from **csq**/**scu** topologies (Figure 6a), the **scu** topology was confirmed through nitrogen adsorption experiments (Figure 6b).[8,10] The solid-state UV-vis spectra was collected for each functionalized MOF derivative that was synthesized (Figure 6c). The addition of chlorine groups onto the linker appears to narrow the absorption spectra of the material while the addition of the nitro, amino, and methyl groups appear to broaden the absorption spectra of the material. In particular, NU-901-*m*-$(NO_2)_4$ shows a particularly broad

absorption profile as compared to the other synthesized NU-1000 derivatives. This material also appears much darker in color than the other synthesized materials—a dark brown powder as compared to powders that vary from light tan-yellow (PCN-224-*o*-$(NO_2)_4$ and NU-1000-*o*-$(NH_2)_4$) to bright yellow (NU-1000, NU-1000-*o*-$Cl_4$, NU-1000-*m*-$Cl_4$, NU-1000-*o*-$(CH_3)_4$) in color. While the NU-1000-*o*-$(NH_2)_4$ and PCN-224-*o*-$(NO_2)_4$ derivatives also broaden the absorption spectrum, they do not broaden the absorption spectrum as much as the NU-901-*m*-$(NO_2)_4$ derivative likely leading to the lighter color of those powders as compared to NU-1000-*m*-$(NO_2)_4$.

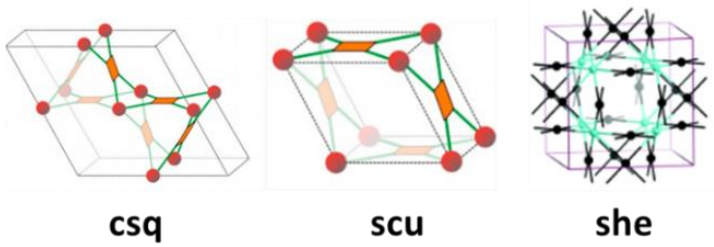


**Figure 5. MOF topologies for NU-1000, NU-1000-*o*-$Cl_4$, NU-1000-*m*-$Cl_4$, NU-1000-*o*-$(CH_3)_4$, NU-1000-*o*-$(NH_2)_4$ (csq), NU-901-*m*-$(NO_2)_4$ (scu), and PCN-224-*o*-$(NO_2)_4$ (she). The csq and scu topologies have similar PXRD patterns but can be distinguished through nitrogen adsorption experiments.**

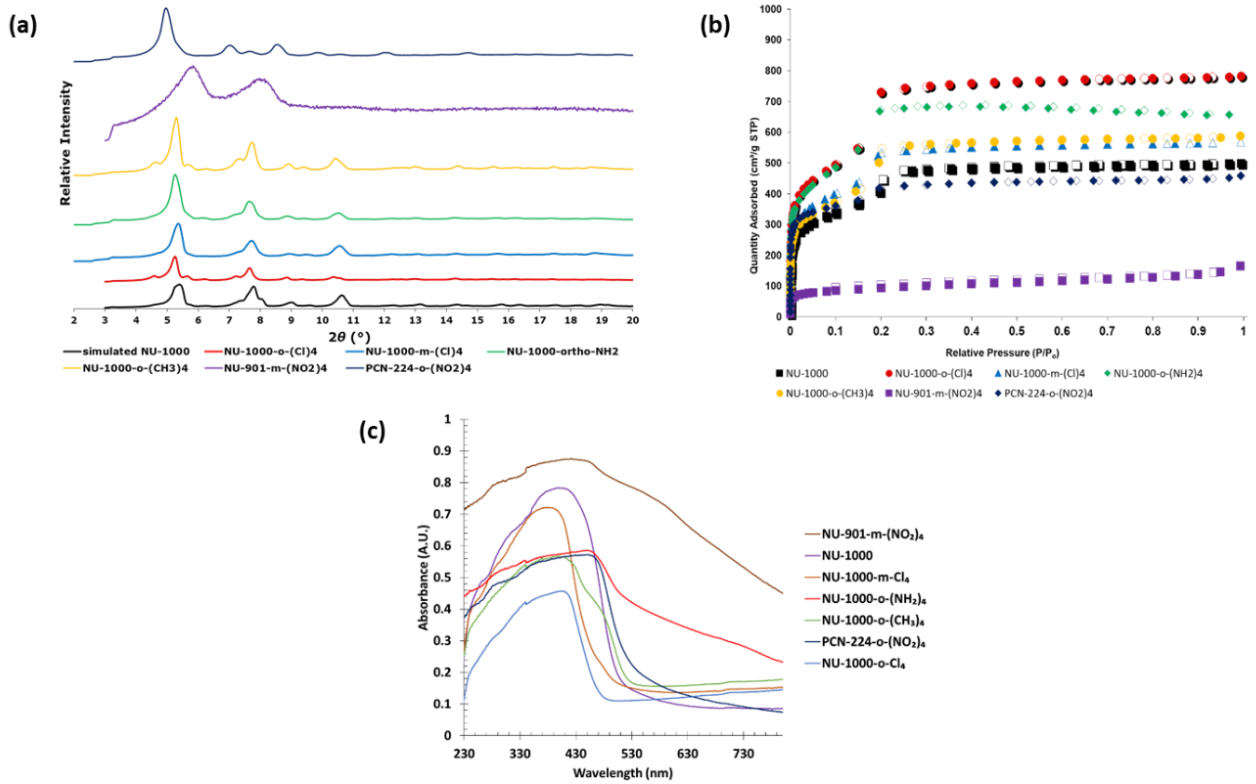


**Figure 6. PXRD pattern for the synthesized MOF derivatives (a). Nitrogen adsorption isotherms of the synthesized MOF derivatives (b). Solid-state UV-vis spectra for the synthesized MOF derivatives (c).**

Each functionalized MOF was reacted with 2-CEES in the presence of blue (465 nm) LED light. The reactions were conducted so that there was a catalytic amount of MOF present relative to the amount of 2-CEES present in the reaction solution (approximately 100:1, 2-CEES:H4TBAPy). PCN-224-*o*-$(NO_2)_4$, NU-901-*m*-$(NO_2)_4$, and NU-1000-*o*-$(NH_2)_4$ showed very little to no reactivity as compared to the baseline material and NU-1000-*o*-$(CH_3)_4$ showed reactivity similar to that of the baseline material. However, NU-1000-*o*-$Cl_4$ and NU-1000-*m*-$Cl_4$ showed marked enhancement in reactivity (Table 1). Interestingly, these materials showed a narrower absorption spectrum as compared to the less reactive derivatives. However, computational data suggests that functionalization of the benzene ring with these moieties does not significantly affect the band gap (Figure 7).

**Table 1. Calculated half-lives for the oxidation of 2-CEES by the synthesized NU-1000 derivatives.**

| MOF | $t_{1/2}$ (min) |
|---|---|
| NU-1000 | 40 |
| NU-1000-*o*-$Cl_4$ | 7.5 |
| NU-1000-*m*-$Cl_4$ | 25 |
| NU-901-*m*-$(NO_2)_4$ | NR |
| PCN-224-*o*-$(NO_2)_4$ | NR |
| NU-1000-*o*-$(NH_2)_4$ | NR |
| NU-1000-*o*-$(CH_3)_4$ | 40 |

(a)

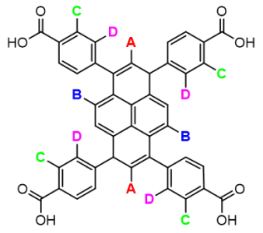


(b)

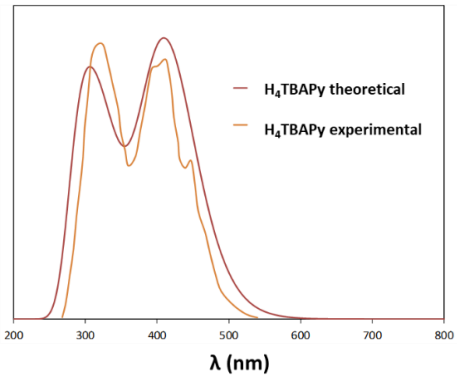


(c)

**Basis Set: B3LYP/3-21G**

| A | B | C | D | band gap (eV) | equiv. phot. wave. (nm) |
|---|---|---|---|---|---|
| | NH2 | | NO2 | 1.934 | 641.3 |
| NH2 | NH2 | | | 2.671 | 464.2 |
| | | | NO2 | 2.775 | 446.9 |
| | NH2 | | | 2.791 | 444.2 |
| NH2 | | | | 3.020 | 410.6 |
| | NO2 | | | 3.051 | 406.4 |
| | | NO2 | | 3.129 | 396.3 |
| NO2 | | | | 3.129 | 396.3 |
| | I | | | 3.195 | 388.1 |
| | | | NH2 | 3.271 | 379.1 |
| | Br | | | 3.283 | 377.7 |
| | | I | | 3.312 | 374.4 |
| | | Br | | 3.316 | 373.9 |
| | | Cl | | 3.318 | 373.7 |
| | | CH3 | | 3.322 | 373.3 |
| | | | | 3.327 | 372.7 |
| | | NH2 | | 3.346 | 370.6 |
| | CH3 | | | 3.354 | 369.7 |
| | Cl | | | 3.362 | 368.8 |
| | | | Cl | 3.510 | 353.3 |
| | | | Br | 3.635 | 341.1 |
| | | | CH3 | 3.685 | 336.5 |
| | | | I | 3.689 | 336.1 |
| I | | | | 3.748 | 330.8 |
| CH3 | | | | 3.755 | 330.2 |
| Cl | | | | 3.759 | 329.8 |
| Br | | | | 3.761 | 329.7 |

**Figure 7. (a) H4TBAPy linker with labeled functionalized positions (A, B, C, and D). (b) DFT prediction of UV-vis spectrum utilizing the B3LYP/3 21G basis set agrees well with experimental data. (c) Computational results of band gap calculations for various functionalized H4TBAPy derivatives.**

Therefore, the enhancement in reactivity is hypothesized to be a result of the heavy chlorine atoms facilitating the intersystem crossing that leads to the reactive triplet state of the MOF as previously observed in TCPP linkers.[11] The ability to reach the triplet state of the MOF is one of the primary factors for the production of singlet oxygen and enhancement of photocatalytic reactivity (Figure 1). While the more darkly colored materials (NU-901-*m*-$(NO_2)_4$, PCN-224-*o*-$(NO_2)_4$, and NU-1000-*o*-$(NH_2)_4$) have overall wider absorption spectra, this spectral enhancement does not appear to translate into an enhancement of the excitement of the material to the triplet state as evident by the lack of reactivity of these materials with 2-CEES. Rather, it is hypothesized that these materials absorb a great deal more light over a wider range of wavelengths but proceed to undergo a self-quenching mechanism as adjacent functionalized linkers can then absorb any transferred energy rather than using it to promote the MOF to the excited triplet state, particularly in the case of NU-901-*m*-$(NO_2)_4$ and PCN-224-*o*-$(NO_2)_4$ as their topology causes the linkers to be in closer proximity to each other than the **csq** topology of NU-1000.

This proposed self-quenching pathway was further confirmed by TAS measurements. The lifetime of the triplet excited state for several of the H4TBAPy linkers was determined in DMF (Table 2). The ester derivative of the linker showed a shorter triplet state lifetime as compared to the carboxylic acid derivative indicating that the acid form of the linker contained within the MOF should have enhanced reactivity overall and that the MOF structure should

contribute to an enhanced triplet state lifetime and subsequent reactivity with 2-CEES. While each of the linkers tested showed fairly long triplet state lifetimes, H4TBAPy-*m*-$(NO_2)_4$ exhibited the longest triplet state lifetime. This is consistent with the UV-vis data which showed a higher absorptivity of NU-1000-*m*-$(NO_2)_4$ in the visible region as compared to the other NU-1000 derivatives. However, the diminished reactivity of the linker when contained within the MOF framework indicates that the MOF topology is contributing to a self-quenching mechanism that is diminishing the overall reactivity of the MOF.

**Table 2. Summary of T1 lifetimes of various NU-1000 linker derivatives collected in DMF.**

| NU-1000 Linker | $\tau_{T1}$ (μS) |
|---|---|
| $H_4$TBAPy | 50.0 |
| $H_4$TBAPy-OEt | 34.7 |
| $H_4$TBAPy-*o*-$(CH_3)_4$ | 49.0 |
| $H_4$TBAPy-*m*-$(NO_2)_4$ | 59.7 |

While these results are indicative of a self-quenching mechanism, direct confirmation can be achieved through TAS measurements on the MOF derivatives themselves. However, TAS measurements are traditionally limited to materials that are soluble which is not the case for the MOF materials. Therefore, we have 3D printed the MOF samples into an optically transparent resin in the shape of a cuvette for collecting spectral measurements. Several resins were tested for optical transparency and minimum absorbance in the region of interest (Figure 8). The final cuvette shape printed was an angled cuvette (Figure 9) ideal for the fluorescence experiments as its shape minimizes backscattering effects.

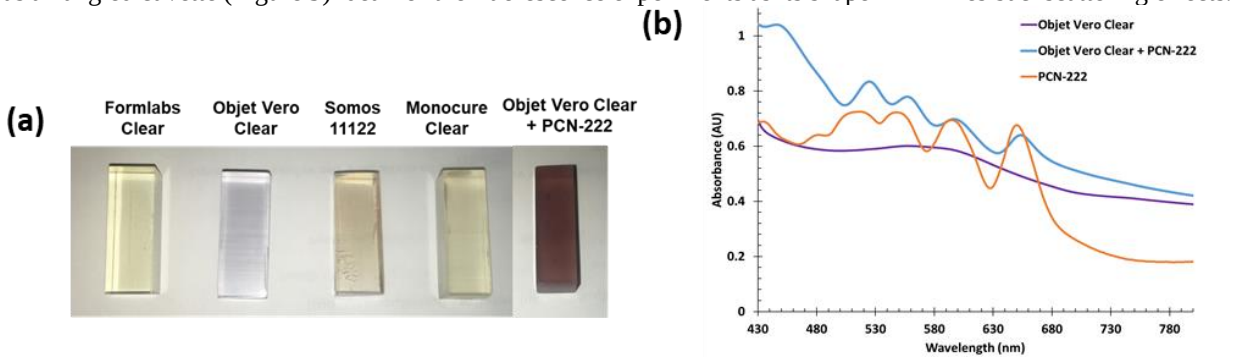


**Figure 8. (a) Photo of the various clear resins tested for 3D printing of cuvettes as well as proof of concept cuvette printed with PCN 222. (b) UV-vis spectra of chosen resin as well as spectra of PCN 222 and cuvette printed with PCN 222 embedded.**

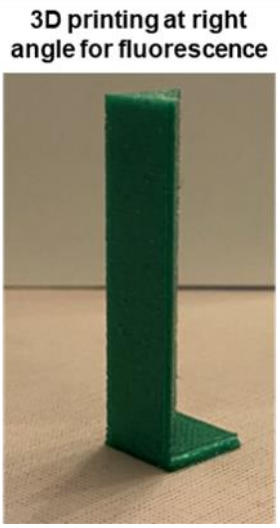


**Figure 9. Prototype angled cuvette shape used for fluorescence experiments to minimize backscattering effects.**

## 4. CONCLUSIONS/FUTURE WORK

Several novel MOF variants were successfully synthesized with functional groups (–Cl, $–NO_2$, $–NH_2$, $–CH_3$) positioned either *ortho*- or *meta*- to the carboxylic acid on the linker. Photocatalytic experiments showed that chlorine atoms significantly improve the photocatalytic reactivity of the material consistent with our hypothesis that heavy halogen groups would enhance the triplet state of the MOF, thereby enhancing photocatalytic reactivity. Computational data suggests that these moieties do not significantly affect the band gap of the material confirming that the lifetime of the triplet state of the MOF is the primary factor affecting the generation of singlet oxygen and reactivity of the photocatalyst with 2-CEES and should be the factor most considered when designing a MOF photocatalyst for the generation of singlet oxygen.

In addition, it was determined that possible self-quenching mechanisms should be carefully considered in the design of MOF photocatalysts. This was evidenced by the fact that PCN-224-*o*-$(NO_2)_4$, NU-901-*m*-$(NO_2)_4$, and NU-1000-*o*-$(NH_2)_4$ absorb more light than the more reactive chlorine derivatives but do not exhibit enhanced photocatalytic reactivity. TAS experiments of the various functionalized linkers in solution further confirmed this theory as H4TBAPy-*m*-$(NO_2)_4$ showed the longest triplet state lifetime indicating that the linker is an appropriate photosensitizer and should enhance reactivity but does not in the crystalline structure indicate that the proximity of linkers within the structure could be causing a self-quenching pathway diminishing the triplet state lifetime. Solid state TAS experiments of the NU-1000 derivatives printed into optically transparent cuvettes will be used to confirm this mechanism. These results not only enhance the general knowledge of these materials but also contribute toward design principles for future MOF-based photocatalysts for the mitigation of toxic chemicals susceptible to oxidation including sulfur mustard, hydrogen sulfide, and other organic pollutants.

## ACKNOWLEDGMENTS

Funding was provided by the U.S. Army via the Surface Science Initiative Program (PE 0601102A Project VR9) at the DEVCOM Chemical Biological Center (CBC). This research was performed while Sergio J. Garibay held a National Research Council post-doctoral research associateship award at DEVCOM CBC.

## REFERENCES

[1] Maza, W.A.; Morris, A.J. Photophysical Characterization of a Ruthenium(II) Tris(2,2′-bipyridine)-Doped Zirconium UiO-67 Metal–Organic Framework. *J. Phys. Chem. C.* **2014**, *118* (17), pp 8803–8817.

[2] Howarth, A.J.; Buru, C.T.; Liu, Y.; Ploskonka, A.M.; Hartlieb, K.J.; McEntee, M.; Mahle, J.J.; Buchanan, J.H.; Durke, E.M.; Al-Juaid, S.S.; Stoddart, J.F.; DeCoste, J.B.; Hupp, J.T.; Farha, O.K. Postsynthetic Incorporation of a Singlet Oxygen Photosensitizer in a Metal–Organic Framework for Fast and Selective Oxidative Detoxification of Sulfur Mustard. *Chem. - Eur. J.* **2017**, *23* (1), pp 214–218.

[3] Liu, Y.; Buru, C.T.; Howarth, A.J.; Mahle, J.J.; Buchanan, J.H.; DeCoste, J.B.; Hupp, J.T.; Farha, O.K. Efficient and selective oxidation of sulfur mustard using singlet oxygen generated by a pyrene-based metal–organic framework. *J. Mater. Chem. A.* **2016**, *4* (36), pp 13809–13813.

[4] Liu, Y.; Howarth, A.J.; Hupp, J.T.; Farha, O.K. Selective Photooxidation of a Mustard-Gas Simulant Catalyzed by a Porphyrinic Metal–Organic Framework. *Agnew. Chem., Int. Ed.* **2015**, *54* (31), pp 9001–9005.

[5] DeRosa, M.C.; Crutchley, R.J. Photosensitized singlet oxygen and its applications. *Coord. Chem. Rev.* **2002**, *233–234*, pp 351–371.

[6] Tranchemontagne, D.J.; Mendoza-Cortes, J.L.; O'Keeffe, M.; Yaghi, O.M. Secondary building units, nets and bonding in the chemistry of metal-organic frameworks. *Chem. Soc. Rev.* **2009**, *38* (5), pp 1257–1283.

[7] Islamoglu, T.; Ortuño, M.A.; Proussaloglou, E.; Howarth, A.J.; Vermeulen, N.A.; Atilgan, A.; Asiri, A.M.; Cramer, C.J.; Farha, O.K. Presence versus proximity: the role of pendant amines in the catalytic hydrolysis of a nerve agent simulant. *Agnew. Chem., Int. Ed.* **2018**, *57* (7), pp 1949–1953.

[8] Kirchon, A.; Feng, L.; Drake, H.F.; Joseph, E.A.; Zhou, H-C. From fundamentals to applications: a toolbox for robust and multifunctional MOF materials. *Chem. Soc. Rev.* **2018**, *47* (23), pp 8611–8638.

[9] Frisch, M.J.; Trucks, G.W.; Schlegel, H.B.; Scuseria, G.E.; Robb, M.A.; Cheeseman, J.R.; Scalmani, G.; Barone, V.; Petersson, G.A.; Nakatsuji, H.; Li, X.; Caricato, M.; Marenich, A.V.; Bloino, J.; Janesko, B.G.; Gomperts, R.; Mennucci, B.; Hratchian, H.P.; Ortiz, J.V.; Izmaylov, A.F.; Sonnenberg, J.L.; Williams-Young, D.; Ding, F.; Lipparini, F.; Egidi, F.; Goings, J.; Peng, B.; Petrone, A.; Henderson, T.; Ranasinghe, D.; Zakrzewski, V.G.; Gao, J.; Rega, N.; Zheng, G.; Liang, W.; Hada, M.; Ehara, M.; Toyota, K.; Fukuda, R.; Hasegawa, J.; Ishida, M.; Nakajima, T.; Honda, Y.; Kitao, O.; Nakai, H.; Vreven, T.; Throssell, K.; Montgomery, J.A., Jr.; Peralta, J.E.; Ogliaro, F.; Bearpark, M.J.; Heyd, J.J.; Brothers, E.N.; Kudin, K.N.; Staroverov, V.N.; Keith, T.A.; Kobayashi, R.; Normand, J.; Raghavachari, K.; Rendell, A.P.; Burant, J.C.; Iyengar, S.S.; Tomasi, J.; Cossi, M.; Millam, J. M.; Klene, M.; Adamo, C.; Cammi, R.; Ochterski, J.W.; Martin, R.L.; Morokuma, K.; Farkas, O.; Foresman, J. B.; Fox, D.J. *Gaussian 16*, Revision C.01, Gaussian, Inc., Wallingford, CT, 2016.

[10] Gomez-Gualdron, D.A.; Gutov, O.V.; Krungleviciute, V.; Borah, B.; Mondloch, J.E.; Hupp, J.T.; Yildirim, T.; Farha, O.K.; Snurr, R.Q. Computational design of metal-organic frameworks based on stable zirconium building units for storage and delivery of methane. *Chem. Mater*. **2014**, *26* (19), pp 5632–5639.

[11] Nifiatis, F.; Athas, J.C.; Gunaratne, K.D.D.; Gurung, Y.; Monette, K.M.; Shivokevich, P.J. Substituent Effects of Porphyrin on Singlet Oxygen Generation Quantum Yields. *Open Spectrosc. J*. **2011**, *5*, pp 1–12.

# Towards understanding the role of material voids and porosity on transport

Angela M. Zeigler[a]*, Roseanna N. Zia[b], Brian K. Ryu[b], Mark J. Varady[a], Melissa S. Hulet[c], Bradley R. Ruprecht[d]
[a]U.S. Army Combat Capabilities Development Command Chemical Biological Center, Research & Technology Directorate, 8198 Blackhawk Rd, Aberdeen Proving Ground, MD 21010
[b]Department of Chemical Engineering, Stanford University, 443 Via Ortega, Stanford, CA 94305
[c]Leidos 1750 Presidents St, Reston, VA 20190
[d]U.S. Army Combat Capabilities Development Command Chemical Biological Center, Engineering Directorate, 8198 Blackhawk Rd, Aberdeen Proving Ground, MD 21010

## ABSTRACT

Additive manufactured materials are limited in field use as a result of inherent porosity and voids. A fundamental understanding of how the mesoscale structure affects the chemical transport diffusion through three dimensional printed polymeric materials allows for full exploitation of the technology. Understanding of the efficacy of such materials includes detailed understanding of the migration rates through the material of solvent-suspended particles of various sizes and how the rate varies with the tortuosity of the void network. Studies of flow through porous media are well-established in the literature, but the geometry and connectivity of pore structures that arise from different additive manufacturing techniques have not been well studied, preventing the development of predictive models for mass transport. Using a combination of experiments and computational studies, in which the constructive framework for our methods were constructed in the first year of the project, we have developed further algorithms for characterizing the tortuosity of additively printed material and how changes in this tortuosity affect the migration rate of solvent-suspended macromolecules. Changes in morphology emerging from fused deposition modeling, selective laser sintering, and stereolithography are modeled computationally and studied experimentally. We conclude with a discussion of how the method can be modified based on the newest experimental results.

**Keywords:** additive manufacturing, 3D printing, transport, voids, porosity, diffusion, mesoscale, micro-CT

## 1. INTRODUCTION

Three dimensional (3D) printing, a phenomenon closely related to additive manufacturing, has emerged as a technology of interest to the Army due to its potential in easing logistics burden and building Army readiness as related to the 2018 Army Strategy.[1] Applications for 3D-printed materials may include body armor, weapon components, or even personal protective equipment (PPE). Also, in light of the COVID-19 pandemic, there has been an exponential increase in printing PPE and medical supplies[2] as a last resort to aid in the sudden supply shortage. However, there is a significant knowledge barrier to implement 3D printing as a long-term solution, as the effects of porosity and defects on permeability of polymeric materials are not well known.[3,4] Therefore, a fundamental understanding of the effect of transport across voids and the porous network would allow for full exploitation of the technology.

Depending on the additive manufacturing method utilized, there may be an inherent presence of voids or other subsurface defects.[5,6] Fused deposition modeling (FDM) is a method that requires heating of the polymeric material as it is extruded through a small nozzle. For the desired product, the nozzle is programmed to build the piece layer-by-layer, from bottom to top, and as the melted polymer is deposited, it fuses to the previous layer. This method potentially allows for voids or defects to form between the fused layers. Other printing parameters, such as the printing head temperature, mechanical layering speed, etc., may also create subsurface voids. Selective laser sintering (SLS) is a powder bed-based method where a $CO_2$ laser is programmed to form the shape of the desired product by melting and fusing the powder together layer-by-layer as powder is continuously added. The potential of unfused granules from the feedstock could allow for potential voids or defects in the substructure.[7] Stereolithography (SLA) uses a

photochemical process to optically cure a product pulled from a liquid vat of the polymeric material. The material is cured typically by a UV lamp layer-by-layer starting from the top to bottom. Again, there is a potential for voids or defects to form between the cured layers. In each case, only specific polymeric materials may be utilized depending on the method; therefore, the impact of understanding the mechanisms of transport through these polymeric materials may affect the degree to which they can serve as protective material.

Our first year, or FY19, proceedings report focused on establishing the necessary experimental and modeling infrastructure for the research. This infrastructure was the foundation for the investigation of the influence of voids and porosity on transport of a chemical of interest through a bulk polymer. We limited this study to a reasonable scope, utilizing the following: (1) the FDM method of a black polycarbonate acrylonitrile butadiene styrene (PC-ABS) thermoplastic, (2) the SLS method with glass filled nylon, and (3) the SLA method using elastomeric polyurethane (EPU40).

Three microscopy methods were performed to capture the dimensions of pores and voids in the 3D-printed material. Confocal optical microscopy in visible wavelengths and scanning electron microscopy were performed. However, it was difficult to extract quantifiable data and porosity was not visible on the surfaces imaged. Therefore, measurements of the substructure of the 3D-printed polymeric materials proceeded with the method of X-ray microtomography (micro-CT). Lastly, an experimental design was constructed for measuring the transient breakthrough times of the solvents and preliminary tests were performed.

Tortuosity, meaning pore interconnectedness, is the heart of the breakthrough problem that cannot be quantified from visual data. To our knowledge, no established technique exists yet in laboratory samples, computational models, or theory that unambiguously *measures* both feature-size distribution and connectivity.[8,9] We have evaluated existing methods for computationally characterizing the tortuosity and permeability of the experimental samples. Examples have included Lattice-Boltzmann or Brownian dynamics simulations to model flows or diffusing particles. Each method has its advantages and disadvantages. An advantage of these methods is the ability to directly extract tortuosity and permeability via *in silico* experiments; the disadvantage is the need for development of computational tools and computational cost. Analytical methods develop Kozeny-Carman type equations to obtain explicit expressions for permeability and tortuosity of porous media. The main advantage of these methods is the ability to obtain a simple expression for effective tortuosity and permeability. However, such expressions can only be obtained for simple, well-defined geometries such as a packed bed of spheres. Due to restrictions caused by COVID-19, our second year progress focused primarily on the advancements of the computational modelling efforts defining “tortuosity”, followed by the experimental breakthrough laboratory efforts to compare to the simulations.

## 2. EXPERIMENTAL APPROACH

### 2.1 Microscopy methods

Micro-CT is a non-invasive microscopy method that utilizes X-rays to record images of an object that is rotated around an axis; this technology is analogous to medical facility computerized axial tomography X-ray imaging, or CAT scans. A 3D image is constructed from the data using image reconstruction software or computerized algorithms. The advantage of this technology is that a spatial resolution of ~100 nm is possible. The 3D-printed parts of our study were characterized using micro-CT instrumentation at the Combat Capabilities Development Command (DEVCOM) Army Research Laboratory (ARL) in Adelphi, MD. The data received was encoded as an MPEG movie file, where each pixel in an image represents a voxel that is a volume element in the data. A length scale was present in the data that permitted the determination of the length of each voxel. The micro-CT data contain raw voxel intensities, which require further post-processing to obtain meaningful information of voids.

### 2.2 Computational modeling

The large-scale atom/molecule massively parallel simulator (LAMMPS)[10] software platform is a computational algorithm that successfully models very large-scale systems because it is highly optimized for parallel processing across thousands of processors. A unified atom approach is used to perform the simulation to work at the micrometer (μm) scale. However, when the simulation length scale becomes greater than 10 nm, the number of individual atoms becomes computationally intractable, and therefore requires treating a group of atoms as a single particle. In addition, the primary way to define network conductivity is via bulk permeability, which smears out the internal structure and thus is not predictive. This is because computational models explicitly record positions of solid strands, not voids.

To approach these challenges, a high-fidelity model was constructed of a 3D-printed material by self-assembly of macromolecules to produce a tortuous network similar to those created by 3D printing. We implemented skeletonization methods[11] to analyze the 3D micro-CT data to obtain condensed features of the void structure. This step, as shown in Figure 1 (a) and (b) enables efficient analysis of experimentally obtained large micro-CT scan data, consisting of over $10^9$ voxel points. This was performed by establishing implementation for 3D skeletonization methods in order to examine the void structure and an implementation example shown in Figure 1 (c) and (d). An example of how the skeletonization approach works is shown below.

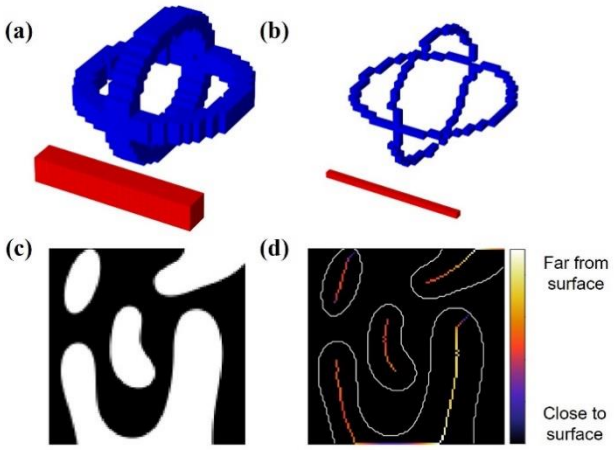


**Figure 1. Condensing of object features from (a) to (b) illustrates the application of skeletonization algorithms for curve extractions similar to reference Cao et al.[11] How these skeletonization methods may be applied to obtain void structure from micro-CT scan data is illustrated in (c) and (d).**

Skeletonization methods (formally, medial axis transformations) are commonly used in computational image analysis of 2D or 3D images. These transformations compress the images while preserving the most important structural features present in images such as approximate size, shape, and connectivity.[12,13]

### 2.3 Laboratory breakthrough measurements

The design for our breakthrough measurements set-up is shown in Figure 2. Several modifications were made in FY20, including encapsulating the source for temperature control and automating the on/off knobs for introduction of solvent vapors in order to run experiments unattended, overnight due to COVID-19 restrictions. These restrictions were placed to limit the number of people in the lab at once and limit the amount of time people were allowed in the labs. In our preliminary data from FY19, there were some slight inconsistencies when initially using an acrylic-based photopolymer sample mount. Therefore, in FY20, the flow cell sample mount to hold the 1 inch x 1 inch x varying thickness (0.02 inch, 0.05 inch, and 0.1 inch) samples was manufactured into a stainless steel piece to ensure no interaction of the sample holder with the interrogating solvent vapors.

The probe solvent is put into a saturator cell and introduced to the top side of the sample as a saturated vapor flow (in nitrogen). A recessed area of the source holds the polymeric sample with a channel for an O-ring to make a seal and ensure isolated exposure to only one side of the sample. A dry nitrogen flow is introduced to the other side of the sample where the inlet of a mass spectrometer detects very low levels of vapor as it permeates the sample. Flows on both sides of the sample are adjusted to minimize the pressure differential across the sample. The mass spectrometer signal is monitored as a function of time after release of the isopropanol alcohol (IPA) vapor to determine breakthrough time and vapor concentrations. Background levels were recorded and then the IPA introduction initiated after 60 minutes. A LabVIEW program from National Instruments™ was set up to make the turning on and off of the saturated vapor more precise and repeatable. The solvent vapor diffusivity is computed through the solid sample using steady state concentrations of solvent in the saturated vapor and nitrogen gas.

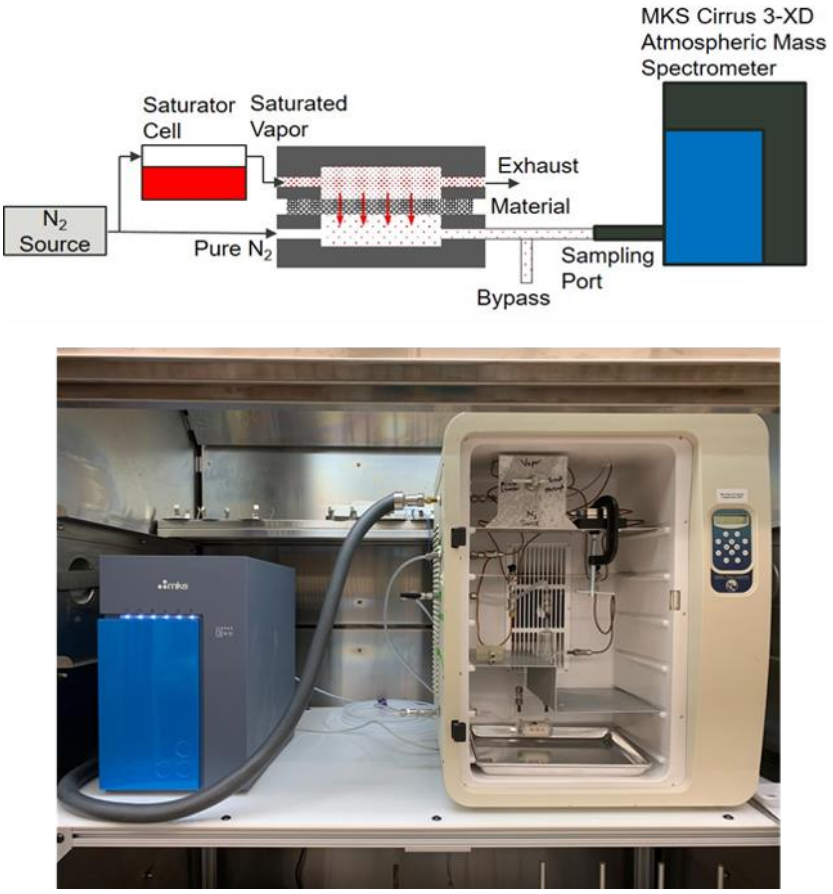


**Figure 2. (top) Design for breakthrough measurements. Schematic of the finalized design structure. (bottom) Photograph of the lab set-up within engineering controls.**

## 3. RESULTS AND DISCUSSION

Our approach, using the newly developed skeletonization methods, focused on streamlining the collected micro-CT scans involving billions of pixels into a skeleton of voids. The computational code developed allowed for extraction of the voxels that correspond to voids. The end product of this lengthy progress is summarized in the computational modeling Figure 3a-f. These newly developed algorithms account for the interconnectedness of the pores and identified how many new paths become accessible as migrating molecules get smaller.

The skeleton void structure and analysis process shown in Figure 3 represents one of the 3D-printed samples analyzed, in this case the PC-ABS sample utilizing the FDM method. In Figure 3a, a binarized voxel matrix is shown, where the void space, or void voxels, are shown in grayscale. The length of one side of the cube is 1,890 µm. In Figure 3b through Figure 3d, a color range legend indicates the thickness of the skeletonized voxels at different points of view. The voxel thickness regions closer to the surface are bluer and as small as 13 µm, while the voxel thickness regions far from the surface are in red and as large as 70 µm. For real life scale comparisons, a 13 µm thick voxel pathway is the size between a human red blood cell and a pollen spore, while a thick void pathway closer to 70 µm is about the diameter of an average human hair. Beyond just void sizes, the skeletonization reveals every connected path from one side of the material to the other. This allows for interrogation of the sample for detailed information. Application of Fourier transforms to our 3D grid of voids enabled us to find the frequency of repeating void structures of approximately 310 µm, with the most dominant length scale corresponding to a period of 291 µm.

From this periodic structure, we infer that the voids arise from the additive manufacturing process, as opposed to the material itself. This is just one snapshot. We need a systematic way to extract all length scales of periodicity in order to inform changes in 3D printing process settings.

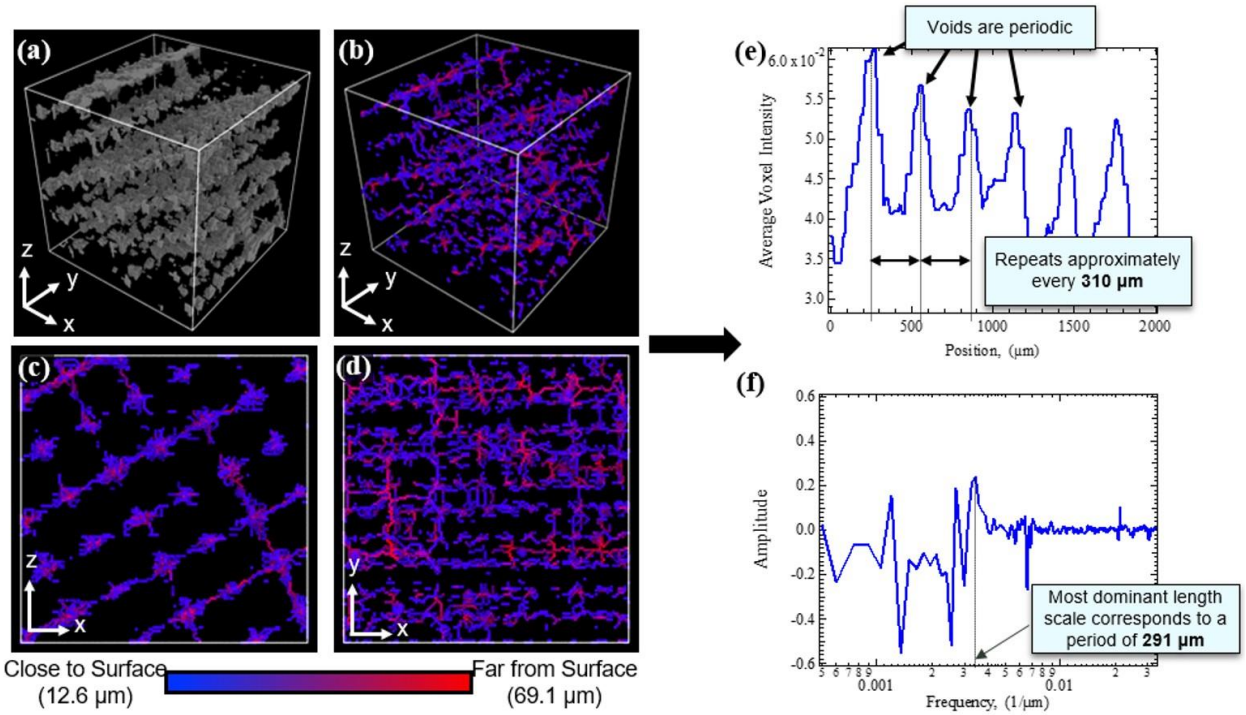


**Figure 3. Detailed 3D analysis of micro-CT scan data. (a) Binarized 3D voxel matrix where solid voxels are made transparent and void voxels are shown in gray. (b) Perspective view of a skeleton of 3D voxel matrix where color represents thickness of the original void structure. Color of skeleton indicates the thickness of the skeletonized void region, ranging from blue for narrow to red for wide. (c) A front view of the void skeleton. (d) A top-down view of the void skeleton. Length of each side of cube shown in (a)–(d) is 1,890 µm. The thickness of periodic void networks is approximately 60 µm. (e) Average void voxel intensity, averaged over *y*- and *z*-directions, as a function of position in the *x*-direction. We observe peaks repeating every 290–300 µm along the *x*-direction. (f) Fourier transform of the average void voxel intensity in (e). The frequency of the most dominant peak, indicated by the black dotted line, represents the most prominent frequency in voxel intensities, which corresponds to a period of 291 µm.**

In Figure 4, thus far, we have focused on the computational modelling of three samples: PC-ABS, glass-filled nylon, and an EPU40, each printed using a different additive manufacturing technique. Skeletonization analysis of the micro-CT data from these three samples indicate that all three samples contain periodic void structures much larger than the molecular length scale, suggesting these voids are related to the 3D manufacturing process. The PC-ABS, printed via FDM, has a lattice-like interconnected void structure. The glass-filled nylon, printed via SLS, has a periodic, spherical, and disconnected void structure. The EPU40, printed via SLA, has a periodic, interconnected void structure with a distinct shape. These results form a foundation from which we can move forward in FY21 with a couple of key questions. The first question is how we can exert control over the periodic structure, and thus the breakthrough time, by controlling the manufacturing process; conversely, can we bound the breakthrough time based on the material. However, our most recent experimental data results indicate that there is a secondary transport process that emerges.

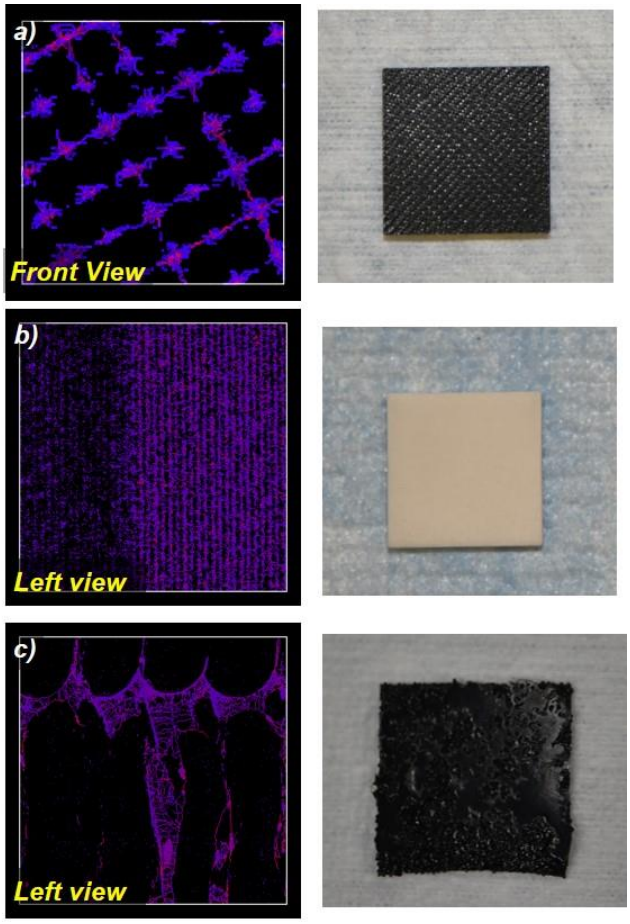


**Figure 4. Void structure analyzed via skeletonization of void voxels. (a) PC-ABS printed via FDM. (b) Glass-filled nylon via SLS. (c) EPU40 via SLA.**

Our FY19 work found variation in breakthrough time depending on which of the three materials we tested, which ranged from almost instantaneous to an hour. If we put these in order of fastest to slowest transient breakthrough time, PC-ABS (FDM) > glass-filled nylon (SLS) > EPU40 (SLA). The shape of that profile was consistent with our model of migration through interconnected, macromolecular sized pores that we have been constantly modifying through FY20. This combination validated our ability to measure and model pore structure at the microscale and connect it to transport at the macroscale. An example of this quantitative agreement is shown in Figure 5.

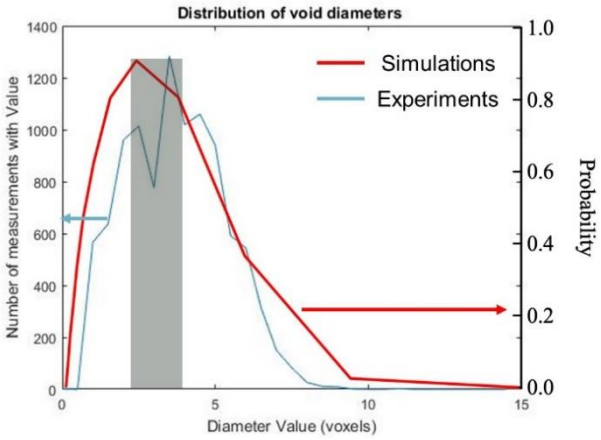


**Figure 5. Validation of computational modelling capabilities compared to experimental data. The grey box indicates the most probable void size is approximately 39 µm. However, the void size distribution indicates many smaller voids, suggesting that detailed prediction of breakthrough requires quantitative description of pore connectedness, or tortuosity.**

Our most recent breakthrough measurement results are shown in Figure 6. In that set of data, the breakthrough magnitude (in molar flux of the solvent) is shown on the vertical *y*-axis versus time on the horizontal *x*-axis, for each of the three 3D-printed materials. Two chemicals were tested, methanol (MeOH) shown in red and IPA shown in blue for each printed method. For monitoring the breakthrough magnitude (*y*-axis) of each solvent, the mass to charge ratio was integrated over the corresponding range for each chemical (30.2–31.2 for MeOH and 44–44.5 for IPA). Independent calibration experiments were run for each solvent to enable conversion of the peak area to a partial pressure, which in turn was used to compute the molar flux using the volumetric flow rate of the sweep $N_2$ gas flow and the ideal gas law. For the time scale of the breakthrough measurements (*x*-axis), we expanded the run times up to 48 hours, and in certain cases 72 hours; in the plots, we truncated this as there was no observed changes beyond the truncation point.

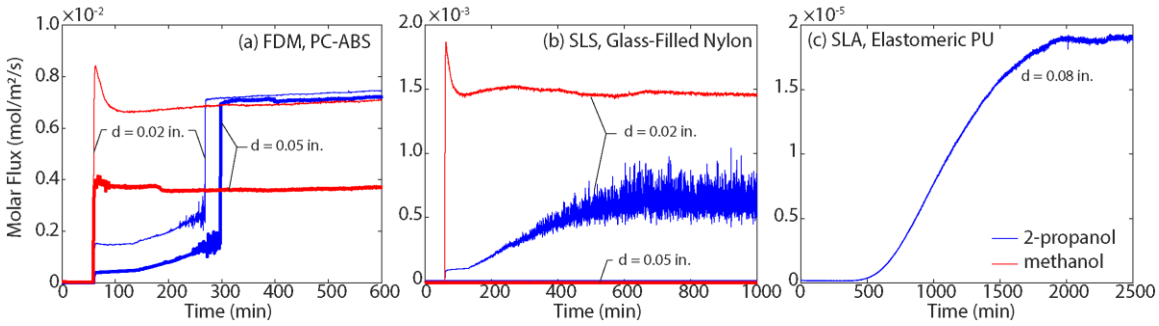


**Figure 6. The measured breakthrough dynamics of methanol (red) and IPA (blue) in (a) PC-ABS samples printed via FDM show up to two breakthrough regimes depending on probe solvent; (b) Glass-filled nylon samples printed via SLS show only one near instantaneous breakthrough regime with probe solvents, or at thicker samples no breakthrough at all; and (c) EPU40 samples printed via SLA show only one very gradual breakthrough regime with probe solvents after 72 hours of exposure. Thickness of lines represent various thicknesses of samples (0.02 inch and 0.05 inch).**

First, in observations of the PC-ABS printed samples via FDM, up to two regimes of breakthrough were identified depending on the probe solvent. For MeOH (in red) only one breakthrough regime is observed, the first and near instantaneous breakthrough time. For the IPA (in blue) two regimes were identified. Additionally, these two regimes are consistently observed as the thickness of the FDM sample was increased, the thin line signifying the 0.02-inch thick sample and the thick line signifying the 0.05-inch thick sample. Both are shown to have identical behavior.

Comparing the MeOH and IPA breakthrough of PC-ABS in the first regime, the molar flux of MeOH is much higher, which could be explained by difference in molar volume. This second regime with the IPA, at about 250–300 minutes (4.5–5 hours), suggests a solution-diffusion, meaning a saturation point consistent with transport through the solid polymer. This sharp change suggests an anomalous (non-Fickian) diffusion. Analyzing in terms of glassy polymers, meaning the 3D-printed materials the polymeric chain is essentially frozen in place, there is the potential of unoccupied volumes of space (i.e., fixed cavities). The diffusion process is assumed to be very low and slow. In order for the IPA to move through the system, the molecules then must potentially jump from cavity to cavity, taking a much longer path and timescale to diffuse through the polymer compared to the interconnected pore network (the first regime). This also means that the IPA is being concentrated by the polymer. MeOH may not have this second regime because it may not be soluble in PC-ABS material.

Second, in observations with the glass-filled nylon printed samples via SLS method, no such secondary mechanism emerges, at least with breakthrough testing performed so far with both MeOH and IPA. Again, the MeOH breakthrough is almost immediate, but with an order of magnitude lower molar flux compared to the PC-ABS material. This could be explained by the less connected, smaller pores as observed in the micro-CT data results. Again, IPA is slower than MeOH, which could be because of molar volume. Furthermore, as indicated by the lack of data (lines shown at 0 along the axis), thicker samples of SLS have no reported breakthrough through 72 hours of exposure.

Lastly, in observations with the EPU40 printed samples via SLA method, the breakthrough of IPA is much more gradual, indicating a pure solution-diffusion mechanism. Breakthrough measurements of MeOH are currently being performed. These results anchor our future outlook for the coming year as we expand our computational modelling to include these newly observed experimental results of multiple breakthrough mechanisms.

## 4. CONCLUSIONS

Two significant advances were made in the progress in our second year. First, attaining representation of tortuosity via skeletonization algorithms facilitated the advancement of our computational modeling. The modelling allows the ability to (1) monitor individual migrating macromolecules within large groups and (2) construct a network using data from both experimental breakthrough measurement and micro-CT scans to closely replicate the real samples.

The second significant advance was the observation of two breakthrough regimes dependent on the 3D-printed material and solvent, in which the second mechanism revealed due to the modification of extending experimental methods to run operations up to 48–72 hours. As we plan to expand our chemical solvents for interrogation of the 3D-printed samples, the laboratory measurements give us validation points for our model, especially for replicating trends in transport properties of a series of solvents as a function of known porosity parameters. We can then continue modification based on the newest experimental results revealing a secondary migration mechanism and leverage this data to tune fabrication parameters for optimal material performance base on the application required.

## ACKNOWLEDGEMENTS

The authors thank the U.S. Army DEVCOM Chemical Biological Center for funding this work via the Surface Science Initiative Program (PE 0601102A Project VR9). The authors also thank the original principal investigator Dr. Jerry Cabalo, now at the Chemical Security Analysis Center at the Department of Homeland Security, and Dr. Harvey Tsang of DEVCOM ARL for assisting with the micro-CT measurements of the 3D-printed parts.

## REFERENCES

[1] Milley, M.; Esper, M. *The Army Strategy*; The U.S. Army: Washington D.C., 2018; pp 1–11.
[2] *3D Printing in FDA's Rapid Response to COVID-19. 2020*; U.S. Food & Drug Administration: U.S. Government Printing Office: Washington, DC, 2020.
[3] Mizokami, K. The U.S. Army Is Working on 3D Printed Body Armor. https://www.popularmechanics.com/military/research/a28425864/us-army-28425863d-printing-body-armor/ (accessed July 27, 2019), *Popular Mechanics*, July 18, 2019.
[4] Robson, S. Yokota airmen improve gas mask with 3D printer, potentially saving Air Force $8 million or more. https://www.stripes.com/news/yokota-airmen-improve-gas-mask-with-3d-printer-potentially-saving-air-force-8-million-or-more-1.531504 (accessed July 27, 2019), *Stars and Stripes*, June 7, 2018.
[5] Cerniglia, D.; Scafidi, M.; Pantano, A.; Rudlin, J. Inspection of additive-manufactured layered components. *Ultrasonics.* **2015**, *62*, pp 292–298.
[6] Lewis, G.K.; Schlienger, E. Practical considerations and capabilities for laser assisted direct metal deposition. *Mater. Des.* **2000**, *21* (4), pp 417–423.
[7] Zhang, D.; Niu, W.; Cao, X.; Liu, Z. Effect of standard heat treatment on the microstructure and mechanical properties of selective laser melting manufactured Inconel 718 Superalloy. *Mater. Sci. Eng., A.* **2015**, *644*, pp 32–40.
[8] Berg, S.; Rücker, M.; Ott, H.; Georgiadis, A.; van der Linde, H.; Enzmann, F.; Kersten, M.; Armstrong, R.T.; de With, S.; Becker, J.; Wiegmann, A. Connected pathway relative permeability from pore-scale imaging of imbibition. *Adv. Water Resour.* **2016**, *90*, pp 24–35.
[9] Ahrenholz, B.; Niessner, J.; Helmig, R.; Krafczyk, M. Pore-scale determination of parameters for macroscale modeling of evaporation processes in porous media. *Water Resour. Res.* **2011**, *47* (7), W07543.
[10] Plimpton, S. Fast Parallel Algorithms for Short-Range Molecular Dynamics. *J. Comput. Phys.* **1995**, *117* (1), pp 1–19.
[11] Cao, J.; Tagliasacchi, A.; Olson, M.; Zhang, H.; Su, Z. Point Cloud Skeletons via Laplacian Based Contraction. In *Proceedings of the SMI 2010 Shape Modeling International Conference,* Aix-en-Provence, France, 21-23 June 2010; IEEE Computer Society, 2010; Vol 1, pp 187–197.
[12] Lee, T.-C.; Kashyap, R.L.; Chu, C.-N. Building skeleton models via 3-D medial surface/axis thinning algorithms. *CVGIP Graph. Model. Image Process.* **1994**, *56* (6), pp 462–478.
[13] Arcelli, C.; Sanniti di Baja, G.; Serino, L. Distance-driven skeletonization in voxel images. *IEEE Transactions on Pattern Analysis and Machine Intelligence.* **2011**, *33* (4), pp 709–720.

# A combined density functional theory and grand canonical Monte Carlo approach to modeling multi-component adsorption

Ivan O. Iordanov[a]*, Trenton M. Tovar[b], Lawford Hatcher[c], Jared B. DeCoste[a]
[a]U.S. Army Combat Capabilities Development Command Chemical Biological Center, Research & Technology Directorate, 8198 Blackhawk Rd, Aberdeen Proving Ground, MD 21010
[b]Leidos, 1750 President St, Reston, VA 20190
[c]Minority Undergraduate Student Internship Program, 8198 Blackhawk Rd, Aberdeen Proving Ground, MD 21010

## ABSTRACT

Novel nano-scale materials often require computational support in order to provide a mechanistic understanding of their unusual properties. Probing adsorption of gases in nanoporous materials typically requires calculating both thermodynamic properties through classical methods and local binding energies calculated with quantum methods. In this work, we use grand canonical Monte Carlo and density functional theory methods to examine the binding of small polar and non-polar gases on ZIF-8 and the binding of carfentanil in a wide variety of metal-organic frameworks. We find that the polarity of the gas does not have a significant effect on the adsorption loading in ZIF-8. We also find experimentally that there is an atypical time-gated chemisorption reaction for NO adsorbed on UiO-66-$NH_2$. Finally, we look at the relationship between the binding energy of the opiate carfentanil, and the size of the pores of metal-organic frameworks. The result is a volcano plot—showing the optimal pore size for binding of carfentanil to be commensurate with its size, ~4.5 Å.

**Keywords:** density functional theory, computational chemistry, adsorption, metal-organic frameworks, grand canonical Monte Carlo, porous materials

## 1. INTRODUCTION

Adsorption in porous materials has numerous diverse applications ranging from filtration of toxic chemicals, to gas separation and $CO_2$ sequestration. Given the importance of porous materials, there has been significant interest in improving porous materials—such as amorphous carbons or zeolites—as well as inventing new classes of porous materials. Metal-organic frameworks (MOFs) are a relatively new class of porous materials invented by the Omar Yaghi group.[1] MOFs are a modular material consisting of inorganic metallic centers called secondary building units (SBU) connected by organic linkers. By changing out the linkers or SBUs, nearly infinite combinations of MOFs can be created, allowing for nearly endless variation in the properties of the material. The combination of the number of possible MOF structures, their crystallinity, as well as the intrinsic dependence of their properties on their atomistic structure make MOFs an excellent class of materials for investigation and optimization though computational means.

Extensive high-throughput computational studies have been done, searching for a MOF optimal for a particular application (e.g., $CO_2$ sequestration)[2,3] or property (e.g., high surface area).[4] These studies enable relatively fast screening of thousands of MOFs, which would be prohibitively difficult to do solely experimentally. It is also common practice to include hypothetical MOFs,[5] or functionalized MOFs that have not been currently synthesized, allowing computational studies to guide future synthesis when optimizing for a particular purpose. Furthermore, due to the complex geometry and chemistry of these structures, computational studies are often done in conjunction with experimental work in order to jointly provide mechanistic understanding. Classical forcefield methods, such as the grand canonical Monte Carlo (GCMC) method, are typically used when modeling thermodynamics-related properties of MOFs, such as adsorption and diffusion, as well as structural motifs like defects that can have patterns on a multiple-unit cell-length scale. On the other hand, chemical reactions and detailed structural analysis of individual unit cells are typically done using density functional theory (DFT) due to its high accuracy and ability to handle chemical reactions. In this work, we use both methods to study adsorption within MOFs, with the goal of improving the adsorption of weakly interacting species within MOFs.

## 2. METHODS

### 2.1 Density functional theory

DFT is an *ab initio* quantum chemical method used to calculate atomic properties with high accuracy. Unlike previous quantum mechanics-based methods—such as configuration interaction—in DFT, the total energy is a functional of the total electron density instead of the multi-electron wavefunction.[6] This simplification makes much larger simulations feasible, while typically maintaining a similar level of precision as other quantum mechanics-based methods. The primary approximation in DFT is in the treatment of the exchange and correlation interactions between electrons, which is approximated through different exchange and correlation functionals. Multiple functionals have been developed over the years[7] in an attempt to improve the accuracy of DFT for different classes of problems. Due to the large size and crystalline nature of MOFs and most other porous materials, crystalline MOF calculations are usually performed using the Perdew-Burke-Ernzerhof (PBE) functional.[8] PBE is one of the oldest, fastest, and most widely implemented generalized gradient approximation functionals, with a generally comparable accuracy to other generalized gradient approximation functionals, and we have used it in all of the calculations in this work.

Due to the crystallinity of MOFs, we have elected to use plane-wave basis sets within periodic boundary conditions to model the full unit cell of the MOF structure. The calculations were done using the open source Quantum Espresso code, which implements plane-wave DFT and many related properties calculations. The lattice vectors are taken from experimental X-ray diffraction measurements and used as-is; although, we have checked the lattice parameters by running cell relaxation calculations to confirm that there are no significant distortions. Electron orbitals are described using mixed pseudopotentials from the standard solid-state pseudopotentials efficiency database,[9] with 50/400 Ry cutoffs for the wavefunctions/electron density. Initially, calculations were also performed using the projector augmented wave pseudopotentials included with Quantum Espresso. The difference in binding energies for adsorbates depending on the pseudopotential used were less than 0.01 eV. All calculations included a semi-empirical van der Waals correction due to Grimme et al.[10] because of the importance of van der Waals interactions for physisorption. Due to the size of the cells, all calculations only included the Γ k-point.

### 2.2 Grand canonical Monte Carlo

While DFT has many advantages in atomistic simulations, it is difficult to run DFT simulations on time scales long enough to provide meaningful statistical ensemble averages for thermodynamic properties, like temperature or pressure of gases. In order to run long/large enough simulations, the quantum interactions between electrons must be approximated using classical forcefield potentials. GCMC simulations are the primary framework for full-scale simulations of adsorption. Using classical forcefields, simulations can be run for any temperature/pressure combination, allowing for full isotherms to be simulated through a series of calculations. GCMC calculations were done using the RASPA software package,[11] using a combination of built-in and TraPPE potentials[12] for the adsorbates. The framework is kept fixed, thus not needing a forcefield parametrization, and the built-in RASPA generic MOF values are used for the Lennard-Jones parametrization.

### 2.3 Isotherms and synthesis

Zeolitic imidazolate framework-8 (ZIF-8) was synthesized as described by Pan et al.[13] Separate aqueous solutions of $Zn(NO_3)_2{\cdot}6H_2O$ and 2-methylimidazole were mixed by stirring at room temperature for 1 hour. The product was collected by centrifuging and was washed three times with deionized water before methanol exchange. Isotherms for CO and NO were measured on a Micromeritics® 3Flex 3500 instrument. Before measurements, all samples were degassed under vacuum at 120 °C to remove water and record an accurate weight.

## 3. RESULTS

### 3.1 Adsorption in ZIF-8

Initial work focused on adsorption of small polar and non-polar gases in ZIF-8. ZIF-8 consists of small (~10 Å-diameter) pores containing zinc metal centers that are connected with imidazole linkers.[14] ZIFs can be considered a subset of MOFs with more restrictive SBU/linker combinations; they have been investigated intensely due to their topological similarity to zeolites. Our initial hypothesis was that there will be stronger binding between the polar gases and the framework compared to the non-polar ones.

DFT calculations (Figure 1) show that there is no correlation between polarity of the gas and its binding energy. The most likely reason is that the van der Waals interactions dominate the overall binding, due to relatively small or inaccessible framework dipole moments. Examining the binding orientations and locations of the adsorbates (Figure 2) confirms that the optimal binding is near the linkers, optimizing the van der Waals interactions through close proximity with multiple parts of the framework. The binding geometry suggests that the binding energy could be increased by creating pores or other geometric motifs with sizes commensurate with the adsorbate size, which we will consider in Section 3.3. Adsorption isotherm experiments broadly confirmed the computational results, showing that there is no particular increase in adsorption loading with polarity.

| | $CH_4$ | $CO_2$ | CO | NO | $N_2$ | $O_2$ |
|---|---|---|---|---|---|---|
| DFT BE (eV) | 0.196 | 0.227 | 0.191 | 0.185 | 0.172 | 0.267 |
| Loading 0.01 bar | 0.004 | 0.009 | 0.001 | | | |
| Loading 0.1 bar | 0.330 | 0.617 | 0.017 | | | |

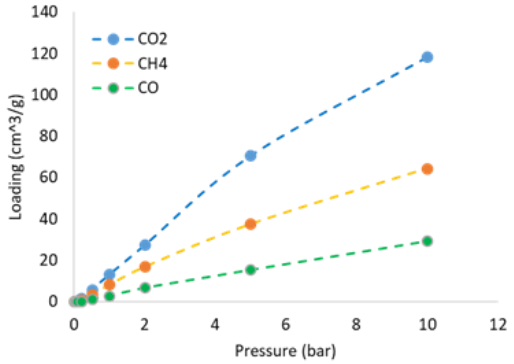


**Figure 1. (left) DFT binding energies and low pressure GCMC adsorption loadings for polar and non-polar gases. GCMC adsorption values follow same ordering as DFT binding energies. (right) Full GCMC isotherms showing adsorption at higher pressures.**

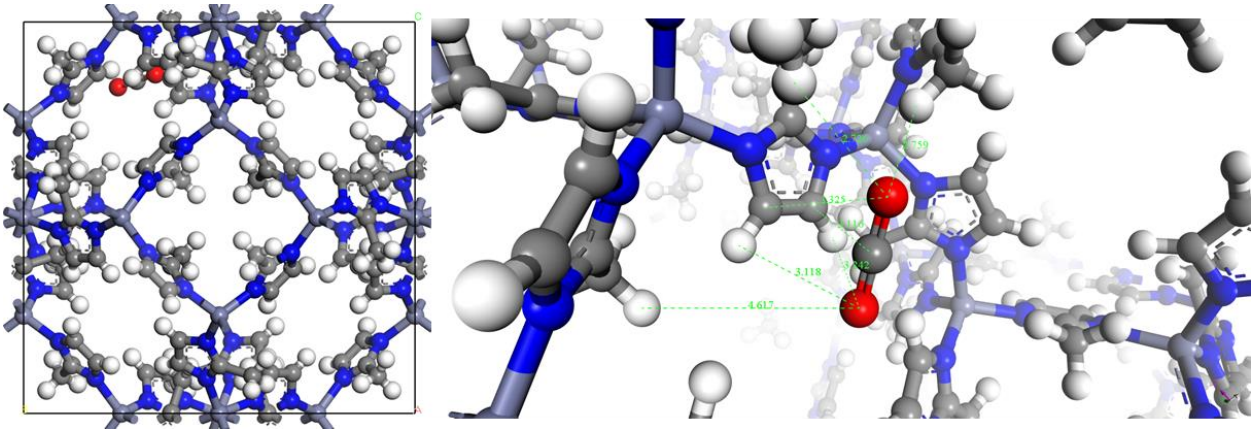

**Figure 2. $CO_2$ adsorption in ZIF-8. Full unit cell on the left, zoom in on binding site on right. Note the close proximity of multiple linkers to the adsorbate at the binding site, showing how "enveloping" sites can improve van der Waals binding energy.**

### 3.2 NO adsorption and reaction in UiO-66-$NH_2$

Subsequent to our work on adsorption of polar and non-polar gases in ZIF-8, we ran an adsorption isotherm for NO within UiO-66-$NH_2$, a very well-studied MOF with potential filtration applications. NO was found to have a rather peculiar isotherm (Figure 3), with very low uptake at low pressures, followed by an irreversible step uptake at higher pressures. This dynamic is in contrast to the NO isotherms on ZIF-8 and UiO-66, both of which showed reversible weak physisorption. The initial low uptake of the NO isotherm on UiO-66-$NH_2$ indicates an initiation period before chemisorption can occur. This is very different than previously reported isotherms of NO on MOFs. Typically, MOFs with coordinatively unsaturated metal sites show a step isotherm; however, the step occurs immediately at the lowest measured pressure point.[15] When the sample is re-evacuated, a second isotherm shows only reversible physisorption. Interestingly, the physisorptive uptake is higher than the initial uptake on a fresh UiO-66-$NH_2$ sample; meaning, the treated sample has a stronger interaction with NO.

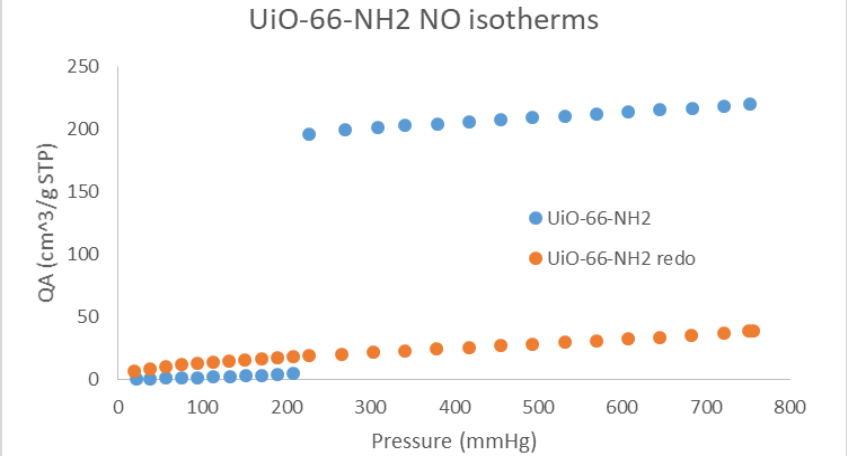


**Figure 3. NO isotherms on fresh UiO-66-$NH_2$ (blue) and UiO-66-$NH_2$ already treated with NO (orange).**

Reaction of NO with pendant amines has been shown for IRMOF-3 and UMCM-1-$NH_2$.[16] However, the reaction takes place at high NO pressures, and an isotherm was never measured. To explore the pressure effect, UiO-66-$NH_2$ was exposed to NO at pressures of 189 mmHg (below the step) and 760 mmHg (above the step). The two samples were digested with nitric acid and the solution was measured by nuclear magnetic resonance (NMR), shown in Figure 4. For both samples, NMR spectroscopy shows the doublet peaks of the bdc-$NH_2$ linker shift from an untreated sample. However, the shift is different for each treatment pressure meaning that different species formed at each pressure. This indicates that the initiation phase forms a stable complex before reaction to the final product. $N_2$ isotherms after the reactions show only ~25 % lower surface areas, suggesting UiO-66-$NH_2$ maintains most of its structure after the reaction. *In situ* diffuse reflectance infrared Fourier transform spectroscopy experiments and further DFT/GCMC calculations are planned to further explore the reaction.

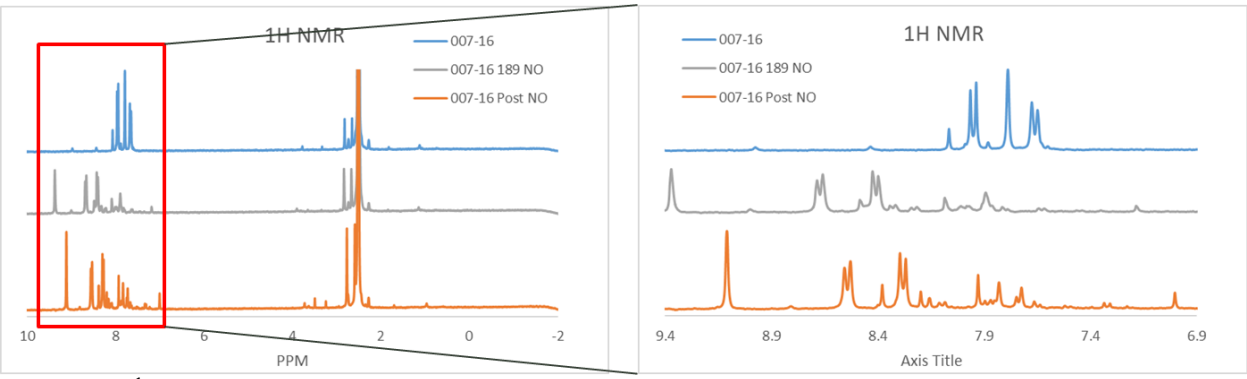


**Figure 4. $^1$H NMR of UiO-66-$NH_2$ (blue), UiO-66-$NH_2$ treated at 189 mmHg NO (gray), and UiO-66-$NH_2$ treated at 760 mmHg (orange).**

### 3.3 Pore size effect for adsorption

Pore size effects are known to have important effects in gas adsorption and separations applications, for example, in adsorption in the hierarchical pores of amorphous carbon and in the cracking of hydrocarbons using zeolites in the petrochemical industry. However, there has been comparatively little research in tailoring nano-scale pores in MOFs in order to increase physisorption adsorption at low pressures. Most research has focused on larger pores for increased adsorption at high pressure or chemical modifications for improved binding. In this section, we describe our initial work in investigating this approach to improve adsorption.

#### *3.3.1 Pore size effect for carfentanil*

Carfentanil is a dangerous opiate—approximately 10,000 times more potent than morphine.[17] Understanding how it interacts with surfaces and how to protect personnel or neutralize it is of general interest to the Army. Aside from its practical importance, it is also a useful test molecule for improving adsorption through pore size modulation due to its large size and generally unreactive nature. Therefore, we have done DFT binding energy calculations for carfentanil in a variety of MOFs, looking to establish a pore size verses binding energy relationship.

The results can be seen in Figure 5, which shows a typical volcano plot relationship between pore size and binding energy, centered around the approximate radius of carfentanil, ~4.5 Å. The pore sizes shown were measured as the radii of spheres contained within the pores and not allowed to overlap the van der Waals radii of the surrounding atoms. Such a measurement can lead to some discrepancy as the real pore geometry deviates from the spherical shape, but it approximates most of the cage-like pores of MOFs and provides a consistent basis for comparison. Given that the adsorbate itself does not have a perfectly spherical shape and is able to bend to accommodate geometrical features, it is not expected for there to be perfect correlation between pore size and adsorbate size, but the results are quite consistent with a pore size/adsorbate size binding improvement effect. Note that some MOFs have multiple pores with different sizes and are listed at different locations depending on each pore size.

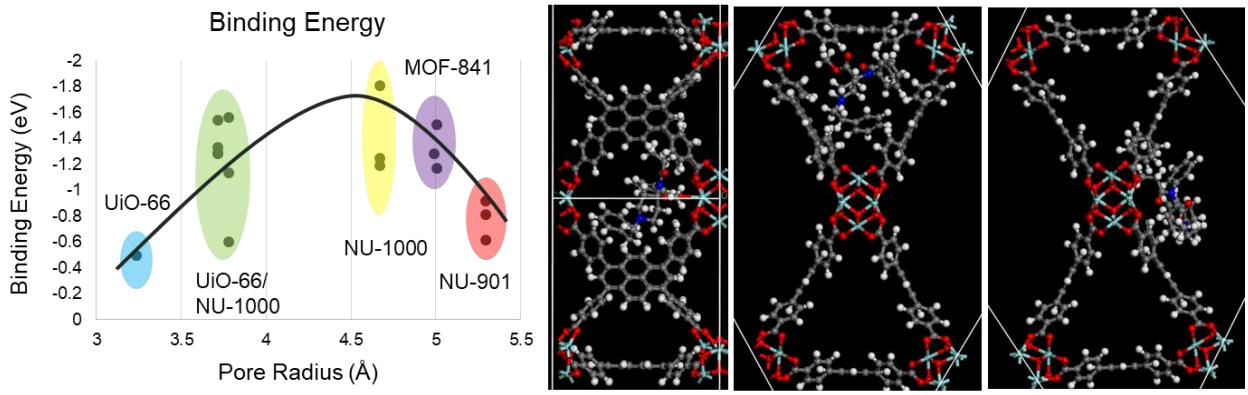


**Figure 5. Binding energy of carfentanil versus MOF pore size. Volcano plot curve shows maximum near carfentanil radius (4.5 Å). (left) Largest pore of NU-1000 is not shown, although it is consistent with the trend, with a binding energy of 0.7 eV and a 14.4 Å pore radius. (right) Carfentanil within the three pores of NU-1000; smallest, medium, and largest from left to right.**

The adsorption of carfentanil is primarily due to van der Waals interactions; however, we also find that carfentanil can create a hydrogen bond between the oxygen in the ester group and undercoordinated metal sites on $Zr_6O_8$ SBUs, if the geometry allows it. By twisting the carfentanil structure to allow/deny hydrogen bond formation, its contribution to the total binding can be approximated as ~0.5 eV—significant but still lower than the overall van der Waals binding. Multiple binding energies are shown in Figure 5 for most pores since multiple binding orientation converged, showing the spread in binding energy due purely to binding orientation as opposed to pore size. The inclusion of hydrogen bonding (or lack thereof) is the reason for the larger spread in binding energies shown for NU-1000 and UiO-66.

Overall, these results show a promising pathway to improving physisorption of analytes in MOFs in a way that will be size-selective as opposed to reliant on chemical reactivity. This approach could improve adsorption of chemical warfare agents in protective equipment, since chemical warfare agents have larger sizes than most ambient chemicals, and pore sizes could be tuned to improve their adsorption while allowing smaller molecules through. Future work will further investigate this possibility and use this as a basis for future projects.

### *3.3.2 Modifying pore size through modulators*

In the previous section, we described the process of changing out different MOFs in order to optimize the pore size to bind a particular analyte with a similar size. However, instead of changing the MOF itself, there are two other options that allow for finer control of pore sizes without changing the underlying MOF structure and its topology. The first is to attach functional groups to the MOF linkers. Functional groups are typically attached to the benzene rings of the linkers in order to change the chemical reactivity of the MOF; however, attaching bulky hydrocarbons should allow for changes in pore sizes without changing the chemical properties of the material. The second option is to attach so-called "modulators" to the undercoordinated sites that are part of the normal topology of some MOFs—such as NU-901 and NU-1000. Both MOFs have four unoccupied sites, each of which allows for the attachment of a linker through two carboxylate acids. If a modulator with just one carboxylic acid is attached, we can decrease the size of the pores or change their shape without changing the connectivity of the pore network. We have already done DFT calculations on the binding energies of the modulators to the SBU of previously synthesized NU-901 analogs (Figure 6) and are looking into using these optimized structures for binding energy calculations of hydrocarbons. The combination of functionalizing linkers and attaching modulators should allow for fine modulation of pore sizes and improved optimization of the binding of different analytes.

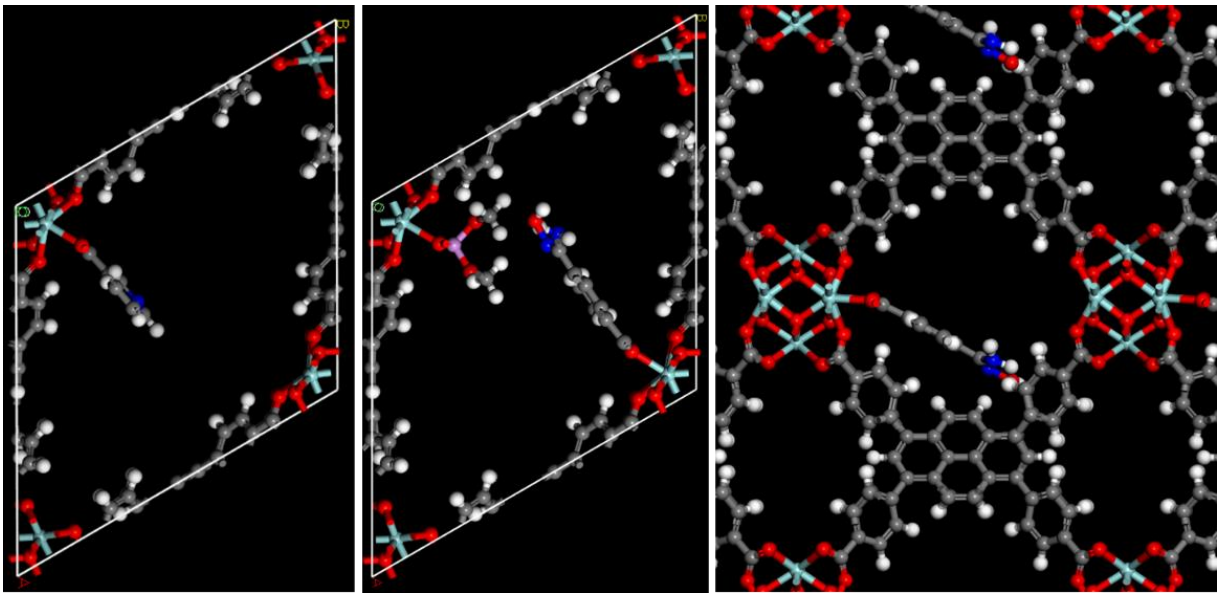

**Figure 6. (left) Modulators attached to NU-901: pyridine, (middle) DMP and oxime, and (right) oxime. Note that NU-901 has two pores and, depending on which of the four sites on the SBU the modulator is attached to, it can extend in either pore. The two figures on the left show modulators in the large pore, whereas the last rotates the view through 90 degrees to show the small pore with a modulator nearly spanning the length of the pore. Addition of modulators that are approximately as large as the pore can effectively split the pore and effectively increase the surface area of the MOF.**

## 4. CONCLUSION

Computational and experimental methods were used to investigate and improve adsorption in MOFs. Initial work focused on small polar/non-polar gases in ZIF-8, showing that van der Waals interactions dominate adsorption even for polar gases, and that the preferred binding orientation allows for interactions with multiple linkers to improve the binding. Experimental isotherms confirmed that polarity does not have a large effect in this case, but we also found an atypical chemisorption/reaction of NO on UiO-66-$NH_2$. In this case, there is a delay between dosing and reaction, as well as possible pressure dependence of the products. Finally, we have looked into improving physisorption by matching pore size with adsorbate size, specifically in the case of carfentanil. A volcano plot showed the expected binding energy max near the radius of the adsorbate. Further work will focus on finer modulation of pore sizes through use of modulators and functionalization for smaller adsorbate molecules.

## ACKNOWLEDGMENTS

Funding was provided by the U.S. Army via the Surface Science Initiative Program (PE 0601102A Project VR9) at the U.S. Army Combat Capabilities Development Command Chemical Biological Center. This research was performed while Lawford Hatcher was a Minority Undergraduate Student Internship Program student at the U.S. Army Combat Capabilities Development Command Chemical Biological Center.

## REFERENCES

[1] Zhou, H.-C.; Long, J.R.; Yaghi, O.M. Introduction to Metal–Organic Frameworks. *Chem. Rev.* **2012**, *112* (2), pp 673–674.

[2] Jasuja, H.; Zang, J.; Sholl, D.S.; Walton, K.S. Rational Tuning of Water Vapor and $CO_2$ Adsorption in Highly Stable Zr-Based MOFs. *J. Phys. Chem. C.* **2012**, *116* (44), pp 23526–23532.

[3] Han, S.; Huang, Y.; Watanabe, T.; Dai, Y.; Walton, K.S.; Nair, S.; Sholl, D.S.; Meredith, J.C. High-Throughput Screening of Metal–Organic Frameworks for $CO_2$ Separation. *ACS Comb. Sci.* **2012**, *14* (4), pp 263–267.

[4] Colón, Y.J.; Snurr, R.Q. High-throughput computational screening of metal–organic frameworks. *Chem. Soc. Rev*. **2014**, *43*, pp 5735–5749.
[5] Wilmer, C.E.; Leaf, M.; Lee, C.Y.; Farha, O.K.; Hauser, B.G.; Hupp, J.T.; Snurr, R.Q. Large-scale screening of hypothetical metal–organic frameworks. *Nat. Chem.* **2012**, *4*, pp 83–89.
[6] Kohn, W.; Sham, L.J. Self-Consistent Equations Including Exchange and Correlation Effects. *Phys. Rev.* **1965**, *140* (4A) pp A1133–A1138.
[7] Yu, H.S.; He, X.; Li, S.L; Truhlar, D.G. MN15: A Kohn–Sham global-hybrid exchange–correlation density functional with broad accuracy for multi-reference and single-reference systems and noncovalent interactions. *Chem. Sci.* **2016**, *7* (8), pp 5032–5051.
[8] Perdew, J.P.; Burke, K.; Ernzerhof, M. Generalized Gradient Approximation Made Simple. *Phys. Rev. Lett.* **1996**, *77* (18), pp 3865–3868.
[9] Lejaeghere, K.; Bihlmayer, G.; Björkman, T.; Blaha, P.; Blügel, S.; Blum, V.; Caliste, D.; Castelli, I.E.; Clark, S.J.; Dal Corso, A.; de Gironcoli, S.; Deutsch, T.; Dewhurst, J.K.; Di Marco, I.; Draxl, C.; Dułak, M.; Eriksson, O.; Flores-Livas, J.A.; Garrity, K.F.; Genovese, L.; Giannozzi, P.; Giantomassi, M.; Goedecker, S.; Gonze, X.; Grånäs, O.; Gross, E.K.U.; Gulans, A.; Gygi, F.; Hamann, D.R.; Hasnip, P.J.; Holzwarth, N.A.W.; Iuşan, D.; Jochym, D.M.; Jollet, F.; Jones, D.; Kresse, G.; Koepernik, K.; Küçükbenli, E.; Kvashnin, Y.O.; Locht, I.L.M.; Lubeck, S.; Marsman, M.; Marzari, N.; Nitzsche, U.; Nordström, L.; Ozaki, T.; Paulatto, L.; Pickard, C.J.; Poelmans, W.; Probert, M.I.J.; Refson, K.; Richter, M.; Rignanese, G.-M.; Saha, S.; Scheffler, M.; Schlipf, M.; Schwarz, K.; Sharma, S.; Tavazza, F.; Thunström, P.; Tkatchenko, A.; Torrent, M.; Vanderbilt, D.; van Setten M.J.; Van Speybroeck, V.; Wills, J.M.; Yates, J.R.; Zhang, G.-X.; Cottenier, S. Reproducibility in density functional theory calculations of solids. *Science*, **2016**, *351* (6280), pp aad3000-1–aad3000-7.
[10] Grimme, S.; Ehrlich, S.; Goerigk, L. Effect of the damping function in dispersion corrected density functional theory. *J. Comput. Chem.* **2011**, *32* (7), pp 1456–1465.
[11] Dubbeldam, D.; Calero, S.; Ellis, D.E.; Snurr, R.Q. RASPA: molecular simulation software for adsorption and diffusion in flexible nanoporous materials. *Mol. Simul.* **2015**, *42* (2), pp 81–101.
[12] Eggimann, B.L.; Sunnarborg, A.J.; Stern, H.D.; Bliss, A.P.; Siepmann, J.I. An online parameter and property database for the TraPPE force field. *Mol. Simul.* **2013**, *40* (1–3), pp 101–105.
[13] Pan, Y.; Liu, Y.; Zeng, G.; Zhao, L.; Lai, Z. Rapid synthesis of zeolitic imidazolate framework-8 (ZIF-8) nanocrystals in an aqueous system. *Chem. Comm.* **2011**, *47*, pp 2071–2073.
[14] Fairen-Jimenez, D.; Galvelis, R.; Torrisi, A.; Gellan, A.D.; Wharmby, M.T.; Wright, P.A.; Mellot-Draznieks, C.; Düren, T. Flexibility and swing effect on the adsorption of energy-related gases on ZIF-8: Combined experimental and simulation study. *Dalton Trans*, **2012**, *41* (35), pp 10752–10762.
[15] Xiao, B.; Wheatley, P.S.; Zhao, X.; Fletcher, A.J.; Fox, S.; Rossi, A.G.; Megson, I.L.; Bordiga, S.; Regli, L.; Thomas, K.M.; Morris, R.E. High-Capacity Hydrogen and Nitric Oxide Adsorption and Storage in a Metal-Organic Framework. *J. Am. Chem. Soc.* **2007**, *129* (5), pp 1203–1209.
[16] Nguyen, J.G.; Tanabe, K.K.; Cohen, S.M. Postsynthetic diazeniumdiolate formation and NO release from MOFs. *CrystEngComm.* **2010**, *12* (8), pp 2335–2338.
[17] George, A.G.; Lu, J.J.; Pisano, M.V.; Metz, J.; Erickson, T.B. Carfentanil-an ultra potent opioid. A*m. J. Emerg. Med*. **2010**, *28* (4), pp 530–532.